universität wien

DISSERTATION

Titel der Dissertation

„Thermoelectric Materials: Phase Equilibria and Crystal Structures“

Verfasserin

Navida Nasir

angestrebter akademischer Grad

Doktor der Naturwissenschaften (Dr. rer.nat.)

Wien, 2010

Studienkennzahl lt. Studienblatt:	A 091 419
Dissertationsgebiet lt. Studienblatt:	419 Chemie
Betreuerin / Betreuer:	Univ. Prof. Dr. Peter Franz Rogl

Dedicated to

My Son Abdur Rehman, to whom I love the most.

My Parents, without their prayers I couldn‘t accomplish this task

My husband, his understanding and support make this job possible.

Table of Content

Acknowledgements i
Abstract ii
Kurzfassung iv
1 Introduction 1
1.1 Thermoelectric effects 1
1.2 Thermoelectric Materials 2
1.3 Clathrates 3
1.4 Antimonides 5
1.5 Task for the Present Work 6
References 7
2 Experimental Techniques 11
2.1 General procedure for synthesis and characterization 11
2.2 Instruments 12
2.2.1 Arc Furnace 12
2.2.2 Ball Mill 13
2.2.3 Hot Press 13
2.2.4 X-Ray Diffraction 15
2.2.4.1 X-Ray Powder Diffractometer and Imaging Plate (IP) 15
2.2.4.2 Preparation of single crystals 16
2.2.4.3 AXS GADDS 17
2.2.4.4 Nonius Kappa diffractometer with area detector CCD 19
2.2.5 Electron Probe Micro Analyzer (EPMA) 20
2.3 Data Analysis 21
2.3.1 STRUKTURE 21
2.3.2 Rietveld Refinement (x-ray powder diffraction) 22
2.3.3 Structure Solutions (x-ray single crystal) 23
2.4 Physical Properties Measurements 24
2.4.1 Electrical resistivity measurements 24
2.4.2 Magnetic Properties Measurements 25
2.4.3 Specific Heat Measurements 26
2.5 References 26
3 Clathrates $Ba_8\{Zn,Cd\}xSi_{46-x}$, x~7: Synthesis and Crystal Structure 27

3.1 Introduction 27
3.2 Experimental 27
3.3 Results and Discussion 28
3.3.1 Crystal Structures of $Ba_8Zn_7Si_{39}$ and $Ba_8Cd_7Si_{39}$ 28
3.3.2 Homogeneity regions of clathrates $Ba_8\{Zn, Cd\}_xSi_{46-x}$ 32
3.4 Conculsion 32
References 33
4 Crystal Structure and Physical Properties of Quaternary Clathrates $Ba_8Zn_xGe_{46-x-y}Si_y$, $Ba_8(Zn,Cu)xGe_{46-x}$ and $Ba_8(Zn,Pd)_xGe_{46-x}$. 37
4.1 Introduction 37
4.2 Experimental 39
4.3 Results and Discussion 39
4.3.1 Crystal Structure of $Ba_8M_xZn_yGe_{46-x-y}$ (M = Pd, Cu) 39
4.3.2 Crystal Structures of the solid solution $Ba_8Zn_xGe_{46-x-y}Si_y$. 50
4.3.3 Phase equilibria in the quaternary systems Ba-(Pd,Cu)-Zn-Ge and Ba-Zn-Ge-Si 55
4.4 Conclusion 57
References 58
5 Synthesis and Characterization of $Ba_8Zn_xGe_{46-x}$ (x = 0, 2, 4, 6) and $Ba_8Ni_xZn_yGe_{46-x-y}$ Clathrates 60
5.1 Introduction 60
5.2 Experimental 60
5.3 Results and Discussion 61
5.4 Conclusion 63
References 65
6 Ternary Systems Sr – {Ni,Cu} – Si: Phase Equilibria and Crystal Structure of Ternary Phases. 67
6.1 Introduction 67
6.2 Experimental 67
6.3 Results and Discussion 68
6.3.1 Phase equilibria in the ternary systems Sr-Ni-Si and Sr-Cu-Si. 69
6.3.2 Crystal structure of ternary phases. 73
6.3.2.1 Ternary compounds with AlB_2 – type structure (τ_1). 74

6.3.2.2 Ternary compounds with the $BaNiSn_3$-structure type (τ_2). 74
6.3.2.3 Ternary compounds with the $ThCr_2Si_2$-structure type (τ_2)..... 75
6.3.2.4 Ternary compounds with the structure types related to $NaZn_{13}$ (τ3). 78
6.4 Conclusion 86
6.5 References 87
7 Crystal Structure of $EPCo_{5-x}Ge_9$ (EP≡Sr, Ba, Eu) 90
7.1 Introduction 90
7.2 Experimental 90
7.3 Results and Discussion 91
7.3.1 Crystal structure of $BaCo_{5-x}Ge_9$ (x=0.29). 92
7.3.2 Isotypic {Sr,Eu}$Co_{5-x}Ge_9$ (x~0.3). 93
7.4 Conclusion 99
References 100
8 Phase Equilibria in Systems Ce-M-Sb (M = Si, Ge, Sn) and Superstructure $Ce_{12}Ge_{9-x}Sb_{23-x}$ (x=3.8±0.1) 101
8.1 Introduction 101
8.2 Experimental 102
8.3 Results and Discussions 103
8.3.1 Binary boundary systems 103
8.3.1.1 The binary phase diagram germanium – antimony. 103
8.3.2 The crystal structure of $Ce_{12}Ge_{9-x}Sb_{23+x}$ 106
8.3.3 Phase equilibria in ternary systems Ce-M-Sb (M = Si, Ge, Sb)..... 114
8.3.3.1 Composition by EPMA 115
8.3.3.2 Composition by EPMA 118
8.4 Conclusions 122
References 123
9 The system Nd-Fe-Sb: Phase Equilibria, Crystal Structures and Physical Properties 125
9.1 Introduction 125
9.2 Experimental 126
9.3 Results and Discussion 127

9.3.1 Binary boundary systems 127
9.3.2 Phase equilibria in the Nd-Fe-Sb system 127
9.3.3 The crystal structure of τ_2 134
9.3.3.1 Crystal Structure of tetragonal τ_2 ($La_2Fe_{5-x}Sb_{10-y}$; x= 1.125; y=5.085)……134
9.3.3.2 Crystal Structure of the orthorhombic τ_2 ($Nd_2Fe_{7-x}Sb_{6-y}$; x=3.04, y=1.03)……...137
9.3.4 Crystal Structure of τ_3 –$Nd_3Fe_3Sb_7$ 145
9.3.5 Crystal Structure of τ_4- $NdFeSb_3$ 150
9.3.6 Magnetic and Transport Properties 151
9.4 Conclusions 156
References 157
10 Antimony rich corner of Ce-TM-Sb Systems (TM= Ti, Zr, Hf, V, Nb, Ta, Cr, Mo, W, Mn, Re, Cu, Ag, Zn, Cd) at 600 °C. 161
10.1 Introduction 161
10.2 Experimental 161
10.3 Results and Discussion 162
References 167
Summary 169
List of Publications 171
CURRICULUM VITAE 173

Acknowledgements

All praises to Almighty Allah, most beneficent, the most merciful who bestowed me with sight to observe and mind to think.

First of all I am greatly honored to express my deepest gratitude to Prof. Peter Rogl for giving me the opportunity to join his research group, for his guidance, valuable scientific discussions, and inspiring attitude throughout the project. I gratefully acknowledge Dr. A. Grytsiv for introducing me to each equipment, data evaluation software and valuable suggestions. His knowledge on phase equilibria, crystal structure and expertise in sample preparations always help me to keep the track. I am also thankful to Mrs. G. Rogl for getting us familiar with German language and especially grateful for her support in many other aspects of my life.

I am thankful to Dr. D. Kaczorowski from Inst. Low Temp. Str. Res., Wroclaw, Poland, for providing me the opportunity to use his experimental facilities. I am thankful to Prof. E. Bauer from Vienna University of Technology and his team for investigating my samples for physical properties evaluation. I am also thankful to Dr. Schmidt, Prof. A. Saccone, Itly, Prof. J. Wosik, Prof. G. E. Nauer, and Dr. Ningxin Zhang in CEST-ECHEM, and S. Puchegger for EPMA measurements. I am grateful to Prof. G. Giester and Prof. H. Effenberger from Inst. of Minr. Cryst. for measuring my single crystal specimens on x-ray diffractometer.

I am thankful to all my colleagues especially N. Melnychenko-Koblyuk, O. Sologub, for their help and cooperation. I am thankful to all my friends specially, Shahroz, Lubna, Azra, Freeha, Zahida, Saadia, Aneesa, Arjumand and an endless list, for their help and pleasant company which make my stay in Vienna memorable. I am especially grateful to Dr. Nabila, Dr. Navida and their family for continuous support and encouragement in all aspects of my life.

I wish to pay my humble thanks to my parents and my parents in law, my sisters, Saima and Samia and all other family members who remember me in their prayers, encourage and extend their full support and cooperation. I highly appreciate my father in law for his encouraging attitude to start my Ph. D.

Finally I could not find the words to express my heartiest feelings for my husband Nasir, his understanding and full support is indespensible in the accomplishment of this work, and my lovely son Abdur Rehman that he is my universe. I really enjoy every moment of my life that I spend with my family.

This project was supported by Higheer Education Commision of Pakistan and Austrian Exchange Service (OeaD) and Acadamic Cooperation and Mobility Unit (ACM), Austria.

Abstract

Global decline of natural energy sources has greatly diverted attention of the scientific community to search for alternative energy sources particularly those which can make use of the exhaust heat into useful energy. Thermoelectric materials have received great attention in this regard and two new classes of intermetallics "Skutterudites" and "Clathrates" are being considered as promising candidates for future thermoelectric applications. Information on phase diagrams and crystal structure of the compounds are mandatory to describe structure-property relationships completely. The present work aims to investigate ternary and quarternary alloy systems forming clathrates, skutterudites and/or antimonides, silicides and germinides and to provide complete information on phase equillibria, formation and the crystal structure of the ternary compounds in potentially thermoelectric systems.

Phase relations were established using light optical microscopy, x-ray diffraction and electron probe micro analysis on polished surfaces of the as cast and annealed alloys in the Sr-poor part of the ternary systems Sr–Ni–Si at 900 °C, Sr–Cu–Si at 800 °C, composition regions $CeSb_2$-Sb-M of the ternary systems Ce-M-Sb (M = Si, Ge, Sn) at 600-200°C , Nd-Fe-Sb system at 800 °C and quaternary system Ba-Pd-Zn-Ge at 800 °C and Sb rich corner of the Ce-TM-Sb (TM = Ti, Zr, Hf, V, Nb, Ta, Cr, Mo, W, Mn, Re, Cu, Ag, Au, Zn, Cd) at 600 °C . A connectivity scheme for the phase equilibria in the "Ba_8Ge_{46}" corner in Ba-Pd-Zn-Ge system at 800 °C has also been derived.

X-ray single crystal diffraction and x-ray powder diffraction were used to established crystal structure of new/unknown ternary compounds and to precisely determine the site occupations and site preference in clathrate solid solutions, $Ba_8Zn_xGe_{46-x-y}Si_y$, $Ba_8(Zn,Cu)_xGe_{46-x}$, and $Ba_8(Zn,Pd)_xGe_{46-x}$. The temperature dependent X-ray single crystal spectra for $Ba_8Zn_7Si_{39}$ (clathrate type I) define an Einstein mode, $\Theta_{E,U33}$ = 80 K. Detailed studies on crystal structures of more than 20 compounds were performed, out of which $SrNi_{9-x}Si_{4+x}$ (x=2.7,S.G. *P*4/*nbm*), $BaCo_{5-x}Ge_9$ (x=0.29, S. G. *Pnma*), $Ce_{12}Ge_{9-x}Sb_{23+x}$ (3.3<x<4.2, S.G. C222), $Nd_2Fe_{5-x}Sb_{6-y}$ (x= 1.04, y=1.025, S.G. *Immm*), $La_2Fe_{5-x}Sb_{6-y}$ (x=1.125,y=1.085, S.G. *I*4/*mmm*), $Nd_3Fe_3Sb_7$ (S.G. $P6_3/m$) adopt unique structure types. Group-subgroup relations were determined according to the Bärnighausen formalism for compounds related by symmetry reduction.

Physical properties comprising magnetization, resistivity and specific heat were measured for $RE_2Fe_{5-x}Sb_{10-y}$ (RE=Ce, Nd), $NdFeSb_3$ and $Nd_3Fe_3Sb_7$. $NdFeSb_3$ orders antiferromagnetically below ~3.0 K and the effective magnetic moment (3.68 μ_B) corresponds to free Nd^{+3}. Effective magnetic moments for $Nd_2Fe_{5-x}Sb_{10-y}$ and $Ce_2Fe_{5-x}Sb_{10-y}$ derived from MCW fits were attributed to contributions from both sublattices Nd^{+3} or Ce^{+3} and Fe^{+2}.

Kurzfassung

Die weltweite Abnahme von natürlichen Energiequellen hat die Aufmwerksamkeit der Wissenschafter auf die Suche nach alternativen Energiequellen gerichtet, speziell auf solche, die es möglich machen, Abgaswärme in brauchbare Energie umzusetzen. Thermoelektrische Materialien haben diesbezüglich große Aufmerksamkeit erhalten und zwei neue Klassen von Verbindungen, die Skutterudite und Clathrate, werden als viel versprechende Kandidaten für zukünftige thermoelektrische Anwendungen in Betracht gezogen. Informationen über Phasendiagramme und Kristallstrukturen dieser Verbindungen sind unerlässlich um die Zusammenhänge zwischen Struktur und Eigenschaft komplett zu beschreiben. Die vorliegende Arbeit hat das Ziel, ternäre und quaternäre Verbindungssysteme die Clathrate, Skutterudite und/oder Antimonide, Silicide und Germanide bilden zu untersuchen und eine ausführliche Information über Phasengleichgewicht, Bildung und Kristallstruktur von ternären Verbindungen in möglichen thermoelektrischen Systemen zu erstellen.

Phasenbeziehungen wurden ermittelt indem Lichtmikroskopie, Röntgenstreuung und elektronenmikroskopische Analysen an polierten Oberflächen von im Lichtbogen geschmolzenen und gesinterten Proben vorgenommen wurden und zwar im Sr-armen Teil des Sr-Ni-Si-Systems bei 900°C, des Sr-Cu-Si-Systems bei 800°C, im Phasenabschnitt $CeSb_2$-Sb-M von ternären Systemen Ce-M-Sb (M = Si, Ge, Sn) bei 600°-200° C, im Nd-Fe-Sb- System bei 800°C und im quaternären System Ba-Pd-Zn-Ge bei 800°C und im Sb-reichen Teil des Ce-TM-Sb (TM = Ti, Zr, Hf, V, Nb, Ta, Cr, Mo, W, Mn, Re, Cu, Ag, Au, Zn, Cd) bei 600°C. Ein Reaktionsschema für die Phasengleichgewichte im „Ba8Ge46“ Bereeich des Ba-Pd-Zn-Ge –Systems wurde ebenfalls erstellt.

Röntegenstreuung am Einkristall und Röntgenpulveraufnahmen wurden verwendet um die Kristallstruktur von neuen/unbekannten ternären Verbindungen aufzustellen und um die genauen Besetzungsverhältnisse der kristallographischen Positionen in Clathrat Mischkristallen nämlich $Ba_8Zn_xGe_{46-x-y}Si_y$, $Ba_8(Zn,Cu)_xGe_{46-x}$, und $Ba_8(Zn,Pd)_xGe_{46-x}$ zu bestimmen. Die temperaturabhängigen Röntgenaufnahmen am Einkristall $Ba_8Zn_7Si_{39}$ (Clathrate Typ I) definieren eine Einstein Temperatur $\Theta_{E,U33}$= 80K. Detaillierte Studien an der Kristallstruktur von mehr als 20 Verbindungen

wurden durchgeführt, davon bilden $SrNi_{9-x}Si_{4+x}$ (x=2.7,S.G. *P*4/*nbm*), $BaCo_{5-x}Ge_9$ (x=0.29, S. G. *Pnma*), $Ce_{12}Ge_{9-x}Sb_{23+x}$ (3.3<x<4.2, S.G. C222), $Nd_2Fe_{5-x}Sb_{6-y}$ (x= 1.04, y=1.025, S.G. *Immm*), $La_2Fe_{5-x}Sb_{6-y}$ (x=1.125,y=1.085, S.G. *I*4/*mmm*), $Nd_3Fe_3Sb_7$ (S.G. $P6_3/m$) eigenständige Strukturtypen. Beziehungen zwischen Gruppen und Untergruppen wurden nach dem Bärnighausen Formalismus hergestellt, für Verbindungen die durch Symmetrieerniedrigung miteinander in Verbindung stehen.

Physikalische Eigenschaften wie Magnetisierung, Widerstand und spezifische Wärme wurden für $RE_2Fe_{5-x}Sb_{6-y}$ (RE=Ce, Nd), $NdFeSb_3$ und $Nd_3Fe_3Sb_7$ gemessen. $NdFeSb_3$ zeigt unter ~3.0K antiferromagnetische Ordnung und das effektive magnetische Moment (3.68 μ_B) entspricht dem von freiem Nd^{+3}. Tatsächliche magnetische Momente für $Nd_2Fe_{5-x}Sb_{10-y}$ und $Ce_2Fe_{5-x}Sb_{10-y}$, erhalten von MCW-Fits wurden auf die Beiträgen von beiden Untergittern Nd^{+3} oder Ce^{+3}..und Fe^{+2} zurückgeführt.

1 Introduction

The biggest challenge of the century is to solve the energy crises as natural resources are at the risk of being exhausted. Out of all available primary energy sources i.e. thermal power, nuclear power, and natural gas, about 34 % of energy is used while 66 % is lost as waste heat. Scientists from all over the world are searching for retrieval of energy from this waste heat. One of the possible solutions to utilize this waste heat is thermoelectric power generation.

1.1 Thermoelectric effects

The concept of thermoelectric power generation is based on the Seebeck effect, which was observed first time by Thomas Seebeck in 1821 [1, 2]. The charge carriers in metals and semiconductors are free to move much like gas molecules, carrying charge as well as heat. By applying a temperature gradient to a material, the mobile charge carriers tend to diffuse from the hot end to the cold end. This results in accumulation of charge at the cold end (negative for electrons (n-type material), positive for holes (p-type materials)), which results in electrostatic potential. Steady state is then reached between the chemical potential for diffusion and the electrostatic repulsion due to the build-up of charge. This property is known as the Seebeck effect and forms the basis for thermoelectric power generation. If the hot ends of the n-type and p-type material are electrically connected, and a load is connected across the cold ends, the voltage produced by the Seebeck effect will cause a current to flow through the load, generating electrical power. The electrostatic potential developed is directly proportional to the temperature difference between hot and cold ends and is given by the expression

$\Delta V = S\Delta T$, where S is Seebeck coefficient.

A thermoelectric generator made up of a series of n-type and p-type thermoelectric elements, utilizes the heat flow across the temperature gradient to produce electric current (Figure 1). On the other hand in Peltier effect [3] an applied current (I) can drive the heat flow (*Q)* through a metal, thereby producing cooling at one end.

The Peltier effect is characterized by the formula

$Q = \pi TI$, where π *is the* Peltier coefficient.

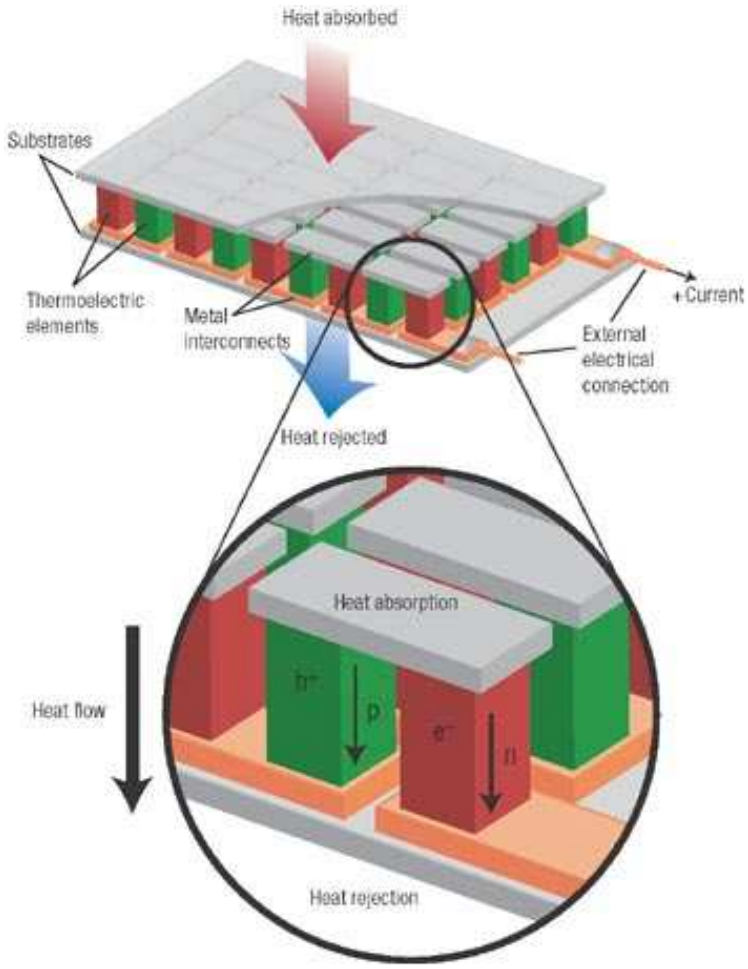

Figure 1. Thermoelectric module showing the direction of charge flow on both cooling and power generation [4].

1.2 Thermoelectric Materials

The efficiency of the TE material is determined by its dimensionless figure of merit

$ZT = S^2\sigma T/\kappa$

Where S is the Thermopower (Seebeck coefficient), σ is the electricl conductivity κ is thermal conductivity and T is absolute temperature. High ZT values correspond to high thermoelectric efficiency; therefore good thermoelectrics should have high Seebeck coefficient and high electrical conductivity in combination with low thermal conductivity [4]. These properties cannot be optimised independently e.g. electrical conductivity is proportional to the charge carrier concentration, while thermal

conductivity also increases with increase of charge carrier concentration. The Seebeck coefficient on the other hand decreases with increase of charge carrier concentration. Therefore metals exhibits high electrical conductivity but in combination with low thermopower and high thermal conductivity. Insulators on the other hand possessing high Seeback coefficient but with obviously no electrical conductivity result in ZT values around zero. Typical thermoelectrics therefore are neither metals nor insulators but narrow gap semiconductors.

One of the important criterions to reduce thermal conductivity and to enhance Seebeck coefficient is the complexity of the crystal structure. There are large number of materials with open structured crystal lattice which have voids in the lattices and can accommodate guest atoms or molecules e.g oxides, zeolites etc. Two relatively new material classes that have received great interest in the field of thermoelectrics are the skutterudites [6, 7, 8, 5] and clathrates [10, 8, 11, 9]. These materials are described as phonon-glass electron crystals (PGECs) [12]. PGECs exhibit thermal conductivity like glass and electrical conductivity like perfectly ordered single crystal.

1.3 Clathrates

The term “clathrate” is used in chemistry to describe compounds with cage of host atoms, which can accommodate guest atoms inside the cage. The earliest known example was chlorine hydrate [13, 14] where Cl_2 gas molecules are present as guest. Other “gas hydrates” (ice clathrates) were reported for CH_4, C_2H_2, PH_3, Co_2 etc. The structure of these compounds was disclosed first time by Stackelberg and coworkers with cubic symmetry [15, 16] for two types of inclusion hydrates; type I, $M_6[H_2O]_{46}$ (space group $Pm\bar{3}n$) and type II $M_8[H_2O]_{136}$ or $M_8M'_{16}[H_2O]_{136}$ (space group $Fd\bar{3}m$)[17, 18, 19, 20]. Intermetallic Clathrates of group 14 elements were first reported by Kasper et al.; [21] and then followed by systematic investigations of Cros et al [22, 23, 24, 25]. About nine types of intermetallic clathrates have been found till now [9] out of which clathrate I and II are most commonly studied for thermoelectric applications

Type I clathrate compounds with cubic space group $Pm\bar{3}n$ crystallize in structure type K_4Ge_{23-x} and consist of a tetrahedraly bonded open framework where framework atoms are bonded to each other through sp^3 hybridization. The unit cell consists of 46 atoms arranged in the forming of two large framework cages; dodecahedra consisting of 20 atoms and tetrakaidecahedra of 24 atoms shown in Figure 2. Guest atoms are encapsulated inside these cages. Small cage (dodecahedra) accommodate 2a site of guest atoms while tetrakaidecahedra host 6d site of guest atoms. The properties of the clathrate materials can be fine tuned by proper choice of guest atoms. The thermal vibrations of these guest atoms play role in reducing lattice thermal conductivity by scattering heat phonons due to their vibrations as they are loosely bound to host atoms. Clathrates with empty cages are semiconductors. The guest atoms donate valence electrons to the conduction band of the host changing the character of a material to metallic. For semiconducting applications this effect can be compensated by substitution of an appropriate number of host atoms of group IV with group III e.g. $Ba_8Ga_{16}Ge_{30}$ is semiconductor. Most of the clathrate phases follow the Zintle rule where charge compensation between guests and cages is carried out by partial substitution of cage atoms. Currently experimental and theoretical research is devoted to the synthesis of new clathrate phases, which could be promising for thermoelectric performance.

Type-I clathrates with general formula $A_8B_{16}X_{30}$ (A=Ba, Sr, Eu; B=Ga, Al, In; X=Si, Ge) are the most studied clathrate phases and are considered promising for high temperature thermoelectric applications [10, 26, 27, 28, 29, 30]. The highest figure of merit is reported for single crystal $Ba_8Ga_{16}Ge_{30}$ [27]. A wide range of clathrates I is formed by the formula $Ba_8TM_8MGe_{38}$ (TM=Zn, Cd) or with general formula $Ba_8TM_{6-x}MX_{40-x}$ (TM = Ni, Cu, Pd, Ag, Pt, Au; X=Si, Ge) [31, 32, 33, 34, 35, 36, 37, 38]. Despite many efforts focused on the cross-substituted transition metals (TM) type I clathrates [39, 40, 41, 42, 43], the ZT values are still lower than state of the art thermoelectric materials. Theoretical and experimental research attempts to achieve high figure of merit by fine-tuning the substitution and compositions of clathrate I [44, 45, 46].

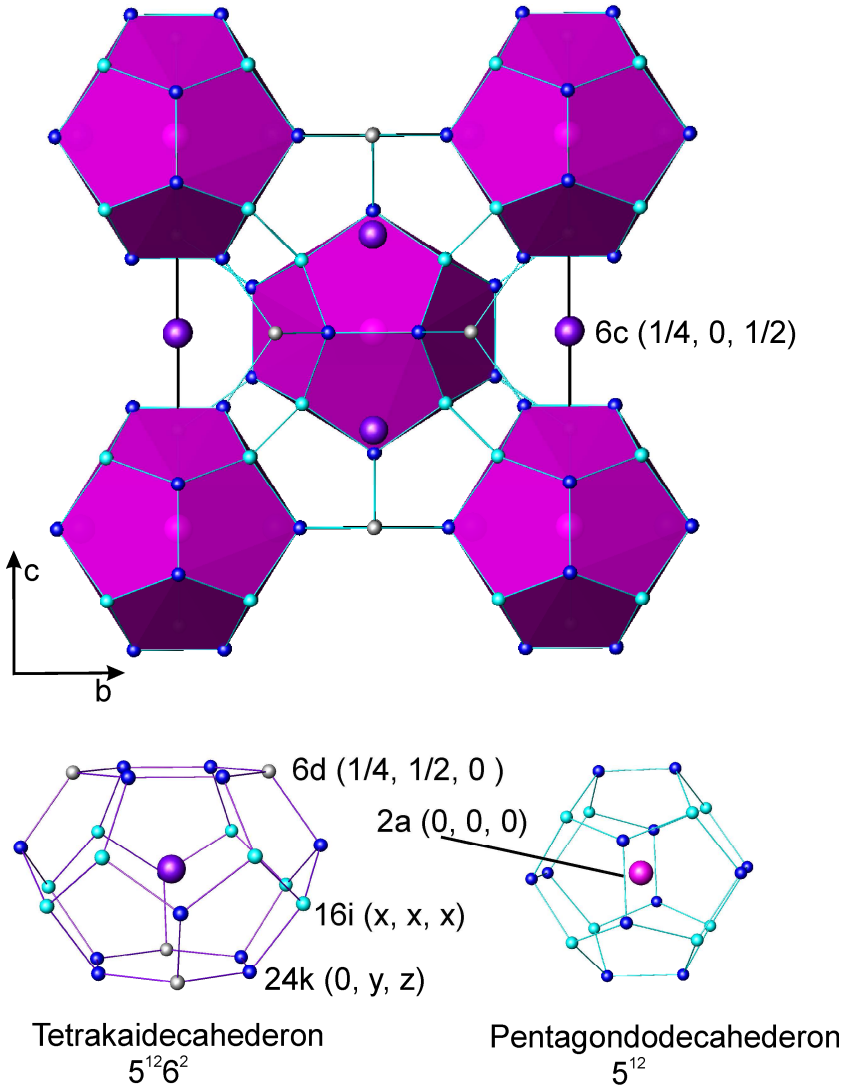

Figure 2: Crystal structure of typical clathrate type I (space group $Pm\bar{3}n$, K_4Ge_{23-x} type).

1.4 Antimonides

A large group of thermoelectric materials is formed by a class of antimonides, which crystallize with skutterudite structure (cubic, space group $Im\bar{3}$). Skutterudites are the open structured materials where voids in the structure can be filled with different filler atoms, which can act as rattlers scattering the heat carrying phonon. (RE, EP)-TM-Sb (RE= rare earths, EP=alkaline earths, TM =transition metals) are potential systems forming skutterudites. High figure of merit ZT>1 has triggered research in these materials [47, 48, 49, 50,]. Other examples of antimony based thermoelectric

materials i. e β-Zn_4Sb_3, $Yb_{14}MnSb_{11}$, Mo_3Sb_7, AZn_2Sb_2 etc are described in details in [51] and the Refs. mentioned therein.

1.5 Task for the Present Work

For the material applications it is important to know details about the structure, stability and phase relations including surrounding phases. Due to the increased complexity of chemistry and processing techniques of advanced alloys, the knowledge of phase equilibria become vital for a material scientist or engineer. The properties of an alloy depend on the relative proportion of the phases as well as their structural arrangement at the microscopic level. Thus, the number of phases, their volume fraction, and their representation in space describes the microstructure. Microstructure of the alloy gives important information regarding phase field, solid solubility, and homogeneity range in solid phase and phase stability. On the other hand crystal structure of the materials is directly related to the physical properties, therefore determination and exploration of the structural details are vital for better understanding of the upcoming physical properties.

The thesis covers the search for novel thermoelectric materials in perspective regions of the ternary systems: {rare earth, alkaline earth}–{Group IV, transition metals}–{antimony, Group IV}. The combination of the selected elements is in line with the appearance of compounds and solid solutions at the verge of metal to semiconducting properties as a key requisite for good thermoelectric behaviour. The work was accomplished as follows

i) Search for the existence of new clathrate type I materials in the above mentioned systems and to elucidate details of the crystal structure. In this regard two new compounds $Ba_8\{Zn, Cd\}_7Si_{39}$ were found and their crystal structure was established by x-ray single crystal (XRSC) and x-ray powder diffraction (XRPD).

ii) Optimization of thermoelectric behaviour of selected quaternary clathrates by appropriate substitutions and variation in compositions. For this case a series of quaternary Ge based clathrates with substitution of Zn, Pd, Cu, and Si were studied in a wide composition range.

iii) Preparation of single-phase clathrate materials in the form appropriate for the physical properties studies. In this case two series of clathrates were synthesised in desired amounts and forms (powders or compact cylinders).

iv) Determination of the phase relations for quaternary clathrates and determination of single-phase regions for quaternary clathrate phases in selected systems.

v) Determination of the crystal structure of novel ternary compounds discovered during the investigation of ternary systems. Several ternary compounds were found in clathrate forming systems (germanides and silicides) as well as in systems with antimony. Crystal structures were determined for all these compounds by XRSC and XRPD.

vi) Development of the isothermal sections and determination of the homogeneity ranges for solid solutions. Partial or complete isothermal sections were constructed for Ce-(Si,Ge,Sn)-Sb, Sr-(Cu,Ni)-Si, Ce-TM-Sb, Ba-Pd-Zn-Ge, and Nd-Fe-Sb systems.

vii) Study of the physical properties of selected new compounds. In this part low temperature magnetic, electrical transport and specific heat measurements were performed for ternary antimonides of rare earths and iron.

For all these investigations a wide range of powder metallurgical as well as melting techniques were used for alloy preparation. Light optical microscopy (LOM) and Electron probe micro analysis (EPMA) served for chemical characterization of the alloys. Crystal structure determinations were accomplished with the help x-ray powder diffraction and x-ray single crystal instruments. Details of all methods are given in Chapter 2.

References

[1] T.J. Seebeck, Abh. K. Akad. Wiss., Berlin, 289, 1821.

[2] T.J. Seebeck, Abh. K. Akad. Wiss. Berlin, 265, 1823.

[3] J.C. Peltier, Ann. Chim. 56, 371 (1834)

[4] G. Jeffrey Snyder, Eric S. Toberer, Nature Mater. 7 (2008) 105.

[5] B. C. sales, Handbook of the physics and Chemistry of the Rare Earths, 33, Elsevier Science, Amsterdam, 2002.

[6] G. S. Nolas, D. T. Morelli, T. M. Tritt, Annu. Rev. Mater. Sci. 29 (1999) 89.

[7] C. Uher, Semiconduct. Semimet. 69 (2001) 139.

[8] G. S. Nolas, J. Sharp, H. J. Goldsmid, Thermoelectrics: Basic Principles and New Materials Developments, Springer-Verlag, Heidelberg (2001).

[9] P. Rogl, Thermoelectrics Handbook: Macro to Nano, ed. D. M. Rowe (Boca Raton: CRC, 2006), pp. 32-1

[10] G. S. Nolas, J. L. Cohn, G. A. Slack, B. Schujman, Appl. Phys. Lett. 73 (1998) 178.

[11] G. S. Nolas, Thermoelectrics Handbook: Macro to Nano, ed. D. M. Rowe (Boca Raton: CRC, 2006), pp. 33-1

[12] G. A. Slack, CRC Handbook of Thermoelectrics, ed. D. M. Rowe, (Boca Raton, FL: CRC 2006), p. 407.

[13] H. Davy, Phil. Trans. Ray. Soc., 101 (1811) 155.

[14] M. Faraday, Quart. J. Sci., 15 (1823) 71.

[15] J. Pietuchowsky, Diploma Thesis, Bonn, 1940.

[16] H. R. Mueller, M. von Stackelberg, Naturwiss. 39 (1952) 20.

[17] M. von Stackelberg, H. R. Mueller, Z. Electrochem. 58 (1954) 25.

[18] M. von Stackelberg, H. R. Mueller, Z. Electrochem. 58 (1954) 40.

[19] W. F. Claussen, J. Chem. Phys. 19 (1951) 259.

[20] M. von Stackelberg, H. R. Mueller, J. Chem. Phys. 19 (1951) 1319.

[21] J. S. Kasper, P. Hagenmuller, M. Pouchard, C. Cros, Sci. 150 (1965) 1713.

[22] C. Cros, M. Pouchard, P. Hagenmuller, C. R. Hebd. Seances Acad. Sci. 260 (1965) 4764.

[23] C. Cros, M. Pouchard, P. Hagenmuller and J. S. Kasper, Bull. Soc. Chim. Fr. (1968) 2737

[24] C. Cros, M. Pouchard and P. Hagenmuller, Bull. Soc. Chim. Fr., (1971) 379.

[25] C. Cros and J.C. Benejat, Bull. Soc. Chim. Fr., (1972) 1739.

[26] A. Bentien, E. Nishibori, S. Paschen, B. B. Iversen, Phys. Rev. B: Condens. Matter and Mater. Phys. 71 (2005) 144107-1.

[27] A. Saramat, G. Svensson, A. E. C. Palmqvist, C, Stiewe-; E. Mueller, D. Platzek, S. G. K. Williams, D. M Rowe, J. D. Bryan, G. D. Stucky, J. Appl. Phys. 99 (2006) 23708-1.

[28] M. A. Avila', K. Suekuni, K. Umeo and T. Takabatake Physica B: Condens. Matter 383 (2006) 124.

[29] J. Martin, S. Erickson, G. S. Nolas, P. Alboni, T. M. Tritt, J. Yang, J. Appl. Phys. 99 (2006) 44903-1.

[30] M. A. Avila, K. Suekuni, K. Umeo, H. Fukuoka, S. Yamanaka, T. Takabatake, Phys. Rev. B 74 (2006) 125109

[31] G. Cordier, P. Woll, J. Less Common Metals 169 (1991) 291.

[32] N. Melnychenko-Koblyuk, A. Grytsiv, P. Rogl, M. Rotter, E. Bauer, G. Durand, H. Kaldarar, R. Lackner, H. Michor, E . Royanian, M. Koza, G. Giester, Physical *Review* B: Condensed Matter and Materials Physics 76 (2007) 144118

[33] N. Melnychenko-Koblyuk, A.Grytsiv, P. Rogl, M. Rotter, E. Bauer, R. Lackner, L. Fornasari, F. Marabelli, G. Giester, Physical Review B: Condens. Matter and Mater. Phys. 76 (2007) 195124.

[34] N. Melnychenko-Koblyuk, N.; Grytsiv, L. Fornasari, H. Kaldarar, H. Michor, F. Röhrbacher, M. Koza, E. Royanian, P. Rogl, M. Rotter, E. Bauer, H. Schmid, F. Marabelli, A. Devishvili, M. Doerr, Giester, G. J. Phys. Con. Mat. 19 (2007) 216223

[35] N. Melnychenko-Koblyuk, A. Grytsiv, St. Berger, H. Kaldarar, H. Michor, F. Röhrbacher, E. Royanian, P. Rogl, E. Bauer, H. Schmid, G. Giester, J. Phys. Con. Mat. 19 (2007) 046203

[36] N. Melnychenko.Koblyuk, A. Grytsiv, P. Rogl, E. Bauer, R. Lackner, E. Royanian, M. Rotter, G. Giester, J. Phys. Soc. Jpn. 77 (2008) 54.

[37] N. Melnychenko-Koblyuk, A. Grytsiv, P. Rogl, H. Schmid, G. Giester, J. Solid Stat. Chem., 182 (2009) 1754.

[38] N. Nasir, A. Grytsiv, N. Melnychenko-Koblyuk, P. Rogl, E. Bauer, R. Lackner, E. Royanian, G. Giester, A. Saccone, J. Phys.: Cond. Mat., 21(2009), 385404

[39] S. Johnsen, A. Bentien, G. K. H. Madsen, B. B. Iversen, Chem. Mater. 18 (2006) 4633.

[40] S. Johnsen, A. Bentien, G. K. H. Madsen, M. Nygren, B. B. Iversen, Phys. Rev. B 76 (2007) 245126.

[41] Ya. Mudryk, P. Rogl, C. Paul, S, Berger, E. Bauer, G. Hilscher, C. Godart, H. Noel, J. Phys. Condens. Matter. 14 (2002) 7991.

[42] M. Hokazono, H. Anno, K. Matsubara, Mater. Trans. 46 (2005) 1485-9

[43] H. Anno, M. Hokazono, H. Takakura, K. Matsubara, 24thInternational Conference on Thermoelectrics ICT, IEEE Cat. No.05TH8854C (2005) 102-5

[44] E. S. Toberer, A. F. May, G. Jeffrey Snyder, Chem. Matter 22 (2010) 624.

[45] X. Shi, J. Yang, S. Bai, J. Yang, H. Wang, M. Chi, J. R. Salvador, W. Zhang, L. Chen, W. Wong-Ng, Adv. Funct. Mat. 20 (2010) 755.

[46] G. S. Nolas, X. Lin, J. Martin, M. Beekman, H. Wang, J. Elec. Mat. 38 (2009) 1052.

[47] X. Shi, H. Kong, C.P. Li, C. Uher, J. Yang, J.R. Salvador, H. Wang, L. Chen, W. Zhang, Appl. Phys. Lett. 92 (2008) 182101.

[48] L. Zhang, A. Grytsiv, P. Rogl, E. Bauer, M. J. Zehetbauer, J. Phys. D: Appl. Pys. 42 (2009) 225405.

[49] G. Rogl, A. Grytsiv, E. Bauer, P. Rogl, M. Zehetbauer, Intermet., 18 (2010) 394.

[50] G. Rogl, A. Grytsiv, E. Bauer, P. Rogl, M. Zehetbauer, Intermetal., 18 (2010) 57.

[51] H. Kleinke, Chemistry of Materials 22 (2010) 604.

2 Experimental Techniques

2.1 General procedure for synthesis and characterization

Alloys samples were prepared by either arc melting or by powder metallurgy depending on the type of reacting elements. Arc melted samples (1-2g) were prepared from elemental ingots of high purity 99.9% in Ti gettered argon on a water-cooled copper hearth. Samples were remelted three times for complete homogenization. Weight losses were compensated beforehand by adding extra amounts of the most volatile element e.g Sb, Ba, Sr etc. Usually weight losses were less than 0.1 wt. %. Oxygen/moisture sensitive elements such as rare earths, Ba, Sr were surface cleaned and weighed under cyclohexane. Alloys button were then cut into several pieces, some of which were sealed in evacuated quartz tubes and annealed at different temperatures depending on requirements for the individual system. In order to overcome the difficulty of arc melting strongly evaporating elements in systems like Ba-Zn(Cd)-Si or Ce(Ba)-TM-Sb an alternative route of powder metallurgy was employed. Master alloys were prepared by reactions in evacuated quartz tubes. The powderized master alloys were mixed with filings of the low melting element, compacted into tablets and sintered. The reaction products were powderized again and recompacted and sintered again for complete reaction. Clathrate samples were hand milled or ball milled and hot pressed. The general layout for the procedure is sketched in Figure 1. As cast and annealed samples were investigated by X-ray powder Diffraction (XRPD), Light Optical Microscopy (LOM) and Electron Micro Probe Analysis (EMPA). X-ray single crystal (XRSC) studies were used for determination of structure of new/unknown ternary compounds. Samples from selected systems were cut into bars or discs of specified dimensions for the measurements of physical properties comprising magnetization, resistivity and specific heat measured in the temperature range (1.9-400 K).

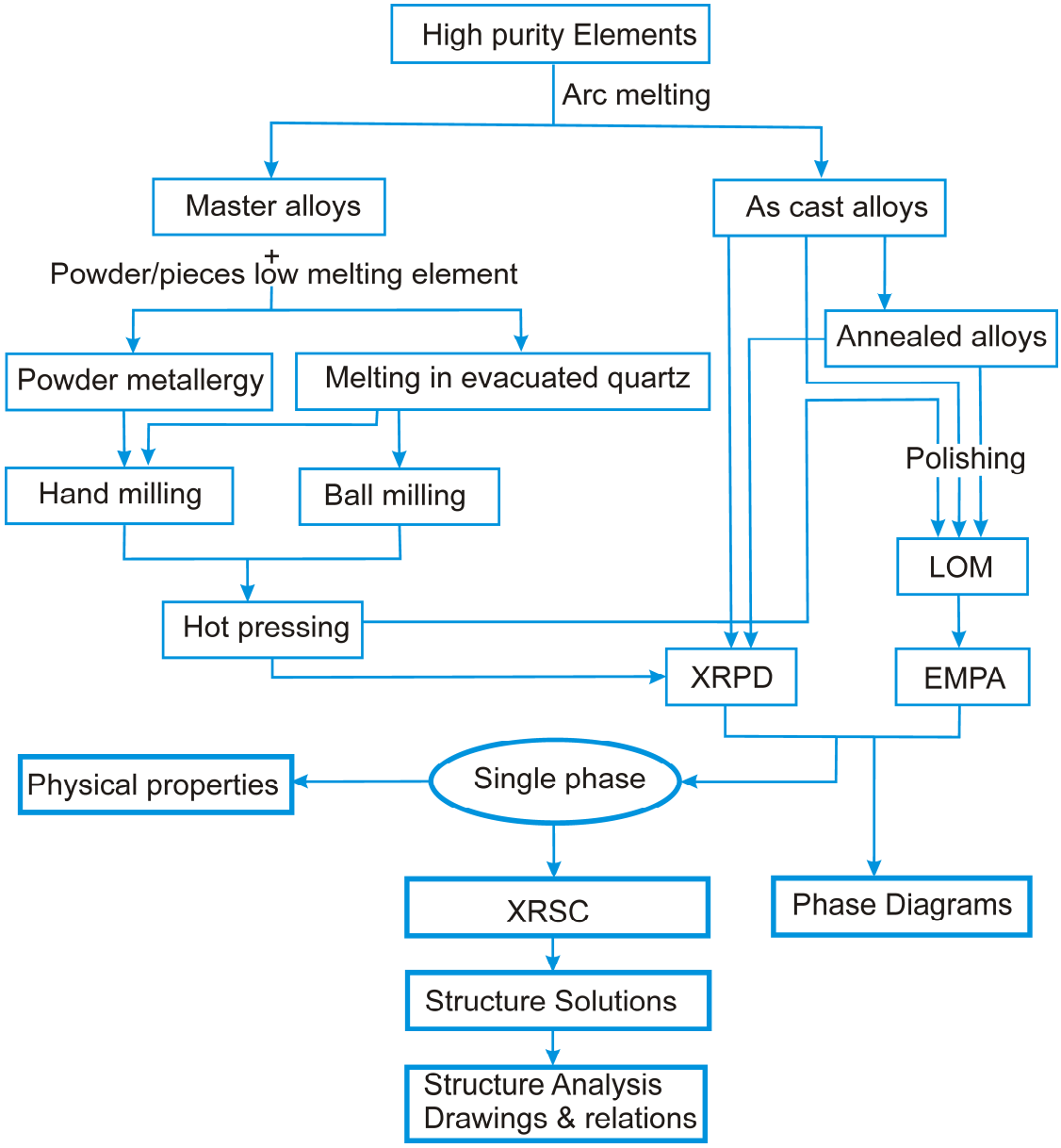

Figure 1. General layout of the experimental procedure

2.2 Instruments

2.2.1 Arc Furnace

Most of the samples preparations were accomplished by classical arc-melting as discussed above. Figure 2 shows arc-melting furnance used in the present work with tungsten electrode and copper hearth. Furnace is evacuated to 0.1 Pa using a vacuum pump and flushed with argon 3-5 times before each melting. Finally the melting

chamber is filled with argon up to ~0.7-0.8 bar prior to melting. A continuously circulating water system is attached with the system for efficient cooling. Ti-getter is first melted in order to absorb any air, and arc is moved slowly towards the sample until it is melted completely and again arc is moved to the Ti-getter until the sample is cooled and power is switched off.

Figure 2. Arc melting furnaces.

2.2.2 Ball Mill

For studies of physical properties of the materials expected to be interesting from thermoelectric application it was necessary to prepare dense single-phase samples. The task was accomploished by ball milling and hot pressing. Fritsch "pulverisette 4" vario-planetary mill system was employed for ball milling using tungsten carbide balls and containers (Figure 3). The following ball milling conditions were used in the present work: Rotation speed of main disk (Rs) = 175 rpm, planetary ratio (PR)= -2.5, ball to powder ratio BPR=20, size of the balls ϕ_b= 10 mm and process control agent = Ar.

2.2.3 Hot Press

Bulk powders can be compacted into dense material by employing hot pressing. A hot press system “HP W 200/250-2200-200-KS” from FCT System GmbH, shown in

Figure 4 was used for densifying required materials in the present work. The system is equipped with a high density graphite heater. The maximum heating temperature and applied force limits are 2200 °C and 14 kN, respectively. Inert atmosphere of N_2, Ar or vacuum can be used for sintering. The powders of the sample either hand milled or ball milled are loaded in a graphite die of diameter 1cm. Optimization of the hot pressing conditions is necessary in order to achieve maximum density, completetion of reaction in combination with reduction of losses due to evaporation of volatile elements which can shift the composition of the final sample. In the present work the condition optimised for hot pressing was 800 °C and 56 MPa.

Figure 3.Overall view of Fritsch Vario-planetary mill pulverisette 4

Figure 4. Overall view of Hot-press FCT

2.2.4 X-Ray Diffraction

Since its discovery in 1895 by Röntgen, X-ray radiation has found wide range of applications in the fields of medicine, geology, material science, chemistry, environmental science, and pharmaceutical industries etc. X-ray diffraction technique is most commonly used for the identification of the crystalline materials and determination of their crystal structure on the basis of their unique diffraction pattern, which can be used as “fingerprint”. The wavelength of the x-rays is comparable to the spacing between the lattice planes, and three-dimensional lattices of the atoms can act as diffraction grating for x-rays as discovered by Max von Laue in 1912. The principle of the X-ray diffraction is based on constructive interference of the diffracted beam. X-rays are generated in a cathode ray tube and are monochromatized by a monochromator crystal to yield a beam, which is collimated and directed towards the sample. After interaction with the sample, these x-ray are diffracted at various angles θ depending on the d spacing between the atom planes. Constructive interference occurs according to Bragg’ s equation ($2d\sin\theta = n\lambda$), where θ is the angel between incident ray and scattering plane and λ is the wavelength of the characteristic x-rays. X-ray powder diffraction is useful for the identification of single-phase materials, number and type of phases in multiphase samples, strain analysis, determination of crystallite size, quantitative determination of the phases, unit cell and crystal structure determination. For more precise and accurate determination of the Laue symmetry, space group, thermal motion, site occupancy and bonding in certain crystal structures, x-ray single crystal diffraction is essential specially for completely new or unknown structures. However to get a suitable single crystal from a material is not always an easy job. Only crystals with sufficiently large size (25-50 μ), regular shape and with no internal defects or twinning or considered suitable for diffraction experiments.

2.2.4.1 X-Ray Powder Diffractometer and Imaging Plate (IP)

A Huber Imaging Plate (IP) camera G670 with Guinier geometry in combination with Cu $K_{\alpha 1}$ radiation (λ =0.154051nm) was used for the X-ray powder diffraction measurements. The overall view and schematic diagram for the beam path is shown

in Figure 5. The Guinier camera consists of an image storage foil, which is positioned inside the camera housing with the sensitive side facing inward precisely on the focal circle with radius of 90mm. This image storage foil is made of polyester and coated with homogenous powder luminescent storage material (photo-stimulatable phosphore) consisting of bariumflourobromide with a trace amount of Eu^{2+} ($BaFBr:Eu^{2+}$) which act as luminescence centers [1]. After exposure time the image plate is scanned by a vertical linear red diode laser beam within approx. 5 seconds. The resulting blue photo stimulated luminescence (PSL) emanating from the areas subjected to X-ray exposure is amplified during the scanning process by a photo multiplier and then registered and converted into digital number counts by a 16-bit A/D converter [1]. This data can be transformed into different formats to visualize graphics and to perform Rietveld refinement. Image Plate can be reused multiple times by erasing the image with a white halogen lamp.

Cu $K_{\alpha 1}$ radiation (λ =0.154051nm) was produced with generator parameters 30mA and 40kV while the measurements were performed in the 2-theta range (8° $\leq 2\theta \leq$100°) with the step size 0.005.

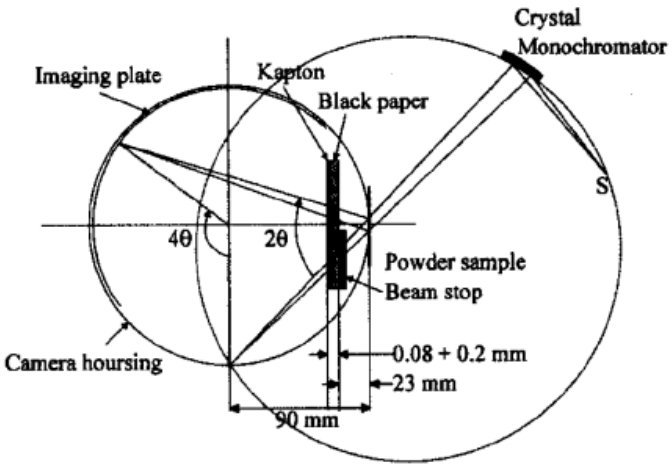

Figure 5. Overal view of IP (Guiner Huber G670) (left) and Schematic of Geometry (right).

2.2.4.2 Preparation of single crystals

Microsize (25~50μm) single crystal fragments of regular shape are collected from crushed alloys containing the required compound as major phase. The crystal is mounted on the top of a glass fibre by glue (see Figure 6). The quality, unit cell

dimensions and Laue symmetry of a crystal were firstly determined by the AXS-GADDS texture goniometer (General Area Detector Diffraction System, GADDS). For X-ray intensity data collection, a four-circle Nonius Kappa diffractometer equipped with a CCD (Charge-Coupled Device) area detector and employing graphite monochromated Mo-K_α radiation (λ = 0.071073 nm) is used in the present work.

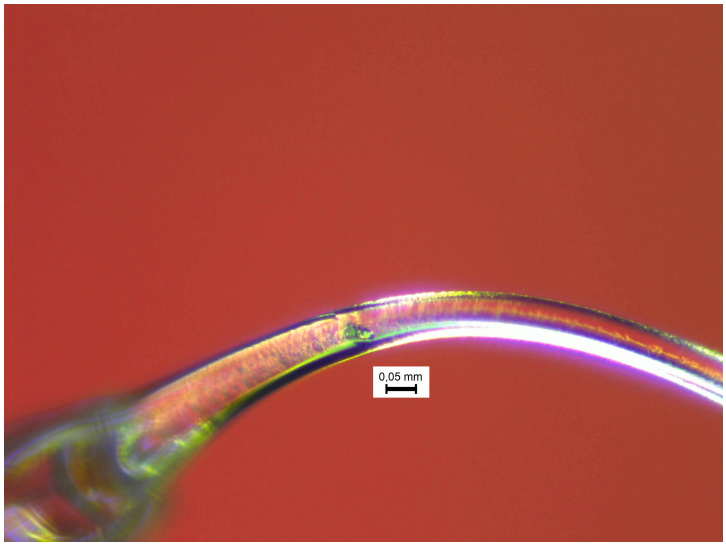

Figure 6. Single crystal mounted in transparent glue on top of a glass fibre.

2.2.4.3 AXS GADDS

Figure 7 and 8 presents the overview and schematic of the GADDS (General Area Detector Diffraction System) respectively, by Bruker AXS Inc. The key feature of GADDS is the high-performance two-dimensional AXSHI-STAR area detector, which is the most sensitive photon counter with large area. The advantage of the area detector is the enhanced speed of data collection, which can be 10,000 times faster than a point detector. The 2D images collected by GADDS contain more information for different applications as compared to an 1D image obtained by conventional diffraction systems. Various measurements e.g. phase identification and quantification, lattice parameters, refinement, texture analysis, stress measurements and percent crystallinity are possible with GADDS. In addition small angle X-ray scattering (SAXS) data collection can be performed at high speed which is useful for a variety of samples like polymers, fibres, biomaterials, single crystals to analyse and display anisotropic features in 2D image.

Various configurations of GADDS system can fulfil the requirements for different applications and samples. The GADDS system mainly consists of five major units, (i) an x-ray generator to produce X-rays, (ii) X-ray optics to condition the primary X-ray beam,(iii) a goniometer and sample stage to establish and manipulate the geometric relationship between primary beam, sample, and detector, (iv) a sample alignment and monitor to assist users in positioning the sample into the instrument center and in monitoring the sample state and position,(v) a detector (HI-STAR Area Detector System) to intercept and record the s X-ray scattered from a sample and to save and display the diffraction pattern into a two-dimensional image frame. Detailed information on each part is available in the GADDS user's manual.

Figure 7. Overall view of the AXS GADDS system.

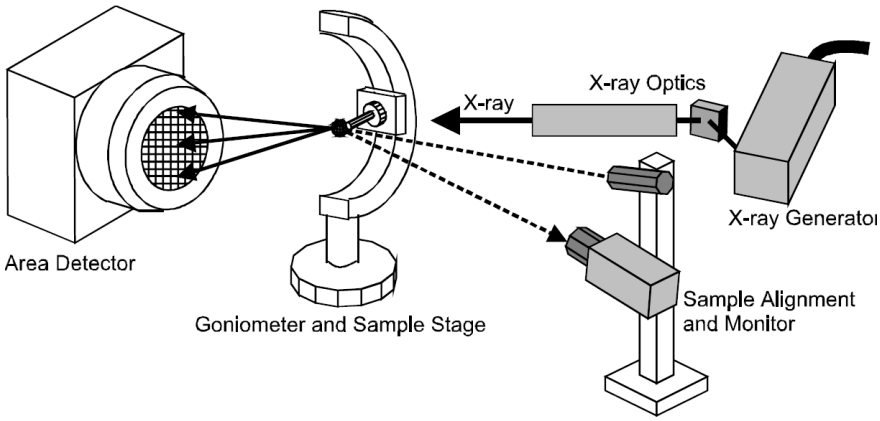

Figure 8. Five major units in a GADDS system: X-ray generator (sealed tube); X-ray optics (monochromator and collimator); goniometer and sample stage; sample alignment and monitor (laser-video); and area detector.

2.2.4.4 Nonius Kappa diffractometer with area detector CCD

X-ray single crystal diffraction was performed on a Nonius Kappa diffractometer equipped with a CCD area detector. Overall view of the instrument is shown in Figure 9. The diffractometer consist of an x-ray source, three axes goniometer (Omega, Kappa, Phi) for adjusting position of the crystal, and theta axis and DX to position the two-dimensional detector. Position of the mounted crystal is adjusted by microscope, which displays the image on the computer. X-rays are produced by HV generator and rotating anode generator. The generated x-rays are controlled by main shutter, a fast shutter, a monochromater and a collimator before passing through the crystal. Diffracted x-rays hit the detector through a beryllium window and are transformed into light photons by a phosphor. The image size is reduced to the size of CCD by a fibre optic taper. The light photons are converted to electrons by CCD, which consists of silicon capacitors (pixels) where generated electrons can be trapped. The detector reads out and amplified the signals, which are digitised in the controller and are transferred directly to computer. A multi-stage peltier element is used to cool CCD, while a mixture of water-ethylene glycol at 0°C in a close circuit liquid cooler helps cooling the warm side of peltier element. Details on technical informations can be found from: (http://www.nonius.com/KappaCCD/manuals/techinfo/techinfo.html).

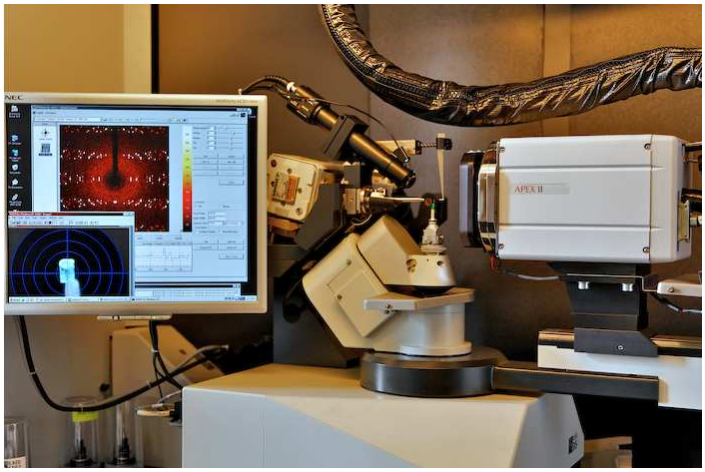

Figure 9. Overall view of Nonius Kappa CCD diffractometer (from; http://algol.fis.uc.pt:8080/CEMDRX/equipment/pictures-of-equipment/kappa_apex_2.jpg/view).

2.2.5 Electron Probe Micro Analyzer (EPMA)

Small pieces from as cast (in case of arc melting) as well as annealed samples were embedded in electroconductive resin by using a SIMPLIMET 3 hotmolding press (Buehler, Lake Bluff, Illinois USA, operation parameters: 2.9×10^{7} Pa; 150°C; duration 1.5 min). The embedded samples were ground using sand papers of different SiC grit size. The samples were polished using alumina powder with grain size 0.3 micron and 0.05 micron on a fine polishing cloth. Surface of the polished samples were cleaned by supersonic waves and finally with alcohol.

In order to ensure fine quality of the polishing samples were examined in a light optical microscope as guide line for investigation in scanning electron microscopy (SEM) and energy dispersive x-rays (EDX) analysis.

Working Principle

An accelerated and focused beam (approximately 1 micron diameter) of electrons is bombarded on to polished surface of the specimen. These high energy electrons have sufficient energy to excite the electrons from the inner shell of the target material, leaving a vacancy which can be filled by electron from higher shell accompanied by emission of x-rays. The wavelengths of these x-rays are characteristic and unique for every element in the periodic table and therefore are used for quantitative analysis. Interaction of electrons with sample is mainly associated with libration of heat but it also produces X-ray Bremsstrahlung secondary and backscattered electrons. Secondary electrons are of common interest for topology and backscattered electrons are used for enhanced contrast to see different phases in multiphase samples.

Quantitative analysis can be done by measuring the intensities of the characteristic x-rays of the elements in the sample

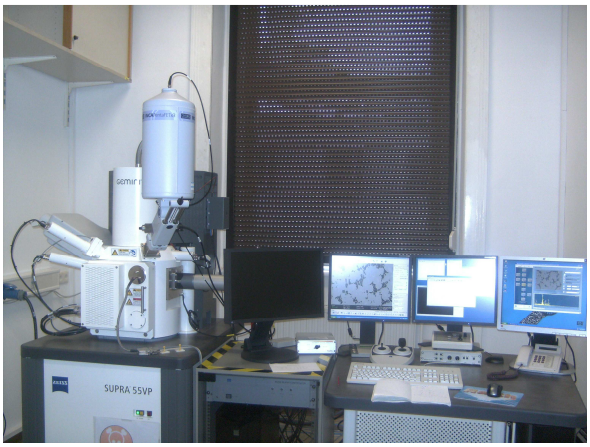

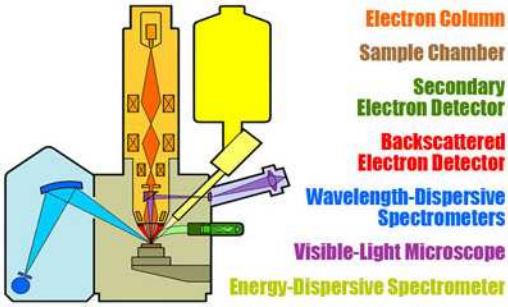

Figure 10. Overal view of the Electron Microprobe Analyser (EMPA) (left) and Schematic cut-away diagram of a typical microprobe: (http://serc.carleton.edu/details/images/843.html)

EPMA consists of the following main parts, from top to bottom: (i) An electron "gun", which is most commonly a W-filament cathode (ii) A series of electromagnetic lenses located in the vertical column of the instrument is used to condense and focus the electron beam emitted from the source. It comprises the electron optics and operates in an analogous way to light optics. (iii) A sample chamber, with movable sample stage (X-Y-Z), that is under a vacuum to prevent gas and vapour molecules from interfering with the electron beam on its way to the sample, (iv) a light microscope allows for direct optical observation of the sample (v) A variety of detectors arranged around the sample chamber that are used to collect x-rays and electrons emitted from the sample.

2.3 Data Analysis

2.3.1 STRUKTURE

Precise lattice parameters were calculated by least-squares fits to indexed 4θ-values employing Ge or Si as internal standard (a_{Ge} = 0.5657906 nm, a_{Si} =0.5431065nm). The XRPD patterns for samples without and with standard are measured. Individual peaks in the patterns with and without Ge/Si were defined using programme STRUKTURE [2]. A correction curve is then created by comparing peak positions of the standard (calculated) with those in the experimental spectrum. Correction in all peak positions of the sample is then made by employing this correction curve in

Programme X15. Programme X15 was also used for indexation of the observed intensity from different phases, which are either isotypes (literature) or new structures solved from single crystal. The input data for isotypes or known structure is provided by programme LAZY PULVERIX. The indexed peaks are then used to calculate lattice parameters with standard deviation by programme GITTER. LAZY PULVERIX and GITTER are integrated in programme MENUE.

2.3.2 Rietveld Refinement (x-ray powder diffraction)

Information about the crystal structure of the compound (types of atoms, positional parameters, temperature factors, occupancies) with isotypic structure can be extracted from the x-ray powder pattern by using Rietveld refinement [3, 4] with program Fullprof [5]. In the Rietveld technique, the observed intensity is fitted with calculated pattern based on calculations from crystal structure, profile parameters, instrument and specimen related factors using least-squares refinement cycles. This least squares fits tends to minimise the function S_y, which is defined as

$$S_y = \sum_i w_i (y_i - y_{ci})^2 \qquad 2.1$$

Where $w_i = 1/y_i$, y_i and y_{ci} are observed and calculated intensities at the ith step. The Rietveld method needs an appreciably good starting model as the key feature of the method is the structure refinement and not structure solution, therefore no advance efforts are needed to assign the observed intensity to specific Bragg reflections or to resolve overlapping reflections. The calculated intensities y_{ci} are determined from $|F_k|^2$ values calculated from structural model plus background.

$$y_{ci} = s\sum_K L_k |F_k|^2 \phi(2\theta_i - 2\theta_K) P_K A + y_{bi} \qquad 2.2$$

Where s = scale factor, K = Miller indices, h, k, l, for a Bragg reflection, L_k = the Lorentz, polarization, and multiplicity factors, ϕ = is the reflection profile function, Pk = proffered orientation function, A= absorption factor, F_k = structure factor for the Kth Bragg reflection, and y_{bi} = background intensity at the ith step.

The structure factor F_k can be calculated as

$$F_K = \sum_j N_j f_j \exp\left[2\pi i\left(hx_j + ky_j + lz_j\right)\right]\exp\left[-M_j\right] \qquad 2.3$$

Where h, k, l are Miller indices, x_j, y_j, z_j are the position parameters for the jth atom in the unit cell

$$M_j = 8\pi^2\overline{\mu_s^2}\sin^2\theta/\lambda^2 \qquad 2.4$$

$\overline{\mu_s^2}$ is the root mean square thermal displacement of the jth atom parallel to the diffraction vector, and N_j is the site occupancy multiplier of the jth atom site. Various parameters (scale factor, background, lattice parameters, atom positions, peak shapes, occupancies, temperature factors etc.) are refined until best fit between observed and calculated values is reached. The adequacy of the final structural model is judged by various R-values defined below

$$R_F = \frac{\Sigma\left|(I_K(obs))^{1/2} - (I_K(calc)^{1/2})\right|}{\Sigma(I_K(obs))^{1/2}} \qquad \text{R-structure factor} \qquad 2.5$$

$$R_B = \frac{\Sigma\left|I_K(obs) - I_K(calc)\right|}{\Sigma I_K(obs)} \qquad \text{R-Bragg factor} \qquad 2.6$$

$$R_P = \frac{\Sigma\left|y_i(obs) - y_i(calc)\right|}{\Sigma y_i(obs)} \qquad \text{R-Pattern} \qquad 2.7$$

$$R_{wP} = \left\{\frac{\Sigma w_i(y_i(obs) - y_i(calc))^2}{\Sigma w_i(y_i(obs))^2}\right\}^{1/2} \qquad \text{R-weighted pattern} \qquad 2.8$$

R_{wp} is the most meaningful from mathematical point of view because the numerator is the residual being minimized; therefore it also best reflects the progress of the refinement. Detailed description of the Rietveld refinement procedure using Program FULPROF can be found in refs. [5,6].

2.3.3 Structure Solutions (x-ray single crystal)

For the evaluation of x-ray single crystal diffraction data, no absorption corrections were required because of rather small and regular shapes of the investigated crystals. Initial unit cell parameters and Laue symmetry were determined by measurements on

the AXS-GADDS diffractometer as discussed before. Intensity data collected on Nonius Kappa CCD diffractometer were used for structural determinations by the programs SHELXS97 and SHELXL-97-2 [7] integrated in the Oscail interface which was downloaded from: http://shelx.uni-ac.gwdg.de/SHELX/. Program ABSEN, which is also integrated within Oscail interface was used to determine possible space groups on the basis on extinction rules. Initial atom positions were found by direct or Paterson methods with the program SHELXS97 [7]. Final solutions were found by performing subsequent least square refinement cycle using SHELXL-97-2 [7].

2.4 Physical Properties Measurements

2.4.1 Electrical resistivity measurements

The electrical resistivity was measured over the temperature interval 4.5–290 K employing a standard dc four-probe technique. Electrical resistivity can be expressed in terms of Ohm's law by the equation,

$\rho = U/I*A/l$ where I is the applied constant current, U is the measured voltage, A is the cross section of the sample and l is the length between two potential contacts on the sample.

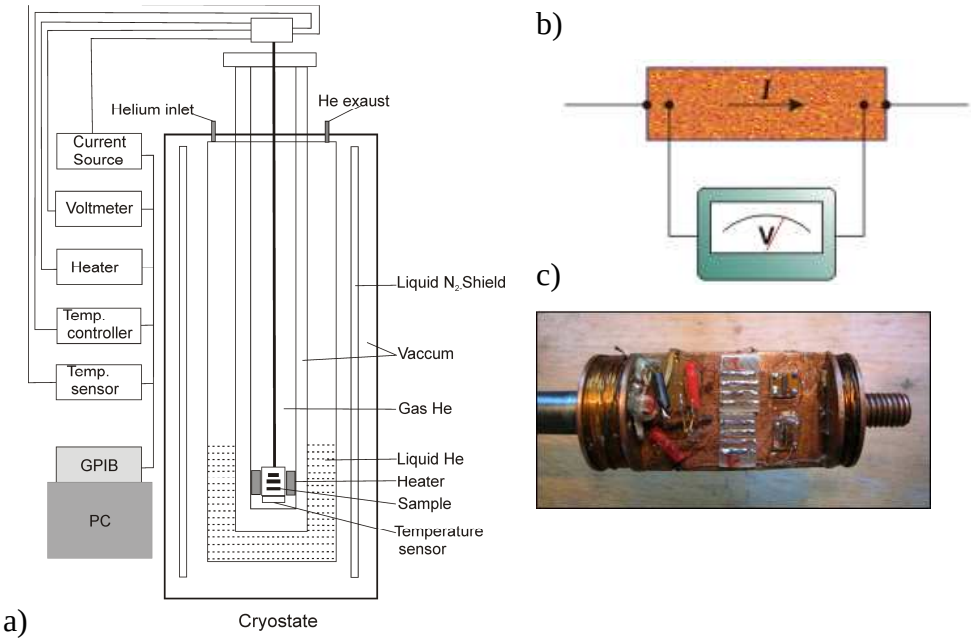

Figure 11. Resistivity measurement setup a) Schematic layout for cryostat; b) Sample connected with four probe.
(From: http://www.int.pan.wroc.pl/zbm/methods/resistivity/resistivity.html).

Figure 11 shows the low temperature measurement set up for resistivity (ρ). The rectangular bar-shape specimen was connected with four probes (Figure 11b): two outer for applying current and two inner for measuring the observed voltage. The sample with four probes was mounted on a sample holder (Figure 11c) and inserted in the sample chamber in the cryostat (Figure 11a). Helium gas in the sample chamber served to establish thermal contacts between sample and Diode sensor type DT-470 (temperature sensor). A constant current (9mA) was supplied from a dc current source. The temperature of the sample was controlled by a temperature controller Neocera LTC-11. Schematic layout for cryostat is shown in Figure 11a.

2.4.2 Magnetic Properties Measurements

Magnetic measurements were performed in the temperature range 1.72–400 K in applied external magnetic fields up to 5 T using the Quantum Design MPMS-5 SQUID magnetometer. The MPMS system consists of several superconducting components: a super conducting magnet to generate large magnetic field, a superconducting detection coil which couple inductively to the sample, a Superconducting Quantum Interface Device (SQUID) connected to the detection coil, and a superconducting magnetic shield surrounding the SQUID.

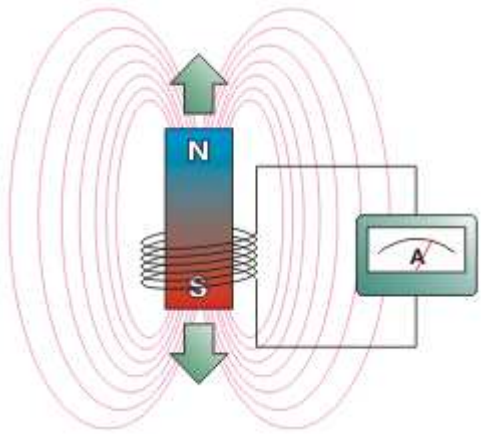

Figure 12. Over all view of SQUID (left) Schematic diagram (from: http://www.int.pan.wroc.pl/zbm/methods/mpms/mpms.html)

A measurement on MPMS is performed by moving the sample through the superconducting detection coil located outside the sample chamber in the centre of a magnet. When the sample moves through the detection coil, the magnetic moment of the sample induces an electric current in the coil. SQUID functions as highly linear current to voltage converter and any change of current in the detection coils produces a corresponding variation in the SQUID output voltage, which is proportional to the magnetic moment of the system. Detailed information about functioning of each part of the MPMS is available in the Brochure "Fundamentals of Magnetism and Magnetic Measurements Featuring Quantum Design Magnetic Property Measurement Systems".

2.4.3 Specific Heat Measurements

Specific heat measurements were performed in a quantum design physical properties measurement system (PPMS). The small sample of few milligrams is glued on a sapphire plate, which has small value of the absolute heat capacity at low temperatures. The sample is heated with some power ΔQ and the increase in temperature ΔT is measured. The heat capacity can be calculated as $C=\Delta Q/\Delta T$.

2.5 References

[4] H. M. Rietveld. Acta Crystallogr. 22(1967) 151.

[3] H. M. Rietveld, J. Appl. Crystallogr. 2 (1969) 65.

[5] T. Roisnel, Rodriguez-Carvajal, J. Mater Sci. Forum 118 (2001) 378.

[2] W. Wacha, Diploma Thesis, TU-Wien (1989).

[1] Guinier Imaging Plate Camera G670 Instruction Manual, HUBER Diffraktionstechnik GmbH & Co. KG, Sommerstrasse 4 D-83253 Rimsting.

[6] R.A. Young (ed.), The Rietveld Method (IUCr Monographs on Crystallography), Oxford University Press Inc., New York (1995).

[7] G. M. Sheldrick. University of Göttingen, Germany; Windows version by McArdle, Natl. Univ. Ireland, Galway (1997).

3 Clathrates $Ba_8\{Zn,Cd\}xSi_{46-x}$, x~7: Synthesis and Crystal Structure

3.1 Introduction

In recent studies of type-I clathrate systems $Ba_8M_xGe_{46-x}$ (M is a transition element, x ~ 8) we have dealt with the physical properties of Zn/Cd-containing clathrate germanide systems [1, 2] and have demonstrated that increasing Zn/Cd-content drives the metallic system towards a metal-to-insulator transition. The present paper extends our systematic investigation to ternary clathrate phases in the homologous silicide systems, where compounds $Ba_8Zn_xSi_{46-x}$ and $Ba_8Cd_xSi_{46-x}$ are hitherto unknown.

Binary $Ba_8Ge_{43\ \ 3}$ (open squared box denotes vacancy) clathrate phase with three framework defects is stable only in the temperature range 770-810°C [3, 4] while Ba-M-Si clathrates have no binary counterpart $Ba_8Si_{46-x\ \ x}$ stable under normal pressure [5]. Superconducting hP-$Ba_{8-x}Si_{46}$ (T_C = 9.0 K, x = 7.76) is only stable above 3 GPa and at temperatures higher than 800°C [6]. A simple Zintl count for $Ba_8\{Zn,Cd\}_8Si_{38}$, however, indicates proximity to semiconducting behaviour, which in turn may develop interesting thermoelectric properties. Therefore the main tasks of the present work are to elucidate details of the crystal structure of novel ternary clathrates $Ba_8\{Zn,Cd\}_xSi_{46-x}$. Furthermore two different routes of sample preparation, i.e. sintering powder compacts and hot-pressing are employed.

3.2 Experimental

Alloys with a weight of 2-4 grams were prepared from elemental ingots (Ba 99.9, Zn, Cd 99.99 and Si 99.999 mass. %) by reaction in vacuum-sealed quartz tubes at T=800°C for 4 days. Afterwards the reaction products were powderized to a particle size below 100µm. Samples for physical property measurements were compacted in cylinders with diameter 10 mm and height 6 mm by (a) cold-pressing in a steel die (5 MPa) followed by sintering treatment (see below) and (b) hot-pressing in a graphite die at 800°C (argon atmosphere, pressure 56 MPa, FCT hot press system HP W

200/250 2200-200-KS). Cold- and hot-pressed cylindrical specimens were then annealed in vacuum-sealed quartz tubes at T=800°C for 2-4 days followed by quenching in cold water.

Single crystals of $Ba_8Zn_7Si_{39}$ were grown by self-flux method from melt $Ba_8Zn_7Si_{39}$+10Zn (mass. %) that was cooled from 900° to 600°C with a rate of 3°C/hour. The metal flux was solved in hydrochloric acid. Inspection on an AXS-GADDS texture goniometer assured high crystal quality, unit cell dimensions and Laue symmetry of the specimens prior to X-ray intensity data collection on a four-circle Nonius Kappa diffractometer equipped with a CCD area detector employing graphite monochromated MoK_{α}. No absorption correction was necessary because of the rather regular crystal shape and small dimensions of the investigated specimen. Orientation matrix and unit cell parameters for a cubic system were derived using the program DENZO. The structure was solved by direct methods and refined with the SHELXL-97 and SHELXS-97 programs. X-ray powder diffraction (XPD) data were collected with a Guinier-Huber image plate system ($CuK_{\alpha 1}$ or $FeK_{\alpha 1}$; $8° < 2\theta < 100°$). Precise lattice parameters were calculated by least-squares fits to indexed 2θ-values employing Ge as internal standard (a_{Ge} = 0.565791 nm). The X-ray powder diffraction intensity spectra were analysed by Rietveld refinements [7].

The hot pressed samples were polished using standard procedures and were examined by optical metallography and scanning electron microscopy (SEM). Compositions for hot-pressed samples were determined via Electron Probe Micro-Analyses (EPMA) on a Carl Zeiss EVO 40 equipped with a Pentafet Link EDX system operated at 20 kV. Physical properties, which comprise electronic and thermal transport as well as thermoelectricity (details are given in ref. [1, 2]), were measured on both sintered and hot pressed samples of Zn containing clathrates and on hot pressed samples of Cd containing clathrate (due to lack of dense sintered samples for Cd clathrate).

3.3 Results and Discussion

3.3.1 Crystal Structures of $Ba_8Zn_7Si_{39}$ and $Ba_8Cd_7Si_{39}$

For a single crystal, grown by self-flux method from melt $Ba_8Zn_7Si_{39}$+10Zn (mass. %), X-ray intensity data were collected at three temperatures, 100, 200 and 300 K, in

order to evaluate atom site preferences. Extinctions were consistent with a primitive cubic lattice (space group $Pm\bar{3}n$, (a = 1.04372(1) nm) and indicated isotypism with the structure of clathrate type-I for all temperatures studied. No extra reflections were detected that would indicate a larger unit cell a' = 2a as reported for binary $Ba_8Ge_{43}\square_3$ [4]. The heavy barium atoms were unambiguously found in sites 2a (0, 0, 0) and 6c (¼, 0, ½). With a significant difference in the X-ray scattering power of Zn and Si atoms, the electron density distribution for the remaining sites appeared as follows (at 300 K): (i) Wyckoff site 16i is completely occupied by Si-atoms, whereas (ii) a random atom distribution with different Zn/Si ratio is found for the two sites 6d (0.77Zn + 0.23Si) and 24k (0.91Si + 0.09Zn). There is practically no change in atom distribution as a function of temperature. From the relative size of the rather isotropic atom displacement parameters for the sites 6d, 16i, 24k, vacancies seem not to play a significant role and all sites are found to be fully occupied. The structure refinement yields an overall formula $Ba_8Zn_7Si_{39}$ close to the nominal starting composition and to EPMA (in at.% $Ba_{15.3}Zn_{13.4}Si_{71.3}$ = $Ba_8Zn_{7.0}Si_{37.3}$). Table 1 summarizes all crystallographic information derived from the structure determination. Interatomic distances are consistent with the sum of atom radii.

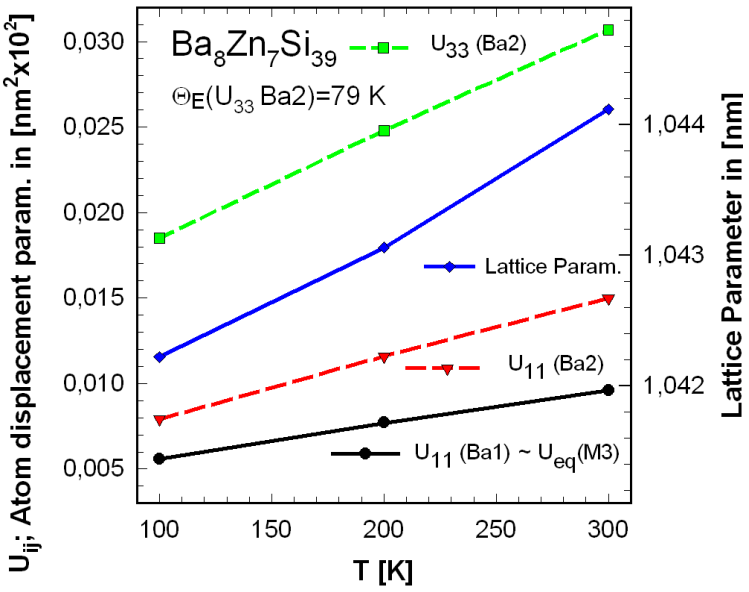

Fig.1: Temperature displacement parameters and lattice parameters of $Ba_8Zn_7Si_{39}$ vs. temperature.

The ADP parameters for Ba atoms located in the 6c site (Ba2) show a significant anisotropy in contrast to Ba1 atoms, which seem to have normal behaviour (Table 1

and Fig.1). Similarly ADP's of framework atoms reveal a rather spherical atom shape, also indicative for the absence of any significant amount of vacancies in the framework. If the $Ba_8Zn_7Si_{39}$ crystal is considered as a simple Debye solid with Ba2 atoms behaving like Einstein-oscillators, the thermal displacements and the Einstein temperatures $\Theta_{E,Uii}$ are related by

$$U_{ii} = \frac{\hbar^2}{2m_{Ba}k_B\Theta_{E,ii}}\coth\left(\frac{\Theta_{E,Uii}}{2T}\right),$$

where m_{Ba} is the atomic mass of Ba. From the linear slope $\Delta U_{ii}/\Delta T$ in Figure 1 the force constants, $K_{ii} = 4\pi^2 m\nu_{ii,\,Ba}^2$ [gsec^{-2}], the frequency of vibrations ν_{ii} [10^{12} sec^{-1}], and hence the Einstein temperatures, $\Theta_{E,Uii}$ [K] can be extracted. From symmetry constraints U_{11} is different from U_{22}=U_{33} yielding $\Theta_{E,U11}$ = 99 K and $\Theta_{E,U33}$ = 80 K in line with a slightly flattened rotational ellipsoid of Ba2 atoms. Although from symmetry constraints U_{11} is different from U_{22}=U_{33} the linear slopes $\Delta U_{ii}/\Delta T$ are indifferent for ADP parameters of framework atoms. A contour plot of electron density for the Ba2-atom at 100 K from a difference Fourier synthesis $F_{obs\text{-}Ba2}$, as shown in Fig.2, revealed a rather uniform and round shape with little hints towards off-centre positions of the Ba2-atom. Off-centre behaviour was recently documented from low temperature neutron diffraction on a single crystal of $Ba_8Zn_8Ge_{38}$ [8]. It is interesting to note that Ba1 atoms (spherical by symmetry) do not show a thermal displacement factor enhanced over the general ADP values for framework atoms. Thus no special rattling or off-centre effect can be observed for Ba1-atoms. Rietveld refinement of the X-ray powder data for the alloy with nominal composition $Ba_8Zn_8Si_{38}$ is in perfect agreement with the observed intensities and with the atom parameters derived from the single crystal study and again yields a formula $Ba_8Zn_7Si_{39}$.

Due to lack of single crystals for the Cd-containing specimen, the X-ray powder intensity spectrum for nominal composition $Ba_8Cd_8Si_{38}$ was analysed. Indexing prompted a cubic unit cell close to that established for $Ba_8Zn_7Si_{39}$. Analysis of the X-ray intensities, absence of systematic extinctions, and size of unit cell suggest isotypism with the structure type of clathrate I. Results of Rietveld refinements are compiled in Table 2. Comparing the structural details for the two novel compounds $Ba_8\{Zn,Cd\}_7Si_{39}$ we observe that the 6d site (M1) is fully occupied by Cd atoms, and

unambiguously reveals a random occupation of 0.96 Si + 0.04 Cd for the 24k site (M3), resulting in the chemical formula $Ba_8Cd_{6.8}Si_{39.2}$ in good agreement with EPMA data that yield 6.1 Cd per unit cell.

$Ba_8Zn_7Si_{39}$

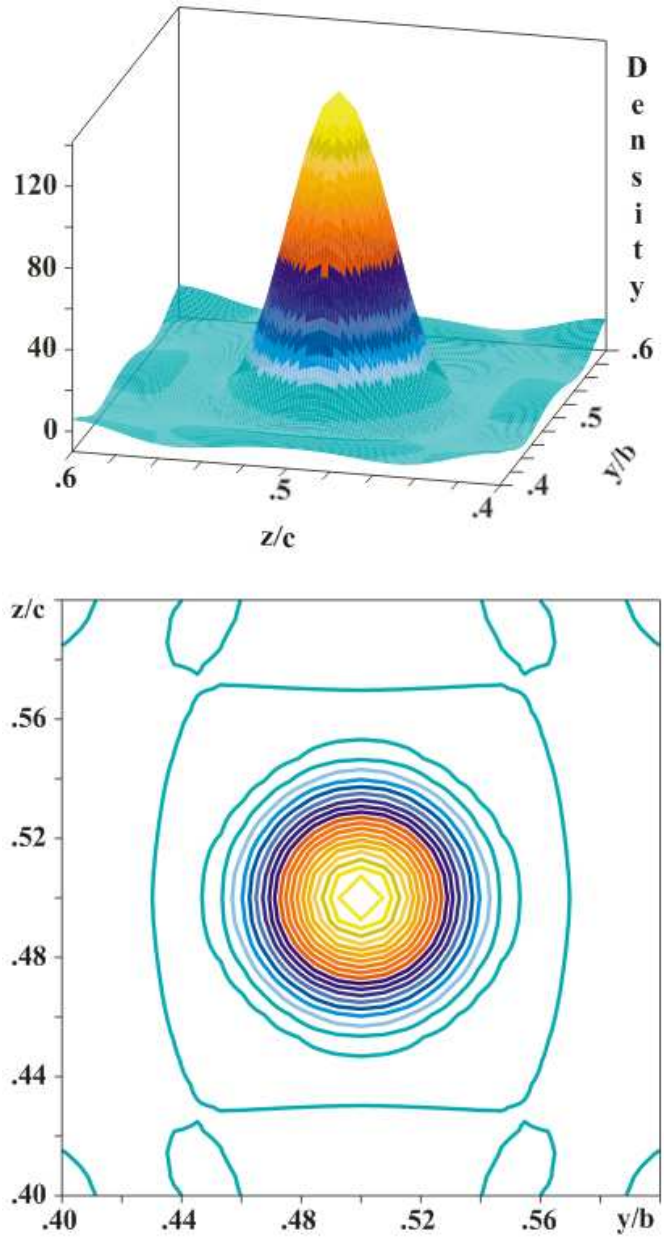

Fig. 2: Contour plot of electron density at 100 K for Ba2-atom from difference Fourier $F_{obs-Ba2}$ (top: three dimensional view, bottom projection on y-z plane).

3.3.2 Homogeneity regions of clathrates $Ba_8\{Zn, Cd\}_xSi_{46-x}$

XPD and EPMA of samples, prepared for x = 3, 6, 8, 8.5, 9, 10 and annealed at 800°C consistently yielded lattice parameters with only a small scatter (a=1.04369(2) to 1.04412(2) for the Zn-clathrate and a=1.05817(2) to 1.05866(2) for the Cd-clathrate) indicating a homogeneity region of not more than ~1 at% (Zn or Cd) in consistency with EPMA data, which for all alloys revealed a chemical formula of $Ba_8Zn_{6.9}Si_{39.1}$ and $Ba_8Cd_{6.1}Si_{39.9}$, respectively. As the error bar on the EDAX-EPMA data is about 1 at.% Zn but about 1.8 at% Cd we assume for both compounds the formula $Ba_8\{Zn, Cd\}_{\sim 7}Si_{\sim 39}$ referring to our detailed structural analyses (see above). With the composition defined, samples for physical property measurements were prepared (see experimental). Single phase condition could be attained from a nominal starting composition $Ba_8\{Zn,Cd\}_8Si_{38}$ with about extra 2% Zn(Cd) to compensate evapouration of the metals during preparation. The final product contained less than 2 % secondary phases such as Si + $Ba\{Zn,Cd\}_2Si_2$.

Whereas the germanium-based clathrate systems $Ba_8\{Zn,Cd\}_xGe_{46-x}$ reveal a continuous solid solution deriving from binary $Ba_8Ge_{43}\square_3$ [1,2], $Ba_8\{Zn,Cd\}_7Si_{39}$ clathrates have no binary counterpart $Ba_8Si_{46-x}\square_x$ ($Ba_{8-}\square Si_{46-x}$ is not stable at 800°C under normal pressure [5 ,6]) and consequently exhibit only a very small homogeneity range in the ternary. In both cases, however, Zn, Cd-metals can be considered as stabilizers of a truly ternary type I clathrate silicide compound.

3.4 Conculsion

Novel type I clathrates $Ba_8\{Zn,Cd\}_{\sim 7}Si_{\sim 39}$, have been found to exist at 800°C with no appreciable homogeneity range. Single crystal data for $Ba_8Zn_7Si_{39}$ evidence a random Zn/Si atom distribution in atom sites 6d and 24k. The 6d site is completely occupied by Cd atoms. Einstein temperature of about 80 K was derived for Ba (2) atoms with the temperature dependent Debye-Waller factor. It is interesting to note that the electron density for the Ba(2) atoms offers little evidence for an off-centre atom position.

References

[1] N. Melnychenko-Koblyuk, A. Grytsiv, St. Berger, H. Kaldarar, H. Michor, F. Röhrbacher, E. Royanian, E. Bauer, P. Rogl, H. Schmid, G. Giester, J. Phys. Condens. Mat. 19 (2007) 046203-26.

[2] N. Melnychenko-Koblyuk, A. Grytsiv, St. Berger, H. Kaldarar, H. Michor, F. Röhrbacher, E. Royanian, E. Bauer, P. Rogl, H. Schmid, G. Giester J. Phys. Condens. Mat. 19 (2007) 216223 1-26.

[3] Carrillo-Cabrera, J. Curda, K. Petters, M. Baenitz, Y. Grin, H. G. von Schnering, Z. Kristallogr. New Crystal Structures 215 (20003) 21.

[4] W. Carrillo-Cabrera, S. Budnyk, Y. Prots and Y. Grin, Z. Anorg. Allg. Chem. 630 (2004) 2267.

[5] Pauling File Binaries Edition, release 2002/1, Version 1.0, ASM Intl, Materials Park, OH, USA.

[6] H. Fukuoka, J. Kiyoto and S. Yamanaka J. Phys. & Chem. Solids 65 (2004) 333.

[7] T. Roisnel, J. Rodriguez-Carvajal Materials-Science-Forum 118 (2001) 378.

[8] M. Christensen and B. B. Iversen J. Phys.: Cond. Matter 20 **(**2008)104244.

[9] E. Parthé Gelato L, B. Chabot, M. Penzo, K. Cenzual, R. Gladyshevskii 1994 *TYPIX - Standardized Data and Crystal Chemical Characterization of Inorganic Structure Types* (Berlin Heidelberg: Springer – Verlag).

Table 1. X-Ray single crystal data for $Ba_8Zn_7Si_{39}$ at various temperatures (ω-scans, scan width 2°; redundancy > 12) and X-ray powder diffraction (XPD) data for $Ba_8Cd_7Si_{39}$; both compounds isotypic with clathrate–type I; space group $Pm\overline{3}n$; No. 223; structure settings standardized with program *Structure Tidy* [9].

Parameter/temperature	**SC, 300 K**	**SC, 200 K**	**SC, 100 K**	**XPD, 300K**
Formula from refinement	$Ba_8Zn_{6.9}Si_{39.1}$	$Ba_8Zn_{7.0}Si_{39.0}$	$Ba_8Zn_{6.9}Si_{39.1}$	$Ba_8Cd_{6.8}Si_{39.2}$
Crystal size	80x54x70	80x54x70	80x54x70	-
a [nm]	1.04412(2)	1.04306(2)	1.04222(2)	1.05866(3)
μ_{abs} [mm^{-1}]	11.38	11.40	11.43	
Data collection, 2Θ range (°)	2≤2Θ≤72.6; 130 sec/frame	2≤2Θ≤72.0; 130 sec/frame	2≤2Θ≤72.5; 130 sec/frame	8≤2Θ≤100
Total number of frames	188 ; 6 sets	188 ; 6 sets	188 ; 6 sets	
Reflections in refinement	421≥4σ(F_o) of 527 [1836]	422≥4σ(F_o) of 519 [1805]	436≥4σ(F_o) of 21 [1811]	141
Number of variables	20	20	20	18
Mosaicity	<0.45	<0.46	<0.44	$R_F = \Sigma\|F_o-F_c\|/\Sigma F_o=0.055$
$R_F^2 = \Sigma\|F_0^2-F_c^2\|/\Sigma F_0^2$	0.0175	0.0160	0.0160	$R_I = \Sigma\|I_o-I_c\|/\Sigma I_o=0.074$
R_{Int}	0.066	0.066	0.067	$R_{wP}=[\Sigma w_i\|y_{oi}-y_{ci}\|^2/\Sigma w_i\|y_{oi}\|^2]^{½}=0.063$
wR2	0.039	0.036	0.037	$R_P = \Sigma\|y_{0i}-y_{ci}\|/\Sigma\|y_{0i}\| =0.045$
GOF	1.098	1.113	1.152	$R_e = [(N-P+C)/\Sigma w_i y^2_{oi})]^{½} =0.017$
Extinction (Zachariasen)	0.0028(2)	0.0014(1)	0.0010(1)	$\chi^2 = (R_{wP}/R_e)^2 =14.2$
Ba1 in 2a (0,0,0); occ.	1.00(1)	1.00(1)	1.00(1)	1.015(5)
$U_{11}=U_{22}=U_{33}$	0.00959(9)	0.0077(1)	0.00560(9)	B_{iso} [in 10^2 nm^2]=0.45(4)
Ba2 in 6c (¼,0,½); occ.	1.00(-)	1.00(-)	1.00(-)	1.02(3)
U_{11}; $U_{22} = U_{33}$	0.0150(1); 0.0307(1)	0.0116(1); 0.0248(1)	0.0079(1); 0.0185(1)	B_{iso} [in 10^2 nm^2]=1.38(5)
M1 in 6d (¼,½,0); occ.	0.226(3) Si+0.774 Zn	0.226(3) Si+0.774 Zn	0.228(3) Si+0.772 Zn	1.01(1)Cd
U_{11}; $U_{22} = U_{33}$	0.0106(2); 0.0089(2)	0.0082(2); 0.0066(2)	0.0052(2); 0.0043(2)	B_{iso} [in 10^2 nm^2]=1.08
SI2 in 16i (x,x,x) ; occ. [1)]	1.008(3)	1.007(3)	1.012(4)	1.02(3)

Parameter/temperature	SC, 300 K	SC, 200 K	SC, 100 K	XPD, 300K
x:	0.18462(4)	0.18463(3)	0.18459(4)	0.1835(2)
$U_{11}=U_{22}=U_{33}$; $U_{23}=U_{13}=U_{12}$	0.0083(1); -0.0008(1)	0.0066(1); -0.0007(1)	0.0048(1); -0.0004(1)	B_{iso} [in 10^2 nm^2]=0.95(8)
M3 in 24k (0,y,z); occ.	0.907(2) Si+0.093 Zn	0.905(2) Si+0.095 Zn	0.907(1) Si+0.093 Zn	0.96(1) Si + 0.04Cd
y; z	0.11787(5); 0.30524(5)	0.11785(4); 0.30530(4)	0.11784(5). 0.30537(5)	0.1151(2); 0.2968(3)
U_{11};U_{22};U_{33}	0.0096(2); 0.0101(2)	0.0075(2); 0.0078(2)	0.0052(2); 0.0059(2)	B_{iso} [in 10^2 nm^2]=1.15(7)
U_{23} [in 10^2 nm^2]	0.0092(2); 0.0001(1)	0.0076(2); 0.0001(1)	0.0058(2); 0.0002(1)	
Residual density; max; min	0.82; -1.11	1.01; -1.04	0.67; -1.11	
Principal mean square atomic	Ba1 0.0096 0.0096 0.0096	Ba1 0.0077 0.0077 0.0077	Ba1 0.0056 0.0056 0.0056	
displacements U	Ba2 0.0307 0.0307 0.0151	Ba2 0.0248 0.0248 0.0116	Ba2 0.0185 0.0185 0.0079	
	M1 0.0106 0.0089 0.0089	M1 0.0082 0.0066 0.0066	M1 0.0052 0.0044 0.0044	
	Si2 0.0092 0.0092 0.0067	Si2 0.0073 0.0073 0.0053	Si2 0.0053 0.0053 0.0039	
	M3 0.0101 0.0096 0.0092	M3 0.0079 0.0076 0.0075	M3 0.0062 0.0055 0.0055	

Interatomic distances, standard deviation less than 0.0002 nm

Ba1-	8Si2	0.3339	0.3335	0.3332	0.3365
	12M3	0.3416	0.3413	0.3411	0.3370
Ba2-	8M3	0.3530	0.3526	0.3523	0.3622
	4M1	0.3691	0.3688	0.3685	0.3743
	8Si2	0.3876	0.3872	0.3869	0.3936
	4M3	0.4031	0.4027	0.4025	0.4105
M1-	4M3	0.2457	0.2454	0.2452	0.2582
	4Ba2	0.3691	0.3688	0.3685	0.3743
Si2-	1Si2	0.2365	0.2362	0.2361	0.2395
	3M3	0.2406	0.2404	0.2402	0.2439

Parameter/temperature		SC, 300 K	SC, 200 K	SC, 100 K	XPD, 300K
	1Ba1	0.3339	0.3335	0.3332	0.3365
M3-	2Si2	0.2406	0.2404	0.2402	0.2395
	1M1	0.2457	0.2454	0.2452	0.2437
	1M3	0.2461	0.2459	0.2456	0.2582
	1Ba1	0.3416	0.3413	0.3411	0.3370
	2Ba2	0.3530	0.3526	0.3523	0.3622

4 Crystal Structure and Physical Properties of Quaternary Clathrates $Ba_8Zn_xGe_{46-x-y}Si_y$, $Ba_8(Zn,Cu)xGe_{46-x}$ and $Ba_8(Zn,Pd)_xGe_{46-x}$.

4.1 Introduction

Semiconducting compounds with clatharate-type I structure continue to be of considerable attraction for thermoelectric application. The structure of the typical type I clathrate consists of a framework of Si- or Ge-atoms forming two different types of polyhedral cages each of which can host a large guest atom. The possibility of substitution at guest atoms sites and/or framework atom sites can fine-tune electronic and thermal transport properties of the material. Our recent research has been devoted to Ba-, Ge- and Si- based clathrate systems such as $Ba_8M_x\{Si,Ge\}_{46-x-y}\square_y$ (M = Mn, Fe, Co, Zn, Cd, Pd, Pt, Cu; □ = vacancy) where detailed structural analyses and phase equilibria have been studied [1, 2, 3, 4, 5, 6]. Substitution of M in Ge- based clathrates was shown to reduce the concentration of vacancies in parent binary $Ba_8Ge_{43}\square_3$ [7]. For Si-based clathrates, transition metals M atoms can act as a stabilizer for a ternary clathrate compound as binary $Ba_{8-\square}Si_{46}$ is stable only above ~3 GPa [8]. It was demonstrated that substitution of M-atoms drives the metallic system towards metal-to-insulator transition, giving rise to interesting thermoelectric properties [1-5]. It was further established that M atoms preferentially occupy the 6d site, which for low M-contents is also associated with vacancies in Ge- based clathrates [1, 2, 4].

Although research has concentrated on the substitution of Group III and transition metal elements for Group IV atoms (Si, Ge) still little has been done to study the effect of substitution of Si for Ge. Superconductivity and crystal structure of the solid solutions $Ba_{8-\square}Si_{46-x}Ge_x$($0 \leq x \leq 23$) have been reported in Ref. [8]. Cage size control of guest vibrations and thermal conductivity was studied in $Sr_8Ga_{16}Si_{30-x}Ge_x$ [9]. Structural and transport properties of $Ba_8Ga_{16}Si_xGe_{30-x}$were investigated in Ref. [10],

whereas Nenghabi and Myles [11] have recently studied the structural and electronic properties of $Ba_8Ga_{16}Si_xGe_{30-x}$ and $Sr_8Ga_{16}Si_{30-x}Ge_x$ for x = 0, 5, 15.

Although $Ba_8Ga_{16}Ge_{30}$ was shown to exhibit a figure of merit ZT=1.4 at 600°C [12], the rather high costs for Ga and Ge exclude any large scale technical application. But low price elemental combinations for clathrates have so far suffered from insufficiently high thermoelectric efficiency for TEG-applications in for instance automotive exhaust systems. In order to improve the thermoelectric figure of merit ZT, we pursue two options simultaneously: (a) electron band structure engineering by introduction of elements with significant electron DOS at the Fermi level (for instance Pd (see DOS calculation by Johnsen [13]), and (b) phonon engineering to reduce lattice thermal conductivity via introduction of additional scattering of heat carrying phonons on lattice defects (i.e. random substitution –disorder, etc.) and nanostructuring grain size in nanostructured bulk material. Thus the present work therefore attempts to synthesise vacancy free type I quaternary clathrate phases. For this task it will be necessary to evaluate structural details and phase relations for (i) partial substitution of Zn by Pd or Cu in clathrate $Ba_8Zn_xGe_{46-x}$ ($6 < x < 7.7$) and (ii) substitution of Ge for Si in the solid solution $Ba_8Zn_xGe_{46-x-y}Si_y$ ($7 < x < 7.7$).

Our previous and detailed studies on clathrate systems revealed that there is no vacancy in the 6d site for $x_{Zn} \geq 6$ in $Ba_8Zn_xGe_{46-x}$ [1], for $x_{Pd} \geq 3.8$ in $Ba_8Pd_xGe_{46-x}$ [2], and for $x_{Cu} \geq 5.5$ atoms in $Ba_8Cu_xGe_{46-x}$ clathrates [4]. For all these values the ternary solid solutions approach a semiconducting behaviour. Therefore the M to Ge ratio was kept at 6:40 for all quaternary alloys and only the clathrate solid solutions with $x_{(M+Zn)} \geq 6$ were prepared and investigated. Whereas the germanium-based clathrate system $Ba_8Zn_xGe_{46-x}$ reveals a continuous solid solution deriving from binary $Ba_8Ge_{43}\square_3$ with three framework defects in the 6d site [1, 7], $Ba_8Zn_7Si_{39}$ clathrates have no binary counterpart $Ba_8Si_{46-x}\square_x$ ($Ba_{8-\square}Si_{46-x}$ is not stable at 800°C under normal pressure [8, 14] and was said to exhibit defects at the 2a site occupied by Ba [8]). Consequently there is only a very small homogeneity range in the ternary clathrate $BaZn_xSi_{46-x}$ around x~7, however, with no defects were encountered for Ba in site 2a [5]. In order to provide a semiconducting framework in the quarternary clathrate solid solution $Ba_8Zn_xGe_ySi_{46-x-y}$, Zn contents were always kept ≥7.

4.2 Experimental

Alloys with a weight of 2-4 grams for all quaternary systems, Ba-Pd-Zn-Ge, Ba-Cu-Zn-Ge, and Ba-Zn-Si-Ge were prepared in two steps. In the first step master alloys $Ba_8M_xGe_{46-x}$ (M = Cu, Pd) and $Ba_8Ge_xSi_{46-x}$ were prepared by argon arc melting from elemental ingots (purity better than 99.9 mass %) on a water cooled copper hearth. In the second step the proper amount of Zn according to stoichiometry was added to each master alloy and vacuum-sealed in quartz tubes. Reactions were carried out at 800°C for 4 days followed by quenching in cold water. Afterwards the reaction products were powdered to a particle size below 100 μm. Samples for physical property measurement were compacted in cylinders with diameter 10 mm and height 6 mm by hot pressing in a graphite die at 800°C (argon atmosphere, pressure 60 MPa, FCT hot press system HP W 200/250 2200-200-KS). The cylindrical specimens were then annealed in vacuum-sealed quartz tubes at T = 800°C for 2 to 4 days followed by quenching in cold water.

In order to see the influence of the grain size on the physical properties, one sample with nominal composition $Ba_8Zn_8Ge_{19}Si_{19}$ was ball-milled to a grain size well below 1 μm (Fritsch Vario-Planetary mill Pulverisette 4 with tungsten carbide (WC) walled container and WC-balls) and hot pressed.

Details of the various techniques of characterization of compositions via light optical and scanning electron microscopy (SEM, EPMA on a Carl Zeiss DSM 962 equipped with a Link EDX system operated at 20kV and 60μA; binary Ba_8Ge_{43} and ternary compounds were used as internal standards); of crystal structure (x-ray powder (XRP) and single crystal (XRSC) diffraction on single crystals $Ba_8Pd_3Zn_3Ge_{40}$ and $Ba_8Cu_3Zn_3Ge_{40}$) and of physical properties, which comprise electronic and thermal transport have been described in our previous papers [1, 2].

4.3 Results and Discussion

4.3.1 Crystal Structure of $Ba_8M_xZn_yGe_{46-x-y}$ (M = Pd, Cu)

In order to evaluate atom site preference in both solid solutions $Ba_8Pd_xZn_yGe_{46-x-y}$ (x = 1, 2, 2.25, 2.4; y= 3.3, 3.75. 4, 5) and $Ba_8Cu_xZn_{6-x}Ge_{40}$ (x = 2, 3, 4, 5.2, 5.25, 5.5, 5.75), x-ray powder profiles were collected at room temperature from single-phase samples. X-ray intensity data were recorded from single crystals selected from mechanically crushed alloys with nominal composition $Ba_8Pd_3Zn_3Ge_{40}$ and $Ba_8Cu_3Zn_3Ge_{40.}$ In all cases extinctions were consistent with a primitive cubic lattice (space group $Pm\bar{3}n$, a~1.1nm). Ba-atoms, being heavy scatterers, were unambiguously found at the 2a and 6c site. Constant electron density at the sites 16i and 24k exclusively reveals Ge occupation in these sites. Metal atoms (Zn, Pd/Cu) randomly share the site 6d. A statistical mixture of three species (Zn, Pd/Cu and possible vacancies), however, cannot be elucidated by refinement of x-ray data. In our previous work [1] we have shown that the presence of vacancies in the site 6d significantly affects the bonding to the neighboring atoms in the 24k site, resulting in split sites $24k_1$and $24k_2$ [1]. As in the present case no split for the 24k site was observed the 6d site was considered as fully occupied by a statistical mixture (Zn:Pd/Cu) where the occupation of Zn and Pd/Cu was fixed from EMPA data (see Tables 3 and 4). The vacancy-free crystal structure was also confirmed by structural analysis performed on single crystals selected from the samples with composition at the middle of the solid solutions e.g $Ba_8Pd_3Zn_3Ge_{40}$, $Ba_8Cu_3Zn_3Ge_{40}$. Compositions and crystal structure details for x- ray single crystal and Rietveld refinements are given in Tables 1, 2, 3 and 4. The variation of lattice parameters vs. M (Pd, Cu) is shown in Figure 1. It can be seen that lattice parameters for $Ba_8Pd_xZn_yGe_{46-x-y}$ do not show any appreciable change with increasing Pd content owing to the small difference in the atomic radii of Zn and Pd. On the other hand because of the smaller size of Cu than Zn, shrinkage of the unit cell with increase of Cu content is observed. Positional parameters vs. M content are shown in Figures 2 and 3.

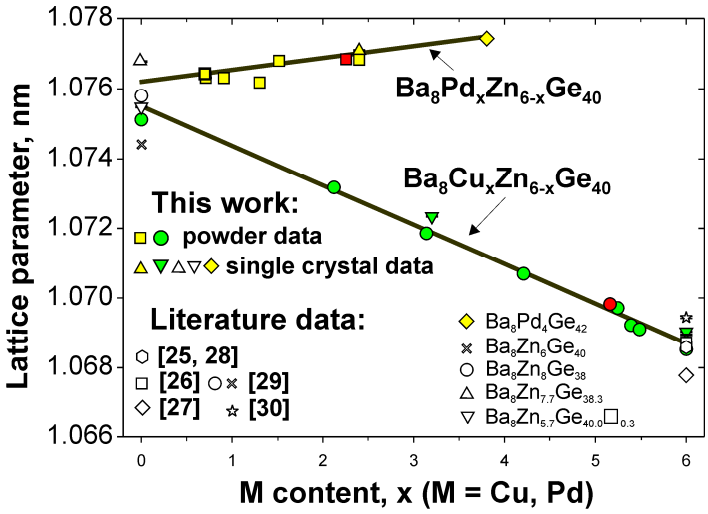

Figure. 1: Lattice parameters vs. M-content in $Ba_8M_xZn_{6-x}Ge_{40}$.

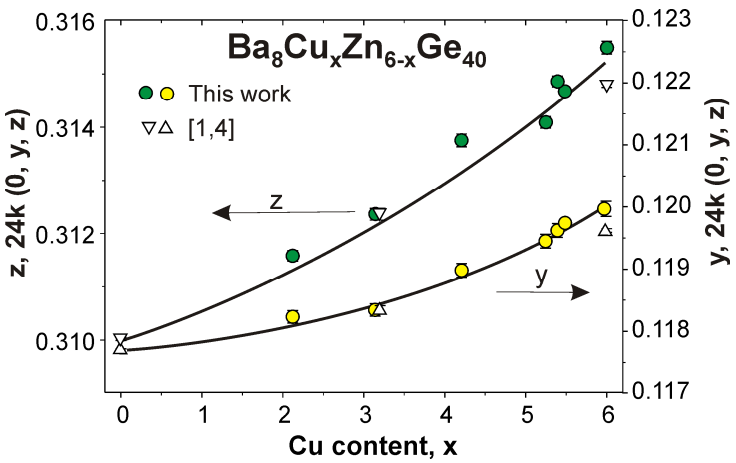

Figure. 2: Atom parameters (y, z) vs. Cu content in $Ba_8Cu_xZn_{6-x}Ge_{40}$

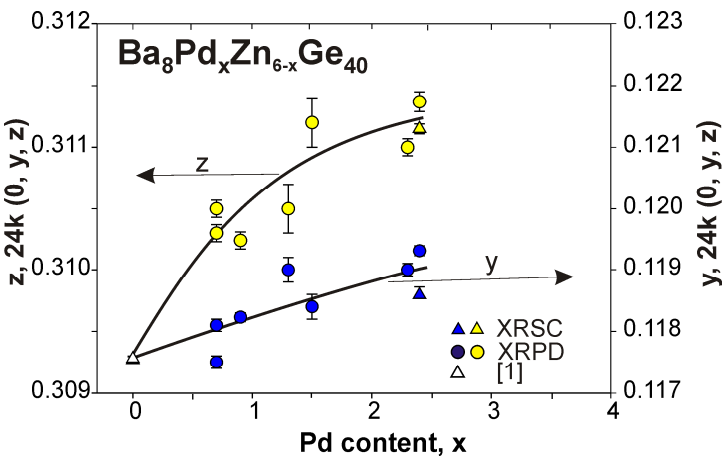

Figure 3: Atom parametrs (y, z) parameters vs. Pd content in $Ba_8Pd_xZn_{6-x}Ge_4$

Table 1: Composition from EMPA and crystallographic data for $Ba_8Pd_xZn_yGe_{46-x-y}$ and $Ba_8Cu_xZn_yGe_{46-x-y}$ alloys.

Nominal composition	EMPA, at %				EMPA, formula[1)]	Accepted composition	Lattice parameter	Ge2 in 16i	Ge3 in 24k (0,y,z);	
	Ba	M	Zn	Ge			a, nm	(x,x,x)	y	z
$Ba_8Pd_3Zn_3Ge_{40}$	14.91	4.47	6.06	74.56	$Ba_8Pd_{2.40}Zn_{3.25}Ge_{40.01}\square_{0.34}$	$Ba_8Pd_{2.4}Zn_{3.33}Ge_{40.3}$	1.07683(1)	0.18266(5)	0.11931(8)	0.31137(8)
						$Ba_8Pd_{2.4}Zn_{3.3}Ge_{40.3}$[2)]	1.07709(2)	0.18327(3)	0.11859(4)	0.31115(4)
$Ba_8Pd_2Zn_4Ge_{40}$	15.06	2.86	8.30	73.78	$Ba_8Pd_{1.52}Zn_{4.41}Ge_{39.19}\square_{0.88}$	$Ba_8Pd_{1.5}Zn_{4.4}Ge_{40.1}$	1.07680(2)	0.1833(1)	0.1184(2)	0.3112(2)
$Ba_8Pd_{2.25}Zn_{3.75}Ge_{40}$	15.01	2.44	8.49	74.06	$Ba_8Pd_{1.30}Zn_{4.53}Ge_{39.47}\square_{0.70}$	$Ba_8Pd_{1.3}Zn_{4.5}Ge_{40.2}$	1.07618(1)	0.1827(12	0.1190(2)	0.3105(2)
$Ba_8PdZn_5Ge_{40}$	15.02	1.71	9.59	73.68	$Ba_8Pd_{0.91}Zn_{5.11}Ge_{39.24}\square_{0.74}$	$Ba_8Pd_{0.9}Zn_{5.1}Ge_{40.00}$	1.07631(2)	0.18270(5)	0.11823(7)	0.31024(7)
$Ba_8PdZn_5Ge_{40}$	15.09	1.34	10.68	72.89	$Ba_8Pd_{0.71}Zn_{5.66}Ge_{38.64}\square_{0.99}$	$Ba_8Pd_{0.7}Zn_{5.7}Ge_{39.6}$	1.07632(2)	0.18335(7)	0.1175(1)	0.3103(1)
$Ba_8Pd_2Zn_7Ge_{37}$	14.94	1.30	11.03	72.73	$Ba_8Pd_{0.70}Zn_{5.90}Ge_{38.95}\square_{0.45}$	$Ba_8Pd_{0.7}Zn_{5.9}Ge_{39.4}$	1.07643(1)	0.18305(9)	0.1181(1)	0.3105(1)
$Ba_8Pd_{2.4}Zn_{3.3}Ge_{40.3}$	14.84	4.17	6.72	74.27	$Ba_8Pd_{2.24}Zn_{3.62}Ge_{40.04}\square_{0.08}$	$Ba_8Pd_{2.3}Zn_{3.6}Ge_{40.1}$	1.07664(2)	0.18305(8)	0.1190(1)	0.3110(1)
$Ba_8Cu_2Zn_4Ge_{40}$	14.63	3.88	6.71	74.78	$Ba_8Cu_{2.12}Zn_{3.67}Ge_{40.89}\square_{-0.68}$	$Ba_8Cu_{2.1}Zn_{3.7}Ge_{40.2}$	1.07318(1)	0.18304(7)	0.1182(1)	0.3116(1)
$Ba_8Cu_3Zn_3Ge_{40}$	14.66	5.76	5.16	74.42	$Ba_8Cu_{3.15}Zn_{2.81}Ge_{40.61}\square_{-0.57}$	$Ba_8Cu_{3.2}Zn_{2.8}Ge_{40.0}$	1.07185(2)	0.18282(8)	0.1183(1)	0.3124(1)
						$Ba_8Cu_{3.2}Zn_{2.8}Ge_{40.0}$[2)]	1.07234(2)	0.18331(8)	0.11834(6)	0.31240(6)
$Ba_8Cu_4Zn_2Ge_{40}$	14.72	7.75	3.38	74.15	$Ba_8Cu_{4.21}Zn_{1.84}Ge_{40.30}\square_{-0.35}$	$Ba_8Cu_{4.2}Zn_{1.8}Ge_{40.0}$	1.07069(2)	0.18396(1)	0.1190(1)	0.3137(1)
$Ba_8Cu_{5.25}Zn_{0.75}Ge_{40}$	14.74	9.66	1.42	74.18	$Ba_8Cu_{5.24}Zn_{0.77}Ge_{40.26}\square_{-0.27}$	$Ba_8Cu_{5.2}Zn_{0.8}Ge_{40.0}$	1.06971(1)	0.18242(8)	0.1194(1)	0.3141(1)
$Ba_8Cu_{5.5}Zn_{0.5}Ge_{40}$	14.86	10.01	0.93	74.20	$Ba_8Cu_{5.39}Zn_{0.50}Ge_{39.95}\square_{0.16}$	$Ba_8Cu_{5.4}Zn_{0.5}Ge_{40.1}$	1.06922(2)	0.18237(8)	0.11961(8)	0.3149(1)
$Ba_8Cu_{5.75}Zn_{0.25}Ge_{40}$	14.93	10.24	0.69	74.14	$Ba_8Cu_{5.49}Zn_{0.37}Ge_{39.73}\square_{0.41}$	$Ba_8Cu_{5.5}Zn_{0.4}Ge_{40.1}$	1.06910(2)	0.18332(7)	0.11973(2)	0.31467(1)
$Ba_8Cu_{5.2}Zn_{0.8}Ge_{40}$	15.09	8.70	2.13	74.06	$Ba_8Cu_{4.6}Zn_{1.13}Ge_{39.25}\square_{1.01}$[3)]	$Ba_8Cu_{5.2}Zn_{0.8}Ge_{40.0}$	1.06994(2)	0.18322(8)	0.1194(1)	0.3134(1)

[1)] Ba sublattice (2a and 6d sites) was found to be fully occupied.

[2)] Lattice parameters and crystallographic data after X-ray single crystal refinement.

Table 2. X-Ray single crystal data for $Ba_8Pd_xZn_{6-x}Ge_{40}$ and $Ba_8Cu_xZn_{6-x}Ge_{40}$ (room temperature, ω-scans, scan width 2°; redundancy >10); clathrate –type I; space group $Pm\bar{3}n$; No. 223; standardized with program *Structure Tidy* [16].

Parameter/compound[1)]	**$Ba_8Pd_3Zn_3Ge_{40}$**	**$Ba_8Cu_3Zn_3Ge_{40}$**
Formula from refinement	**$Ba_8Pd_{2.40}Zn_{3.25}Ge_{40.38}$**	**$Ba_8Cu_{3.20}Zn_{2.80}Ge_{40.00}$**
Crystal size	50x58x60 μm^3	50x58x60 μm^3
a [nm], Ge standard	1.07683(1)	1.07185(2)
μ_{abs} [mm^{-1}]	32.16	35.27
Data collection, 2Θ range(°)	2≤2Θ≤72.0; 50 sec/frame	2≤2Θ≤72.0; 50 sec/frame
Total number of frames	201 6 sets	201 6 sets
Reflections in refinement	470≥4σ(F_o) of 567	523≥4σ(F_o) of 567
Mosaicity	<0.45	<0.45
Number of variables	17	16
$R_F^2 = \Sigma\|F_0^2-F_c^2\|/\Sigma F_0^2$	0.0245	0.0178
R_{Int}	0.0376	0.0153
wR2	0.0534	0.0322
GOF	1.121	1.158
Extinction (Zachariasen)	0.0011(1)	0.0016(1)
Ba1 in 2a (0,0,0); occ.	1.00(1)	1.00(1)
$U_{11}=U_{22}=U_{33}$ [in $10^2 nm^2$]	0.0106(2)	0.0096(1)
Ba2 in 6c (¼,0,½); occ.	1.00(1)	1.00(1)
U_{11}; $U_{22} = U_{33}$	0.0248(4); 0.0537(3)	0.0182(2); 0.0382(2)
M1 in 6d (¼,½,0); occ.	0.54(1)Zn[2)]+0.40(1)Pd[2)]+0.06(1) (3)Ge	0.53(1)Cu[2)]+0.47(1)Zn[2)]
U_{11}; $U_{22} = U_{33}$	0.0143(4); 0.0106(3)	0.0117(3); 0.0097(1)
Ge2 in 16i (x,x,x) ; occ.	1.00(1)	1.00(1)
x:	0.18327(3)	0.18331(2)
$U_{11}=U_{22}=U_{33}$; $U_{23}=U_{13}=U_{12}$	0.0099(1); -0.0009(1)	0.0087(1); -0.0008(1)
Ge3 in 24k (0,y,z); occ.	1.00(1)	1.00(1)
y, z	0.11859(4); 0.31115(4)	0.11864(2); 0.31240(2)
U_{11}; U_{22}	0.0111(2); 0.0126(2)	0.0099(1); 0.0105(1)
U_{33}; U_{23}	0.0106(2); 0.0009(1)	0.0094(1); 0.0006(1)
Residual density $e^-/Å^3$; max; min	1.67; -1.50	0.92; -0.74
Principal mean square atomic displacements U	Ba1 0.0106 0.0106 0.0106	Ba1 0.0096 0.0096 0.0096
	Ba2 0.0537 0.0537 0.0248	Ba2 0.0382 0.0382 0.0182
	M1 0.0143 0.0106 0.0106	M1 0.0117 0.0097 0.0097
	Ge2 0.0108 0.0108 0.0080	Ge2 0.0095 0.0095 0.0070
	Ge3 0.0129 0.0111 0.0103	Ge3 0.0108 0.0099 0.0092
Interatomic distances, standard deviation less than 0.0003 nm		
Ba1 – 8Ge2	0.3418	0.3403
- 12Ge3	0.3586	0.3582
Ba2 - 8Ge3	0.3607	0.3583
- 4M1	0.3807	0.3790
- 8Ge2	0.4005	0.3987
- 4Ge3	0.4160	0.4142
M1 - 4Ge3	0.2477	0.2455
- 4Ba2	0.3807	0.3790
Ge2 – 1Ge2	0.2489	0.2476
- 3Ge3	0.2505	0.2501
- 1Ba1	0.3418	0.3403
Ge3- 1M1	0.2477	0.2455
- 2Ge2	0.2505	0.2501
- 1Ge3	0.2554	0.2543
- 1Ba1	0.3586	0.3582
- 2Ba2	0.3607	0.3583

[1)]Nominal composition.[2)] Pd, Cu, Zn fixed after EMPA.

Table 3a: X-ray powder data for $Ba_8Pd_xZn_{6-x}Ge_{40}$ at x= 0.70, 0.71, 0.91, 2.40; (room temperature, image plate data collection, Cu $K_{\alpha 1}$ radiation, Θ range 8≤2Θ≤100); clathrate type I, space group $Pm\bar{3}n$; No. 223; standardized with program *Structure Tidy* [16].

Parameter/compound[1)]	**$Ba_8Pd_2Zn_7Ge_{37}$**	**$Ba_8Pd_1Zn_5Ge_{40}$**	**$Ba_8Pd_1Zn_5Ge_{40}$**	**$Ba_8Pd_{2.4}Zn_{3.3}Ge_{40.3}$**
Composition, EMPA at.%	**$Ba_8Pd_{0.70}Zn_{5.90}Ge_{38.95}$**	**$Ba_8Pd_{0.71}Zn_{5.66}Ge_{38.64}$**	**$Ba_8Pd_{0.91}Zn_{5.11}Ge_{39.24}$**	**$Ba_8Pd_{2.24}Zn_{3.62}Ge_{40.04}\square_{0.08}$**
Composition from refinement	**$Ba_8Pd_{0.70}Zn_{5.90}Ge_{39.40}$**	**$Ba_8Pd_{0.71}Zn_{5.66}Ge_{39.63}$**	**$Ba_8Pd_{0.91}Zn_{5.11}Ge_{39.98}$**	**$Ba_8Pd_{2.4}Zn_{3.6}Ge_{40.0}$**
a [nm], Ge standard	1.07643(1)	1.07632(2)	1.07631(2)	1.07664(2)
Reflections measured	144	144	148	145
Number of variables	24	28	24	17
$R_F = \Sigma\|F_o-F_c\|/\Sigma F_o$	0.0641	0.0685	0.0714	0.063
$R_I = \Sigma\|I_o-I_c\|/\Sigma I_o$	0.0836	0.0787	0.0652	0.049
$R_{wP}=[\Sigma w_i\|y_{oi}-y_{ci}\|^2/\Sigma w_i\|y_{oi}\|^2]^{½}$	0.0875	0.0864	0.0433	0.040
$R_P = \Sigma\|y_{oi}-y_{ci}\|/\Sigma\|y_{oi}\|$	0.0557	0.0573	0.0328	0.026
$R_e = [(N-P+C)/\Sigma w_i y^2_{oi})]^{½}$	0.0288	0.0195	0.0297	0.023
$\chi^2 = (R_{wP}/R_e)^2$	9.25	19.6	2.12	3.20
Atom parameters				
Ba1 in 2a (0,0,0); occ.	1.00(1)	1.00(1)	1.00(1)	1.00(1)
B_{iso} (10^2 nm^2)	0.37(6)	0.36(5)	0.32(3)	0.46(5)
Ba2 in 6c (¼,0,½); occ.	1.00(1)	1.00(1)	1.00(1)	1.00(1)
B_{iso} (10^2 nm^2)	3.04(6)	2.83(5)	2.75(4)	2.96(6)
M1[2)] in 6d (¼,½,0); occ.	0.12(1)Pd+0.88(1)Zn	0.12(1)Pd+0.88(1)Zn	0.15(1)Pd+0.85(1)Zn	0.38(1)Pd+0.60(1)Zn+0.02(1)Ge
B_{iso} (10^2 nm^2)	0.97(8)	0.70(6)	0.99(4)	0.81(6)
M2 in 16i (x,x,x) ; occ.	0.04(1)Zn+0.96(1)Ge	0.02(1)Zn+0.98(1)Ge	1.00(1)Ge	1.00(1)Ge
x	0.18305(9)	0.18335(7)	0.18270(5)	0.18312(8)
B_{iso} (10^2 nm^2)	0.88(4)	0.79(4)	0.98(3)	0.73(4)
Ge3 in 24k (0,y,z); occ.	1.00(1)	1.00(1)	1.00(1)	1.00(1)
y; z	0.1181(1); 0.3105(1)	0.1175(1); 0.3103(1)	0.11823(7); 0.31024(7)	0.1189(1); 0.3110(1)
B_{iso} (10^2 nm^2)	0.55(4)	0.52(3)	0.67(2)	0.63(3)
Interatomic distances, standard deviation less than 0.0003 nm				
Ba1 – 8M2	0.3413	0.3418	0.3406	0.3413
- 12Ge3	0.3576	0.3571	0.3573	0.3583
Ba2 - 8Ge3	0.3608	0.3607	0.3610	0.3608
- 4M1	0.3806	0.3805	0.3805	0.3805
- 8M2	0.4005	0.4003	0.4007	0.4004
- 4Ge3	0.4162	0.4168	0.4160	0.4154
M1 - 4Ge3	0.2485	0.2491	0.2487	0.2476
- 4Ba2	0.3806	0.3805	0.3805	0.3805
M2 – 1M2	0.2496	0.2485	0.2497	0.2494

Parameter/compound[1)]	$Ba_8Pd_2Zn_7Ge_{37}$	$Ba_8Pd_1Zn_5Ge_{40}$	$Ba_8Pd_1Zn_5Ge_{40}$	$Ba_8Pd_{2.4}Zn_{3.3}Ge_{40.3}$
- 3Ge3	0.2501	0.2503	0.2509	0.2501
- 1Ba1	0.3413	0.3418	0.3406	0.3413
Ge3- 1M1	0.2485	0.2491	0.2487	0.2476
- 2M2	0.2501	0.2503	0.2509	0.2501
- 1Ge3	0.2542	0.2528	0.2545	0.2559
- 1Ba1	0.3576	0.3571	0.3573	0.3583
- 2Ba2	0.3608	0.3607	0.3610	0.3608

[1)]Nominal composition.
[2)] Pd, and Zn fix after EMPA.

Table 3b: X-ray powder data for $Ba_8Pd_xZn_{6-x}Ge_{40}$ at x= 1.30, 1.52, 2.40; (room temperature, image plate data collection, Cu $K_{\alpha 1}$ radiation, Θ range 8≤2Θ≤100); clathrate type I, space group $Pm\overline{3}n$; No. 223; standardized with program *Structure Tidy* [16].

Parameter/compound[1)]	$Ba_8Pd_{2.25}Zn_{3.75}Ge_{40}$	$Ba_8Pd_2Zn_4Ge_{40}$	$Ba_8Pd_3Zn_3Ge_{40}$
Composition, EMPA at.%	$Ba_8Pd_{1.30}Zn_{4.53}Ge_{39.47}$	$Ba_8Pd_{1.52}Zn_{4.41}Ge_{39.19}$	$Ba_8Pd_{2.40}Zn_{3.25}Ge_{40.00}$
Composition from refinement	$Ba_8Pd_{1.30}Zn_{4.53}Ge_{40.17}$	$Ba_8Pd_{1.52}Zn_{4.41}Ge_{40.07}$	$Ba_8Pd_{2.40}Zn_{3.25}Ge_{40.35}$
a [nm], Ge standard	1.07618(1)	1.07680(2)	1.07683(1)
Reflections measured	144	145	143
Number of variables	24	27	24
$R_F = \Sigma\|F_o-F_c\|/\Sigma F_o$	0.0776	0.0788	0.0734
$R_I = \Sigma\|I_o-I_c\|/\Sigma I_o$	0.0833	0.0835	0.0683
$R_{wP}=[\Sigma w_i\|y_{oi}-y_{ci}\|^2/\Sigma w_i\|y_{oi}\|^2]^{½}$	0.0591	0.0562	0.0479
$R_P = \Sigma\|y_{oi}-y_{ci}\|/\Sigma\|y_{oi}\|$	0.0449	0.0383	0.0345
$R_e = [(N-P+C)/\Sigma w_i y^2_{oi})]^{½}$	0.0183	0.0202	0.0232
$\chi^2 = (R_{wP}/R_e)^2$	10.4	7.70	4.28
Atom parameters			
Ba1 in 2a (0,0,0); occ.	1.00(1)	1.00(1)	1.00(1)
B_{iso} (10^2 nm^2)	0.38(5)	0.37(7)	0.36(4)
Ba2 in 6c (¼,0,½); occ.	1.00(1)	1.00(1)	1.00(1)
B_{iso} (10^2 nm^2)	3.00(8)	2.65(7)	3.59(4)
M1[2)] in 6d (¼,½,0); occ.	0.22(1)Pd+0.75(1)Zn+0.03(1)Ge	0.25(1)Pd+0.74(1)Zn+0.01(1)Ge	0.40(1)Pd+0.54(1)Zn+0.06(1)Ge
B_{iso} (10^2 nm^2)	0.77(6)	0.98(7)	0.97(5)
Ge2 in 16i (x,x,x) ; occ.	1.00(1)Ge[)]	1.00(1)Ge[)]	1.00(1)Ge
x	0.1827(1)	0.1833(1)	0.18266(5)
B_{iso} (10^2 nm^2)	0.98(5)	0.84(6)	0.94(5)
Ge3 in 24k (0,y,z); occ.	1.00(1)	1.00(1)	1.00(1)
y, z	0.1190(2); 0.3105(2)	0.1184(2); 0.3112(2)	0.11931(8); 0.31137(8)
B_{iso} (10^2 nm^2)	0.72(3)	0.59(4)	0.81(2)

Interatomic distances, standard deviation less than 0.0003 nm			
Ba1 - 8Ge2	0.3405	0.3419	0.3407
- 12Ge3	0.3578	0.3586	0.3591
Ba2 - 8Ge3	0.3611	0.3606	0.3609
- 4M1	0.3805	0.3807	0.3807
- 8Ge2	0.4006	0.4005	0.4009
- 4Ge3	0.4152	0.4161	0.4152
M1 - 4Ge3	0.2480	0.2478	0.2471
- 4Ba2	0.3805	0.3807	0.3807
Ge2 - 1Ge2	0.2495	0.2487	0.2501
- 3Ge3	0.2509	0.2506	0.2512
- 1Ba1	0.3405	0.3419	0.3407
Ge3- 1M1	0.2480	0.2478	0.2471
- 2Ge2	0.2495	0.2506	0.2501
- 1Ge3	0.2561	0.2550	0.2570
- 1Ba1	0.3578	0.3586	0.3591
- 2Ba2	0.3611	0.3606	0.3609

[1)]Nominal composition.

[2)] Pd, and Zn fix after EMPA.

Table 4a: x-ray powder data for Ba8CuxZn6-xGe40 at x= 2.1, 3.2, 4.2; (room temperature, image plate data collection, Cu Kα radiation, Θ range 8≤2Θ≤100); clathrate type I, space group $Pm\bar{3}n$; No. 223); standardized with program Structure Tidy [16].

Parameter/compound[1)]	**$Ba_8Cu_2Zn_4Ge_{40}$**	**$Ba_8Cu_3Zn_3Ge_{40}$**	**$Ba_8Cu_4Zn_2Ge_{40}$**
Composition, EMPA	**$Ba_8Cu_{2.1}Zn_{3.7}Ge_{40.9}$**	**$Ba_8Cu_{3.2}Zn_{2.8}Ge_{40.6}$**	**$Ba_8Cu_{4.2}Zn_{1.8}Ge_{40.3}$**
Composition from refinement[2)]	**$Ba_8Cu_{2.1}Zn_{3.9}Ge_{40.0}$**	**$Ba_8Cu_{3.2}Zn_{2.8}Ge_{40.0}$**	**$Ba_8Cu_{4.2}Zn_{1.8}Ge_{40.0}$**
a [nm], Ge standard	1.07318(1)	1.07185(2)	1.07069(2)
Reflections measured	143	143	143
Number of variables	25	25	25
$R_F = \Sigma\|F_o-F_c\|/\Sigma F_o$	0.064	0.084	0.087
$R_I = \Sigma\|I_o-I_c\|/\Sigma I_o$	0.080	0.071	0.072
$R_{wP}=[\Sigma w_i\|y_{oi}-y_{ci}\|^2/\Sigma w_i\|y_{oi}\|^2]^{½}$	0.077	0.086	0.098
$R_P = \Sigma\|y_{oi}-y_{ci}\|/\Sigma\|y_{oi}\|$	0.050	0.061	0.072
$R_e = [(N-P+C)/\Sigma w_i y^2_{oi})]^{½}$	0.021	0.019	0.018
$\chi^2 = (R_{wP}/R_e)^2$	13.6	20.5	23.4

Parameter/compound[1)]	**$Ba_8Cu_2Zn_4Ge_{40}$**	**$Ba_8Cu_3Zn_3Ge_{40}$**	**$Ba_8Cu_4Zn_2Ge_{40}$**
Atom parameters			
Ba1 in 2a (0,0,0); occ.	1.00(1)	1.00(1)	1.00(1)
B_{iso} (10^2 nm^2)	0.50(5)	0.37(5)	0.65(6)
Ba2 in 6c (¼,0,½); occ.	1.00(1)	1.00(1)	1.00(1)
B_{iso} (10^2 nm^2)	2.47(5)	2.64(5)	2.29(5)
M1[2)] in 6d (¼,½,0); occ.	0.35(1)Cu+0.650Zn	0.53(1)Cu+0.47(1)Zn	0.70(1)Cu+0.30(1)Zn
B_{iso} (10^2 nm^2)	0.45(9)	0.93(8)	0.39(9)
Ge2 in 16i (x,x,x) ; occ.	1.00(1)	1.00(1)	1.00(1)
x	0.18304(7)	0.18282(8)	0.18396(1)
B_{iso} (10^2 nm^2)	0.88(3)	0.91(4)	0.81(4)
Ge3 in 24k (0,y,z); occ.	1.00(1)	1.00(1)	1.00(1)
y; z	0.1182(1); 0.3116(1)	0.1183(1); 0.3124(1)	0.1190(1); 0.3137(1)
B_{iso} (10^2 nm^2)	0.86(3)	0.66(3)	0.63(4)
Interatomic distances, standard deviation less than 0.0003 nm			
Ba1 - 8Ge2	0.3402	0.3394	0.3412
- 12Ge3	0.3576	0.3580	0.3592
Ba2 - 8Ge3	0.3591	0.3583	0.3573
- 4M1	0.3794	0.3790	0.3785
- 8Ge2	0.3993	0.3990	0.3979
- 4Ge3	0.4150	0.4145	0.4136
M1 - 4Ge3	0.2468	0.2457	0.2438
- 4Ba2	0.3794	0.3790	0.3785
Ge2 - 1Ge2	0.2489	0.2494	0.2449
- 3Ge3	0.2499	0.2499	0.2509
- 1Ba1	0.3402	0.3394	0.3412
Ge3- 1M1	0.2468	0.2457	0.2438
- 2Ge2	0.2499	0.2499	0.2509
- 1Ge3	0.2539	0.2537	0.2548
- 1Ba1	0.3576	0.3580	0.3592
- 2Ba2	0.3591	0.3583	0.3573

[1)]Nominal composition.

[2)] Cu, and Zn fix after EMPA.

Table 4b: X- ray powder diffraction data for Ba8CuxZn6-xGe40 at x=5.2, 5.4, 5.5; (room temperature, image plate data collection, Cu Kα1 radiation, Θ range 8≤2Θ≤100); (space group $Pm\bar{3}n$), standardized with programme Structure Tidy [16].

Parameter/compound[1)]	**$Ba_8Cu_{5.25}Zn_{0.75}Ge_{40}$**	**$Ba_8Cu_{5.5}Zn_{0.5}Ge_{40}$**	**$Ba_8Cu_{5.75}Zn_{0.25}Ge_{40}$**	**$Ba_8Cu_{5.2}Zn_{0.8}Ge_{40}$**
Composition, EMPA	**$Ba_8Cu_{5.2}Zn_{0.8}Ge_{40.3}$**	**$Ba_8Cu_{5.4}Zn_{0.5}Ge_{40.0}$**	**$Ba_8Cu_{5.5}Zn_{0.4}Ge_{39.7}$**	**$Ba_8Cu_{5.2}Zn_{0.8}Ge_{40}$**
Composition from refinement	**$Ba_8Cu_{5.2}Zn_{0.8}Ge_{40.0}$**	**$Ba_8Cu_{5.4}Zn_{0.6}Ge_{40.0}$**	**$Ba_8Cu_{5.5}Zn_{0.5}Ge_{40.0}$**	**$Ba_8Cu_{5.2}Zn_{0.8}Ge_{40}$ [3)]**
a [nm], Ge standard	1.06971(1)	1.06922(2)	1.06910(2)	1.06994(2)
Reflections measured	144	143	143	143
Number of variables	25	25	25	22
$R_F = \Sigma\|F_o-F_c\|/\Sigma F_o$	0.059	0.089	0.051	0.067
$R_I = \Sigma\|I_o-I_c\|/\Sigma I_o$	0.075	0.094	0.056	0.065
$R_{wP}=[\Sigma w_i\|y_{oi}-y_{ci}\|^2/\Sigma w_i\|y_{oi}\|^2]^{½}$	0.069	0.095	0.089	0.034
$R_P = \Sigma\|y_{oi}-y_{ci}\|/\Sigma\|y_{oi}\|$	0.045	0.071	0.062	0.022
$R_e = [(N-P+C)/\Sigma w_i y^2_{oi})]^{½}$	0.029	0.017	0.011	0.020
$\chi^2 = (R_{wP}/R_e)^2$	5.62	30.8	64.2	2.86
Atom parameters				
Ba1 in 2a (0,0,0); occ.	1.00(1)	1.00(1)	1.00(1)	1.00(1)
B_{iso} (10^2 nm^2)	0.46(5)	0.32(5)	0.53(6)	0.63(6)
Ba2 in 6c (¼,0,½); occ.	1.00(1)	1.00(1)	1.00(1)	1.00(1)
B_{iso} (10^2 nm^2)	2.45(5)	2.64(5)	2.51(5)	2.67(6)
M1[2)] in 6d (¼,½,0); occ.	0.87(1)Cu+0.13(1)Zn	0.90(1)Cu+0.10(1)Zn	0.92(1)Cu+0.08(1)Zn	
B_{iso} (10^2 nm^2)	0.86(7)	0.92(8)	0.82(7)	1.44(9)
Ge2 in 16i (x,x,x) ; occ.	1.00(1)	1.00(1)	1.00(1)	1.00(1)
x	0.18242(8)	0.18237(8)	0.18332(7)	0.18322(8)
B_{iso} (10^2 nm^2)	0.96(4)	0.98(4)	0.60(3)	1.18(4)
Ge3 in 24k (0,y,z); occ.	1.00(1)	1.00(1)	1.00(1)	1.00(1)
y; z	0.1194(1); 0.3141(1)	0.11961(8); 0.3149(1)	0.11973(2); 0.31467(1)	0.1194(1); 0.3134(1)
B_{iso} (10^2 nm^2)	0.56(3)	0.40(3)	0.81(3)	0.86(4)
	Interatomic distances, standard deviation less than 0.0003 nm			
Ba1 - 8Ge2	0.3380	0.3377	0.3395	0.3394
- 12Ge3	0.3594	0.3601	0.3599	0.3588
Ba2 - 8Ge3	0.3569	0.3564	0.3565	0.3573
- 4M1	0.3782	0.3780	0.3780	0.3782
- 8Ge2	0.3984	0.3982	0.3976	0.3979
- 4Ge3	0.4128	0.4126	0.4124	0.4127
M1 - 4Ge3	0.2430	0.2421	0.2422	0.2436
- 4Ba2	0.3782	0.3780	0.3780	0.3782
Ge2 - 1Ge2	0.2504	0.2505	0.2469	0.2474

Parameter/compound[1)]	**$Ba_8Cu_{5.25}Zn_{0.75}Ge_{40}$**	**$Ba_8Cu_{5.5}Zn_{0.5}Ge_{40}$**	**$Ba_8Cu_{5.75}Zn_{0.25}Ge_{40}$**	**$Ba_8Cu_{5.2}Zn_{0.8}Ge_{40}$**
- 3Ge3	0.2499	0.2502	0.2505	0.2499
- 1Ba1	0.3380	0.3377	0.3395	0.3394
Ge3- 1M1	0.2430	0.2421	0.2422	0.2436
- 2Ge2	0.2499	0.2502	0.2505	0.2499
- 1Ge3	0.2555	0.2558	0.2560	0.2555
- 1Ba1	0.3594	0.3601	0.3599	0.3588
- 2Ba2	0.3569	0.3564	0.3565	0.3573

[1)]Nominal composition.

[2)] Pd, and Zn fix after EMPA.

4.3.2 Crystal Structures of the solid solution $Ba_8Zn_xGe_{46-x-y}Si_y$.

The crystal structure of the solid solution $Ba_8Zn_xGe_{46-x-y}Si_y$ (y = 0, 8.7, 18.9, 18.2, 27.3; 7.0 ≤x≤ 7.7) was evaluated by Rietveld refinement of x-ray powder diffraction profiles. In all cases cubic symmetry was confirmed and all measured reflections were indexed in space group $Pm\bar{3}n$. No superstructure reflections indicating a doubling of the unit cell [7] were observed (Fig. 5). The lattice parameters show a linear increase with increasing Ge content (Fig. 4), a fact which is in line with the difference of the atomic radii of Ge and Si. The lattice parameters increases by about 3.1 % between the end points of the solid solution. In order to elucidate site preferences for Ge/Si substitution the following structural model was used. Ba atoms were placed unambiguously on 2a and 6c sites and no defect was observed for the 2a site [5] for the Si-rich solid solution in contrast to binary $Ba_{8-\square}Si_{46}$ [8].

Starting with Si distributed on all framework sites (6d, 16i, 24k), refinement of occupation factors for all sites (see Fig. 4) resulted in the following trends for the electron densities with increase of Ge content: (i) an almost linear increase in the 6d site (ii) a linear increase in electron density for the 24k site, whilst (iii) a strong negative deviation from linearity was observed for the 16i site. Considering such a distribution of electron densities on one side and ordinal number of the elements, interatomic distances (Figure 4) and atomic radii of the elements on the other side, a model for atom site preference was established which is outlined in Table 6 and Figure 4.

The small change of the electron density in site 6d can be attributed to the Zn/Si substitution. Rietveld refinements for this site reveal a statistical mixture (Si+Zn) for $Ba_8Zn_{7.3}Ge_{10.6}Si_{28.1}$, and $Ba_8Zn_{7.2}Ge_{19.9}Si_{18.9}$ whereas for higher Ge contents the site was fully occupied by Zn (see Table 6 and Fig. 4). The very small difference in x-ray scattering power of Ge and Zn does not allow reliable refinements even with compositional constraints from EPMA data. Therefore we assume a linear change of the Zn content in the 16i and 24k sites between occupancies that were established for the end members of the series $Ba_8Zn_7Si_{39}$ [5] and $Ba_8Zn_8Ge_{38}$ [1]. Accordingly only the Ge/Si ratios for the 16i and 24k sites were refined. These refinements reveal Si/Ge substitutions as shown in Table 6, Figure 4 and the resulting chemical formulae

are in good agreement with EPMA for all members of the series. Obviusly there is a strong deviation from linearity, particularly for the 16i site. In order to prove the reliability of such site preference we performed refinements considering simply a linear change of the atom distribution in these sites (marked by dotted lines Figure 4). All these models, however, were ruled out by the refinements. The results are in agreement with a study of the ternary solid solution $Ba_{8-\square}Si_{46-x}Ge_x$ ($0 \leq x \leq 23$) [8], where at smaller Ge-contents Ge-atoms have a strong preference for the 24k site whilst at higher concentration Ge enters the 16i site.

Similarly, vacancies in the 6d site were not confirmed by Rietveld refinements due to significant disagreement with the resulting formulae and EPMA. All results for Rietveld refinements are shown in Table 6 and Figure 5. It should be noted, that the refinement of the x-ray powder profile for the sample prepared by ball-milling and hot-pressing yields practically the same results as for the hand-milled and hot-pressed sample with similar composition.

The interatomic distances also increase monotonically with increasing Ge contents in line with the bigger atomic radii of Ge as compared to Si (see Figure 4). Important interatomic distances are plotted vs. Ge/(Ge+Si) in Figure 4, where a pronounced effect in case of distances M2-M2 and M3-M3 with increasing Ge content is associated with the occupancy factor for the 16i and 24k site vs. Ge/Si substitution (see Figure 4). Variation of the free parameters x for the site 16i (x, x, x) and y, z for the site 24k (0, y, z) with increasing Ge content is shown in Figure 6. The linear increase of the z parameter with increasing Ge-content is in line with the difference in atomic radii, $r_{Ge}>r_{Si}$, whereas the y parameters simultaneously pass through a maximum.

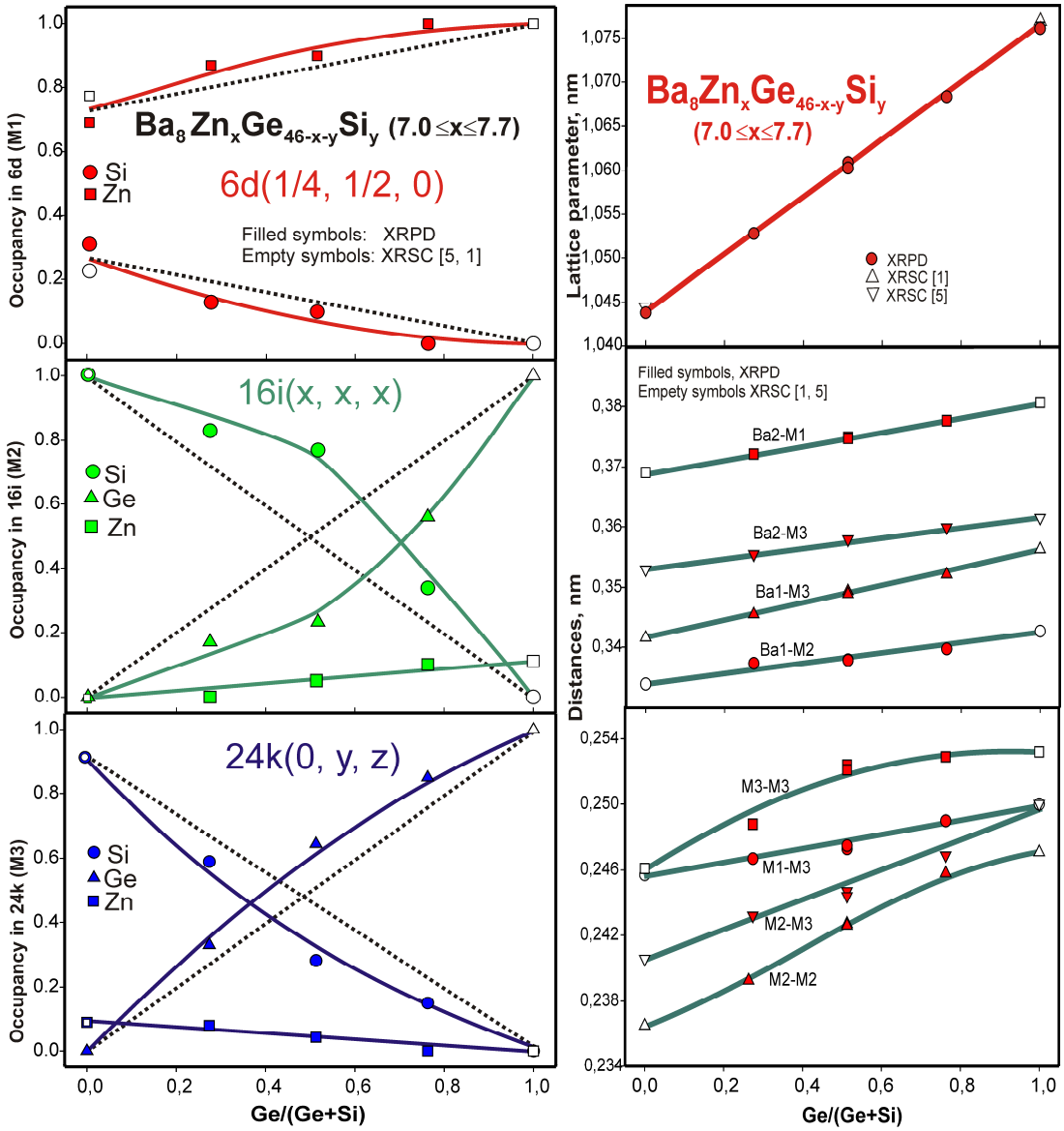

Figure. 4: Lattice parameters, occupancies and interatomic distance vs. Ge/(Ge+Si) in $Ba_8Zn_xGe_{46-x-y}Si_y$ clathrates.

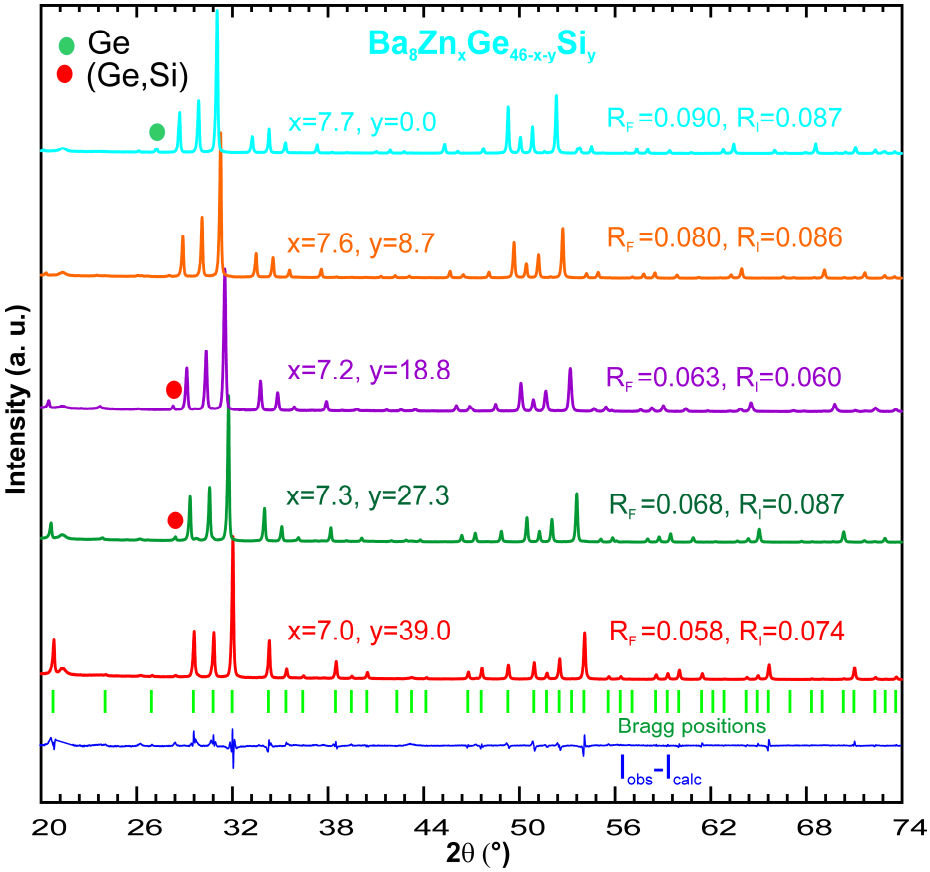

Figure. 5: Comparison of XRPD profiles and Rietveld refinement for $Ba_8Zn_xGe_{46-x-y}Si_y$ clathrates.

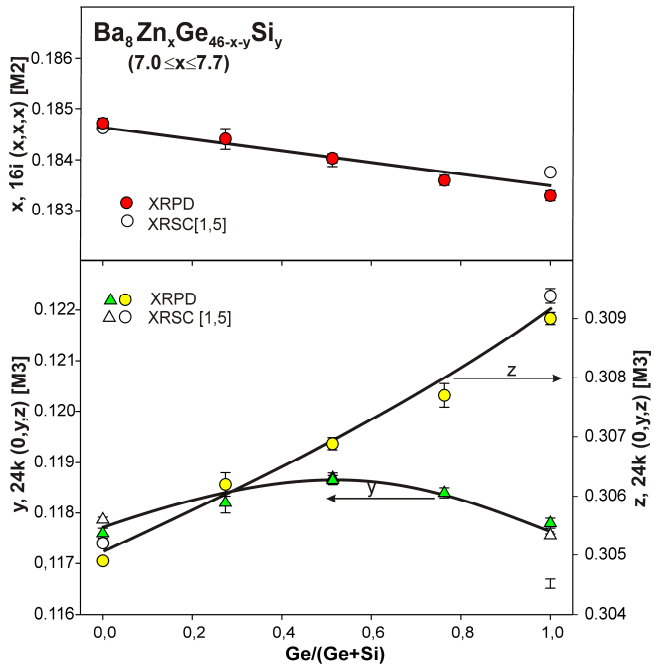

Figure. 6: Atom parameters vs. Ge/(Ge+Si) in $Ba_8Zn_xGe_{46-x-y}Si_y$ clathrates.

Table5. EPMA and structural data for $Ba_8Zn_xGe_{46-x-y}Si_y$ solid solution.

Nominal composition	EMPA, at %				EMPA, formula	Accepted composition	Lattice parameter a, nm
	Ba	Zn	Ge	Si			
$Ba_8Zn_8Ge_{10}Si_{28}$	15.28	14.0	20.8	49.9	$Ba_8Zn_{7.3}Ge_{11.4}Si_{27.3}$	$Ba_8Zn_{7.3}Ge_{10.6}Si_{28.1}$	1.05278(2)
$Ba_8Zn_8Ge_{19}Si_{19}$	14.8	13.6	36.6	35	$Ba_8Zn_{7.4}Ge_{19.7}Si_{18.9}$	$Ba_8Zn_{7.4}Ge_{19.8}Si_{18.8}$	1.06086(2)
$Ba_8Zn_8Ge_{19}Si_{19}$	15.0	13.5	38.0	33.5	$Ba_8Zn_{7.2}Ge_{20.6}Si_{18.2}$	$Ba_8Zn_{7.2}Ge_{19.9}Si_{18.9}$	1.06026(2)
$Ba_8Zn_8Ge_{28}Si_{10}$	14.7	14.1	55.0	16.2	$Ba_8Zn_{7.6}Ge_{29.7}Si_{8.7}$	$Ba_8Zn_{7.6}Ge_{29.3}Si_{9.1}$	1.06833(2)
$Ba_8Zn_8Si_{38}$	-	-	-			$Ba_8Zn_7Si_{39}$	1.04382(2)[5]
$Ba_8Zn_8Ge_{38}$	-	-	-			$Ba_8Zn_{7.7}Si_{38}$	1.07647(3) [1]

Table 6. X- ray powder diffraction data for $Ba_8Zn_xGe_{46-x-y}Si_y$ solid solution (room temperature, image plate data collection, Cu $K_{\alpha 1}$ radiation, Θ range 8≤2Θ≤100); (space group $Pm\bar{3}n$), standardized with programme *Structure Tidy* [16].

Parameter/compound[1)]	**$Ba_8Zn_8Ge_9Si_{29}$**	**$Ba_8Zn_8Ge_{19}Si_{19}$**	**$Ba_8Zn_8Ge_{29}Si_9$**
Composition, EMPA	**$Ba_8Zn_{7.3}Ge_{11.4}Si_{27.3}$**	**$Ba_8Zn_{7.2}Ge_{20.6}Si_{18.2}$**	**$Ba_8Zn_{7.6}Ge_{29.7}Si_{8.7}$**
Composition from refinement[2)]	**$Ba_8Zn_{7.3}Ge_{10.6}Si_{28.1}$**	**$Ba_8Zn_{7.2}Ge_{19.9}Si_{18.9}$**	**$Ba_8Zn_{7.4}Ge_{29.3}Si_{9.1}$**
a [nm], Ge standart	1.05278(2)	1.06026(2)	1.06833(2)
Reflections measured	135	143	145
Number of variables	22	22	20
$R_F = \Sigma\|F_o-F_c\|/\Sigma F_o$	0.066	0.066	0.080
$R_I = \Sigma\|I_o-I_c\|/\Sigma I_o$	0.085	0.061	0.086
$R_{wP}=[\Sigma w_i\|y_{oi}-y_{ci}\|^2/\Sigma w_i\|y_{oi}\|^2]^{½}$	0.066	0.028	0.051
$R_P = \Sigma\|y_{oi}-y_{ci}\|/\Sigma\|y_{oi}\|$	0.043	0.020	0.038
$R_e = [(N-P+C)/\Sigma w_i y^2_{oi})]^{½}$	0.026	0.023	0.030
$\chi^2 = (R_{wP}/R_e)^2$	6.22	1.46	2.83
Atom parameters			
Ba1 in 2a (0,0,0); occ.	1.0(1)	1.0(1)	1.0(1)
B_{iso} (10^2 nm^2)	0.71(6)	0.97(5)	1.11(6)
Ba2 in 6c (¼,0,½); occ.	1.0(1)	1.0(1)	1.00(1)
B_{iso} (10^2 nm^2)	2.33(5)	2.88(5)	3.32(6)
M1 in 6d (¼,½,0); occ.	0.87(1)Zn+0.13(1)Si	0.90(1)Zn+0.10(1)Si	1.0(1)Zn
B_{iso} (10^2 nm^2)	0.86(8)	0.50(6)	1.30(8)
M2 in 16i (x,x,x) ; occ.	0.83(1)Si+0.17(1)Ge	0.77(1)Si+0.23(1)Ge+0.05(1)Zn[3)]	0.34(1)Si+0.56(1)Ge+0.1(1)Zn
x	0.1844(2)	0.18421(9)	0.1836(1)
B_{iso} (10^2 nm^2)	1.26(8)	1.22(5)	1.60(6)
M3 in 24k (0,y,z); occ.	0.59(1)Si+0.338(1)Ge+0.08Zn	0.27(1)Si+0.64(1)Ge+0.04(1)Zn[3)]	0.15(1)Si +0.85(1)Ge
y; z	0.1183(2); 0.3061(2)	0.1187(1); 0.3069(1)	0.1184(1); 0.3077(1)
B_{iso} (10^2 nm^2)	0.75(5)	1.02(4)	1.19(4)
Interatomic distances, standard deviation < 0.0003 nm			
Ba1 – 8M2	0.3373	0.3381	0.3397
- 12M3	0.3455	0.3487	0.3522
Ba2 – 8M3	0.3555	0.3576	0.3599
- 4M1	0.3722	0.3747	0.3777
- 8M2	0.3906	0.3937	0.3972
- 4M3	0.4063	0.4085	0.4123
M1 - 4M3	0.2467	0.2475	0.2490
- 4Ba2	0.3722	0.3747	0.3777
M2 – 1M2	0.2392	0.2415	0.2458
- 3M3	0.2432	0.2446	0.2469
- 1Ba1	0.3734	0.3381	0.3379
M3- 2M2	0.2432	0.2446	0.2469
- 1M1	0.2467	0.2475	0.2490
- 1M3	0.2488	0.2516	0.2529
- 1Ba1	0.3455	0.3487	0.3522
- 2Ba2	0.3551	0.3576	0.3599

[1)] nominal composition.[2)] accepted composition.

[3)] Zn fixed considering linear increase or decrease with Ge content

4.3.3 Phase equilibria in the quaternary systems Ba-(Pd,Cu)-Zn-Ge and Ba-Zn-Ge-Si

The partial isothermal sections at 800 °C for ternary boundary systems Ba-Zn-Ge and Ba-Pd-Ge were accepted from our recent investigations [1, 2] and serve as the basis (i) to construct the quaternary phase diagram for the system Ba-Pd-Zn-Ge at 800 °C and (ii) to define the quaternary single-phase clathrate region $Ba_8Zn_xPd_yGe_{46-x-y-z}\square_z$. According to Gibbs's phase rule, a four-component system may involve four phases in equilibrium at constant pressure and temperature. The convenient way to present a quaternary equilibrium at constant P, T is the composition tetrahedron (Roozeboom-Fedorov tetrahedron; simplex). For the correct construction of phase relations among the tie-tetrahedra and adjoining phase fields, the rule of Palatnik and Landau [15] on the association of phase fields may be applied.

The three dimensional phase diagram for the Ba-Pd-Zn-Ge system is shown in Figure 7a. The connectivity scheme plays a key role to complete the construction of the 3D quaternary phase diagram (Figure 7d). The general rules for phase field connection in a four-component system imply that two-, three-, and four-phase regions are connected to a single-phase body via corresponding surfaces, lines and vertices, respectively. The three phase equilibria κ_1+ L+(Ge) (a), κ_1+ τ_2+L (b), κ_1+ τ_2+$BaGe_2$ (c), κ_1+ τ_1+L (e) and κ_1+ τ_1+$BaGe_2$ (f) (for a,b,c,e,f see Fig 7b) involve the κ_1 phase at its maximum solubility for M atoms. Therefore schematic phase equilibria on the basis of the connectivity scheme at 800 °C are presented in Figure 7b.

The tie-tetrahedron corresponding to the four-phase equilibrium κ_1+τ_1+τ_2+L appears as simplex "A" in Figure 7b, which is connected to two three-phase equilibria κ_1+τ_1+L and κ_1+τ_2+L from the ternary boundary systems Ba-Zn-Ge and Ba-Pd-Ge, respectively. The four-phase equilibrium "A" connects to tie-tetrahedron "B" via the three-phase equilibrium κ_1+τ_1+τ_2. The tie-tetrahedron "B" corresponding to the four-phase equilibrium κ_1+τ_1+τ_2+$BaGe_2$ derives from two three-phase equilibria κ_1+τ_1+$BaGe_2$ and κ_1+τ_2+$BaGe_2$ in the ternary systems (see connectivity scheme, Figure 7b and d).

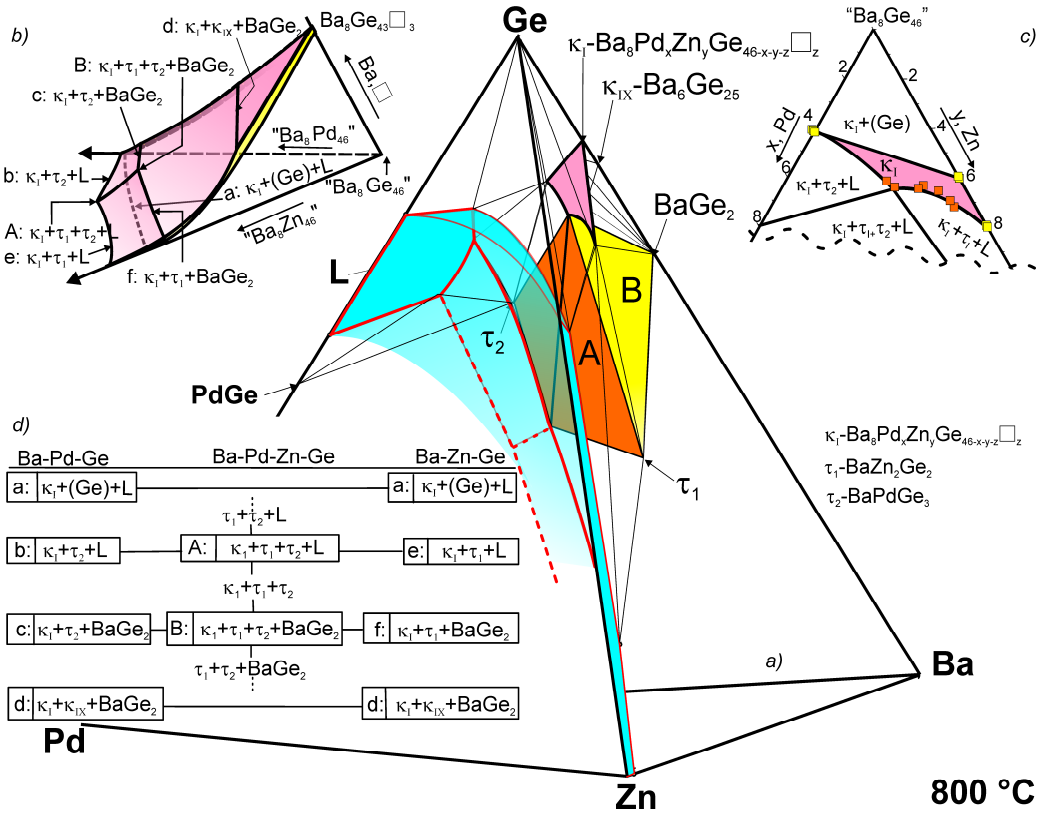

Fig. 7: Ba-Pd-Zn-Ge system at 800 °C: a) Three dimensional view of quaternary phase diagram; b) Schematic phase equilibria; c) partial isothermal section "Ba_8Ge_{46}"-"Ba_8Pd_{46}"-"Ba_8Zn_{46}"; d) connectivity scheme.

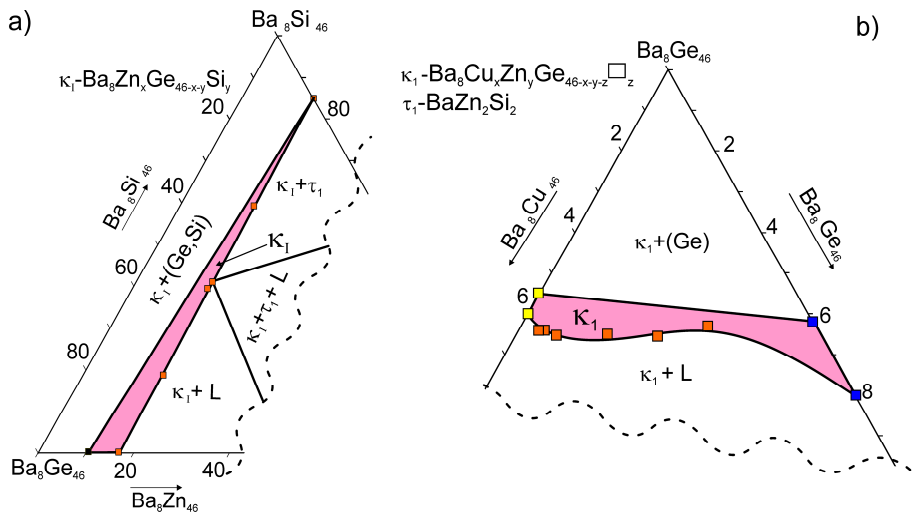

Fig. 8: Partial isothermal section at 800 °C; a) "Ba_8Ge_{46}"-"Ba_8Si_{46}"-"Ba_8Zn_{46}"; b) "Ba_8Ge_{46}"-"Ba_8Cu_{46}"-"Ba_8Zn_{46}"

The partial isothermal section "Ba_8Ge_{46}""Ba_8Pd_{46}""Ba_8Zn_{46}" presented in Figure 7c lies very close to the phase equilibria $\kappa_1+\tau_1+L$ and $\kappa_1+\tau_2+L$, therefore the two-phase

regions connecting the three-phase equilibria with a single-phase region are very narrow and are not shown in this section.

The single-phase region for the clathrate I phase $Ba_8Zn_xPd_yGe_{46-x-y-z}\square_z$ is outlined in Figure 7b where the variation of defects can also be seen. The vacancies present in $Ba_8Ge_{43}\square_3$ disappear at $x_{Zn} = 6$ in $Ba_8Zn_xGe_{46-x}$ and at $x_{Pd} = 4$ in $Ba_8Pd_xGe_{46-x}$.

Liquid surfaces extending from two binary systems Pd-Ge and Zn-Ge to the ternary and finally merging in the quaternary system cover a large part of the isothermal section (Figure 7a).

On the basis of available experimental data on as cast and annealed samples, partial isothermal sections "Ba_8Ge_{46}"-"Ba_8Cu_{46}"-"Ba_8Zn_{46}" and "Ba_8Ge_{46}"-"Ba_8Si_{46}"-"Ba_8Zn_{46}" at 800 °C are presented in Figure 8a and b. The single-phase region of the clathrate phase is outlined in these sections, which is connected to the corresponding two-phase and three-phase equilibria.

4.4 Conclusion

Vacancy-free quaternary clathrate solid solutions $Ba_8Zn_xGe_{46-x-y}Si_y$, $Ba_8(Zn,Cu)_xGe_{46-x}$ and $Ba_8(Zn,Pd)_xGe_{46-x}$ were prepared and characterized by x-ray powder diffraction, x-ray single crystal, EMPA. Complete structural evaluations were made on the basis of x-ray powder diffraction and x-ray single crystal analyses. All compounds crystallize in space group $Pm\bar{3}n$, isotypic with clathrate type I. No defects were observed. Site preference for each case was evaluated. M atoms (Zn,Pd,Cu) in $Ba_8(Zn,Cu)_xGe_{46-x}$, $Ba_8(Zn,Pd)_xGe_{46-x}$ randomly share the site 6d. Linear substitution of Zn at the 6d site in the $Ba_8Zn_xGe_{46-x-y}Si_y$ solid solution was observed. Lattice parameters show a linear increase with increase of Ge for the $Ba_8Zn_xGe_{46-x-y}Si_y$ solid solution.

Isothermal section at 800 °C for the quaternary system Ba-Pd-Zn-Ge was constructed and partial isothermal sections "Ba_8Ge_{46}"-"Ba_8Pd_{46}"-"Ba_8Zn_{46}", "Ba_8Ge_{46}"-"Ba_8Cu_{46}"-"Ba_8Zn_{46}" and "Ba_8Ge_{46}"-"Ba_8Si_{46}"-"Ba_8Zn_{46}" at 800 °C are presented.

References

[1] N. Melnychenko-Koblyuk, A. Grytsiv, L. Fornasari, H. Kaldarar, H. Michor, F. Röhrbacher, M. Koza, E. Royanian, E. Bauer, P. Rogl, M. Rotter, H. Schmid, F. Marabelli, A. Devishvili, M. Doerr and G. Giester, J. Phys.: Conden. Matter 19 **(**2007) 216223.

[2] N. Melnychenko-Koblyuk, A. Grytsiv, P. Rogl, M. Rotter, E. Bauer, G. Durand, H. Kaldarar, R. Lackner, H. Michor, E. Royanian, M. Koza, G. Giester Physical Rev. B 76 (2007)144118.

[3] N. Melnychenko-Koblyuk, A. Grytsiv, St. Berger, H. Kaldarar, H. Michor, F. Röhrbacher, E. Royanian, E. Bauer, P. Rogl, H. Schmid, and G. Giester, J. Phys. Conden. Matter 19 (2007) 046203.

[4] N. Melnychenko-Koblyuk, A. Grytsiv, P. Rogl, H. Schmid, G. Giester, J. Solid State Chem. 182 (2009) 1754.

[5] N. Nasir, A. Grytsiv, N. Melnychenko-Koblyuk, P. Rogl, E. Bauer, R. Lackner, E. Royanian, G. Giester, A. Saccone, J. Phys.: Conden. Matter 21 (2009) 385404

[6] A. Grytsiv, N. Melnychenko-Koblyuk, N. Nasir, P. Rogl, A. Saccone, H. Schmid, Int. J. Mat. Res. (formly Z. Metallkd.) 100 **(**2009) 189.

[7] W. Carrrillo-Cabrera, S. Budnyk, Y. Prots, Y. Grin, Z. Anorg. Allg. Chem. 630 (2004) 7226.

[8] H. Fukuoka, J. Kiyoto, and S. Yamanaka, J. Solid State Chem. 175 (2003) 237-244.

[9] K. Suekuni, M. A. Avila, K. Umeo, T. Takabatake, Phys. Rev. B 75 **(**2007) 195210.

[10] J. Martin, S. Erickson, G. S. Nolas, P. Alboni, T. M. Tritt, J. Yang, J. Appl. Phys. 99 (2006) 044903.

[11] E. N. Nenghabi, C. W. Myles, Physical Rev. B 77 **(**2008) 205203.

[12] A. Saramat, G. Svensson, A. E. C. Palmqvist, C. Stiewe, E. Mueller, D, Platzek, S. G. K. Williams, D. M. Rowe, J. D. Bryan, G. D. Stucky, J. Applied Phys. 99 (2006) 23708-1.

[13] S. Johnsen, A. Bentien, G. K. H. Madsen, M. Nygren, B. B. Iversen, Phys. Rev. B 76 (2007) 245126.

[14] Pauling File Binaries Edition, release 2002/1 Version 1.0, ASM Intl, Materials Park, OH, USA

[15] L. S. Palatnik and A. Landau I 1961 *Phase Equilibria in Multi-Component Systems*, Holt, Rinehart & Winston Inc., NewYork, Chicago, San Francisco, Toronto, London, translated from Kharkov State University Press1964, p 270-320.

[16] E. Parthé, L. Gelato, B. Chabot, M. Penzo, K. Cenzual, and R. Gladyshevskii, TYPIX - Standardized Data and Crystal Chemical Characterization of Inorganic Structure Types (Berlin Heidelberg: Springer – Verlag) 1994

5 Synthesis and Characterization of $Ba_8Zn_xGe_{46-x}$ (x = 0, 2, 4, 6) and $Ba_8Ni_xZn_yGe_{46-x-y}$ Clathrates

5.1 Introduction

As a part of our research on clathrates I with transition metals (TM) and Ge/Si with the formula $Ba_8TM_xGe_{46-y}$, present chapter is designated to the synthesis and characterization of series of clathrates $Ba_8Zn_xGe_{46-x}$ (x = 0, 2, 4, 6) and $Ba_8Ni_xZn_yGe_{46-x-y}$. Alloys $Ba_8Zn_xGe_{46-x}$ (x = 0, 2, 4, 6) were prepared for inelastic scattering experiments [1], while series $Ba_8Ni_xZn_yGe_{46-x-y}$ is the continuation of research regarding fine-tuning the thermoelectric properties of the clathrates by various substitutions at the framework sites. Previously we reported structure, phase equilibria and physical properties on a series of quaternary clathrates [2] where the effect of Pd/Zn, Cu/Zn and Si/Ge substitutions on TE properties were studied in detail. Herein we report on the formation of $Ba_8Ni_xZn_yGe_{46-x-y}$ clathrates where x is fixed at about $0.4<x<1.0$ and y is varied as $6.4<y<7.3$. The purpose is to find the proper combination where we can reach full charge compensation, which can trigger the enhancement of the theroelectric figure of merit.

5.2 Experimental

Master alloys Ba_8Ge_{46-x} (x=0, 2, 4, 6) were prepared by melting elemental ingots (Ba 99.9, and Ge 99.999 mass %) in an electric arc furnace under Ti-gettered argon with a non-consumable tungsten electrode on a water-cooled copper hearth. These master alloys were mixed with Zn (99.99 mass %) in stoichiometeric ratio for nominal compositions $Ba_8Zn_xGe_{46-x}$ (x = 0, 2, 4, 6) and sealed in quartz tubes. The mixtures were melted at 1000˚C for 2 h. Afterwards samples were furnace cooled to 800°C and annealed at this temperature for 4-7 days prior to quenching in cold water. Samples were powderized to small particle size for inelastic scattering measurements.

Clathrate sample $Ba_8Ni_xZn_yGe_{46-x-y}$ were prepared in the following way: Master alloy Ba_8NiGe_{45} was prepared by arc melting with a non-consumable tungsten electrode on

a water-cooled copper hearth whereby Ni is melted stepwise with addition of small amounts of Ge and then this NiGe alloy is melted with Ba three times for complete homogenisation. In order to keep the same synthesis conditions master alloys of the two end members ($Ba_8Zn_xNi_yGe_{46-x-y}$ (x=1, y=7.2, 6.5)) were prepared. Calculated amounts of Zn for the two end members were added to the Ba_8NiGe_{45} master alloy and the mixtures are sealed in evacuated quartz tubes. The mixtures were melted at 1000 °C for ~ 2h and furnace cooled to 800 °C. Afterwords the products were ball-milled to a grain size well below 1 μm (Fritsch Vario-Planetary mill Pulverisette 4 with tungsten carbide (WC) walled container and WC-balls). The other members of the series $Ba_8Zn_xNi_yGe_{46-x-y}$ (x= 6.6, 6.7, 6.8, 6.9, 7.0, 7.1, y=1) were then prepared by taking calculated amounts of the powders from the two end members mixing them and ballmilling again to get completely homogenised. The powders were then hot pressed in cylinders with 10 mm diameter and 6 mm height by hot pressing in a graphite die at 800°C (argon atmosphere, pressure 60 MPa, FCT hot press system HP W 200/250 2200-200-KS).

X-ray powder diffraction (XPD) data from alloys were collected employing a Guinier-Huber image plate system with Cu-Kα_1 radiation (8° < 2θ < 100°). Precise lattice parameters were calculated by least-squares fits to the indexed θ-values employing Ge as internal standard (a_{Ge} = 0.5657906 nm). Chemical compositions for Ni containing clathrates were measured by Electron Probe Micro Analysis EPMA on a Carl Zeiss DSM 962 equipped with a Link EDX system operated at 20kV and 60μA; binary Ba_6Ge_{25} was used as internal standards.

5.3 Results and Discussion

X-ray powder diffraction profiles reveal single-phase materials in almost all cases (trace amounts of Ge may be found in few samples) with clathrate type I structure (S.G $Pm\bar{3}n$; a~1.1nm). No secondary phases of $BaZn_2Ge_2$ or Ba_6Ge_{25} were encountered in $Ba_8Zn_xGe_{46-x}$ (x = 0, 2, 4, 6). Due to temperature range of the existence of $Ba_8Ge_{43}\square_3$ (770-810 °C) [3,4], this phase can be quenched only from high temperatures. Ordering of the vacancies in $Ba_8Ge_{43}\square_3$ results in a superstructure with double unit cell parameter [3]. Superstructure reflections which corresponds to

the doubling of the unit cell parameter were detected from x-ray powder diffraction profiles for quenched $Ba_8Ge_{43}\square_3$ and the pattern was fitted successfully on the basis of double unit cell parameter and with the fully ordered model given in Ref. [3] (S. G. *Ia*-3*d*, a=2.13107(3) nm)) as shown in Figure 1. Ba1 and Ba2 were assigned 16*a* (0, 0, 0) and 48*g* (1/8, y, -y+1/4) respectively, three different sites were assigned to five different Ge: (i) Ge 1 in 24*d* (3/8, 0, ¼)), (ii) Ge 2 in 32*e* (x, x, x), and (iii) Ge3, Ge4 and Ge5 in three 96*h* (x, y, z) sites. The complementary site Ge1′ (24c) is empty. Lattice parameters for $Ba_8Zn_xGe_{46-x}$ (x = 2, 4, 6) show linear increase with increase of Zn corresponding to the ratio of atom radii for Zn and Ge (Figure 2). However no superstructure reflections were observed in either member of ternary clathrate $Ba_8Zn_xGe_{46-x}$ (x = 2, 4, 6) and powder patterns were refined successfully according to the structural models developed by [5].

X-ray powder diffraction patterns for the series $Ba_8Ni_xZn_yGe_{46-x-y}$ (x≤1, y= 6.5, 6.6, 6.7, 6.8, 6.9, 7.0, 7.1, 7.2) were indexed as isotypic to the clathrate type I structure in the space group *Pm*-3*n* with the lattice parameters and EMPA data given in Table 2. In some cases, however, very small amounts (<2%) of the secondary phase NiGe was seen from EMPA. Lattice constants continuously increase with increase of Zn and are always smaller than the lattice parameters for $Ba_8Zn_xGe_{46-x}$ and much larger than the lattice parameters for only Ni containing Ge clathrates in line with atomic radii of Zn and Ni Figure 2.

The powder patterns were refined successfully on the basis of the models described for $Ba_8Zn_xGe_{46-x}$ [5]and $Ba_8Ni_xGe_{46-x}$ [6,7]. Ba1 and Ba2 were assigned to sites 2a (0, 0, 0) and 6c (¼, 0, ½) respectively. Zn and Ni atoms randomly occupy 6d (¼, ½, 0) site [5-7] and extra Zn goes to the 16i site [5], while Ge is assigned 16i (x, x, x) and 24k (0, y, z) sites. Our previous detailed studies reveal that vacancies are completely filled at about Zn ≅ 6 atoms [2,5] and the presence of defects in the 6c site can be reflected from the splitting of the 24k site into 24k1 and 24k2. EMPA data also did not hint towards the vacancies therefore the 6d site is considered to be fully occupied by the Ni+Zn mixture. Due to small contrast in the scattering power of Ni, Zn and Ge the refinement of the occupancies in the framework sites and temperature factors is not easy. Together with this fact, the amounts of Ni added are very small, therefore composition of Ni and Zn is fixed from microprobe data and Ni together with Zn are assigned to the 6d site according to Ref. [5-7]. The Rietveld refinement of

the powder patterns is shown in Figure 3. X-ray powder patterns for all samples were found single phase. In order to confirm that small amounts of Ni (<2 at. %) really enter lattice sites we measured elemental maps for the samples together with EPMA. Results show that Ni is homogenously distributed throughout the samples with overall compositions given in the Table 2.

5.4 Conclusion

Two series of type I clathrates $Ba_8Zn_xGe_{46-x}$ (x = 0, 2, 4, 6) and $Ba_8Ni_xZn_yGe_{46-x-y}$ were prepared and analysed by XRPD and EMPA. The super structure was confirmed by Rietveld refinement of the powder pattern of $Ba_8Ge_{43}\square_3$ (S. G, *Ia*-3_d, a =2.13107(3)). No superstructure reflections were observed in XRPD of the other members of the series. Lattice parameters show increase with increase of Zn. Substitution of Zn in the lattice is confirmed from lattice parameters and EMPA.

Table 1. Lattice parameter for $Ba_8Zn_xGe_{46-x-y}\ \ _y$ ($_y$= vacancy).

Nominal Composition	Lattice parameters a [nm]
$Ba_8Ge_{43}\square_3$	2.13107(3)
$Ba_8Zn_2Ge_{44}$	1.6870(4)
$Ba_8Zn_4Ge_{41}$	1.07165(3)
$Ba_8Zn_6Ge_{40}$	1.07513(2)
$Ba_8Zn_8Ge_{38}$	1.07647(3)[5]

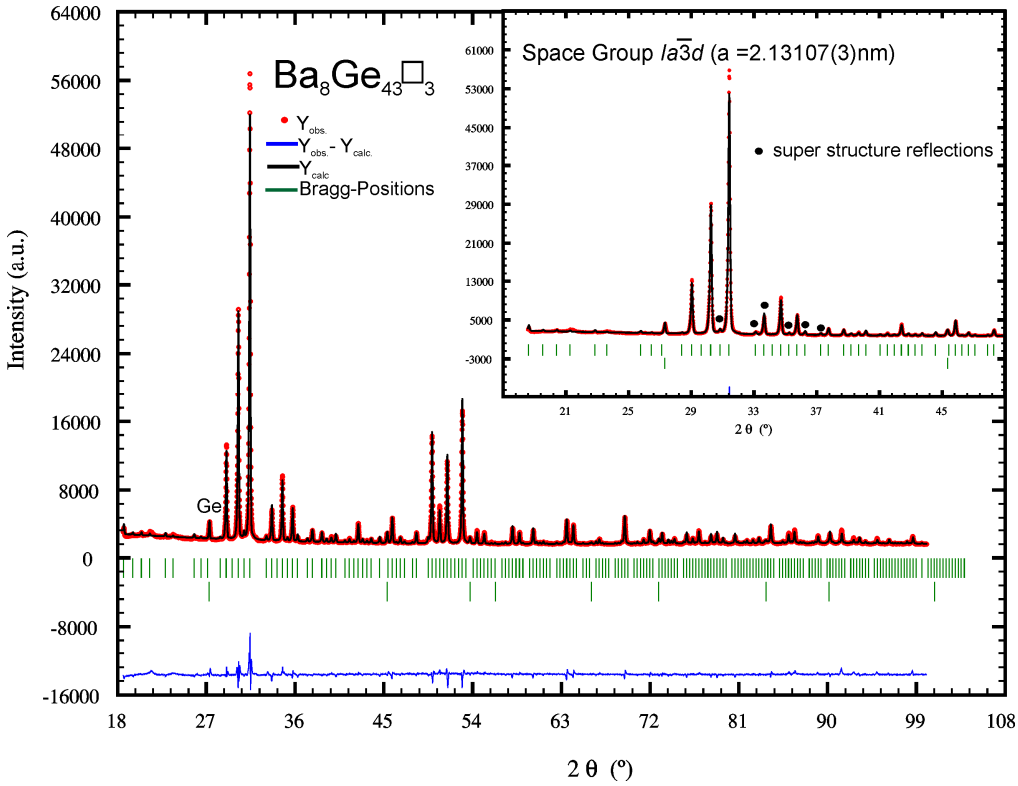

Figure 2. Rietveld refinement of the XRPD profile of $Ba_8Ge_{43}\square_3$ with supercell reflections.

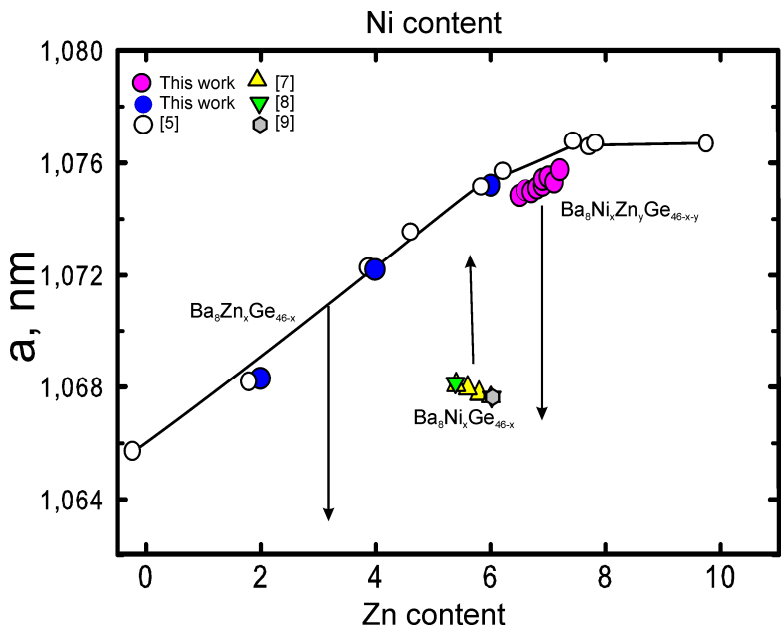

Figure 3. Compositional dependence of lattice parameters vs. Ni, Zn contents

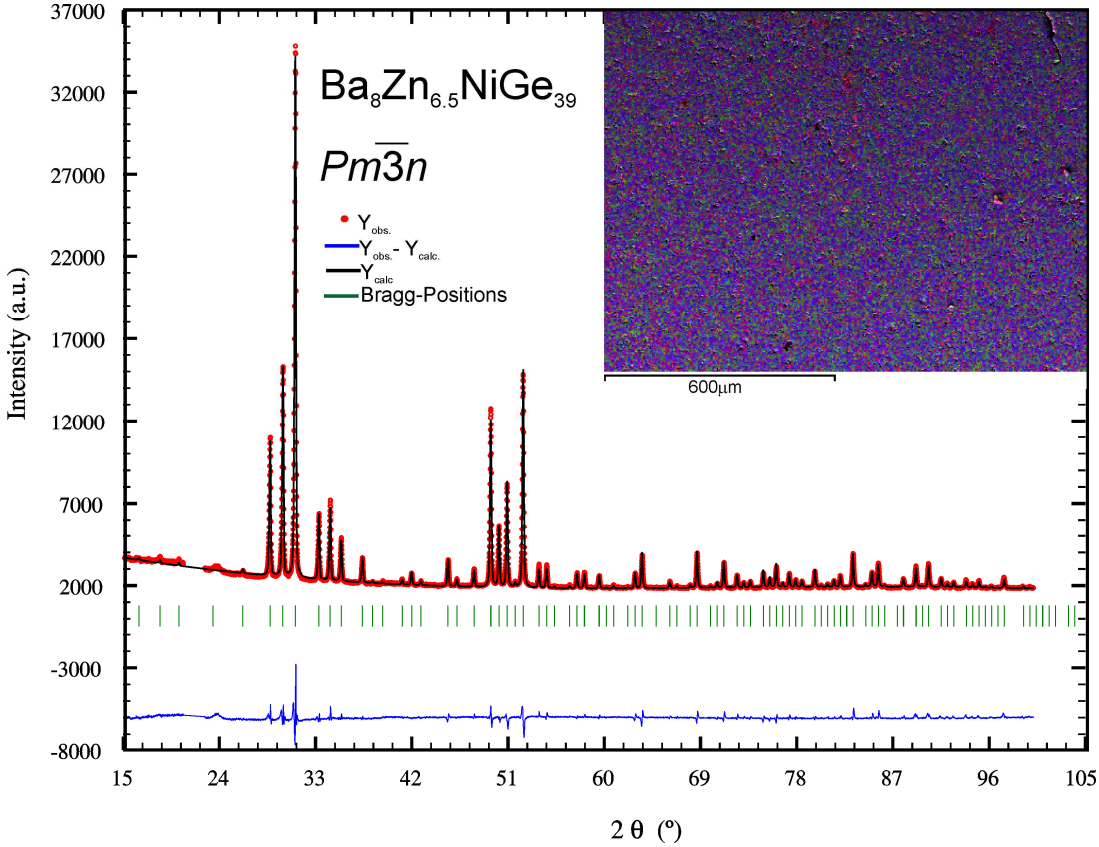

Figure 2. Rietveld refinement of the XRPD profile of $Ba_8Zn_{6.5}NiGe_{39}$. Inset is the element mapping by EDX system.

Table 2. Lattice Parameters for $Ba_8Zn_xNi_yGe_{46-x-y}$.

Nominal Composition	EMPA at. %				Formula from EMPA[a]	Density g/cm^3	Relative density	Lattice Parameters [nm]
	Ni	Zn	Ge	Ba				
$Ba_8Zn_{6,5}NiGe_{38,5}$	1,6	11,8	71,6	15,1	$Ba_8Zn_{6.4}Ni_{0.8}Ge_{38.8}$	5.8602		1.07484(2)
$Ba_8Zn_{6,6}NiGe_{38,4}$	1,4	11,3	71,9	15,3	$Ba_8Zn_{6.1}Ni_{0.8}Ge_{39.1}$	5.8447		1.07502(2)
$Ba_8Zn_{6,7}NiGe_{38,3}$	0,9	12,0	71,6	15,4	$Ba_8Zn_{6.5}Ni_{0.5}Ge_{39.0}$	5.8641		1.07497(1)
$Ba_8Zn_{6,8}NiGe_{38,2}$	1,0	11,9	71,9	15,2	$Ba_8Zn_{6.5}Ni_{0.5}Ge_{39.0}$	5.8452		1.07510(2)
$Ba_8Zn_{6,9}NiGe_{38,1}$	0,7	12,9	71,6	14,8	$Ba_8Zn_{6.97}Ni_{0.4}Ge_{38.7}$	5.866		1.07520(2)
$Ba_8Zn_{7,0}NiGe_{38,0}$						-		1.07540(3)
$Ba_8Zn_{6,9}NiGe_{38,1}$	1,0	13,2	70,8	14,96	$Ba_8Zn_{7.1}Ni_{0.5}Ge_{38.3}$	5.870		1.07541(2)
$Ba_8Zn_{7,0}NiGe_{38,0}$	1,1	12,8	70,9	15,2	$Ba_8Zn_{6.9}Ni_{0.6}Ge_{38.4}$	5.8403		1.07549(2)
$Ba_8Zn_{7,1}NiGe_{37,9}$	0,9	12,8	71,6	14,7	$Ba_8Zn_{6.9}Ni_{0.5}Ge_{38.6}$	5.9693		1.07531(4)
$Ba_8Zn_{7,2}NiGe_{37,8}$	0,9	12,3	71,6	15,2	$Ba_8Zn_{6.7}Ni_{0.5}Ge_{38.5}$	5.8754		1.07575(2)

[a] EMPA data is normalized to Zn+Ni+Ge=46

References

[1] M. M. Koza, M. Johnson, M. Rotter, N. Nasir, A. Grytsiv, P. Rogl, to be

submitted.

[2] N. Nasir, A. Grytsiv, N. Melnychenko-Koblyuk, P. Rogl, I. Bednar, E. Bauer, submitted.

[3] W. Carrillo-Cabrera, S. Budnyk, Y. Prots, Y. Grin Z. Anorg. Allg. Chem. 630 **(**2004) 2267.

[4] W. Carrillo-Cabrera, J. Curda, K. Petters, M. Baenitz, Y. Grin, H. G. von Schnering, Z. Kristallogr. New Cryst. Struct. 215 **(**2000) 321.

[5] N. Melnychenko-Koblyuk, A. Grytsiv, L. Fornasari, H. Kaldarar, H. Michor, F. Röhrbacher, M. Koza, E. Royanian, E. Bauer, P. Rogl, M. Rotter, H. Schmid, F. Marabelli, A. Devishvili, M. Doerr and G. Giester, J. Phys. Condens. Matter 19 (2007) 216223.

[6] H. Zhang, J. Zhao, M. Tang, Z. Man, H. Chen, X. Yang, J. of Phys. and Chem. of Solids 70 (2009) 312-315.

[7] S. Johnsen, A. Bentien, G. K. H. Madsen, M. Nygren, B. B. Iversen, Phys. Rev. B 76 (2007) 245126.

[8] A. Bentien, S. Johnsen, B. B. Iversen, Phys. Rev. B 73 (2006) 094301.

[9] G. Cordier, P. Woll, J. Less-Common-Metals 169 (1991) 291.

6 Ternary Systems Sr – {Ni,Cu} – Si: Phase Equilibria and Crystal Structure of Ternary Phases.

6.1 Introduction

Our recent systematic studies have covered phase relations, crystal chemistry, physical and particularly thermoelectric properties of clathrate compounds in the ternary systems Ba–M–{Si,Ge} with M=Mn, Fe, Co, Pd, Pt, Cu, Zn, Cd. [1-7]. These investigations have also led to the discovery of a family of superconducting skutterudites {Sr,Ba,Eu,Th,U}Pt_4Ge_{12} [8], of a non-centrosymmetric superconductor $BaPtSi_3$ [9] as well as of several new compounds with unique crystal structure: $BaPt_5Si_{12}$ [10] and $EPCo_{4.7}Ge_9$ (EP = Ba, Sr, Eu) [11]. Besides these findings, further compounds have been discovered in the aforementioned ternary systems, which hitherto have not been completely covered by these publications. This particularly concerns the compounds with composition $BaM(Si,Ge)_3$ (M= Pd, Pt, Rh, Ir with $BaNiSn_3$-type structure), $BaM_2(Si,Ge)_2$ (M=Zn, Cd with $ThCr_2Si_2$-type structure) and $BaM_x(Si,Ge)_{2-x}$ (M = Pd, Pt, Cu, Zn, Cd with AlB_2-type). Therefore, the current article will provide information on the crystal structure of the above mentioned phases in the ternary systems Ba-(Pd,Pt,Ir,Rh,Cu,Zn,Cd)-(Si,Ge). As there are few studies on Sr-systems available in literature, the present article will report on the phase equilibria and crystal structure of compounds in the ternary systems Sr-Ni-Si and Sr-Cu-Si.

6.2 Experimental

All samples, each of total amounts of ca. 1g, were prepared in an electric arc furnace under Ti-gettered argon with a non-consumable tungsten electrode on a watercooled copper hearth. The purity of barium and strontium was 99.5 mass%, the purity of metals (Pd, Pt, Ni, Cu, Rh, Ir, Ge and Si) was better than 99.9%. Oxygen sensitive barium and strontium were polished and weight under cyclohexane. The alloys were remelted three times in order to achieve complete fusion and homogeneity. After melting, alloys were subjected to

annealing in evacuated quartz tubes with subsequent quenching in water. Alloys containing Zn and Cd (purity was better than 99.9 %) were prepared from elemental ingots by reaction in vacuum-sealed quartz tubes at T=800 °C for 4 days. Afterwards the reaction products were powdered to a particle size below 100 μm and compacted in cylinders by cold pressing in a steel die prior to annealing. Alloys with $SrSi_2$, and $BaSi_2$, were sensitive to moisture/oxygen and were handled with care.

Samples from the systems Sr-{Cu,Ni}-Si were annealed for 15 days at 800 °C (Ni,Cu) and for 7 days at 900 °C (Ni). X-ray powder diffraction (XPD) data from as-cast and annealed specimens were collected with a Guinier-Huber image plate system (Cu–$K_{\alpha 1}$ or Fe-$K_{\alpha 1}$; 8° < 2θ < 100°). Precise lattice parameters were calculated by least-squares fits to indexed 2θ-values employing Ge as internal standard (a_{Ge} = 0.565791 nm).

Single crystal fragments, suitable for X-ray structure determination were broken from samples with nominal compositions $BaPdGe_3$ $BaPtGe_3$, $BaCd_2Ge_2$ and $SrNi_{9-x}Si_{4+x}$ (x=2.5). Inspection on an AXS-GADDS texture goniometer assured high crystals quality, unit cell dimensions and Laue symmetry of the specimens prior to X-ray intensity data collection on a four-circle Nonius Kappa diffractometer equipped with a CCD area detector and employing graphite monochromated Mo Kα radiation (λ = 0.071073 nm). Orientation matrix and unit cell parameters for tetragonal symmetry were derived using the program DENZO [12]. No absorption correction was necessary because of the rather regular crystal shapes and small dimensions of the investigated specimens. The structures were solved by direct methods and refined with the SHELXL-97 and SHELXS-97 programs [13].

The as cast and annealed samples were polished using standard procedures and were examined by light optical microscopy (LOM) and scanning electron microscopy (SEM). Chemical compositions for phases were determined via a Philips XL30 field emission environmental scanning electron microscope (ESEM-FEG) operated at 20 kV and equipped with an EDX (Energy Dispersive X-Ray) spectrometer supported with Genesis software (USA).

6.3 Results and Discussion

6.3.1 Phase equilibria in the ternary systems Sr-Ni-Si and Sr-Cu-Si.

Sr–Ni–Si. Phase equilibria at 800 °C were found to be similar to those determined after heat-treatment at 900 °C, and therefore the present article reports only the isothermal section at 900 °C (Figure 1). Three ternary compounds τ_1-$Sr(Ni_xSi_{1-x})_2$ (AlB_2-type), τ_2-$SrNiSi_3$ ($BaNiSn_3$-type) and τ_3-$SrNi_{9-x}Si_{4+x}$ (tetragonal primitive structure related to $CeNi_{8.5}Si_{4.5}$-type) were observed and all these compounds were found to crystallize from liquid. Detailed information on the crystal structure of these phases is available from section 3.2. The homogeneity region of τ_1-$Sr(Ni_xSi_{1-x})_2$ with AlB_2-type structure extends from 7.0 at. % Ni (x= 0.10) and continues at least up to 16.0 at. % Ni (x=0.34). τ_1 is in equilibrium with $SrSi_2$ and (Si) (as displayed from alloy $Sr_{33}Ni_4Si_{64}$). The solubility of Ni in $SrSi_2$ was less than 0.5 at. %.

The alloy with nominal composition $Sr_{20}Ni_{20}Si_{60}$ evidences primary crystallization of τ_1 (Figure 2a), followed by secondary peritectic formation of τ_2-$SrNiSi_3$ and a monovariant eutectic (Si)+τ_3 with composition $Sr_{8.6}Ni_{22.1}Si_{69.4}$ (in at. %). This eutectic disappears after anneal at 900 °C (Figure 2b) and the equilibrated alloy consists of three phases τ_1 + τ_2 + (Si). Overall composition of this alloy ($Sr_{19.02}Ni_{18.8}Si_{62.17}$) is slightly shifted from the composition of τ_2-$Sr_{20.1}Ni_{20}Si_{59.9}$ (as determined by EPMA), which explains the presence of secondary phases (Si) and τ_1.

The as cast alloy $Sr_{12}Ni_{23}Si_{65}$ shows primary grains of (Si), secondary crystallization of the ternary compound τ_2-$SrNiSi_3$ and a three-phase eutectic $Sr_{16.4}Ni_{17.9}Si_{65.7}$ (in at. %) which is composed of τ_2, τ_3 and (Si) (see insert in Figure 2c) and tends to coarsen after annealing at 900 °C (Figure 2d). A eutectic with different morphology and composition $Sr_{5.0}Ni_{37.6}Si_{57.4}$ (in at. %) is observed in alloy $Sr_{1.5}Ni_{32.5}Si_{66}$ (Figure 2e): it represents the monovariant crystallization of $NiSi_2$ and τ_3. After annealing at 900 °C a three-phase equilibrium is reached: (Si) + $NiSi_2$ + τ_3 (Figure 2f).

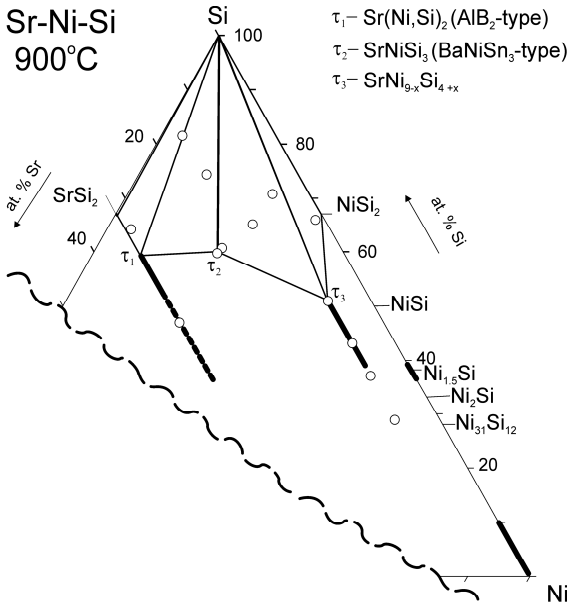

Figure 1: Partial isothermal section of the Sr-Ni-Si system at 900 °C.

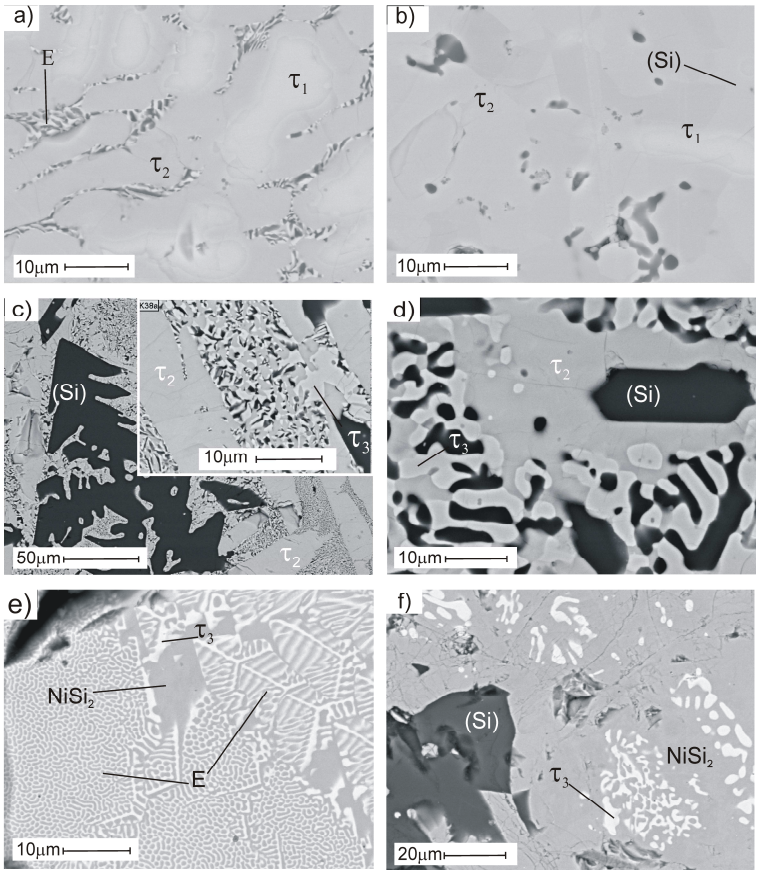

Figure 2: Microstructure of selected Sr-Ni-Si alloys: a) $Sr_{20}Ni_{20}Si_{60}$ (as cast), b) $Sr_{20}Ni_{20}Si_{60}$ 900°C, c) $Sr_{12}Ni_{23}Si_{65}$ (as cast), d) $Sr_{12}Ni_{23}Si_{65}$ (900 °C), e) $Sr_{1.5}Ni_{32.5}Si_{66}$ (as cast), f) $Sr_{1.5}Ni_{32.5}Si_{66}$ (900 °C).

Sr–Cu–Si. The partial isothermal section at 800 °C is shown in Figure 3. Crystal structures of the ternary phases within the investigated compositional region were found to be consistent with data in literature concerning τ_1-$Sr(Cu_xSi_{1-x})_2$ (x=0.33) ([14], AlB_2-type), τ_2-$SrCu_2Si_2$ ([15], $ThCr_2Si_2$-type) and τ_3-$SrCu_{9-x}Si_{4+x}$ ([16], $CeNi_{8.5}Si_{4.5}$-type). However, tetragonal τ_3-$SrCu_{9-x}Si_{4+x}$ ($0 \leq x \leq 1.0$) undergoes a structural transformation into a cubic structure τ_3'-$SrCu_{13-x}Si_x$ ($1.8 \leq x \leq 4$; $NaZn_{13}$–type; for details see chapter 3.2). Thus the as-cast sample with nominal composition $SrCu_9Si_4$ was indexed as a two-phase mixture of tetragonal $CeNi_{8.5}Si_{4.5}$-type (a=0.81339(6) nm and c=1.1620(3) nm) and cubic $NaZn_{13}$-type (*a*=1.1445(3) nm). After heat treatment at 800 °C for 10 days (i) only the tetragonal phase prevails with lattice parameters a=0.81277(3) nm and c=1.1610(1) nm and (ii) none of the annealed alloys reveals a mixture of cubic and tetragonal structures. As a group-subgroup relation exists between these two structure types, we suggest, that both phases, τ_3-$SrCu_{9-x}Si_{4+x}$ and τ_3'-$SrCu_{13-x}Si_x$, are part of one continuous single-phase region at 800 °C where the homogeneity region of τ_3'-$SrCu_{13-x}Si_x$ extends up to 80.0 at % Cu. This composition at 800 °C was found to be in equilibrium with liquid, and therefore big crystals of τ_3'-$SrCu_{13-x}Si_x$ (x= 1.8) and copper-based solid solution (96 at. % from EPMA) grew during annealing of the sample at this temperature (Figure 4a). The liquid crystallizes as a ternary eutectic (insert in Figure 4a) with composition $Sr_{16.2}Cu_{71.1}Si_{12.7}$ (at. %).

The single phase region of τ_2–$SrCu_{2-x}Si_{2+x}$ with $ThCr_2Si_2$-type was found to extend up to ~31.5 at. % Cu (x = 0.4). The solid solution τ_1–$Sr(Cu_xSi_{1-x})_2$ with AlB_2 type was established to start at $x \geq 0.15$. Rieger et al. [14] reported an AlB_2-type phase at x=0.33, whereas Dörrscheidt and Schäfer [17] investigated the region $0.25 \leq x \leq 0.5$ where they observed a superstructure ($a=2a_o$ and $c=2c_o$). The composition of τ_1 in equilibrium with (Si) and $SrSi_2$ at 800 °C was determined by EPMA from the alloy $Sr_{14.8}Cu_{3.7}Si_{81.5}$. This alloy in as-cast state shows (Figure 4b) primary dendrites of (Si) and a secondary solidification of τ_1 (9.8 at. % Cu after EPMA). A small amount of $SrSi_2$ was determined by XPD but was not observed by SEM. The as-cast alloy $Sr_{20}Cu_{20}Si_{60}$ (nominal composition) shows the crystallization of τ_1 and τ_2 (Figure 4c). The last liquid crystallizes with formation of τ_3 and a eutectic composed of τ_3 and (Si). After anneal at 800°C the alloy consists of three phases, τ_1, τ_2 and (Si).

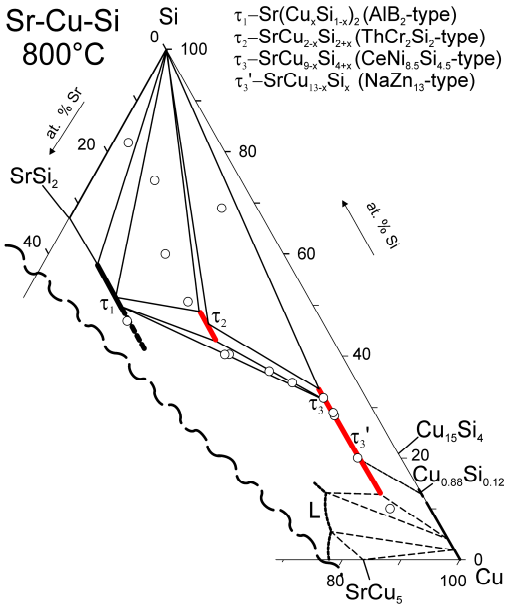

Figure 3: Partial isothermal section of the Sr-Cu-Si system at 800 °C.

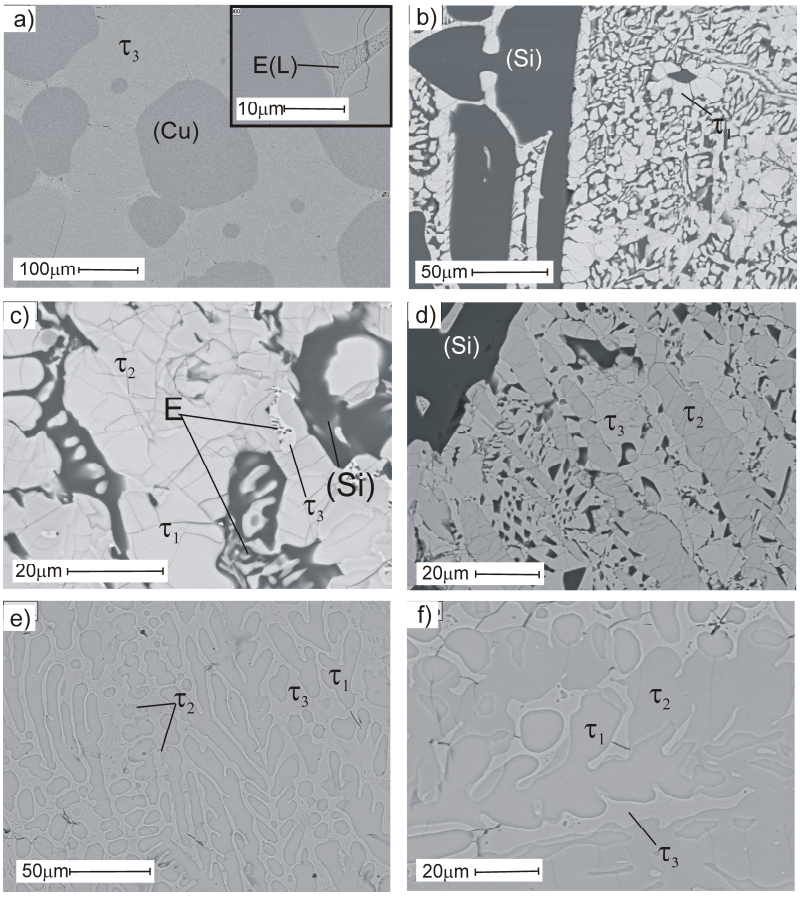

Figure 4: Microstructure of selected Sr-Cu-Si alloys a) $Sr_{7.1}Cu_{83}Si_{10}$ (800°C), b) $Sr_{14.8}Cu_{3.7}Si_{81.5}$ (as cast), c) $Sr_{20}Cu_{20}Si_{60}$ (as cast), d) $Sr_{5.9}Cu_{23.5}Si_{70.6}$ (as cast), e) $Sr_{20}Cu_{40}Si_{40}$ (as cast), f) $Sr_{20}Cu_{40}Si_{40}$ (900 °C).

The microstructure of the as cast alloy $Sr_{5.9}Cu_{23.5}Si_{70.6}$ shows (Figure 4d) primary crystallization of (Si) and big dendrites of τ_2 and τ_3 in almost equal amounts. After annealing the sample consists of three equilibrium phases: (Si), τ_2 and τ_3. Joint crystallization of τ_1 and τ_3 along with a small amount of τ_2 is observed in as-cast alloy $Sr_{20}Cu_{40}Si_{40}$ (Figure 4e). When equilibrated at 800 °C the sample consists of the same phases but with significantly changed volume fractions (Figure 4f).

Data on composition and lattice parameters for phases coexisting in equilibrium in the ternary Sr–(Ni,Cu)–Si systems are listed in Table 1.

Table 1: Three-phase equilibria and lattice parameters for Sr–Ni–Si (900°C) and Sr–Cu–Si (800°C) systems.

Phase Region	**Phase**	**Composition by EPMA in at. %**			**Lattice Parameters**	
		Sr	Ni/Cu	Si	a (nm)	c (nm)
Sr–Ni–Si						
(Si) + $SrSi_2$ + τ_1	(Si)	-	-	-	0.54318(2)	-
	$SrSi_2$	-	-	-	0.65370(3)	
	τ_1	32.7	8.3	59.0	0.40564(4)	0.47039(4)
	(Si)	-	-	100.0	0.5430	
(Si) + τ_1+ τ_2	τ_1	33.7	7.0	59.3	0.40567(3)	0.46952(7)
	τ_2	20.1	19.7	60.5	0.41958(3)	0.97915(7)
(Si) + τ_2+ τ_3	(Si)	97.4	1.5	1.1	0.54308(2)	-
	τ_2	19.7	19.8	60.5	0.41935(5)	0.9793(1)
	τ_3	7.1	42.0	50.8	0.78526(4)	1.1202(2)
(Si) + $NiSi_2$+ τ_3	(Si)	100.0	-	-	0.54303(3)	-
	$NiSi_2$	1.7	34.5	63.8	0.54071(4)	-
	τ_3	7.7	43.1	49.2	0.78596(5)	1.1216(2)
Sr–Cu–Si						
(Si) + $SrSi_2$+ τ_1	(Si)	-	-	100.0	0.54310(6)	-
	$SrSi_2$	-	-	-		-
	τ_1	33.3	9.8	56.9	0.40759(3)	0.47085(7)
	(Si)	-	-	100.0		-
(Si) + τ_1+ τ_2	τ_1	33.3	15.6	51.1	0.41079(4)	0.46255(7)
	τ_2	20.0	31.3	48.7	0.41871(5)	1.0022(2)
(Si) + τ_2+ τ_3	(Si)	-	-	100.0	0.54292(3)	-
	τ_2	20.0	33.8	46.2	0.41881(1)	1.00267(8)
	τ_3	7.1	58.9	33.9	0.8052(2)	1.158(4)
τ_1+ τ_2+ τ_3	τ_1	33.3	17.1	49.5	0.41136(2)	0.46228(7)
	τ_2	20.0	36.7	43.3	0.41944(8)	0.9979(2)
	τ_3	7.1	62.2	30.7	0.80994(7)	1.1607(2)

6.3.2 Crystal structure of ternary phases.

Data on the crystal structure of ternary phases for systems Sr-Cu-Si and Sr-Ni-Si are summarized in Table 2. The table compiles also information on isotypic compounds in ternary systems Ba-M-(Si,Ge). All listed compounds belong to three structural families (i) hexagonal AlB_2-type, (ii) tetragonal $BaAl_4$-type ($ThCr_2Si_2$ and $BaNiSn_3$ structure types) and (iii) cubic $NaZn_{13}$-type (and tetragonal derivative structure types: $CeNi_{8.5}Si_{4.5}$ and $SrNi_{9-x}Si_{4+x}$). Results of the refinements for x-ray single crystal and powder diffraction intensities for these compounds are listed in Tables 3 and 4 showing fine agreement with the assigned prototypes.

6.3.2.1 Ternary compounds with AlB_2 – type structure (τ_1).

Despite no binary compounds $Sr(Si,Ge)_2$ and $Ba(Si,Ge)_2$ are known with AlB_2–type, this structure type is frequently observed in ternary systems (Sr,Ba)-M-(Si,Ge) (Table 2). A small addition of a third element may stabilize this structure type that appears to be very abundant, particularly in ternary systems with Si. Evidence on an enhanced thermodynamic stability of AlB_2-type phases τ_1 in ternary systems Sr-(Ni,Cu)-Si follows from the observation of primary crystallization (see for example Figure 2a) and congruent formation from liquid. The crystal structure of τ_1-$Sr(Cu_xSi_{1-x})_2$ (x=0.15) is confirmed from Rietveld refinements as a simple AlB_2-type as no un-indexed x-ray reflections that may be attributed to superstructures were observed. However, we do not exclude the existence of the superstructure for higher values of x, as reported by [17]. Lattice parameters for the ternary phases with AlB_2 type agree well with values reported in literature.

6.3.2.2 Ternary compounds with the $BaNiSn_3$-structure type (τ_2).

Single crystals isolated from melted alloys with compositions $BaPdGe_3$ and $BaPtGe_3$ reveal body centred tetragonal unit cells. Structural solutions performed by direct methods were not successful in the highest possible S. G. *I*4/*mmm*, however, the structures were resolved in the non-centrosymmetric subgroup *I*4*mm*. Four independent atom positions were found which agree well with the group-subgroup scheme in the Bärnighausen formalism [18, 19]. Germanium atoms adopt two crystallographically independent sites 2a (0, 0, z) and 4b (0, ½, z), Pd(Pt) atoms solely occupy the 2a site (0, 0, z) fully consistent with atom order of the $BaNiSn_3$-type [20]. Single crystal refinement data for $BaPdGe_3$ and $BaPtGe_3$ are listed

in Table 4 and are consistent with results of [21] for $BaPtGe_3$. X-ray Rietveld refinements for $BaPdSi_3$, $BaPtSi_3$, $BaRhGe_3$, $BaIrGe_3$, $SrNiSi_3$, found in corresponding ternary systems, confirm isotypism with the $BaNiSn_3$-type (Table 4).

Interatomic distances for all these compounds agree well with the sum of atomic radii for exception of relatively short bonds M-Ge1(Si1) and M-Ge2(Si2) (Table 3). Such observation for $BaPtGe_3$ was attributed [21] to strong Pt-Ge interaction. However, such "short" distances are typical for almost all binary M-Ge and M-Si compounds [22].

6.3.2.3 Ternary compounds with the $ThCr_2Si_2$-structure type (τ_2).

Inspection of a single crystal, isolated from melted sample with nominal composition $BaCd_2Ge_2$, reveals a body centred tetragonal unit cell. Structural solution by direct methods in the highest possible symmetry (S. G. I4/mmm) yielded three independent atom positions. For Ba-atoms in 2a (0, 0, 0), Cd in 4d (0, ¼, ½) and Ge in the 4e (0, 0, z) sites, the structure successfully refines to R_{F2} = 0.021 and a residual electron density 1.53ē/$Å^3$ (see Table 3). X- ray Rietveld refinement for $BaZn_2Si_2$ confirms isotypism with $ThCr_2Si_2$ type (see Table 4).

The only free atom parameters ~0.38 < z < ~0.39 in combination with ratios (2.3 < c/a < 2.5) for compounds $BaCd_2Ge_2$, $BaZn_2Si_2$, $BaZn_2Ge_2$, and $SrCu_{2-x}Si_{2+x}$ fit to the range observed for the majority of $ThCr_2Si_2$ type compounds [23] and were suggested to enable short Cr-Si ad Si-Si distances as also observed for $BaCd_2Ge_2$, $BaZn_2Si_2$, $BaZn_2Ge_2$, and $SrCu_{2-x}Si_{2+x}$.

Table 2: Crystal structure for selected ternary compounds in A-T-M systems (A= Sr, Ba, T= Ni, Cu, Pd, Pt, Zn, Cd, Rh, Ir and M= Si, Ge).

Compound	Lattice Parameters [nm]		Method	Reference
	a	***c***		
$ThCr_2Si_2$-structure type (*I*4/*mmm*)				
$BaCd_2Ge_2$	0.46735(6)	1.1448(1)	SC	This work
$BaZn_2Ge_2$	0.45390(3)	1.05279(6)	PD	This work
	0.4527(2)	1.0555(3)	SRRS	[26]
$BaZn_2Si_2$	0.4497(1)	1.02049	SC	This work
$SrCu_{2-x}Si_{2+x}$	0.41907(4)	1.0031(2)	PD	[15]; x=0
	0.41881(5)	1.00267(8)	PD	[This work]; x=0.3
$BaNiSn_3$ -structure type (*I*4*mm*)				
$BaPdGe_3$	0.45508(4)	1.03649(5)	SC	This work
$BaPtGe_3$	0.45638(8)	1.0231(1)	SC	This work
	0.45636(2)	1.02341(6)	SC	[21]
$BaPdSi_3$	0.43963(3)	1.0186(2)	PD	This work
$BaPtSi_3$	0.44079(2)	1.0017(2)	PD	This work
$BaRhGe_3$	0.45240(3)	1.0274(1)	PD	This work
$BaIrGe_3$	0.45406(1)	1.02132(1)	PD	This work
$SrNiSi_3$	0.41958(3)	0.97915(7)	PD	This work
AlB_2 -structure type (*P*6/*mmm*)				
$Ba(Pd_xSi_{1-x})_2$	0.41950(3)	0.49594(9)	PD	x= 0.17; This work
$Ba(Pt_xSi_{1-x})_2$	0.41606(4)	0.50150(5)	PD	x= 0.15; This work
$Ba(Cu_xSi_{1-x})_2$	0.41520(8)	0.5058(2)	PD	x=0.19; This work
	0.4117	0.5019	PD	x=0.1; [14]
$Sr(Zn_xSi_{1-x})_2$	0.41639(5)	0.46787(6)	PD	This work
$Sr(Ni_xSi_{1-x})_2$	0.40564(4)	0.47039(4)	PD	x=0.102; This work
	0.4069	0.4663		x=0.25; [27]
$Sr(Cu_xSi_{1-x})_2$	0.40759(3)	0.47085(7)	PD	x=0.15; This work
	0.4108	0.4625	PD	x=0.33; [14]
	0.824(1)	0.921(1)	SC	$0.25 \leq x \leq 0.5$; $a = 2a_0$; $c = 2c_0$ [17]
$Ba(Cu_xGe_{1-x})_2$	0.4309(2)	0.4965(4)	PD	x=0.29; This work
	0.4616; 0.4312	0.4700; 0.4907		x=0.33; 0.50; [14]
$NaZn_{13}$-related structure types (for details see table 5 and 6)				
$SrCu_{13-x}Si_x$	1.15789(8)	-	PD	x=3.6; This work
$SrCu_{9-x}Si_{4+x}$	0.8146(1)	1.1629(2)	SC	x=0; [16]
	0.80722(6)	1.1579(3)	PD	x=1.0; This work
$SrNi_{9-x}Si_{4+x}$	0.78998(3)	1.1337(2)	SC	x=2.7;This work

[1)] SC- single crystal; PD – powder diffraction; SRRS – Synchrotron Radiation Resonant Scattering

Table 3: X-Ray single crystal data for $BaPdGe_3$, $BaPtGe_3$ and $BaCd_2Ge_2$ standardized with program *Structure Tidy* [28]. (radiation: MoKα; 2Θ range (°) = 2≤2Θ≤70; ω-scans, scan width 2° =150 sec/frame; Total number of frames & sets=411 & 8; Anisotropic displacement parameters [in $10^2 nm^2$]).

Parameter/compound	$BaPdGe_3$	$BaPtGe_3$	$BaCd_2Ge_2$
Space Group	*I4mm*	*I4mm*	*I4/mmm*
Composition from EPMA	$Ba_{20.0}Pd_{20.0}Ge_{60.0}$	$Ba_{20.6}Pt_{20.5}Ge_{59.0}$	-
Composition from refinement	$Ba_{20.0}Pd_{20.0}Ge_{60.0}$	$Ba_{20.0}Pd_{20.0}Ge_{60.0}$	$Ba_{20.0}Cd_{40.0}Ge_{40.0}$
Formula from refinement	BaPdGe3	$BaPtGe_3$	$BaCd_2Ge_2$
a, *c* [nm]	0.45508(4), 1.03649(5)	0.45638(8) , 1.0231(1)	0.46735(6); 1.1448(1)
μ_{abs} [mm^{-1}]	33.56	62.49	27.77
V (nm^3)	0.2146	0.2131	0.25004
ρ_x (gcm^{-3})	7.1434	11.6013	6.739
Reflections in refinement	340≥4σ(F_o) of 341	324≥4σ(F_o) of 324	201≥4σ(F_o) of 208
Mosaicity	<0.5	<0.6	<0.5
Number of variables	15	15	9
$R_F^2 = \Sigma\|F_0^2-F_c^2\|/\Sigma F_0^2$	0.014	0.016	0.021
R_{Int}	0.06	0.07	0.06
wR2	0.033	0.039	0.058
GOF	1.106	1.171	1.155
Extinction (Zachariasen)	0.026	0.019	0.024
Residual density $e^-/Å^3$; max; min	1.10; -1.80	1.96; -2.06	1.53; -2.27
Atom parameters			
Ba in 2*a*(0, 0, *z*); *z*	0.60480(2)	0.59989(6)	Ba in 2*a*(0, 0, 0)
$U_{11}= U_{22}; U_{33}$	0.0078(1); 0.0074(2)	0.0048(2); 0.0058(3)	0.0102(2); 0.0169(3)
M(Pd/Pt) in 2*a*(0, 0, *z*); *z*	0.24991(6)	0.24690(3)	Cd in 4*d*(0, 1/2, 1/4)
$U_{11}= U_{22}; U_{33}$	0.0074(1); 0.0073(2)	0.0039(1); 0.0047(2)	0.0143(2); 0.0163(3)
Ge1 in 4*b*(0, 1/2, *z*); *z*	0.35681(6)	0.35324(9)	Ge in 4*e*(0, 0, *z*), 0.38741(6)
$U_{11}; U_{22}; U_{33}$	0.0118(2); 0.0073(2); 0.0070(2)	0.008(3); 0.0032(3); 0.0059(3)	0.0113(2); 0.0118(3)
Ge2 in 2*a*(0, 0, *z*); *z*	0.0000(1)	0.000(2)	-
$U_{11}= U_{22}; U_{33}$	0.0092(2); 0.0086(3)	0.0056(3); 0.0069(4)	-
Interatomic distances [nm]	Standard deviation ≤0.00004		
Ba - 4Ge2	0.3403	0.3385	Ba– 8Ge 0.35503
–4Ge1	0.3432	0.3399	– 8Cd 0.36947
–4Ge1	0.3466	0.3457	Ge– 1Ge 0.25776
–4M	0.3558	0.3565	– 4Cd 0.28178
–1M	0.3672	0.3602	– 4Ba 0.35503
Ge1– 2M	0.2537	0.2525	Cd– 4Ge 0.28178
–2Ge2	0.2721	0.2729	– 4Cd 0.33081
–4Ge1	0.3227	0.3227	– 4Ba 0.36947
–4Ba	0.3432	0.3399	
Ge2– 1M	0.2579	0.2539	
–4Ge1	0.2721	0.2729	
–4Ba	0.3403	0.3385	
M– 4Ge1	0.2537	0.2525	
–1Ge2	0.2579	0.2539	
–4Ba	0.3558	0.3565	
–1Ba	0.3672	0.3602	

6.3.2.4 Ternary compounds with the structure types related to $NaZn_{13}$ (τ3).

Although binary $BaCu_{13}$ with cubic $NaZn_{13}$-type is known [22], no binary Sr-Cu homologue exists. The ternary system Sr-Cu-Si, however, reveals the formation of a cubic ternary phase τ_3'-$SrCu_{13-x}Si_x$ for 1.8<x<4 (see Figure 3). Rietveld refinement confirms structural identity with the $NaZn_{13}$-type (see Table 5). At a silicon content of x ≈ 4 this phase undergoes a structural transformation into tetragonal τ_3-$SrCu_{9-x}Si_{4+x}$ with the $CeNi_{8.5}Si_{4.5}$ structure, which was already earlier established for x=0 from x-ray single crystal data [16]. The homogeneity region of τ_3-$SrCu_{9-x}Si_{4+x}$ at 800 °C extends up to x=1.0. In order to establish the atom site preferences for silicon-rich compositions of τ_3-$SrCu_{9-x}Si_{4+x}$, we performed x-ray Rietveld refinement for alloy with nominal composition x = 1. These refinements reveal that the 4d site (occupied by Cu at x=0) is completely substituted by Si atom resulting in a composition $SrCu_{9-x}Si_{4+x}$ (x=1.0; R_F=0.054; R_I=0.078; Table 5).
An X-ray diffraction spectrum similar to tetragonal $SrCu_{9-x}Si_{4+x}$ is also observed for the ternary phase τ_3 in the Sr–Ni–Si system (Figure 1). However, the x-ray profiles for single-phase compositions (Figure 5) contain a set of reflections that do not belong to the $CeNi_{8.5}Si_{4.5}$-type structure (SG. *I*4/*mcm*). These reflections may be indexed in a primitive tetragonal unit cell. Single crystal fragments taken from samples within the homogeneity region of τ_3 confirm a primitive tetragonal structure with lattice parameter a ≈ 0.79 nm and c ≈ 1.13 nm, but in most cases twining along the *c* - axis was observed. Analysis of the extinctions observed for an untwinned crystal (a ≈ 0.79 nm and c ≈ 1.13 nm) yields *P*4/*nbm* as the highest possible symmetry.

Table 4: X-Ray powder diffraction data for ternary compounds of (Ba, Sr) –M–X, (M=Rh, Ir, Pd, Pt, Ni, Zn, X= Si, Ge) with $BaNiSn_3$ and $ThCr_2Si_2$-type standardized with program *Structure Tidy* [28].

Parameter/compound	$BaIrGe_3$	$BaRhGe_3$	$BaPdSi_3$	$BaPtSi_3$	$SrNiSi_3$	$BaZn_2Si_2$
Space group, Prototype	*I4mm*, $BaNiSn_3$	*I4mm*, $BaNiSn_3$	*I4mm*, $BaNiSn_3$	*I4mm*, $BaNiSn_3$	*I4mm*, $BaNiSn_3$	*I4/mmm*, $ThCr_2Si_2$
Composition, EMPA at.%	-	-	$Ba_{20.0}Pd_{20.0}Ge_{60.0}$	$Ba_{19.6}Pt_{20.3}Si_{60.1}$		-
a ; c [nm], Ge standard	0.45406(1): 1.02132(1)	0.45240(3); 1.0274(1)	0.43963(3); 1.0186(2)	0.44079(2); 1.0017(2)	0.41958(3); 0.97915(7)	0.4497(1); 1.02049
Reflections measured	53	52	50	48	43	51
Θ range	8≤2Θ≤100	8≤2Θ≤100	8≤2Θ≤100	8≤2Θ≤100	8≤2Θ≤100	8≤2Θ≤100
Number of variables	18	24	24	28	24	24
$R_F = \Sigma\|F_o-F_c\|/\Sigma F_o$	0.062	0.057	0.030	0.072	0.045	0.048
$R_I = \Sigma\|I_o-I_c\|/\Sigma I_o$	0.093	0.085	0.046	0.084	0.087	0.062
$R_{wP}=[\Sigma w_i\|y_{oi}-y_{ci}\|^2/\Sigma w_i\|y_{oi}\|^2]^{½}$	0.071	0.057	0.074	0.086	0.073	0.056
$R_P = \Sigma\|y_{oi}-y_{ci}\|/\Sigma\|y_{0i}\|$	0.052	0.044	0.050	0.063	0.047	0.040
$R_e = [(N-P+C)/\Sigma w_i y^2_{oi})]^{½}$	0.027	0.014	0.022	0.019	0.021	0.030
$\chi^2 = (R_{wP}/R_e)^2$	7.13	16.3	11.3	21.3	12.3	3.41
Atom parameters						
Ba/Sr in 2a(0, 0, *z*); *z*	0.5881(2)	0.5897(2)	0.6156(4)	0.5991(9)	0.5984(5)	Ba in 2*a* (0, 0, 0)
B_{iso} (10^2 nm^2)	0.66(3)	0.14(4)	0.62(4)	0.37(6)	0.29(3)	0.9(2)
M in 2a (0, 0, *z*); *z*	0.2385(2)	0.2392(2)	0.2607(4)	0.2477(9)	0.2413(4)	Zn in 4*d* (0, ½, ¼)
B_{iso} (10^2 nm^2)	0.55(2)	0.44(4)	0.06(4)	0.13(4)	0.77(7)	1.1(2)
X1 in 2a(0, 0, *z*); *z*	0.0000(2)	0.0000(3)	0.0000(4)	0.000(2)	0.0000(7)	Si in 4*e* (0, 0, 0.3807(1))
B_{iso} (10^2 nm^2)	1.43(6)	1.52(6)	1.0(1)	1.0(2)	1.7(1)	0.5(3)
X2 in 4b(0, ½, *z*); *z*	0.3442(3)	0.3442(3)	0.3702(6)	0.356(1)	0.3530(5)	
B_{iso} (10^2 nm^2)	1.05(4)	0.53(3)	0.48(5)	0.8(1)	0.78(5)	

Structure solution via direct methods (Table 6) reveals an atomic arrangement similar to that for $SrCu_9Si_4$ (SG, *I*4/*mcm*), but with the difference that two 16l sites were found to be split into 8 fold positions (SG, *P*4/*nbm*) with almost complete atom order (Figure 5 and 6). Refinement of the individual occupancies of all Wyckoff positions and temperature factors suggested a statistical distribution of Ni and Si atoms in sites 16n and 4h resulting in R_{F2} = 0.036 and residual electron densities 1.24,and -1.66 $e^-/Å^3$. Only the occupancy of Si2 in the 8m site was found to be below 1.0. As substitution of about 6% Ni in this site does neither significantly change the R_{F2}-value (0.034) nor the anisotropic atom displacement parameters, complete ordering was kept for this site.

Although the structural solution obtained from the single crystal refinement describes very well the powder pattern for x=2.7 (Figure 5), powder x-ray intensities significantly change for higher silicon contents due to changes in atom order. In order to investigate the site preference for the Si-rich boundary of τ_3, Rietveld refinement was performed for an alloy with nominal composition $Sr_{7.1}Ni_{41.9}Si_{51}$ (containing less than 5 % of secondary Si). Rietveld analysis reveals a very small electron density in the 4h site (M2) in as cast state that corresponds to 0.55 Si atoms and a formula $SrNi_{5.8}Si_{6.3}\square_{0.9}$, whereas profile refinement of the annealed sample forced a complete disappearance of Si from the 4h site ($SrNi_{5.5}Si_{6.5}\square_1$, Table 6). The removal of the 4h site is also backed by the interatomic distances which become very small for $SrNi_{5.8}Si_{6.3}\square_{0.9}$ ($d_{M2\text{-}Si}$ = 0.20421 nm and $d_{Si\text{-}Ni}$=0.21043 nm) and finally for $SrNi_{5.5}Si_{6.5}\square_1$ $d_{M2\text{-}Si}$ =0.19770 nm and $d_{Si\text{-}Ni}$ =0.18557 nm. Although such deficiency has not been reported previously in any ternary variant of the $NaZn_{13}$-type or $CeNi_{8.5}Si_{4.5}$-type, a partial occupancy for the corresponding 8b site was recently established (see Figure 6) for binary $AEZn_{13\text{-}x}$ (AE=Ca, Sr, Ba) [24] and $EuZn_{13\text{-}x}$ [25] ($x \approx 0.25$).

Table 5: X-Ray powder diffraction data for $SrCu_{13-x}Si_x$ and $SrCu_{9-x}Si_{4+x}$; anisotropic displacement parameters /temperature factors are in (10^2 nm^2)

Parameter/compound	**$SrCu_{13-x}Si_x$ (x=3.6)**	**$SrCu_{9-x}Si_{4+x}$ (x=1)**
Prototype	$NaZn_{13}$	$CeNi_{8.5}Si_{4.5}$
Space group	$Fm\bar{3}c$	*I*4/*mcm*
Composition, EMPA at. %	$Sr_{7.1}Cu_{61.7}Si_{31.2}$	$Sr_{7.1}Cu_{62.8}Si_{30.1}$
Composition, refeinment at. %	$Sr_{7.1}Cu_{63.8}Si_{29.0}$	$Sr_{7.1}Cu_{57.1}Si_{35.7}$
a ; c [nm], Ge standard	1.15789(8)	0.80722(6); 1.1579(3)
Reflections measured	51	
Θ range	8≤2Θ≤100	8≤2Θ≤100
Number of variables	27	21
$R_F = \Sigma\|F_o-F_c\|/\Sigma F_o$	0.037	0.054
$R_I = \Sigma\|I_o-I_c\|/\Sigma I_o$	0.045	0.078
$R_{wP}=[\Sigma w_i\|y_{oi}-y_{ci}\|^2/\Sigma w_i\|y_{oi}\|^2]^{½}$	0.061	0.059
$R_P = \Sigma\|y_{oi}-y_{ci}\|/\Sigma\|y_{0i}\|$	0.040	0.043
$R_e = [(N-P+C)/\Sigma w_i y^2_{oi})]^{½}$	0.017	0.02
$\chi^2 = (R_{wP}/R_e)^2$	13.2	9.04
Atom parameters		
Sr	Sr 8a (1/4, 1/4, 1/4);	4a (0, 0, 1/4)
B_{iso}	0.17(4)	1.28(4)
M1	96i (0, 0.11875(4), 0.18069(4))	16k (0.0594(1), 0.2084(2), 0)
B_{iso}	0.60(3)	B_{iso} =1.93(4)
Occ.	0.678 Cu + 0.322 Si	1.0 Cu1
Cu2	-	16l (0.6214(1), 0.1214(1), 0.1806(1))
B_{iso}	-	1.75(4)
Si1	-	16l (0.1726(3), 0.6726(3), 0.1149(3))
B_{iso}		1.93(8)
M2	8b (0, 0, 0)	4d (0, ½, 0)
B_{iso}	0.67(5)	1.3(1)
Occu.	0.802 Cu + 0.198 Si	0.99(3)Si

The group-subgroup relation among several structure variants of fcc-$NaZn_{13}$ has been shown in terms of a Bärnighausen tree [18, 19] by Pöttgen and coworkers [26, 27, 28]. A new branch from $CeNi_{8.5}Si_{4.5}$ (S. G *I*4/*mcm*) leading to $SrNi_{9-x}Si_{4+x}$ (S. G. *P*4/*nbm*) via a *klassengleiche* symmetry reduction of index 2 is shown in Figure 6

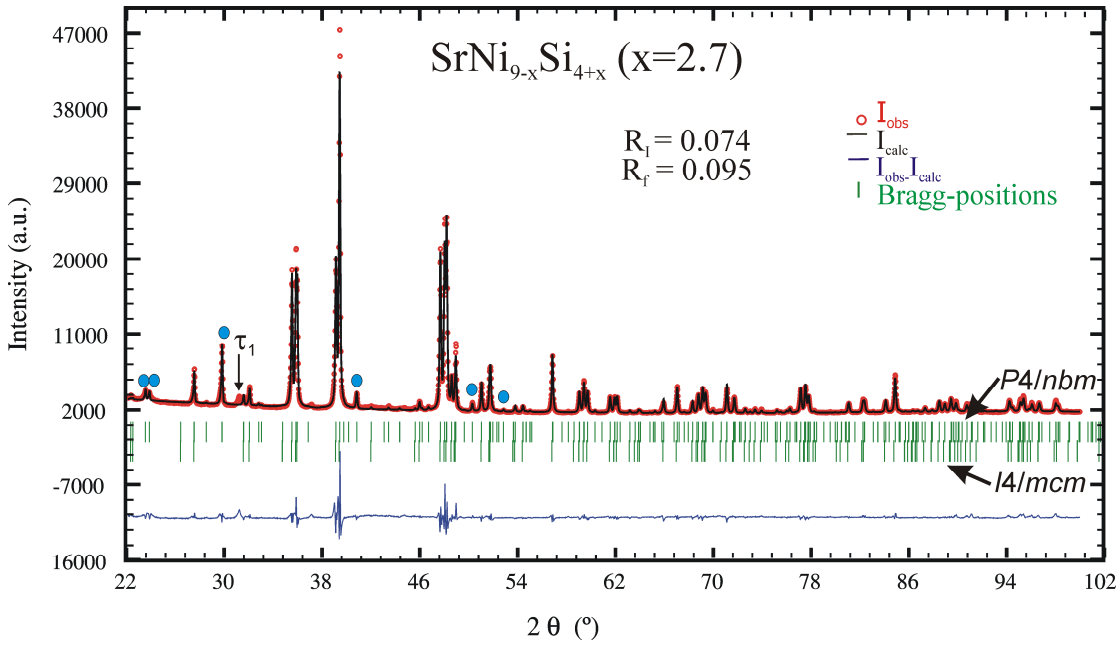

Figure 5: Rietveld refinement of the X-ray powder diffraction profile for $SrNi_{9-x}Si_{4+x}$ (space group *P*4/*nbm*) in comparison with Bragg positions for space group *I*4/*mcm*. Prominent reflections of primitive cell are marked by blue dots.

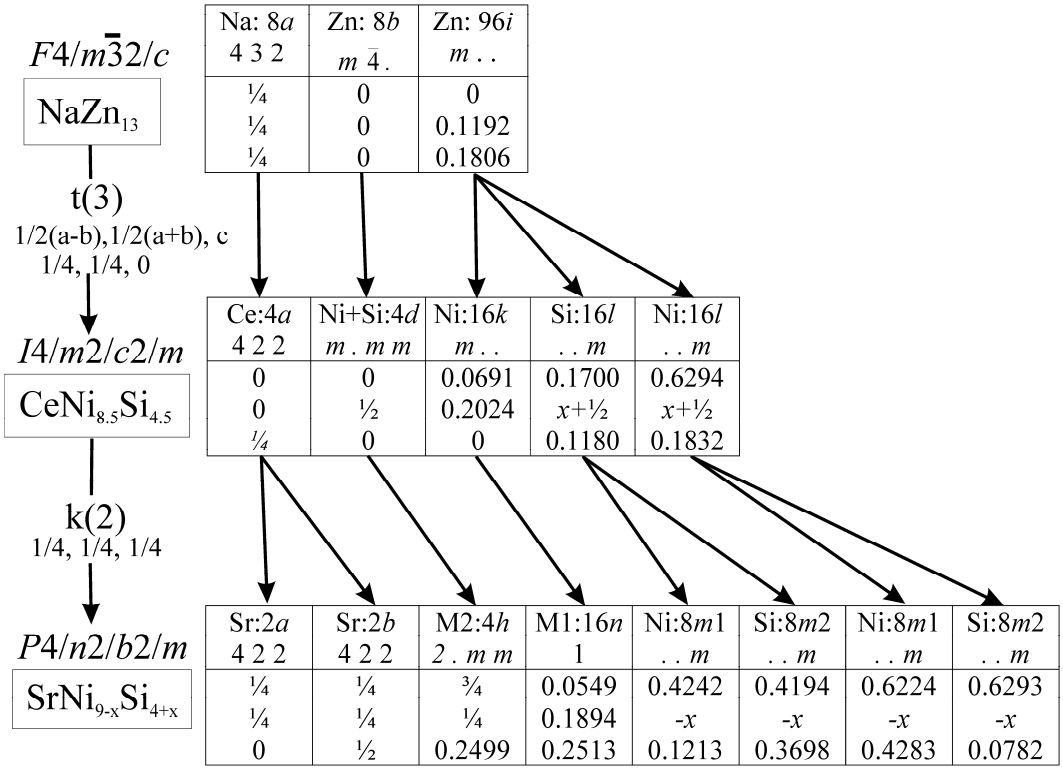

Figure 6: Group-subgroup scheme in Bärnighausen formalism for $NaZn_{13}$ (*Fm*-3*c*) to $SrNi_{9-x}Si_{4+x}$ (*P*4/*nbm*).

Table 6a: X-Ray single crystal and powder diffraction data for $SrNi_{9-x}Si_{4+x}$ (x=2.7) and $SrNi_{5.5}Si_{6.5\ \ 1}$ standardized with program *Structure Tidy* [31]. (Anisotropic displacement parameters [in $10^2 nm^2$]). $SrNi_{5.5}Si_{6.5\ \ 1}$

Parameter/compound	**$SrNi_{9-x}Si_{4+x}$ (x=2.7)**	**$SrNi_{5.5}Si_{6.5\ \ 1}$**
	SC	XPD
Prototype	$SrNi_{9-x}Si_{4+x}$	$SrNi_{9-x}Si_{4+x}$
Space group	*P4/nbm*	*P4/nbm*
Composition, EMPA at.%	$Sr_{7.1}Ni_{50.7}Si_{40.2}$	$Sr_{7.1}Ni_{46.3}Si_{46.5}$
a ; c [nm], Ge standard	0.78998(3); 1.1337(2)	0.78528(5); 1.1213(1)
Reflections measured	$595 \geq 4\sigma(F_o)$ of 929	219
Θ range	$2 \leq 2\Theta \leq 70$; 250 sec/frame	$8 \leq 2\Theta \leq 100$
Total number of frames	397; 9 sets	
Number of variables	47	34
Mosaicity	0.62	$R_F = \Sigma\|F_o-F_c\|/\Sigma F_o = 0.074$
$R_F^2 = \Sigma\|F_o^2-F_c^2\|/\Sigma F_o^2$	0.036	$R_I = \Sigma\|I_o-I_c\|/\Sigma I_o = 0.084$
R_{Int}	0.079	$R_{wP}=[\Sigma w_i\|y_{oi}-y_{ci}\|^2/\Sigma w_i\|y_{oi}\|^2]^{½}=0.048$
wR2	0.086	$R_P = \Sigma\|y_{oi}-y_{ci}\|/\Sigma\|y_{0i}\|=0.034$
GOF	1.008	$R_e = [(N-P+C)/\Sigma w_i y^2_{oi})]^{½} = 0.017$
Extinction	0.000	$\chi^2 = (R_{wP}/R_e)^2 = 7.78$
Residual density $e^-/Å^3$; max; min	1.24; -1.66	-
Atom parameters		
Sr1 in 2*a* (1/4, 1/4, 0); Occ.	1.01(2)	-
$U_{11}=U_{22};U_{33}$ / B_{iso}	0.0081(3); 0.0082(4)	1.4(1)
Sr2 in 2*b* (1/4, 1/4, 1/2); Occ.	1.00(1)	-
$U_{11}=U_{22};U_{33}$ /B_{iso}	0.0083(3); 0.0087(4)	0.6(2)
M1 in 16n (x, y, z); x, y, z	0.05489(8), 0. 18943 (8), 0.25131(6)	0.0518 (3), 0.1913 (3), 0.2511(3)
U_{11}; U_{22}	0.0141(3); 0.0099(3)	B_{iso} =1.03(6)
U_{33}; U_{23}	0.0131(3); 0.0002(3)	-
U_{13}; U_{12}	0.0018(3); 0.0024(2)	-
Occ.	0.493(3)Ni + 0.507(3)Si	0.381(2)Ni + 0.619(2)Si
Ni1 in 8*m* (*x, -x, z*); *x, z*; Occ.	0.42424(6), 0.12135(7); 0.99(2)	0.4186(4), 0.1268(3)
$U_{11}=U_{22};U_{33}$	0.0132(2); 0.0229(4);	B_{iso} =2.59(7)
$U_{23}= -U_{13};U_{12}$	0.0021(2); -0.0023(3)	
Si1 8*m* (*x, -x, z*); *x, z*; Occ.	0.4194(1), 0.3698(1); 1.01(2)	0.4194(7), 0.3682(5)
$U_{11}=U_{22};U_{33}$	0.0129(4); 0.0135(7)	B_{iso}= 1.39(9)
$U_{23}=-U_{13};U_{12}$	0.0029(4); -0.0053(5)	
Ni2 in 8*m* (*x, -x, z*); *x, z*; Occ.	0.62236(6), 0.42835(7); 0.99(2)	0.6260(4), 0.4257(3)
$U_{11}=U_{22};U_{33}$	0.0139(3); 0.0167(4)	B_{iso} =2.43(7)
$U_{23}= -U_{13};U_{12}$	0.0006(3); -0.0013(3)	
Si2 in 8*m* (*x, -x, z*); *x, z*; Occ.	0.6293(1), 0.0782(1); 1.01(2)	0.6256(6), 0.0861(5)
$U_{11}=U_{22};U_{33}$	0.0159(4); 0.0177(8)	B_{iso} =1.40(9)
$U_{23}= -U_{13};U_{12}$	0.0005(4); 0.0034(6)	-
M2 in 4h (¾, ¼, *z*); *z*	0.2499(2)	-
$U_{11}=U_{22};U_{33}$; U_{12}	0.0138(5); 0.0127(8); -0.0008(6)	-
Occ.	0.320(4)Ni + 0.680(4)Si	□

Table 6b: Interatomic distances for $SrNi_{9-x}Si_{4+x}$ (x=2.7) (standard deviation >0.00005).

Sr1-	-8Ni1	0.32145		-Si1	0.25289
	-8M1	0.32497		-Ni2	0.25687
	-8Si1	0.32868		-Ni2	0.25858
Sr2-	-8Ni2	0.32273		-M1	0.27305
	-8Si2	0.32685		-Sr1	0.32497
	-8M1	0.32769		-Sr2	0.32769
Ni1-	-2Si1	0.23373	M2-	-2Si1	0.23303
	-2Si1	0.24625		-2Si2	0.23687
	-M2	0.24777		-2Ni2	0.24327
	-2M1	0.25053		-4M1	0.24565
	-2Ni1	0.25901		-2Ni1	0.24777
	-Ni1	0.28539	Si1-	-M2	0.23303
	-2Sr1	0.32145		-2Ni1	0.23373
Ni2-	-M2	0.24327		-2Ni1	0.24625
	-Si2	0.23404		-2M1	0.24998
	-2Si2	0.24177		-2M1	0.25289
	-M2	0.24331		-Ni2	0.28183
	-2M1	0.25687		-2Sr1	0.32868
	-2M1	0.25858	Si2-	-Ni2	0.23404
	-Si2	0.23448		-Ni2	0.23448
	-2Sr2	0.32272		-M2	0.23687
M1-	2M1	0.22830		-2Ni2	0.24177
	-M2	0.24565		-2M1	0.24915
	-Si1	0.24998		-2Si1	0.26032
	-Si2	0.24915		-Si1	0.26952
	-Ni1	0.25053		-2Sr2	0.32685

Atom arrangements in body centred and primitive tetragonal unit cells along b- axis and along c-axis are compared in Figure 7 and 8. It is easy to see that the atom arrangement in both structures is similar and a primitive super cell is the result of the splitting of two 16l sites. In going from *I*4/*mcm* to *P*4/*nbm* the mirror plane perpendicular to the 4-fold axis is changed to a diagonal glide plane n normal to the c-axis (see Figure 8). The 4-fold axis with inversion centre located at Sr (4*a*) in *I*4/*mcm* changes to a 4-fold axis located at Sr atoms (2a and 2b) and $\bar{4}$ located at M2 (4h) (origin choice 2 dotted) while the inversion centre stays (Figure 8a). Polyhedra around Sr and metal atoms are similar to those in $CeNi_{8.5}Si_{4.5}$-type with little distortion Figure 7b and c.

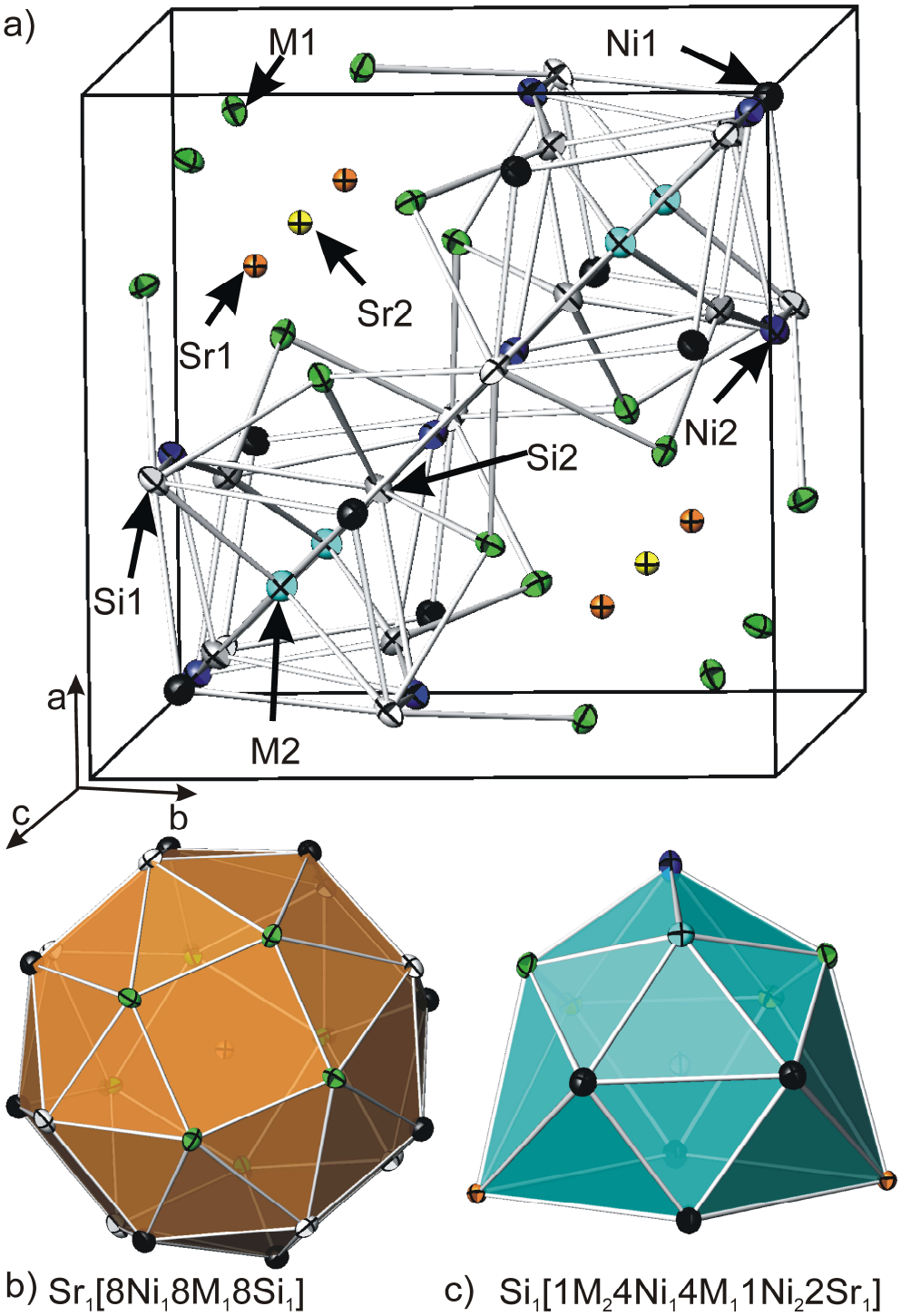

Figure 7: a) Crystal structure of $SrNi_{9-x}Si_{4+x}$ (space group *P*4/*nbm*) in three-dimensional view. Anistropic thermal displacements from single crystal refinement. b) Polyhedra around Sr1 c) Polyhedra around Si 1

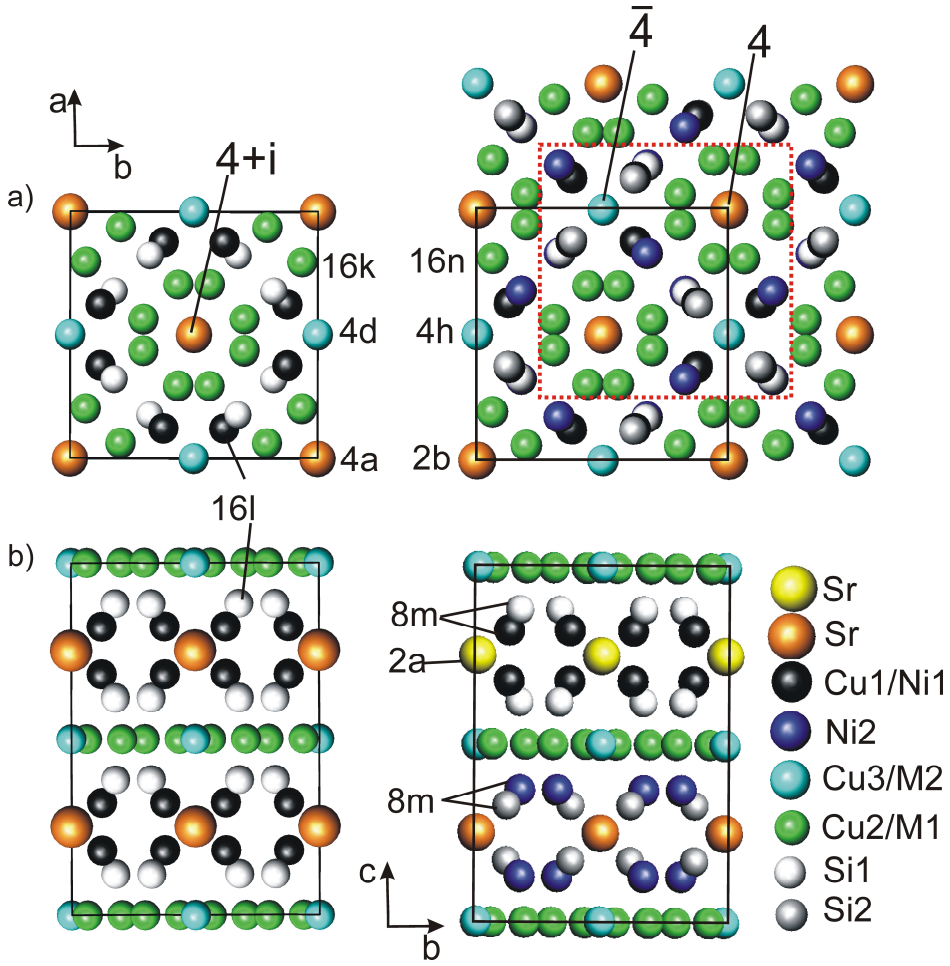

Figure 8: Comparison of atom arrangements in $SrCu_{9-x}Si_{4+x}$ (space group *I*4/*mcm*) and $SrNi_{9-x}Si_{4+x}$ (space group *P*4/*nbm*) along c-axis a) and along a-axis b).

6.4 Conclusion

Phase relations in the Sr-poor regions of the systems Sr–Ni–Si (at 900 °C) and Sr–Cu–Si (at 800 °C) were derived by x-ray diffraction, LOM and EPMA. Two new ternary compounds τ_2-$SrNiSi_3$ ($BaNiS_{n3}$-type), τ_3-$SrNi_{9-x}Si_{4+x}$ (own type) along with previously reported τ_1-$Sr(Ni_xSi_{1-x})_2$ (AlB_2-type) take part in the phase equilibria in Sr–Ni–Si. The structure of τ_3 $SrNi_{9-x}Si_{4+x}$ (own type) was solved by x-ray single crystal analysis and was found to be a primitive tetragonal variant of $NaZn_{13}$-type with S. G. *P*4/*nbm*. At higher Si-concentration defects are formed in the structure of $SrNi_{9-x}Si_{4+x}$. Three already known ternary compounds τ_1-$Sr(Cu_xSi_{1-x})_2$ (AlB_2-type), τ_2-$SrCu_{2-x}Si_{2+x}$ (x=0.16-0.44; $ThCr_2Si_2$-type), τ_3-$SrCu_{9-x}Si_{4+x}$($CeNi_{8.5}Si_{4.5}$-type) in Sr–Cu–Si were confirmed. Compositional polymorphism was observed for $SrCu_{13-x}Si_x$ ($1.8 \leq x \leq 4$) ($NaZn_{13}$-type) and $SrCu_{9-x}Si_{4+x}$

($0 \leq x \leq 1.0$) ($CeNi_{8.5}Si_{4.5}$-type). Structural details were provided for numerous new compounds in the related systems Ba-M-X (M=Pd, Pt, Cu, Zn, Cd, Rh, Ir; X=Si, Ge).

6.5 References

[1] N. Melnychenko-Koblyuk, A. Grytsiv, P. Rogl, M. Rotter, E. Bauer, G. Durand, H. Kaldarar, R. Lackner, H. Michor, E. Royanian, M. Koza, G. Giester, Phys. Rev. B: Condens. Matter Mater. Phys. 14 (2007) 76.

[2] N. Melnychenko-Koblyuk, A. Grytsiv, P. Rogl, M. Rotter, R. Lackner, E. Bauer, L. Fornasari, F. Marabelli, G. Giester, Phys. Rev. B: Condens. Matter Mater. Phys. 76, (2007) 195124.

[3] N. Melnychenko-Koblyuk, A. Grytsiv, , P. Rogl, E. Bauer, , R. Lackner, E. Royanian, M. Rotter, , G. Giester, J. Phys. Soc. Jap. 77 (2008) 54.

[4] A. Grytsiv, N. Melnychenko-Koblyuk, N. Nasir, P. Rogl, A. Saccona, H. Schmid, Int. J. Mat. Res. 100 (2009) 189.

[5] N. Melnychenko-Koblyuk, A. Grytsiv, L. Fornasari, H. Kaldarar, H. Michor, F. Rohrbacher, M. Koza, E. Royanian, E. Bauer, P. Rogl, M. Rotter, H. Schmid, F. Marabelli, A. Devishvili, M. Doerr, G. Giester, J. Phys. Condens. Matter 19 (2007) 26.

[6] N. Melnychenko-Koblyuk, A. Grytsiv, St. Berger, H. Kaldarar, H. Michor, F. Roehrbacher, E. Royanian, E. Bauer, P. Rogl, H. Schmid, G. Giester, J. Phys. Condens. Matter 19 (2007) 046203/1.

[7] N. Melnychenko-Koblyuk, A. Grytsiv, P. Rogl, H. Schmid, G. Giester, J. Solid State Chem. 182 (2009) 1754.

[8] A. Grytsiv, X.-Q. Chen, N. Melnychenko -Koblyuk, P. Rogl, E. Bauer, G. Hilscher, H. Kaldarar, H. Michor, E. Royanian, R. Podloucky, M. Rotter, G. Giester, J. Phys. Soc. Jap. 77 (2008) 121.

[9] E. Bauer, R.T. Khan, H. Michor, E. Royanian, A. Grytsiv, N. Melnychenko-Koblyuk, P. Rogl, D. Reith, R. Podloucky, E.W. Scheidt, W. Wolf, M. Marsman, Phys Rev.B: Condens. Matter Mater. Phys. 80 (2009) 064504.

[10] A. Grytsiv, P. Rogl, E. Bauer, H. Michor, E. Royanian, G. Giester, Intermetallics 18 (2010) 173.

[11] N. Nasir, N. Melnychenko-Koblyuk, A. Grytsiv, P. Rogl, E. Bauer, E. Royanian, H. Michor, G. Hilscher, G. Giester, Intermetallics 17 (2009) 471.

[12] Nonius Kappa CCD Program Package COLLECT, DENZO, SCALEPACK, SORTAV, Nonius Delft, The Netherlands, 1998.

[13] G. M. Sheldrick, SHELXL-97, Program for Crystal Structure Refinement, University of Go¨ttingen, Germany, 1997 (Windows version by McArdle, National University of Ireland, Galway).

[14] W. Rieger, E. Parthe, Monatsh.Chem. 100 (1969) 439.

[15] B. Eisenmann, N. May, W. Müller, H. Schäfer. A. Weiss, J. Winter and G. Ziegleder, Z. Naturforsch, 25b (1970) 1350.

[16] C. Kranenberg, A. Mewis, Z. Anorg. Allg. Chem. 629 (2003) 1023.

[17] W. Dörrscheidt, H. Schäfer, J. Less-Common Met. 78 (1981) 69.

[18] H. Bärnighausen, Commun. Math. 9 (1980) 139.

[19] H. Bärnighausen, U. Müller, Symmetriebeziehungen zwischen den Raumgruppen als Hilfsmittel zur straffen Darstellung von Strukturzusammenhängen in der Kristallchemie, University of Karlsruhe and University /GH Kassel, 1996.

[20] W. Dörrscheidt, H. Schäfer, J. Less-Common Met. 58 (1978) 209.

[21] R. Demchyna, Yu. Prots, W. Schnelle, U. Burkhardt, U. Schwarz, Z. Kristallogr. NCS 221 (2006) 109.

[22] Pauling File Binaries Edition, Version 1.0, ASM Intl, Materials Park, OH, USA, release 2002/1.

[23] G. Just, P. Paufler, J. Alloys Compd. 232 (1996) 1.

[24] M. Wendorff, C. Röhr, J. Alloys Compd. 421 (2006) 24.

[25] B. Saparov, S. Bobev, J. Alloys Compd. 463 (2008) 119.

[26] V. Zaremba, I. R. Muts, Rolf-Dieter Hoffman, R. Pöttgen, Z. Anorg. Allg. Chem. 629 (2003) 2330.

[27] Y. M. Kalychak, V. Zaremba, Y. V. Galadzhun, K. Y. Miliyanchuk, Rolf-Dieter Hoffmann, R. Pöttgen, Chem. Eur. J. 7 (2001) 5343.

[28] Rolf-Dieter Hoffmann, I. Muts, V. Zaremba, R. Pöttgen, Z. Kristallogr. 224 (2009) 446.

[29] D. M. Proserpio, G. Artioli, S. Mulley, G. Chacon, C. Zneng, Chem. Mater. 9 (1997) 1463.

[30] O. I. Bodak, E. I. Gladyshevskii, Dopovidi Akademii Nauk Ukr.'s Koi RSR Seryia A: Fiziko-Tekhnichni ta Matermatichni Nauki 30 (1968) 944.

[31] E. Parthe´, L. Gelato, B. Chabot, M. Penzo, K. Cenzual, R. Gladyshevskii, TYPIX Standardized Data and Crystal Chemical Characterization of Inorganic Structure Types, Springer, Berlin, Heidelberg, 1994.

7 Crystal Structure of $EPCo_{5-x}Ge_9$ (EP≡Sr, Ba, Eu)

7.1 Introduction

As part of a systematic investigation of T-metal substitution in thermoelectric clathrates we have recently studied the phase relations involving the clathrate type I and clathrate type IX phases, $Ba_8T_xGe_{46-x-yy}$ and $Ba_6T_xGe_{25-x}$, with T = Mn, Fe, Co [1]. Particularly the system Ba-Co-Ge has been studied earlier [2, 3] on alloys $Ba_8Co_xGe_{46-x}$ (x = 0, 4, 6) annealed at 700°C and two superconducting transitions (type II superconductors) were reported for x=0 at T_{SC}=10 K and 4 K, but Co-doping ($Ba_8Co_xGe_{46-x-yy}$; x = 4, 6) was said to suppress the 4 K transition completely and to reduce the T_{SC} from 10 to 7 K [2, 3]. Investigated $Ba_8Co_xGe_{46-x}$ alloys, however, were claimed to be multi-phase ((Ge) + unknown phase for x=0 and (Ge) + $CoGe_2$ + unknown phase for x= 4 and 6), but neither contained a clathrate phase nor $BaGe_2$ (the latter phase superconducts below T_{SC}=4.93 K). Our isothermal section covering phase equilibria at 800°C around the two clathrate phases in the Ge-rich region of the Ba-Co-Ge system showed the existence of only one ternary compound labelled τ_1 at a composition $Ba_{6.79}Co_{30.12}Ge_{63.09}$ (from EMPA in at. %) without a sizeable homogeneity region [1]. It is therefore the aim of the present paper (i) to elucidate the crystal structure of the τ_1-phase and to investigate formation isotypic compounds with Sr and Eu.

7.2 Experimental

Alloys with a weight of 1-2 grams were prepared by argon arc-melting (weight loss less than 0.1 %) on a water-cooled copper hearth in Ti-gettered argon from elemental ingots with minimal purity of 99.9 mass %. A single crystal fragment, suitable for X-ray structure determination was broken from an arc-melted sample with nominal composition $Ba_{7.0}Co_{30.4}Ge_{62.6}$, which had been vacuum-sealed in a quartz tube and annealed for 14 days at 700-900°C prior to quenching in cold water. Inspection on an AXS-GADDS texture goniometer assured high crystal quality, unit cell dimensions

and Laue symmetry of the specimens prior to X-ray intensity data collection on a four-circle Nonius Kappa diffractometer equipped with a CCD area detector and employing graphite monochromated MoKα radiation (λ = 0.071073 nm). Orientation matrix and unit cell parameters for a cubic system were derived using the program DENZO [4]. No absorption correction was necessary because of the rather regular crystal shape and small dimensions of the investigated specimen. The structure was solved by direct methods and refined with the SHELXL-97 and SHELXS-97 programs [5].

X-ray examination of polycrystalline materials was performed at room temperature in a Guinier-Huber X-ray camera with an Image Plate recording system ($CuK_{\square 1}$) employing an internal standard of 99.9999 mass% pure Si (a_{Si} = 0.5431065 nm). Quantitative Rietveld refinement of single-phase samples was performed by means of the FULLPROF program [6]. As cast and annealed samples were polished via standard procedures and have been examined by optical metallography and scanning electron microscopy (SEM). Specimen composition was determined by Electron Probe Microanalysis (EPMA) on a Carl Zeiss DSM 962 instrument equipped with a link EDX system operated at 20kV and 60 μA.

7.3 Results and Discussion

Micrographs show that the ternary compound $BaCo_{5-x}Ge_9$ (τ_1) forms incongruently. In the cast alloy $Ba_{7.0}Co_{30.4}Ge_{62.6}$ (see Fig.1) primary crystals of CoGe (black phase) are surrounded by the gray phase τ_1; the last portion of liquid solidifies as clathrate I (κ_I = white phase). After annealing at 800°C the sample is a single-phase ternary compound $BaCo_{4.7}Ge_9$ (compare inset in Fig.1).

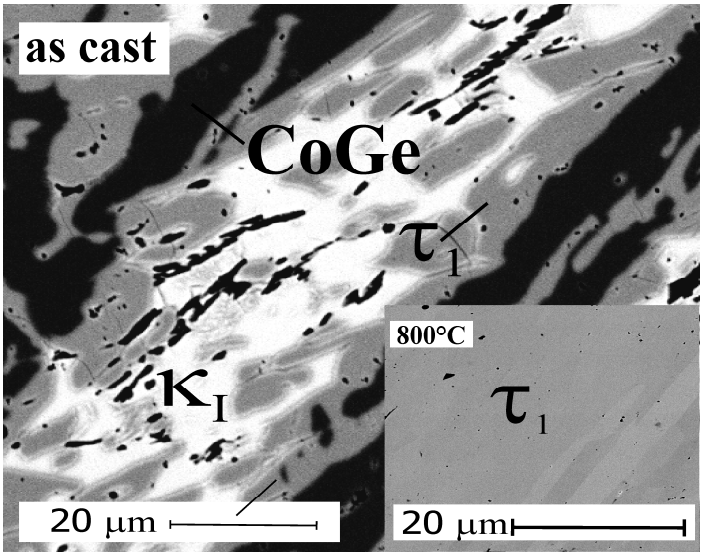

Figure 1. Micrograph of alloy $Ba_{7.0}Co_{30.4}Ge_{62.6}$; as cast (main BSE-image), annealed at 800°C (inset)

7.3.1 Crystal structure of $BaCo_{5-x}Ge_9$ (x=0.29).

Systematic extinctions (hk0) extinct for h=2n+1 and (0kl) extinct for k+ℓ=2n+1, lead to *Pnma*, as the highest symmetric space group, for which determination of the atom arrangement was successful via direct methods revealing 15 independent atom sites in the unit cell. Search for higher symmetry (program PLATON) did not retrieve any further symmetry elements. Differences in X-ray scattering powers of Co- and Ge-atoms are sufficiently large to elucidate atom site occupation. Including Co5-atoms, for which a partial occupation (71%) was obvious from the large atom displacement factor (ADP), a fully ordered atom arrangement is obtained, which refines successfully to low residual values R_{F2} = 0.025 at very small residual electron densities < |2800| e^-/nm^3 employing anisotropic thermal displacement factors for all atoms. Occupancies of all crystallographic sites were refined but except for Co5 did not reveal any significant deviations from full occupation. Refinement yields a formula $BaCo_{4.7}Ge_9$ ($Ba_{6.8}Co_{32.0}Ge_{61.2}$ in at.%) in good agreement with single-phase bulk samples for which EMPA gives a composition in at.% $Ba_{6.8}Co_{30.1}Ge_{63.1}$ (= $BaCo_{4.44}Ge_{9.27}$). Results of the structure determination are listed in Table 1. The crystal structure of $BaCo_{4.7}Ge_9$ is presented in Figure 2 in a three-dimensional view along the [001]-axis. As a main structural feature two infinite walls per unit cell are formed by non-regular pentagonal prisms, which are stacked along their pentagonal

faces and linked along their lateral faces. The two walls with lateral faces parallel to the b-axis are running along the a-axis and are offset by a vector b/2. Pentagonal prism columns made of Ge-atoms – each prism centred by a Ba-atom – alternate with a similar pentagonal Ge-column, each pentagonal prism now centred by a Ge1-atom. Whereas the pentagonal prism is the co-ordination figure for the large Ba-atoms, the next nearest neighbours of Ge1 are three Co-atoms in planar coordination. The two walls (offset by a vector b/2) are linked by non-centred non-regular octahedra [Ge_4Co_2], which are all edge connected and form rows along the walls in b-direction. At the cell edges at 000 we see a set of nested polyhedra running parallel to the b-axis.

Coordination polyhedra in the structure are shown on Figure 3. Coordination figures around all Co atoms are very similar and can be described as distorted tetragonal antiprisms with one additional atom in case of Co1 and two additional atoms for Co2, Co3, Co4 and Co5. Similarities were also found for the coordination figures of Ge2, Ge3, Ge4, Ge5 and Ge8. In these cases next nearest coordination is formed by three cobalt atoms whilst seven germanium atoms are located at somewhat higher distance from the central atom (Table 1c).

The trend among the shortest interatomic distances in $BaCo_{4.7}Ge_9$, $d_{Ge3-Ge8}$ (0.2707 nm) > $d_{Co4-Co5}$ (0.2646 nm) > $d_{Co5-Ge8}$(0.2371 nm), suggests strong Co-Ge bonding (see Table 1c). As a consequence cobalt atoms in $BaCo_{4.7}Ge_9$ are exclusively coordinated by germanium next nearest neighbour atoms. Similarly the closest coordination figure of Ba does not include cobalt atoms. The distances $d_{Co-Ge} \approx 0.23$-0.24 nm observed in $BaCo_{4.7}Ge_9$ agree well with those reported for binary cobalt germanides: 0.234 nm for CoGe (CoGe- and FeSi structure types), 0.239 nm for Co_2Ge and Co_5Ge_7 (Co_2Si – and Co_5Ge_7- types, respectively) [7].

X-ray single crystal data for $BaCo_{4.7}Ge_9$ are confirmed by Rietveld refinement of X-ray powder diffraction intensities.

7.3.2 Isotypic {Sr,Eu}$Co_{5-x}Ge_9$ (x~0.3).

Indexing of the X-ray powder patterns of $SrCo_{5-x}Ge_9$ and $EuCo_{5-x}Ge_9$ in both cases was complete on the basis of an orthorhombic unit cell close to that established for $BaCo_{4.7}Ge_9$. Analysis of the X-ray intensities, systematic extinctions, and size of unit

cells suggest isotypism with the structure type of $BaCo_{4.7}Ge_9$. Only minor amounts of Ge as a secondary phase were encountered for both $\{Sr,Eu\}Co_{5-x}Ge_9$. Rietveld refinements confirm the isotypism among $\{Sr,Ba,Eu\}Co_{5-x}Ge_9$ and again reveal a partial occupation of the Co5-atom site (occ. = 0.7) as also determined for $BaCo_{4.72}Ge_9$. As a typical example of this family of compounds, the X-ray pattern and the corresponding Rietveld profile is shown in Fig. 4 for $EuCo_{4.7}Ge_9$.

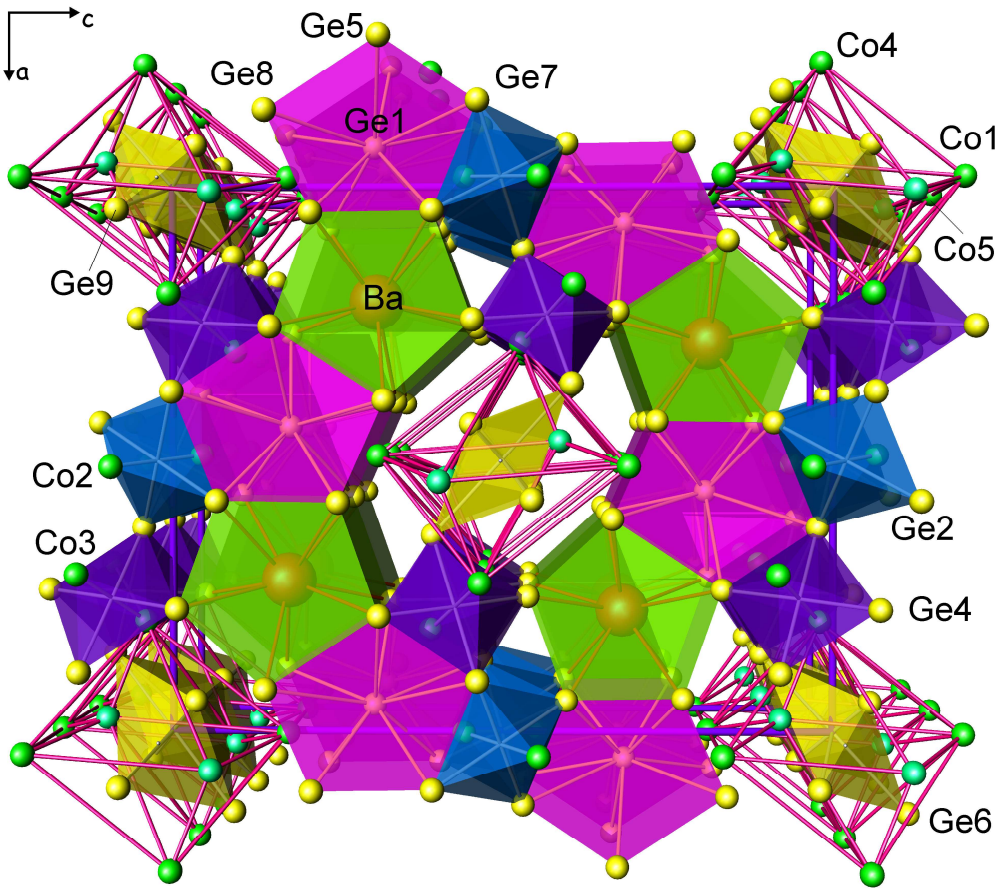

Figure 2. Crystal structure of $BaCo_{4.7}Ge_9$ in perspective view along the short axis *b*.

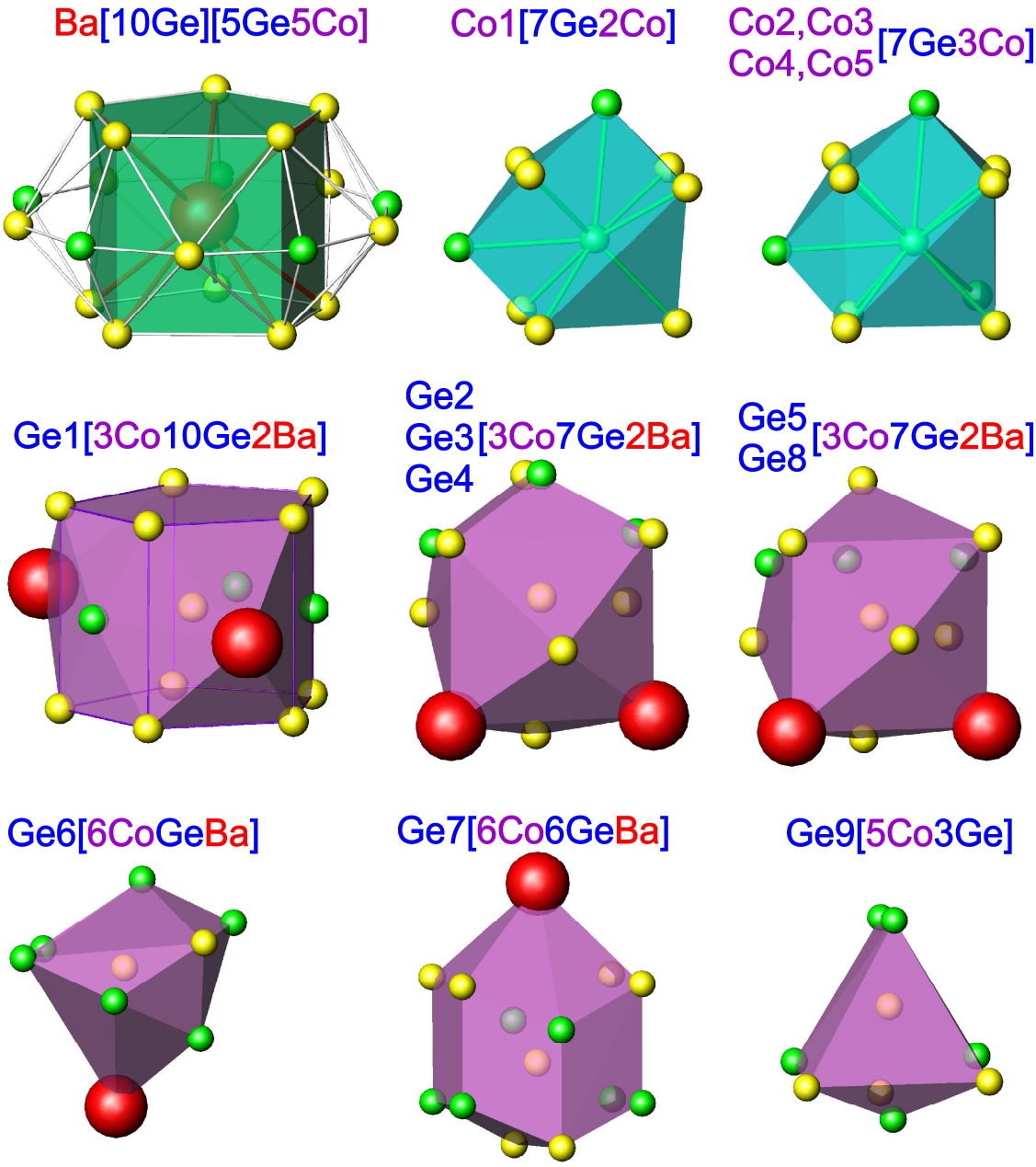

Figure 3. Coordination polyhedra in $BaCo_{4.7}Ge_9$.

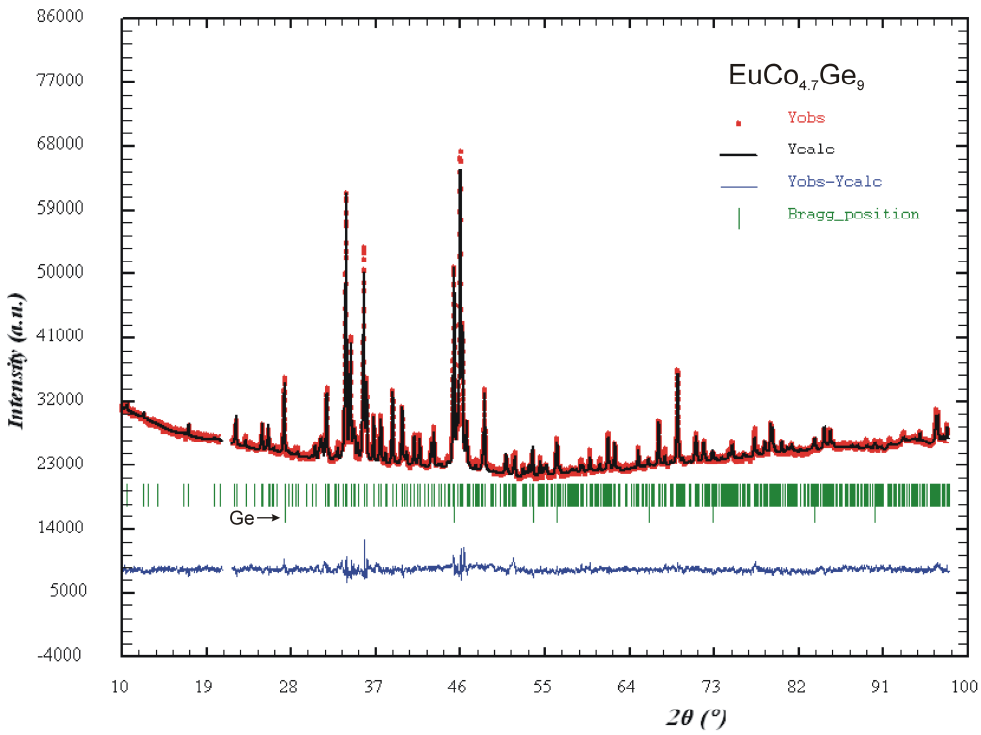

Figure 4. X-ray pattern and corresponding Rietveld profile for $EuCo_{4.7}Ge_9$.

Table 1a. X-Ray single crystal data for $BaCo_{4.7}Ge_9$ (standardized with program *Structure Tidy* [8]; room temperature data, redundancy >8); space group *Pnma*; No. 62.

Parameter/compound	**$Ba_7Co_{30}Ge_{63}$ [1)]**
Composition from EPMA	$Ba_{6.79}Co_{30.12}Ge_{63.09}$
Composition from refinement	$Ba_{6.80}Co_{32.04}Ge_{61.16}$
Formula from refinement	$BaCo_{4.7}Ge_9$
Crystal size	40x57x60 μm^3
a, *b*, *c* [nm]	1.3992(5) 0.40220(2) 1.6993(7)
a, *b*, *c* [nm], Si standard	1.39910(2) 0.40218(2) 1.69882(2)
μ_{abs} [mm^{-1}]	43.31
Data collection, 2Θ range(°);	2≤2Θ≤70
ω-scans, scan width 2°	150 sec/frame
Total number of frames & sets	671; 13 sets
Reflections in refinement	1893≥4σ(F_o) of 2357
Mosaicity	<0.52
Number of variables	93
$R_F^2 = \Sigma\|F_0^2-F_c^2\|/\Sigma F_0^2$	0.025
R_{Int}	0.069
wR2	0.076
GOF	1.108
Extinction (Zachariasen)	0.0011(1)
Residual density ē/nm^3;	max; min 2800; -1770

[1)] Nominal composition

Table 1b. Atom parameters for $BaCo_{4.7}Ge_9$. All atoms in site 4c (x,¼,z). (Atomic displacement parameters are given in $10^2 nm^2$.

Ba		**Co5**		**Ge5**	
occ.	1.00(1)	occ.	0.715(4)	occ.	1.00(1)
x	0.28381(2)	x	0.03441(8)	x	0.26671(5)
z	0.81550(2)	z	0.08683(7)	z	0.17254(4)
U_{11}	0.0104(2)	U_{11}	0.0086(5)	U_{11}	0.0181(3)
U_{22}	0.0068(2)	U_{22}	0.0105(6)	U_{22}	0.0075(3)
U_{33}	0.0085(2)	U_{33}	0.0096(5)	U_{33}	0.0092(3)
U_{13}	0.0003(1)	U_{13}	0.0025(4)	U_{13}	0.0046(2)
Co1		**Ge1**		**Ge6**	
occ.	1.00(1)	occ.	1.00(1)	occ.	1.00(1)
x;	0.00801(6)	x;	0.06051(5)	x	0.36531(4)
z	0.81696(5)	z	0.68755(4)	z	0.60199(4)
U_{11}	0.0075(3)	U_{11}	0.0097(3)	U_{11}	0.0062(3)
U_{22}	0.0067(3)	U_{22}	0.0165(3)	U_{22}	0.0113(3)
U_{33}	0.0069(3)	U_{33}	0.0066(3)	U_{33}	0.0103(3)
U_{13}	0.0003(3)	U_{13}	0.0012(2)	U_{13}	-0.0012(2)
Co2		**Ge2**		**Ge7**	
occ.	1.00(1)	occ.	1.00(1)	occ.	1.00(1)
x;	0.00906(6)	x	0.06756(5)	x	0.37886(4)
z	0.55522(5)	z	0.40340(4)	z	0.03223(4)
U_{11}	0.0063(3)	U_{11}	0.0086(3)	U_{11}	0.0063(3)
U_{22}	0.0078(4)	U_{22}	0.0069(3)	U_{22}	0.0094(3)
U_{33}	0.0073(3)	U_{33}	0.0145(3)	U_{33}	0.0097(3)
U_{13}	-0.0001(3)	U_{13}	0.0033(2)	U_{13}	0.0012(2)
Co3		**Ge3**		**Ge8**	
occ.	1.00(1)	occ.	1.00(1)	occ.	1.00(1)
x;	0.19554(6)	x	0.07045(5)	x	0.39399(5)
z	0.60504(5)	z	0.23042(4)	z	0.33498(4)
U_{11}	0.0061(3)	U_{11}	0.0105(3)	U_{11}	0.0085(3)
U_{22}	0.0076(4)	U_{22}	0.0074(3)	U_{22}	0.0094(3)
U_{33}	0.0074(3)	U_{33}	0.0120(3)	U_{33}	0.0203(3)
U_{13}	0.0004(3)	U_{13}	-0.0038(2)	U_{13}	0.0022(2)
Co4		**Ge4**		**Ge9**	
occ.	1.00(1)	occ.	1.00(1)	occ.	1.00(1)
x;	0.20983(6)	x	0.25490(5)	x	0.56534(5)
z	0.02859(5)	z	0.46058(4)	z	0.54550(4)
U_{11}	0.0072(3)	U_{11}	0.0131(3)	U_{11}	0.0129(3)
U_{22}	0.0071(3)	U_{22}	0.0070(3)	U_{22}	0.0221(4)
U_{33}	0.0079(3)	U_{33}	0.0080(3)	U_{33}	0.0155(3)
U_{13}	-0.0010(3)	U_{13}	-0.0012(2)	U_{13}	0.0073(3)

Table 1c. Interatomic distances for $BaCo_{4.7}Ge_9$; standard deviations less than 0.0003 nm.

Ba1 -	2Ge3 0.3208	Co4 -	1Ge7 0.2366	Ge3 -	2Co1 0.2428	Ge7 -	1Co2 0.2351
CN 10	2Ge8 0.3216	CN 10	2Ge4 0.2371	CN 12	1Co5 0.2491	CN 13	1Co4 0.2366
	2Ge4 0.3227		1Ge9 0.2381		1Ge8 0.2707		2Co2 0.2580
	2Ge5 0.3231		1Ge5 0.2572		1Ge5 0.2917		2Co3 0.2580
	2Ge2 0.3255		2Ge6 0.2589		1Ge2 0.2939		1Ge5 0.2854
Co1 -	1Ge1 0.2318		1Co5 0.2646		2Ge1 0.3057		1Ge2 0.2858
CN 9	1Ge6 0.2425		2Co3 0.2735		2Ge6 0.3100		2Ge4 0.3005
	2Ge3 0.2428		1Ba1 0.3765		2Ba1 0.3208		2Ge2 0.3066
	2Ge8 0.2453	Co5 -	1Ge9 0.2289*	Ge4 -	2Co4 0.2371		1Ba1 0.3961
	1Ge9 0.2470	CN 10	1Ge8 0.2371	CN 12	1Co3 0.2591	Ge8 -	1Co5 0.2371
	2Co5 0.2658		2Ge6 0.2465		1Ge2 0.2795	CN 12	2Co1 0.2453
	1Ba1 0.3859		1Ge3 0.2491		1Ge6 0.2856		1Ge3 0.2707
	1Ba1 0.3860		2Ge9 0.2546		1Ge8 0.2888		1Ge4 0.2888
Co2 -	1Ge7 0.2351		1Co4 0.2646		2Ge7 0.3005		2Ge9 0.2914
CN 10	1Ge1 0.2360		2Co1 0.2658		2Ge9 0.3222		1Ge1 0.3275
	2Ge2 0.2385	Ge1 -	1Co1 0.2318		2Ba1 0.3227		2Ge5 0.3285
	2Ge7 0.2580	CN 15	1Co3 0.2352		1Ge8 0.3285		2Ba1 0.3216
	1Ge2 0.2706		1Co2 0.2360	Ge5-	2Co3 0.2374	Ge9 -	1Co5 0.2289
	1Co3 0.2743		2Ge3 0.3057	CN 12	Co4 0.2572	CN 8	1Co4 0.2381
	2Co2 0.2762		2Ge2 0.3105		Ge7 0.2854		1Co1 0.2470
	1Ba1 0.3841		2Ge5 0.3155		Ge3 0.2917		2Co5 0.2546
Co3 -	1Ge1 0.2352		2Ge7 0.3425		2Ge6 0.2982		2Ge8 0.2914
CN 10	2Ge5 0.2374		2Ge8 0.3275		2Ge1 0.3155		1Ge6 0.2959
	1Ge6 0.2376		1Ba1 0.3806		2Ba1 0.3231		1Ba1 0.3862
	2Ge7 0.2580		1Ba1 0.3872	Ge6 -	1Co3 0.2376		
	1Ge4 0.2591	Ge2 -	2Co2 0.2385	CN 8	1Co1 0.2425		
	2Co4 0.2735	CN 12	1Co2 0.2706		2Co5 0.2465		
	1Co2 0.2743		1Ge4 0.2795		2Co4 0.2589		
	1Ba1 0.3783		1Ge7 0.2858		1Ge4 0.2856		
			1Ge3 0.2939		1Ba1 0.3802		
			2Ge7 0.3066				
			2Ge1 0.3105				
			2Ba1 0.3255				

*the short distance Co5-Ge9 is associated with partial occupancy of the Co5 site (occ.=0.71)

Table 2. X-Ray powder diffraction data for $EPCo_{5-x}Ge_9$ (EP is Sr, Ba, Eu) standardized with program *Structure Tidy* [8]. Space group *Pnma*. Room temperature data from image plate (8≤2Θ≤100), Cu $K_{\alpha 1}$ radiation.

Parameter/compound[1)]	**$Sr_7Co_{30}Ge_{63}$**	**$Ba_7Co_{30}Ge_{63}$**	**$Eu_7Co_{30}Ge_{63}$**
Formula from refinement	**$SrCo_{4.7}Ge_9$**	**$BaCo_{4.6}Ge_9$**	**$EuCo_{4.7}Ge_9$**
a ;b; c [nm], Si standard	1.39389(8); 0.39665(1); 1.67860(9)	1.39910(2) 0.40218(2); 1.69882(2)	1.3910(1); 0.39425(2); 1.6741(2)
Reflections measured	596	618	604
Number of variables	56	55	46
$R_F = \Sigma\|F_o-F_c\|/\Sigma F_o$	0.191	0.137	0.135
$R_I = \Sigma\|I_o-I_c\|/\Sigma I_o$	0.125	0.122	0.112
$R_{wP}=[\Sigma w_i\|y_{oi}-y_{ci}\|^2/\Sigma w_i\|y_{oi}\|^2]^{½}$	0.0140	0.0198	0.0131
$R_P = \Sigma\|y_{oi}-y_{ci}\|/\Sigma\|y_{0i}\|$	0.0104	0.0125	0.0097
$R_e = [(N-P+C)/\Sigma w_i y^2_{oi})]^{½}$	0.0047	0.0055	0.0063
$\chi^2 = (R_{wP}/R_e)^2$	8.97	12.8	4.93
EP in 4c (x,¼,z): x, z	0.2846(3), 0.8148(3)	0.2854(2), 0.8165(2)	0.2834(2), 0.8130(3)
B_{iso} (10^2 nm^2)	0.9(1)	1.3(7)	2.4(7)
Co1 in 4c (x,¼,z): x, z	0.0079(5), 0.8184(6)	0.0086(5), 0.8157(8)	0.0056(5), 0.8222(6)
B_{iso} (10^2 nm^2)	1.0(2)	0.5(2)	0.49(6)
Co2 in 4c (x,¼,z): x, z	0.0125(7), 0.5547(5)	0.0148(7), 0.05511(6)	0.0123(6), 0.5559(5)
B_{iso} (10^2 nm^2)	1.6(3)	0.7(3)	0.49(6)
Co3 in 4c (x,¼,z): x, z	0.1936(5), 0.6039(4)	0.1978(7), 0.6024(5)	0.1927(6), 06072(4)
B_{iso} (10^2 nm^2)	0.7(2)	1.1(2)	0.49(6)
Co4 in 4c (x,¼,z): x, z	0.209(6), 0.0296(4)	0.2103(7), 0.0265(4)	0.2093(6), 0.0319(4)
B_{iso} (10^2 nm^2)	1.7(2)	0.6(2)	0.49(6)
Co5 in 4c (x,¼,z): x, z	0.022(1), 0.0812(8)	0.029(1), 0.0874(9)	0.0296(9), 0.0933(7)
B_{iso} (10^2 nm^2); occ.	0.9(4); 0.7	1.2(5); 0.6	0.49(6); 0.7
Ge1 in 4c (x,¼,z): x, z	0.0632(4), 0.6917(5)	0.0615(4), 0.6919(5)	0.0620(4), 0.6934(4)
B_{iso} (10^2 nm^2)	1.3(2)	1.5(2)	1.5(4)
Ge2 in 4c (x,¼,z): x, z	0.0710(4), 0.3976(3)	0.0684(6), 0.4051(4)	0.0748(5), 0.4015(4)
B_{iso} (10^2 nm^2)	1.0(2)	2.0(2)	1.5(4)
Ge3 in 4c (x,¼,z): x, z	0.0733(4), 0.2300(3)	0.0721(5), 0.2325(4)	0.0732(5), 0.2310(4)
B_{iso} (10^2 nm^2)	0.9(2)	1.3(2)	1.5(4)
Ge4 in 4c (x,¼,z): x, z	0.2555(4), 0.4572(3)	0.2546(4), 0.4576(4)	0.2512(4), 0.4539(4)
B_{iso} (10^2 nm^2)	0.9(2)	1.2(2)	1.5(4)
Ge5 in 4c (x,¼,z): x, z	0.2668,(3), 0.1794(4)	0.2688(4), 0.1741(4)	0.2695(3), 0.1829(5)
B_{iso} (10^2 nm^2)	0.9(1)	0.7(1)	1.5(4)
Ge6 in 4c (x,¼,z): x, z	0.3643(5), 0.6026(3)	0.3694(6), 0.6065(4)	0.3674(5), 0.5982(4)
B_{iso} (10^2 nm^2)	1.1(2)	1.7(2)	1.5(4)
Ge7 in 4c (x,¼,z): x, z	0.3802(5), 0.0352(4)	0.3770(5), 0.0375(4)	0.3780(5), 0.0341(5)
B_{iso} (10^2 nm^2)	1.1(2)	0.6(2)	1.5(4)
Ge8 in 4c (x,¼,z): x, z	0.3909(3), 0.3325(4)	0.3902(4), 0.3393(4)	0.3861(4), 0.3317(5)
B_{iso} (10^2 nm^2)	0.9(1)	1.0(2)	1.5(4)
Ge9 in 4c (x,¼,z): x, z	0.5654(5),0.5456(4)	0.5659(6), 0.5425(5)	0.5615(5), 0.5381(5)
B_{iso} (10^2 nm^2)	0.9(2)	1.0(2)	1.5(4)

[1]Nominal composition

7.4 Conclusion

A novel compound $BaCo_{5-x}Ge_9$ (x=0.29) has been synthesized by arc melting elemental ingots. The crystal structure of $BaCo_{4.7}Ge_9$ was determined from X-ray single crystal counter data as a unique structure type. Isotypic compounds were found for $SrCo_{5-x}Ge_9$ and $EuCo_{5-x}Ge_9$ (x~0.3).

References

[1] A. Grytsiv, N. Melnychenko-Koblyuk , N. Navida, P._Rogl , A. Saccone, H. Scmid, Int. J. Mater. Res. 100 (2009) 189.

[2] L. Yang, J. Ross, IEEE Trans.on Appl. Superconductivity 13 (2003)3047-50.

[3] Li. Yang, J. Ross, J. A. Larrea, E. Baggio-Saitovitch, Physica C 408-410: (2004) 869-71.

[4] Nonius Kappa CCD Program Package COLLECT, DENZO, SCALEPACK, SORTAV. Delft, The Netherlands: Nonius (1998).

[5] Sheldrick G M. SHELXL-97, Program for Crystal Structure Refinement. Windows version by McArdle, Natl. Univ. Ireland, Galway. Germany: University of Göttingen (1997).

[6] Roisnel T, Rodriguez-Carvajal J. Materials-Science-Forum 118 (2001) 378-81.

[7] Pauling File Binaries Edition, Version 1.0, Realize 2002/1, ASM Intl, Materials Park, OH, USA.

[8] Parthé E, Gelato L, Chabot B, Penzo M, Cenzual K, Gladyshevskii R. TYPIX Standardized Data and Crystal Chemical Characterization of Inorganic Structure Types. Berlin, Heidelberg: Springer – Verlag; 1994.

8 Phase Equilibria in Systems Ce-M-Sb (M = Si, Ge, Sn) and Superstructure $Ce_{12}Ge_{9-x}Sb_{23-x}$ (x=3.8±0.1)

8.1 Introduction

Following our general interest in phase equilibria in binary and ternary systems formed by rare earth (RE) with p^2 elements (Si, Ge, Sn) and/or with antimony, the ternary systems Ce-M-Sb were investigated as a logical continuation of our previous studies [1, 2, 3, 4]. Literature information on ternary compounds in these systems is available from [5-10] whereas phase relations were only reported for the Ce-Sb-Ge system for which an isothermal section at 400°C has been determined [6] revealing three ternary compounds: Ce_2GeSb_3 (super structure of $ThGe_2$-type), $Ce_5Ge_3Sb_2$ (unknown structure) and Ce_3GeSb (La_3GeIn-type). A subsequent investigation [7] of ternary rare earth germanium antimonides prepared from Sb-flux yielded the formation of isotypic compounds $RE_6Ge_{5-x}Sb_{11+x}$ (RE = La, Ce, Pr, Nd, Sm, Gd, Tb and Dy) crystallizing in the orthorhombic space group *Immm* ($La_6Ge_{2.8}Sb_{13.2}$ structure type). A detailed structural characterization by X-ray single crystal techniques was performed for $La_6Ge_{2.8(1)}Sb_{13.2(1)}$ and $Nd_6Ge_{4.3(1)}Sb_{11.7(1)}$ whereas for the other representatives of the $La_6Ge_{2.8}Sb_{13.2}$ structure type only lattice parameters were given [7].

Equilibrium phase diagrams Ce-Sn-Sb and Ce-Si-Sb have not been constructed so far, however, ternary compounds with composition $RESn_xSb_2$ (*Cmcm*, $LaSn_{0.75}Sb_2$ type, RE = La, Ce, Pr, Nd and Sm) were reported by [5, 10].

With respect to the limited information on phase equilibria in the ternary systems Ce-M-Sb (M=Si, Ge, Sn), and in view of the contradiction concerning the formation of $Ce_6Ge_{5-x}Sb_{11+x}$ [7] (not mentioned by [6]) the ternary systems Ce-M-Sb (M=Si, Ge, Sn) became the subject of our studies in the region $CeSb_2$-Sb-M (Ge, Sn, Si). Furthermore details will be elucidated for the structures of $Ce_6Ge_{5-x}Sb_{11+x}$ (found to be as superstructure with formula $Ce_{12}Ge_{9-x}Sb_{23+x}$ in current work) and $CeSn_xSb_2$.

8.2 Experimental

All samples, each of a total amount of ca. 1g, were prepared in an electric arc furnace under Ti-gettered argon with a non-consumable tungsten electrode on a water cooled copper heath. The purity of cerium was 99.5 mass%, the purity of antimony, germanium, silicon and tin was better than 99.9%. The alloys were remelted three times in order to achieve complete fusion and homogeneity. Weight losses were found to be less than 1-2 mass% and were attributed to most volatile elements Sb and Sn. Final decision on phase solubilities and extent of phases was based on Electron Probe Micro-Analyses (EPMA) data (see below). After melting, alloys were subjected to annealing in evacuated quartz tubes with subsequent quenching in water. Alloys for the systems Ce-Ge-Sb and Ce-Si-Sb were annealed at 400°C (30 days) and 600°C (14 days) and alloys for the Ce-Sn-Sb system were annealed at 200°C (90 days) and 400°C (14 days).

X-ray powder diffraction data from as-cast and annealed alloys were collected with a Guinier-Huber image plate system (Cu–$K_{\alpha 1}$ or Fe-$K_{\alpha 1}$; $8° < 2\theta < 100°$). Precise lattice parameters were calculated by least-squares fits to indexed 2θ-values employing Ge as internal standard (a_{Ge} = 0.565791 nm).

To determine the crystal structure of $Ce_{12}Ge_{9-x}Sb_{23+x}$, a single crystal fragment, suitable for X-ray structure determination was broken from an arc-melted sample with nominal composition $Ce_{25}Sb_{62.5}Ge_{12}$, which had been vacuum-sealed in a quartz tube and annealed for 14 days at 600°C prior to quenching in cold water. Inspection on an AXS-GADDS texture goniometer assured high crystal quality, unit cell dimensions and Laue symmetry of the specimens prior to X-ray intensity data collection on a four-circle Nonius Kappa diffractometer equipped with a CCD area detector and employing graphite monochromated MoKα radiation (λ = 0.071073 nm). Orientation matrix and unit cell parameters for an orthorhombic system were derived using the program DENZO [11]. No absorption correction was necessary because of the rather regular crystal shape and small dimensions of the investigated specimen. The structure was solved by direct methods and refined with the SHELXL-97 and SHELXS-97 programs [12].

The as cast and annealed samples were polished using standard procedures and were examined by optical metallography and scanning electron microscopy (SEM). Compositions for Ce-Si-Sb and Ce-Ge-Sb alloys were determined via EPMA on a Carl Zeiss DSM 962 equipped with a Link EDX system operated at 20 kV and 60 µA and on a Carl Zeiss EVO 40 equipped with a Pentafet Link EDX system operated at 20 kV. Binary compounds $CeSb_2$ and CeSb were used as EPMA standards. Difference between measured values and nominal compositions were found to be within 3 at. %.

Isothermal reaction temperatures were derived from thermal arrests determined in a calibrated Netzsch STA 409 PG/4/G Luxx Differential Scanning Calorimeter (DSC) employing a heating rate of 5K/min in Al_2O_3 crucibles under a stream of 6N argon. Prior to DTA the alloys were annealed at 520°C for 5-7 days.

8.3 Results and Discussions

8.3.1 Binary boundary systems

Information regarding the binary boundary systems was taken from [13] as well as from [14] on the existence of two modifications for $CeSb_2$. Crystallographic data for the relevant solid phases from literature and/or from our current work are summarized in Table 1. During our investigation we came across two conflicting situations concerning (i) the constitution of the Ge-Sb phase diagram, and (ii) the crystal structure of $Ce_{12}Ge_{9-x}Sb_{23+x}$.

8.3.1.1 The binary phase diagram germanium – antimony.

The binary Ge-Sb phase diagram as a result of our investigation is shown in figure 1a. It differs from the phase diagram given in [13] (compilation of data of various authors [15, 16, 17, 18, 19]) by two major facts: (i) eutectic composition (85.5 at. % Sb after [13] and 77.5 at. % Sb [this work]) and (ii) maximal solubility of Ge in Sb (no solubility after [13] and 6.3 at. % Ge at 592°C [this work]).

Six alloys Ge_xSb_{100-x} (for x = 2.5, 5, 10, 15, 22 and 30 at. %) were investigated in the as-cast state and after anneal at 400°C (45 days), 500°C (7 days), 520°C (7 days) and

580°C (2 days). The binary as-cast alloys with germanium content lower than 22 at. % show primary crystallization of antimony containing up to 6.3 at. % Ge as well as a eutectic with composition $Ge_{22.4}Sb_{77.6}$ (Figure 1b). Alloys with higher germanium content reveal primary grains of germanium and the eutectic at $Ge_{22.6}Sb_{77.4}$ (Figure 1c). The solubility of Ge in primary grains of Sb increases with the overall germanium content of the samples.

In order to determine the exact solubility limits of Ge in antimony at sub-solidus temperatures the sample Ge_5Sb_{95} was annealed at 580, 500 and 400°C for 2, 7 and 45 days, respectively. After annealing at 400 and 500°C the sample shows grains of Sb with a maximal solubility of 2.3 and 2.8 at. % Ge at 400 and 500°C, respectively. At 580°C the sample looks almost single phase with traces of (Ge) consistent with a maximal solubility of 4.1 at. % germanium in antimony. EPMA measurements recorded from grains of the Sb-based solution are plotted in Figure 1a in order to define the solubility range of (Sb). Compositional dependences of lattice parameters of (Sb) as shown in Figure 1d reveal some deviation from linearity in the higher solubility range. The maximum solubility of Ge in Sb (6.3 at. %) at the eutectic temperature (592°C) is measured by EPMA on big primary grains of Sb in the alloy with 22 at. % Ge and 78 at. % Sb; Figure 1b. The puzzling non-linearity of unit cell dimensions vs. composition for more than 5 at. % Ge can neither be explained by tiny Ge-precipitates in the ss-(Sb) (see inset in Fig. 1b) nor by a retrograde solidus of the (Sb)-phase (lattice parameters and EPMA data of hypo- and hyper-eutectic alloys are the same!). On Ge/Sb substitution the unit cell volume decreases (Fig. 1) in line with the difference of the atomic radii of the elements. Whilst the *a*-lattice parameter in Fig. 1 decreases the *c*-parameter increases resulting in an increase of the *c/a* ratio from 2.617 in pure antimony to 2.677 for $Ge_{6.3}Sb_{93.6}$. It is interesting to note that Sn/Sb substitution in the related Sn-Sb system also results in a decrease of the unit cell volume but at variance to the Ge-Sb system the c/a ratio decreases with increasing tin content. Accordingly the c/a-ratio for the rhombohedral Sn-Sb phases finally reaches an ideal value of 2.4495, which corresponds to the transformation from rhombohedral to cubic unit cells. The cubic structure is reported for Sb_2Sn_3 (NaCl-type [20]) and the high-pressure form of SbSn [21].

Despite a serious disagreement with literature data on the eutectic composition in the Ge-Sb system, the temperature of the invariant (eutectic) reaction was determined by DTA at 591.6°C in perfect agreement with literature data (592 °C, see [13]).

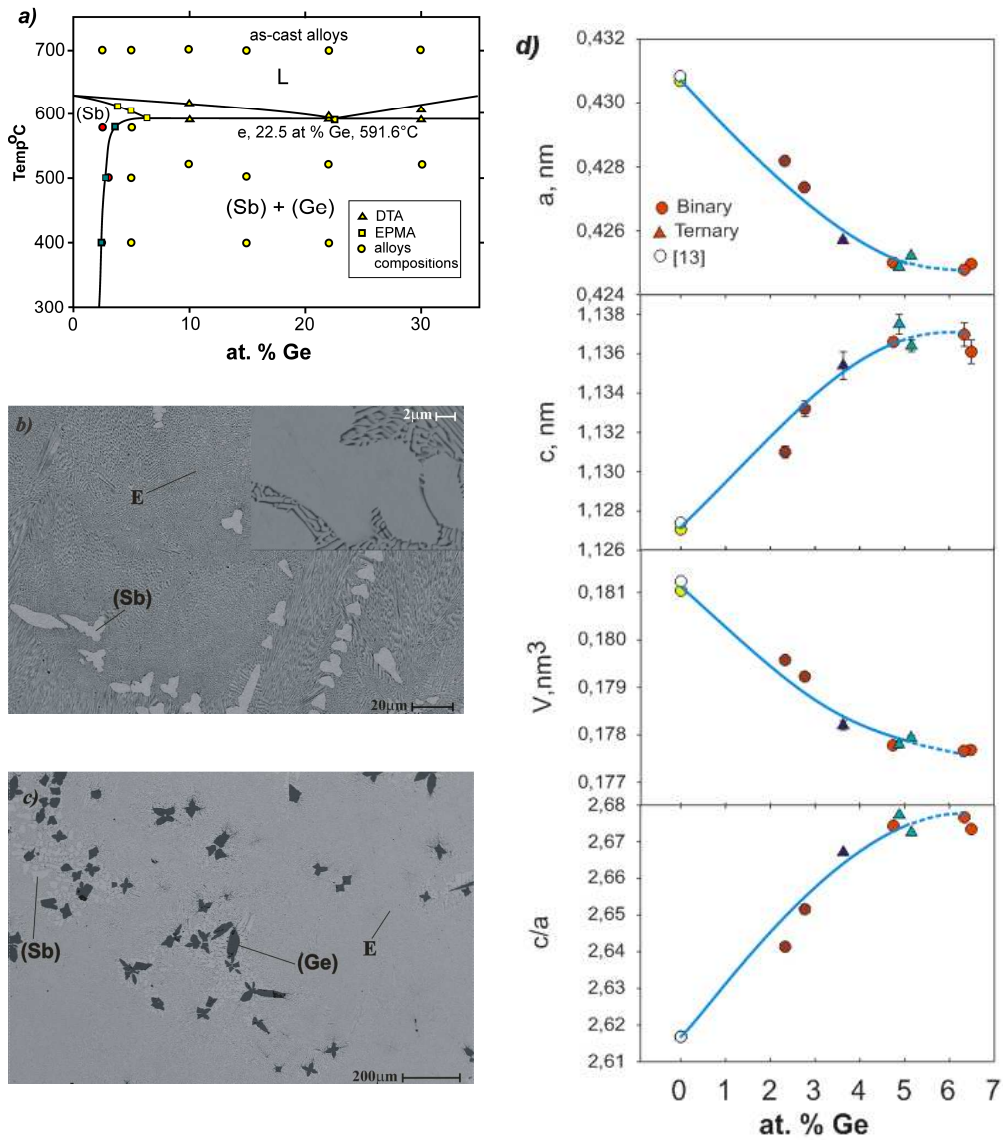

Figure 1. (a) Binary phase diagram Ge-Sb, selected microstructures of as-cast alloys: (b) 22 at.% Ge – Sb, (c) 30 at.% Ge – Sb and (d) compositional dependence of lattice parameters for Sb-based solid solution.

Table 1: Crystal structure data for relevant solid phases in the systems Ce-Sb-M (M=Ge, Si, Sn)

Phase	Pearson Symbol	Space group	Structure Type	Lattice Parameters			Reference
				a (nm)	b (nm)	c (nm)	
(Sb)	hR2	$R\bar{3}m$	As	a=0.45067	α=57.11		[13]
				0.43084	-	1.1274	[13]
(Si)	cF8	$Fd\bar{3}m$	C	0.54306	-	-	[13]
(Ge)		$Fd\bar{3}m$	C	0.56574	-	-	[13]
(Sn)	tI2	$I4_1/amd$	βSn	0.58318	-	0.31818	[13]
CeSb	cF8	$Fm\bar{3}m$	NaCl	0.6407			[26]
α-$CeSb_2$	oC24	*Cmca*	$SmSb_2$	0.6295(6)	0.6124(6)	1.821(2)	[26]
β-$CeSb_2$	-	-	unknown	-	-	-	[14]
SbSn	hR2	rhomb.	Distorted, NaCl	0.4326	-	1.0693	[24]
HP-SbSn	cF8		NaCl	0.5880(4)	-	-	[21][1]
Sb_2Sn_3	cF8	$Fm\bar{3}m$	NaCl	0.615	-	-	[20]
$CeSn_3$	cP4	$Pm\bar{3}m$	$AuCu_3$	0.47214(2)	-	-	[26]
$Ce_6Ge_{5-x}Sb_{11+x}$	oI48	Immm	$La_6Ge_{2.8}Sb_{13.2}$	0.42972(7)	1.0740(1)	2.6791(4)	[7]
$Ce_{12}Sb_{23+x}Ge_{9-x}$	oC184	C*222*	$Ce_{12}Sb_{23+x}Ge_{9-x}$	0.86075(2)	2.15154(4)	2.68227(5)	[this work] x =3.8±0.1
$CeSn_xSb_2$	oC28	Cmcm	$LaSn_{0.75}Sb_2$	0.4228(1)	2.2868(4)	0.4478(1)	[5] for x=1
				0.42370(1)	2.2834(1)	0.44594(2)	[this work] for x= 0.8

[1] unit cell dimension given at 7.5GPa

8.3.2 The crystal structure of $Ce_{12}Ge_{9-x}Sb_{23+x}$

The homogeneity region of $Ce_{12}Ge_{9-x}Sb_{23+x}$, established by EPMA, at 600°C extends from x = 3.3 to x = 4.2. Rietveld refinements performed for the structure model reported by [7] result in an acceptable fit of X-ray powder diffraction intensities. Furthermore, single crystal X-ray data reveal tiny additional reflections (Figure 2a) that were indexed on the basis of an orthorhombic supercell in direction a and b (2a=0.86075(2); 2b=2.15154(4); c=2.68227(5) nm). It should be emphasized, that all experimentally observed intensities are indexed on the basis of the fourfold supercell. Systematic extinctions (h+k=2n) consistent with Bravias *C*-type centring lead to the orthorhombic space groups *Cmmm*, *Cmm*2, *C*222 and $C2_12_12_1$. As all the space groups with higher symmetry had to be rejected because of bad R-values and high residual electron densities, direct methods were used to find a structure solution for space group *C*222. For the space group *C*222 (No. 21) 29 independent atom position were found. The constitution of the unit cell is still closely related to that reported by Lam [7] (see Figures 2b, c ,d). Owing to close Sb18 –Sb18 contacts (0.0624 nm), the occupancy of Sb18 required to be fixed at a theoretical maximum of 50%

(corresponds to Sb4 in [7]). Sites M1, M2, M3, M4 were at first assumed to be occupied only by Ge. Because of the large distances (0.27 nm – 0.28 nm), which are more reasonable for Ge-Sb distances, these sites were explored as a mixture of Ge and Sb, resulting in a considerable decrease in R-value and residual electron density. The occupancy of the site M5 was fixed at a maximum of 50% because of the short interatomic distance M5-M5 = 0.0839 nm, (corresponds to M2 in [7]). The structure refines successfully to a low reliability factor R_{F2} = 0.060 at small residual electron densities less than |5.7| e/ $Å^3$ employing anisotropic thermal displacement factors. Final refinement yields a formula $Ce_{12}Ge_{9-x}Sb_{23+x}$ (x=3.8±0.1) ($Ce_{27.3}Ge_{11.8}Sb_{60.9}$ in at.%) in good agreement with fairly single-phase bulk samples for which EPMA gives a composition $Ce_{26.3}$ $Ge_{12.4}$ $Sb_{61.3}$ (in at. %). Results of the structure determination are listed in Table 2a, b, c. A table on the anisotropic atom displacement parameters (Table 2d) can be obtained from the authors on request. From Table 2b one can see that there are many general positions, which are very close to special positions e.g Ce4 (0.0001, 0.15297, 0.59461) close to (0, y, z) and Ce1 (0.0005, 0.24981, 0.26625) close to (0, ¼, z) which are special positions in the centro-symmetric space groups *Cmmm* and *Cmma*. Attempts to solve the structure within the space groups *Cmmm* and *Cmma*, however, were not successful with R-values not less than 16% and 14% and residual electron densities as high as 27.0 and 13.0 e/ $Å^3$, respectively. When the center of symmetry is removed (*C*222) the R-value immediately drops. The absence of a center of symmetry increases the degree of freedom for the disordered sites M2, M4, which are random mixtures of 34(4)%Ge and 66(4)%Sb, and 85(4)%Ge and 15%Sb, respectively (Figure 2e). These atom sites cannot be related by an inversion center or by a mirror plane. Actually, the different electron density at these sites (M2 & M4) is responsible for the presence of the superstructure in the lattice (see Figure 2b). Refinement of the X-ray powder diffraction profiles strictly based on this structure model was successful with an R-value less than 6% even without refining the positional parameters and occupancies (Figure 3). Parameters from refinement of X-ray powder diffraction are listed in Table 6 (position parameters and occupancies are same as in Table 2b).

Figures 2c and 2d show the geometrical relation in direction b and a, respectively, between the super cell (*C*222) and the sub cell (*Immm*) reported by [7]. From this comparison it is obvious that all atoms on the left side (Figure 2b) are related by a

two-fold axis (parallel c) at (½, ½, 0) to the atoms on the right side thereby giving rise to a doubling of the unit cell in direction b. Similarly, shifting atom Sb3 off the position (0, ¼, 0) to (0, 0.268, 0) creates another Sb3 atom via the two-fold axis (parallel c) at (¼, ¼, z). The doubling of the unit cell in the a-direction can be seen from the atoms M4 (34% Ge and 66%Sb) and M2 (85%Ge and 15%Sb). Figure 2b explains the reason for the superstructure in both directions a and b. Construction of the unit cell is very similar to the subcell established by [7] for $La_6Ge_{2.8(1)}Sb_{13.2(1)}$. The supercell consists of Sb centered trigonal prisms Ce_6Sb. Constituents of these trigonal prisms are (i) vertexes of Ce1, 4 and 5 centered by Sb7 and Sb12, (ii) vertexes of Ce2, 3 and 6 centered by Sb4 and Sb10, which share triangular face to form columns running along [100] as described by [7]. The columns are separated by interconnecting walls of Ge and Sb atoms. A distortion in Sb-ribbons along the a-axis described by [7] is also seen in the present work with the difference that two short distances, $d_{Sb2\text{-}Sb1}$ = 0.2968 nm, alternate with two long distances, $d_{Sb1\text{-}Sb7}$ = 0.3281 nm.

Another difference observed between the two structure types is that the disordered site M2 in $La_6Ge_{2.8}Sb_{13.2}$ is replaced by two different atom sites (disordered site M5 and Sb3) in $Ce_{12}Ge_{9-x}Sb_{23+x}$ (Figure 2b and c).

A formal group-subgroup relation is presented in Figure 2f in the Bärnighausen formalism [22, 23]. Starting from the subcell space group *Immm* the symmetry reduction goes via a “translationengleiche” symmetry reduction of index 2 (t2) to the space group *I*222 followed by an isomorphic transition of index 4 (i4) from *I*222 to *C*222 accompanied by a shift of origin of (0, ½, 0) and a fourfold increase of the cell volume (2a, 2b, c). In going from *I*222 to *C*222 Wyckoff position 4*f* splits into sites 4*e*, 4*e*, 8*l*. Occupancy of 4*f* in the subcell was fixed at 50% [7]. Accordingly after splitting the occupancy in the super cell is again fixed at 50% for the 8*l* site, the 4*e* site is fully occupied by Sb1, while the second 4*e* site remains vacant. Similarly, the 4*g* site, occupied by a random mixture M2 (occ. 50%) in the subcell, splits into the supercell sites 4*g*, 4*g*, 8*l*. Whereas 8*l* is a disordered site M5 (occ. 50%), 4*g* is occupied by Sb3 but the second 4*g* site remains vacant. Thus the atom arrangement in the supercell drifts towards a more ordered arrangement although in some sites still random mixtures of Sb/Ge-atoms prevail. With respect to the fact that all experimentally observed intensities are indexed on the basis of the supercell, which

simply originates from the subcell by atom/vacancy order, we may safely rule out the possibility of a structure masked by twinning.

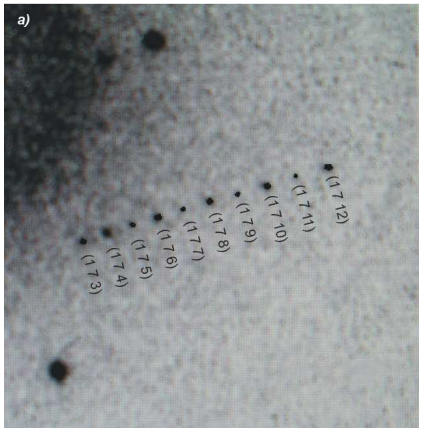

b)

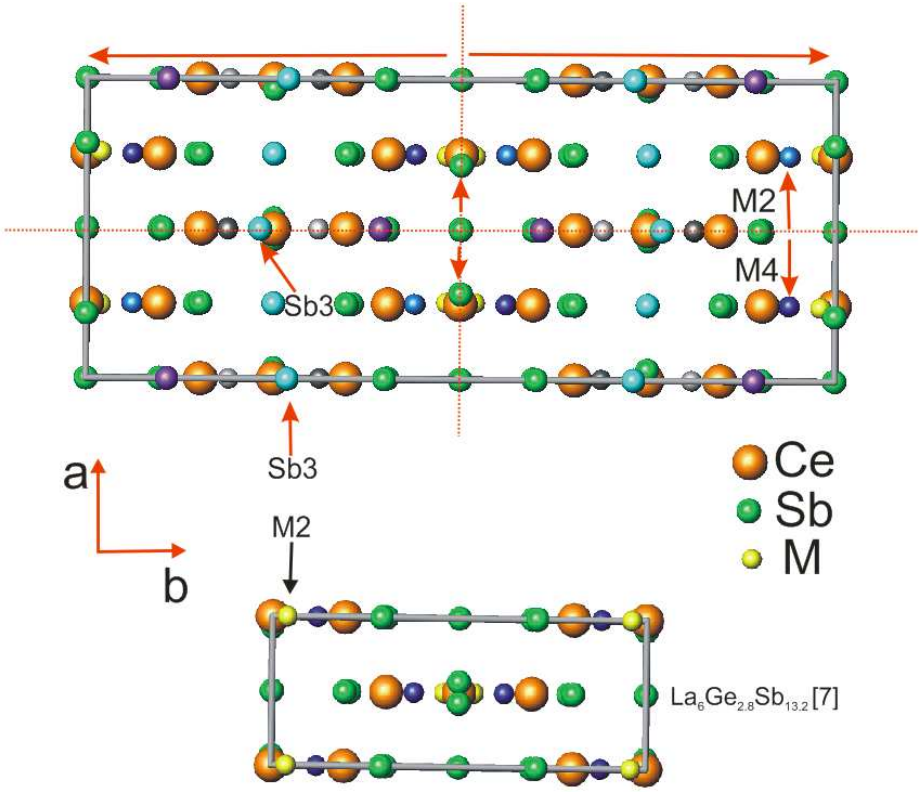

Figure 2. *a)* Array of single crystal X-ray diffraction spots documenting the superstructure. *b)* Comparison between supercell (C222; $Ce_{12}Ge_{9-x}Sb_{23+x}$ (x=3.8±0.1) type) and sub cell (Immm, $La_6Ge_{2.8}Sb_{13.2}$ type [7]).

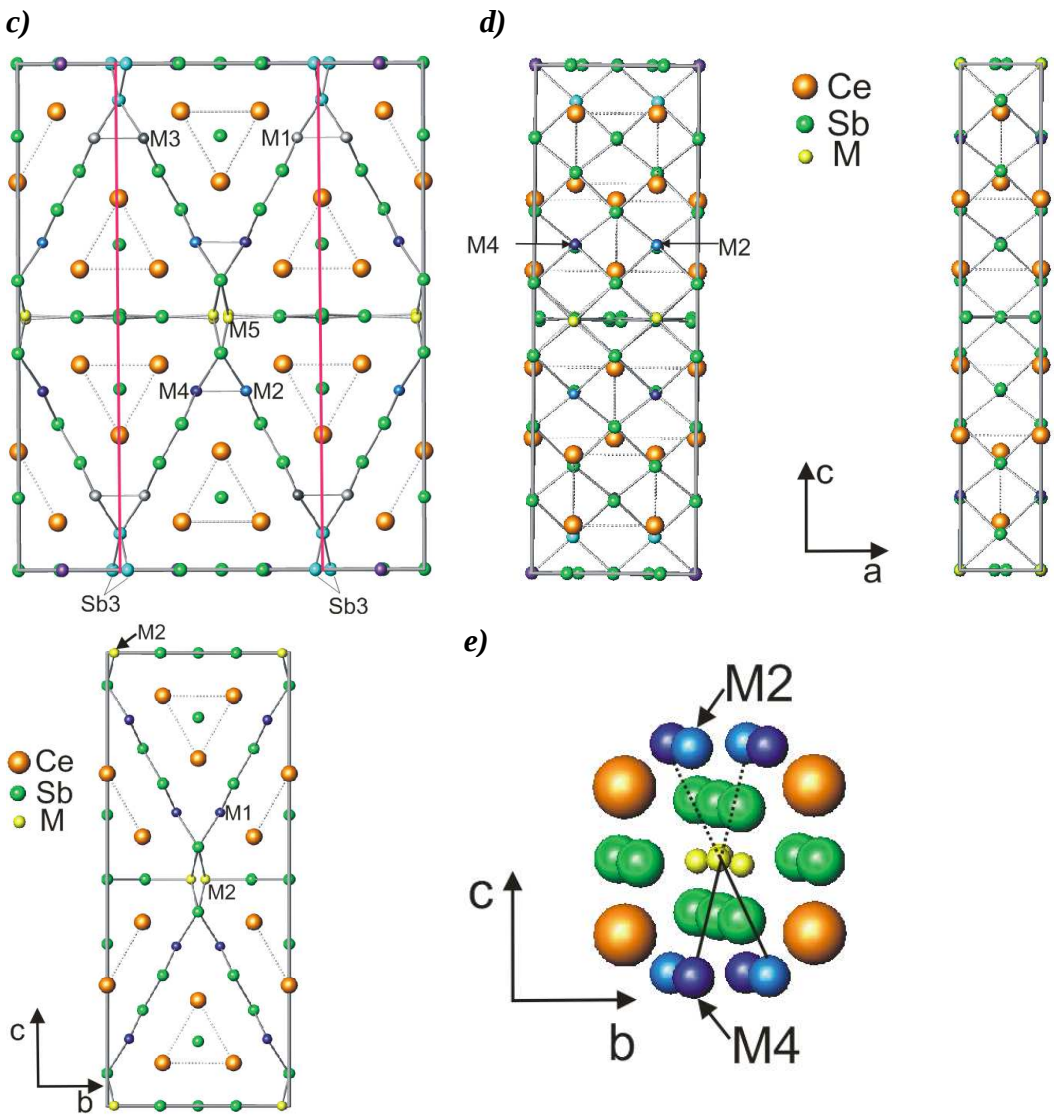

Figure 2. *c)* Comparison of supercell ($Ce_{12}Ge_{9-x}Sb_{23+x}$ (x=3.8±0.1) structure type) with [7] in direction b. *d)* Comparison of super cell ($Ce_{12}Ge_{9-x}Sb_{23+x}$ (x=3.8±0.1) structure type) with [7] in direction a. *e)* Section from the center of unit cell showing absence of center of symmetry. M2 is a disordered site with mixture of 33.8(4)%Ge and 66.1(4)% Sb, M4 is a disordered site with mixture of 85.0(4)% Ge and 15.0(4) % Sb.

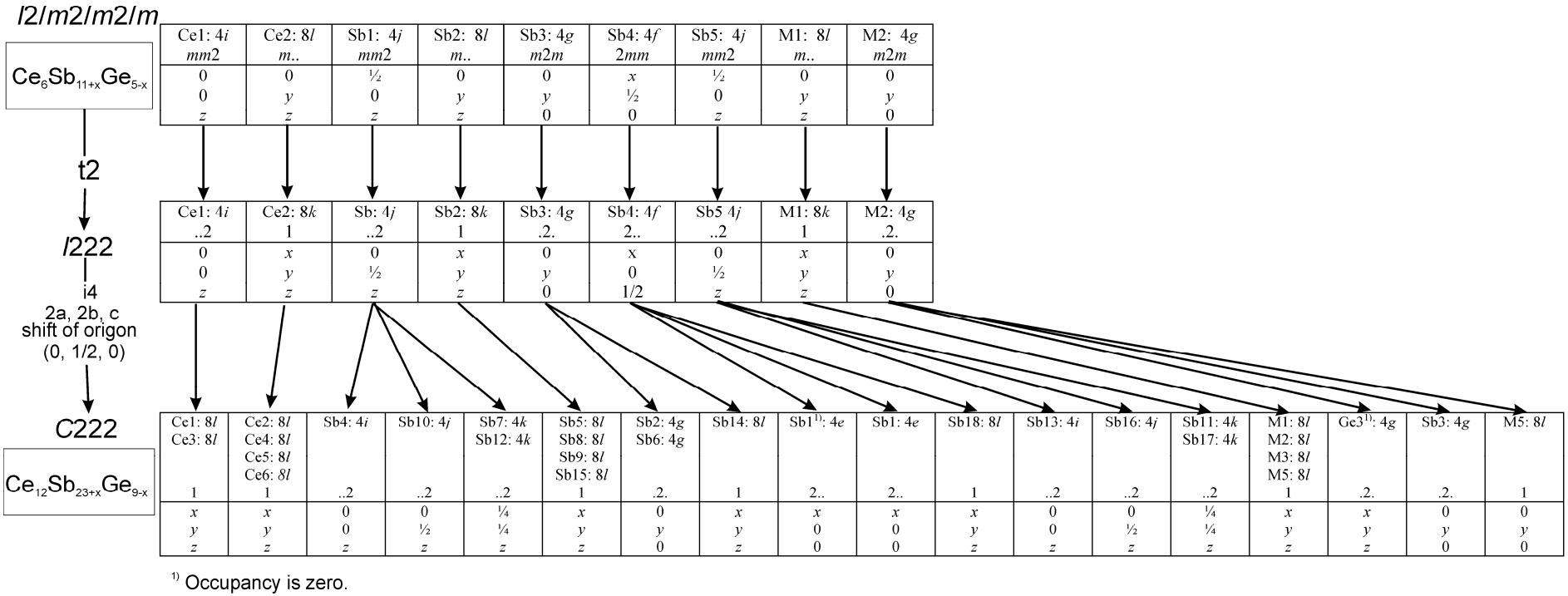

Figure 2. *f)* Group-subgroup scheme in the Bärnighausen formalism [22, 23] for subcell $Ce_6Sb_{11+x}Ge_{5-x}$ [7] to super cell $Ce_{12}Sb2_{3+x}Ge_{9-x}$.

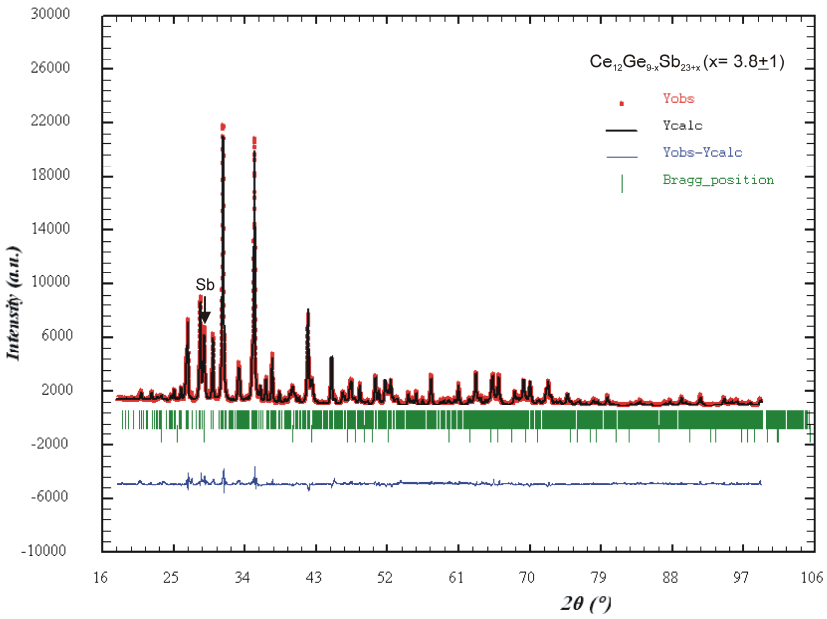

Figure 3. X-ray Rietveld refinement for $Ce_{12}Ge_{9-x}Sb_{23+x}$ (x=3.8±0.1) (nominal composition $Ce_{25}Sb_{62.5}Ge_{12.5}$)

Table 2a. X-Ray single crystal data for **$Ce_{12}Sb_{23+x}Ge_{9-x}$ (x =3.8±0.1). (**Standardized with program *Structure Tidy* [27]; room temperature data, redundancy >8); space group *C*222; No. 21.

Parameter/compound	
Composition from EPMA	$Ce_{26.3}Sb_{61.3}Ge_{12.4}$
Composition from refinement	$Ce_{27.3}Sb_{60.9}Ge_{11.8}$
Formula from refinement	$Ce_{12}Sb_{23+x}Ge_{9-x}$ (x =3.8±0.1).
a, *b*, *c* [nm]	0.86075(2), 2.15154(4), 2.68227(5)
μ_{abs} [mm^{-1}]	35.82
V (nm^3)	4.9674
ρ_x (gcm^{-3})	7.117
Z	8
Radiation	SC, MoKα
Data collection, 2Θ range(°); ω-scans, scan width 2°	2≤2Θ≤70; 150 sec/frame
Total number of frames & sets	411 & 8
Reflections in refinement	4847≥4σ(F_o) of 11936
Mosaicity	<0.52
Number of variables	225
$R_F^2 = \Sigma\|F_0^2-F_c^2\|/\Sigma F_0^2$	0.06
R_{Int}	0.066
wR2	0.1522
GOF	1.066
Extinction (Zachariasen)	0.00006
Residual density $e^-/Å^3$;	max; min 5.71; -7.39

2b. Atom parameters

Atom	Wyck. Pos.	Occ.	*x*	*y*	*z*	Ueq [in $10^2 nm^2$]
Ce1	8*l*	1.0	0.0005(2)	0.24981(4)	0.26625(5)	0.0095(2)
Ce2	8*l*	1.0	0.2506(3)	0.09708(7)	0.09457(6)	0.0103(3)
Ce3	8*l*	1.0	0.25005(10)	0.00045(9)	0.23373(5)	0.0096(2)
Ce4	8*l*	1.0	0.0001(3)	0.15297(5)	0.59461(4)	0.0102(2)
Ce5	8*l*	1.0	0.0001(3)	0.34692(5)	0.40528(4)	0.0104(2)
Ce6	8*l*	1.0	0.2495(3)	0.59678(7)	0.09473(6)	0.0105(3)
Sb1	4*e*	1.0	0.2154(2)	0	0	0.0099(3)
Sb2	4*g*	1.0	0	0.398(1)	0	0.0122(4)
Sb3	4*g*	1.0	0	0.268(2)	0	0.0250(5)
Sb4	4*i*	1.0	0	0	0.143(1)	0.0103(4)
Sb5	8*l*	1.0	0.2521(4)	0.1525(1)	0.21165(8)	0.0125(4)
Sb6	4*g*	1.0	0	0.10776(8)	0	0.0113(4)
Sb7	4*k*	1.0	1/4	1/4	0.3569(1)	0.0119(5)
Sb8	8*l*	1.0	0.5026(4)	0.09743(6)	0.28846(5)	0.0130(3)
Sb9	8*l*	1.0	0.0009(4)	0.09744(6)	0.28841(5)	0.0130(3)
Sb10	4*j*	1.0	0	1/2	0.143(1)	0.0111(4)
Sb11	4*k*	1.0	1/4	1/4	0.0717(1)	0.0203(6)
Sb12	4*k*	1.0	1/4	1/4	0.6424(1)	0.0098(5)
Sb13	4*i*	1.0	0	0	0.428(6)	0.0204(4)
Sb14	8*l*	1.0	0.2503(1)	0.14540(8)	0.49996(8)	0.0146(3)
Sb15	8*l*	1.0	0.2500(4)	0.6526(1)	0.21149(8)	0.0135(4)
Sb16	4*j*	1.0	0	1/2	0.42817(9)	0.0207(4)
Sb17	4*k*	1.0	1/4	1/4	0.928(2)	0.0195(6)
Sb18	8*l*	0.5	0.0345(3)	0.2502(1)	0.5031(1)	0.0132(6)
M1	8*l*	Ge: 0.544(4) Sb: :0.456(4)	0.0007(5)	0.19016(8)	0.14653(7)	0.0148(4)
M2	8*l*	Ge: 0.338(4) Sb: 0.661(4)	0.2498(4)	0.0616(1)	0.3533(1)	0.0205(5)
M3	8*l*	Ge: 0.577(4) Sb: 0.423(4)	0.0013(5)	0.31187(9)	0.14764(7)	0.0173(4)
M4	8*l*	Ge: 0.850(4) Sb: 0.150(4)	0.2503(5)	0.0603(1)	0.6472(1)	0.0173(4)
M5	8*l*	Ge: 0.268(4) Sb: 0.232(4)	0.245(2)	0.019(9)	0.496(8)	0.0115(6)

Table 2c. Interatomic distances for $Ce_{12}Sb_{23+x}Ge_{9-x}$ (x=3.8±0.1); standard deviations less than 0.0004 nm

Ce1	–1Sb7	0.3244		–1Sb10	0.3258		–1Sb15	0.3207	Sb18	–1Sb14	0.2913
	–1Sb12	0.3264		–1M1	0.3260		–1Sb5	0.3219		–1Sb14	0.2924
	–1Sb5	0.3326		–1Sb4	0.3262		–1Ce1	0.3332		–1Ce5	0.3231
	–1Sb9	0.3332	Sb1	–2Sb6	0.2968		–1Ce3	0.3337		–1Ce4	0.3237
	–1Sb8	0.3340		–2Sb2	0.3280		–1Ce3	0.3350		–1Sb14	0.3322
	–1Sb15	0.3342		–2Ce6	0.3299		–1Ce4	0.3358		–1Sb14	0.3332
	–1Sb5	0.3351		–2Ce2	0.3300	Sb10	–2Ce3	0.3251		–1Ce5	0.3363
	–1Sb15	0.3354		–1Sb1	0.3707		–2Ce6	0.3258		–1Ce4	0.3368
	–1M3	0.3451		–1Sb1	0.3299		–2Ce2	0.3262		–1Sb18	0.3711
	–1M1	0.3458		–1Sb2	0.3328	Sb11	–2Sb3	0.2914	M1-	–1M3	0.2619
Ce2	–1M3	0.3225		–1Sb6	0.3341		–2M1	0.3210		–1Sb15	0.2882
	–1M1	0.3255		–1Sb17	0.3351		–2M3	0.3237		–1Sb5	0.2902
	–1Sb10	0.3262		–1Sb15	0.3353		–2Ce2	0.3347		–1Sb17	0.3206
	–1Sb4	0.3268	Sb2-	–1Sb3	0.2800		–1Sb17	0.3861		–1Sb11	0.3210
	–1Sb1	0.3300		–2Sb1	0.3280	Sb12	–2Ce5	0.3258		–1Ce2	0.3255
	–1Sb2	0.3324		–2Ce2	0.3324		–2Ce4	0.3261		–1Ce6	0.3260
	–1Sb6	0.3339		–2Ce6	0.3328		–2Ce1	0.3264		–1Ce1	0.3458
	–1Sb11	0.3347	Sb3-	–1Sb2	0.2800	Sb13	–2M5	0.2825	M2-	–1M4	0.2624
	–1Sb5	0.3359		–2Sb11	0.2914		–2M5	0.2949		–1Sb9	0.2866
Ce3	–1Sb10	0.3251		–2Sb17	0.2922		–2M2	0.3224		–1Sb8	0.2891
	–1Sb4	0.3256		–1Sb6	0.3459		–2M4	0.3230		–1Sb13	0.3224
	–1Sb5	0.3327	Sb4-	–2Ce3	0.3256		–2Ce4	0.3348		–1Ce4	0.3226
	–1Sb8	0.3336		–2Ce6	0.3262		–1Sb13	0.3855		–1Sb16	0.3234
	–1Sb9	0.3337		–2Ce2	0.3268	Sb14	–1M5	0.2727		–1Ce5	0.3235

	–1Sb15	0.3344	Sb5-	–1M3	0.2830		–1Sb18	0.2913		–1Ce3	0.3469
	–1Sb9	0.3350		–1M1	0.2902		–1Sb18	0.2924		–1M5	0.3952
	–1Sb8	0.3350		–1Sb8	0.3204		–2Sb18	0.3322	M3-	–1M1	0.2619
	–1M4	0.3449		–1Sb9	0.3219		–2Ce5	0.3332		–1Sb5	0.2830
	–1M2	0.3469		–1Ce1	0.3326		–2Ce4	0.3332		–1Sb15	0.2869
Ce4	–1M2	0.3226		–1Ce1	0.3351		–1M5	0.3532		–1Ce2	0.3225
	–1Sb18	0.3237		–1Ce3	0.3327	Sb15	–1M3	0.2869		–1Sb11	0.3237
	–1Sb12	0.3261		–1Ce2	0.3359		–1M1	0.2882		–1Ce6	0.3248
	–1M4	0.3262	Sb6-	–2Sb1	0.2968		–1Sb8	0.3200		–1Sb17	0.3249
	–1Sb7	0.3268		–2Ce2	0.3339		–1Sb9	0.3207		–1Ce1	0.3451
	–1Sb14	0.3332		–2Ce6	0.3341		–1Ce1	0.3342	M4-	–1M2	0.2624
	–1Sb14	0.3333		–1Sb3	0.3459		–1Ce3	0.3344		–1Sb8	0.2851
	–Sb13	0.3348	Sb7-	–2Ce1	0.3244		–1Ce6	0.3353		–1Sb9	0.2881
	–Sb9	0.335		–2Ce5	0.3265		–1Ce1	0.3354		–1Sb16	0.3219
	–1Sb18	0.3368		–2Ce4	0.3268	Sb16	–2M5	0.2888		–1Sb13	0.3230
Ce5	–1Sb18	0.3231	Sb8-	–1M4	0.2851		–2M5	0.3009		–1Ce5	0.3252
	–1M2	0.3235		–1M2	0.2891		–2M4	0.3220		–1Ce4	0.3262
	–1M4	0.3252		–1Sb15	0.3200		–2M2	0.3234		–1Ce3	0.3449
	–1Sb12	0.3258		–1Sb5	0.3204		–2CE5	0.3350	M5-	–1Sb14	0.2727
	–1Sb7	0.3265		–1Ce3	0.3336		–1Sb16	0.3854		–1Sb13	0.2825
	–2Sb14	0.3332		–1Ce1	0.3340	Sb17	–2Sb3	0.2922		–1Sb16	0.2888
	–1Sb16	0.3350		–1Ce3	0.3351		–2M1	0.3206		–1Sb13	0.2949
	–1Sb8	0.3354		–1Ce5	0.3354		–2M3	0.3249		–1Sb16	0.3009
	–1Sb18	0.3363	Sb9-	–1M2	0.2866		–2Ce6	0.3351		–1Sb14	0.3532
Ce6	–1M3	0.3248		–1M4	0.2881		–1Sb11	0.3861		–1M2	0.3952

8.3.3 Phase equilibria in ternary systems Ce-M-Sb (M = Si, Ge, Sb)

i) Ce-Si-Sb system: Analysis of the alloys in as-cast state and after anneal at 600°C detected no ternary compounds in the Sb-Si-$CeSb_2$ part of the system. All diffraction peaks were indexed based on structures reported in literature for binary or unary phases revealing the phase equilibria as they are shown on Figure 4. The solubility limits for the phases in the ternary system were determined by EPMA to be less than 0.5 at. %. Microstructure of as-cast alloy $Ce_{30}Si_{35}Sb_{35}$ (Figure 5a) shows the primary crystallization of CeSb, secondary grains of $CeSb_2$ (α) and a eutectic structure. Joint crystallization of α-$CeSb_2$ and (Si) is documented in Figure 5b that shows the primary grains of these phases embedded in the (Sb) matrix. It has to be noted that LOM- and SEM-images of the alloys annealed at 600°C for 30 days are very similar to those observed in as-cast state (Figure 4): only a small coarsening of the eutectic structures was observed. In order to ensure that equilibrium conditions were reached after annealing of bulk alloys at 600°C, powders of the samples

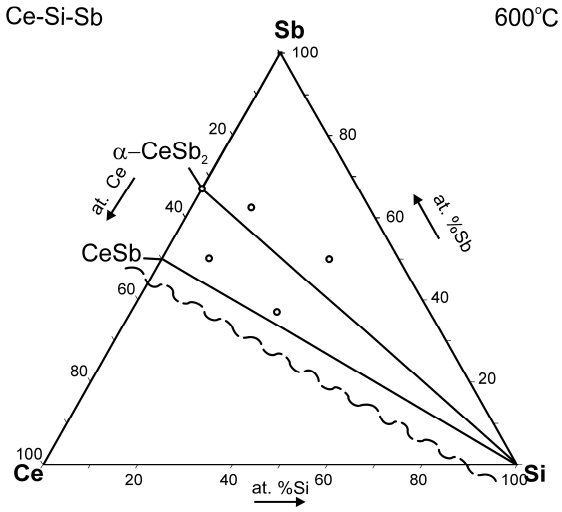

Figure 4: Partial isothermal section of Ce-Si-Sb phase diagram at 600°C.

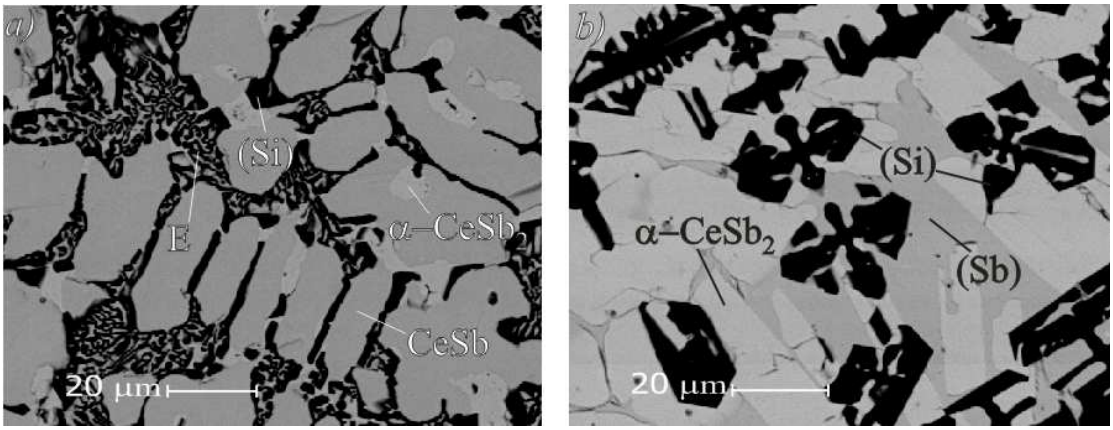

Figure 5. Microstructure of selected Ce-Si-Sb as-cast alloys: *(a)* $Ce_{30}Sb_{35}Si_{35}$ and *(b)* $Ce_{30}Sb_{35}Si_{35}$

Table 3: Ce-Si-Sb System (600°C): Three-phase equilibria and lattice parameters.

Phase Region T(°C)	**Phase**	**8.3.3.1 Composition by EPMA**			**Lattice Parameters**		
		in at. %					
		Ce	Sb	Si	a (nm)	b (nm	c (nm)
α-$CeSb_2$+(Sb)+(Si)	$CeSb_2$	31.4	68.2	0.4	0.6273(1)	0.6151(1)	1.8228(3)
	(Sb)	0.0	100	0.0	0.43085(5)	-	1.12690(2
	(Si)	0.0	9.7	90.3	0.54303(8)	-	-
α-$CeSb_2$+CeSb+(Si)	$CeSb_2$	32.2	67.8	0.0	0.6269(3)	0.6148(3)	1.823(2)
	CeSb				0.64256(5)	-	-
	(Si)	0.0	0.6	99.4	0.54309(8)	-	-

were compacted and additionally heat-treated at 600°C for 60 days. Subsequent X-ray characterization of the sintered samples confirms identical phase equilibria as observed

in as-cast conditions and after anneal of the bulk samples at 600°C. Data on phase composition and lattice parameters are summarized in Table 3.

ii) Ce-Ge-Sb system: Investigation of the region CeSb-Sb-Ge reveals phase equilibria that are different from those reported by [6] for 400°C (Figure 6a). As-cast samples (Figures 7a, c) were found to contain a small quantity of ternary compounds $CeSb_{2-x}Ge_x$ ($ThGe_2$ type structure [6]) and $Ce_{12}Ge_{9-x}Sb_{23+x}$ (3.3x<4.2) (τ, own type structure). LOM and SEM characterization of the alloys in as-cast state and after anneal at 400°C for 20 days yields very similar microstructures. The observation suggests that equilibrium conditions were not reached during anneal at 400°C despite the temperature is close to solidus in the Ge-Sb binary system (592°C, Figure 1a). In order to ensure that samples represent equilibrium conditions, the specimens were annealed at 600°C for 7-10 days. Selected samples were cut in parts and were additionally annealed at 520°C for 7 days and 400°C (30 days). Subsequent characterization of the specimens after anneal at 600°C, 520°C and 400°C reveals phase equilibria that significantly differ from those reported by [6]. An extended crystallization field for binary CeSb covers a significant part of the liquidus surface in the ternary system, and primary crystallization of this phase was observed in alloy $Ce_{30}Sb_{35}Ge_{35}$ (Figure 7a). Besides of primary grains of CeSb the microstructure shows secondary crystallization of the ternary compound $CeSb_{2-x}Ge_x$ (16.1 at % Ge after EPMA) and (Ge). CeSb was also observed in small quantity in the as-cast alloy $Ce_{25}Sb_{50}Ge_{25}$ but it completely disappears after anneal at 600°C (Figure 7b); thus the equilibrated specimen consists of (Ge), α-$CeSb_2$ and $Ce_{12}Ge_{9-x}Sb_{23+x}$ (τ). Primary crystallization of α-$CeSb_2$ is observed in as-cast $Ce_{15}Sb_{50}Ge_{35}$ (Figure 7c) whilst a high temperature modification (β-$CeSb_2$) was detected in both alloys $Ce_{15}Sb_{65}Ge_{20}$, and $Ce_{25}Sb_{70}Ge_5$ (Figure 8a and 8c). The high-temperature modification β-$CeSb_2$ decomposes on cooling and thus the annealed alloys $Ce_{25}Sb_{70}Ge_5$ and $Ce_{25}Sb_{52}Ge_{23}$ (Figure 7b) contain only the low-temperature form of $CeSb_2$.

Based on the character of the crystallization of the as-cast alloys, phase constituents of the annealed samples and DTA (performed on the alloys annealed at 520°C), we constructed the solidus surface and isothermal sections at 600°C and 400°C for the Sb-$CeSb_2$-Ge part of the diagram (Figure 6b-d and Table 4).

Samples from composition triangle (Ge)-(Sb)-τ are in liquid-solid state at 600°C. Consequently the ternary compound (τ) was found in equilibrium with liquid that

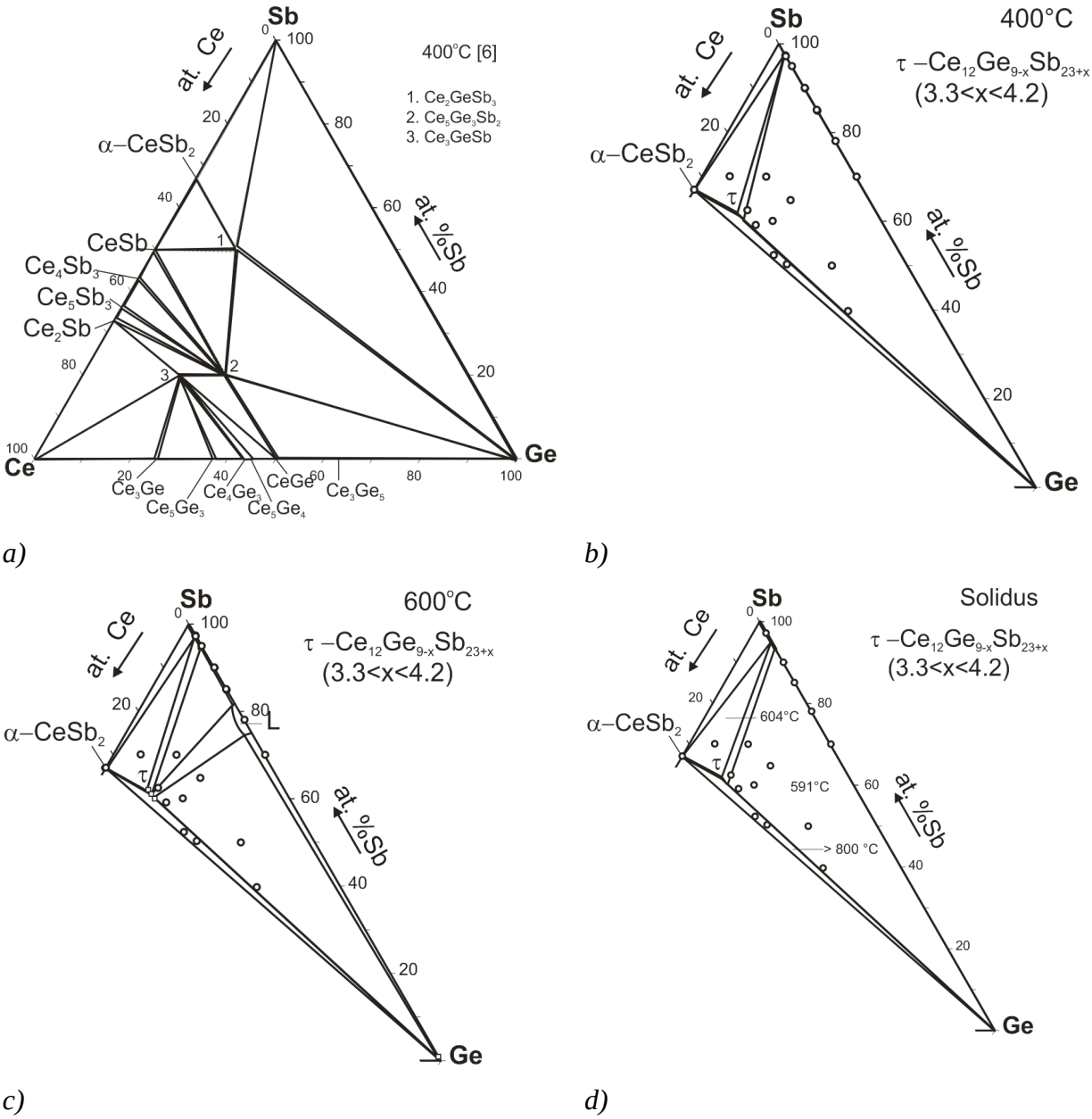

Figure 6: Phase diagram of Ce-Ge-Sb system: *(a)* isothermal section at 400°C after [6], *(b)* 400°C and *(c)* 600°C [this work] and *(d)* solidus surface [this work].

crystallizes on quenching under formation of (Sb) and a cerium-depleted eutectic (Figure 8d). The composition of this ternary eutectic $Ce_{<0.3}Ge_{\sim 23}Sb_{\sim 77}$, as measured by EPMA on as-cast alloys (Figures 7c, 8a and 8c), is very close to the binary Sb-Ge eutectic ($Ge_{22.5}Sb_{77.5}$, see Figure 1a). Particularly, the melting point of the ternary eutectic L= τ + (Ge) + (Sb) (T_E=591 ± 1 °C) is almost identical with the binary invariant reaction L=(Ge)+(Sb) (591.6 °C). The temperature of 604°C on solidus surface (Figure 6d) corresponds to the formation of τ via an invariant reaction L + α-$CeSb_2$ = τ + (Sb). In order to determine the temperature stability range for the ternary compound τ, the alloy

with composition $Ce_{25}Ge_{62.5}Sb_{12.5}$ was annealed at 400°C, 520°C, 600°C, 650°C, 700°C, 750°C, 800°C and 850°C. From XPD the existence of the ternary compound is confirmed for the temperature range from 400°C to 800°C whilst alloys quenched from 850°C do not contain the ternary compound but instead consist of β-$CeSb_2$ + (Ge)+ (Sb). Due to the high vapour pressure of antimony at temperatures above 800°C no DTA analyses were performed to determine the decomposition temperature of this ternary compound.

Table 4: Ce-Ge-Sb System (solidus): Three-phase equilibria and lattice parameters.

Phase Region T(°C)	**Phase**	**8.3.3.2 Composition by EPMA**			**Lattice Parameters**		
		in at. %					
		Ce	Sb	Ge	a (nm)	b (nm)	c (nm)
τ +(Sb)+(Ge)	τ	26.1	61.9	12.0	0.85902(8)	2.1456(1)	2.6773(5)
	(Sb)	-	94.4	5.6	0.42546(6)	-	1.1368(2)
	(Ge)	-	0.8	99.2	0.56561(9)	-	-
τ +α-$CeSb_2$+(Sb)	τ	26.0	63.5	10.5	0.8530(3)	2.1632(3)	2.712(4)
	α-CeSb2	31.7	68.3	0.0	0.62739(7)	0.6153(1)	1.8206(7)
	(Sb)	0.0	96.4	3.6	0.42579(3)	-	1.1362(4)
τ+α-$CeSb_2$+(Ge)	τ				0.86082(3)	2.1506(1)	2.6810(2)
	α-$CeSb_2$				0.6269(3)	0.6150(2)	1.8166(9)
	(Ge)				0.56575(4)	-	-

Phase equilibria at 400°C were found to be the same as at subsolidus temperature (Figure 6b). The difference only concerns the maximal solubility of Ge in Sb that decreases from 6.3 at. % Ge at solidus temperatures to about 2.4 at. Ge at 400°C.

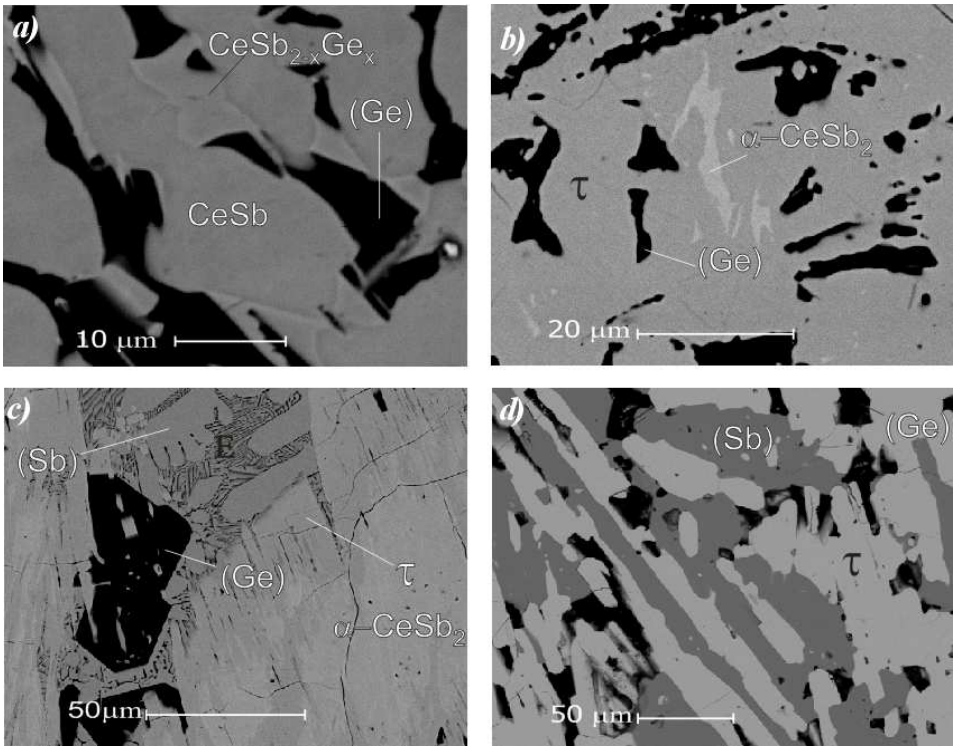

Figure 7. Microstructure of selected Ce-Ge-Sb alloys: *a)* $Ce_{30}Sb_{35}Ge_{35}$ (as-cast), *b)* $Ce_{25}Sb_{52}Ge_{23}$ (600°C), *c)* $Ce_{15}Sb_{50}Ge_{35}$ (as-cast), *d)* $Ce_{15}Sb_{50}Ge_{35}$ (600°C)

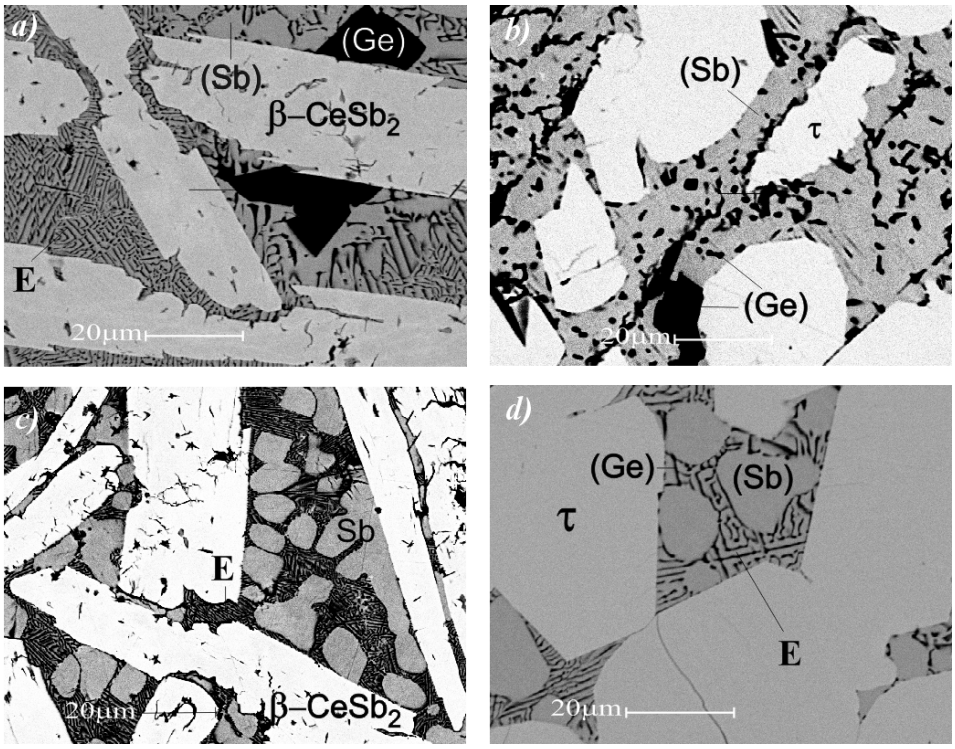

Figure 8. Microstructure of selected Ce-Ge-Sb alloys: *a)* $Ce_{15}Sb_{65}Ge_{20}$ (as-cast), *b)* $Ce_{15}Sb_{65}Ge_{20}$ (600°C), *c)* $Ce_{25}Sb_{70}Ge_{5}$ (as-cast), *d)* $Ce_{12}Sb_{62.5}Ge_{12.5}$ (600°C)

<u>*iii) Ce-Sn-Sb system:*</u> Ce-Sn-Sb alloys were investigated in three states: as-cast, after anneal of the bulk samples at 400 (15 days) and 200°C (60 days). Isothermal sections at

400°C and 200°C have been determined for the region CeSb-Sb-Sn-$CeSn_3$ and are presented in Figure 9 (see also data in Table 5). Formation of the ternary compound $CeSn_xSb_2$ is confirmed: the phase crystallizes incongruently and coexists in equilibrium with liquid at 400°C. Crystallographic data for $CeSn_xSb_2$ in Table 6 were obtained from Rietveld refinements. Lattice parameter data concerning the solid phases in equilibrium at 400°C are listed in Table 5. X-rays analysis confirms the rhombohedral symmetry for SbSn (distorted NaCl [24]) instead of the cubic NaCl type [21]. Antimony and SbSn reveal very similar X-ray diffraction patterns that differ only slightly by the angular position of the diffraction maxima. In correspondence with the difference in the atomic radii of Sb and Sn the unit cell volume and *c* - lattice parameter decrease with increase of tin content whilst *a* - increases. Following this trend towards the particular c/a ratio 2.4495 will render the X-ray diffraction spectrum very similar to that of Sb_2Sn_3 with NaCl type structure. However, we neither observe this cubic structure nor we can confirm the existence of the various rhombohedral modifications of SbSn reported in [24, 25].

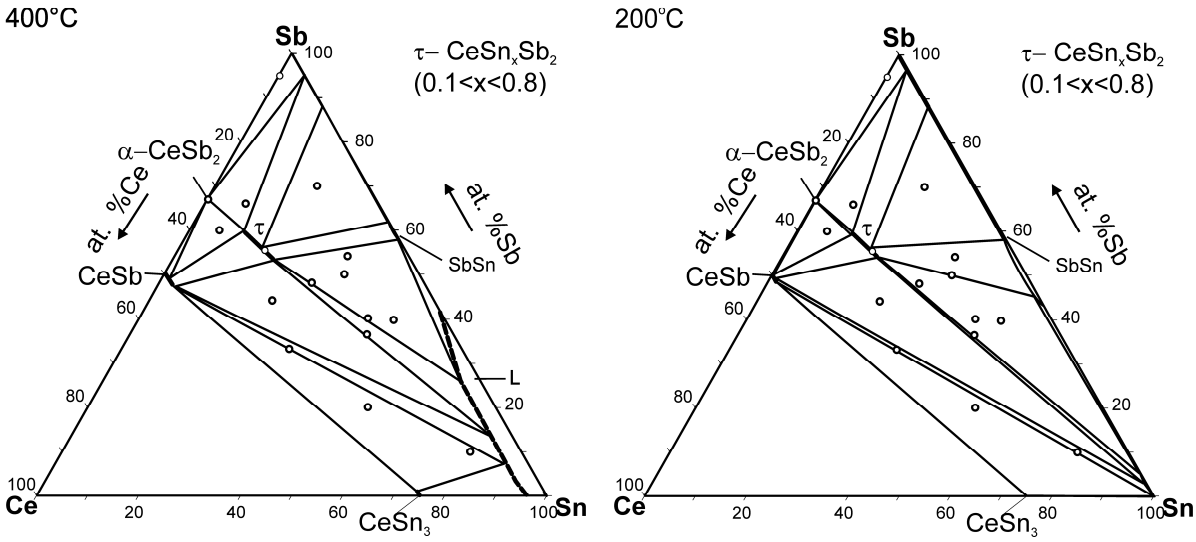

Figure 6: Phase diagram of Ce-Ge-Sb system: *(a)* isothermal section at 400°C after [6], *(b)* 400°C and *(c)* 600°C [this work] and *(d)* solidus surface [this work].

Table 5: Ce-Sn-Sb System: Three-phase equilibria and lattice parameters for alloys annealed at 400°C and 200°C.

Phase Region T(°C)	**Phase**		**Lattice Parameters**	
		a (nm)	b (nm)	c (nm)
400°C				
τ +SbSn+(Sb)	τ	0.42420(4)	2.2827(2)	0.44556(6)
	SbSn	0.4324(1)	-	1.0731(5)
	(Sb)	0.42597(4)	-	1.1456(2)
τ + α-$CeSb_2$ +(Sb)	τ	0.42477(5)	2.2808(2)	0.44369(3)
	α-$CeSb_2$	0.6380(1)	0.6027(9)	2.00(1)
	(Sb)	0.42732(8)	-	1.1417(2)
τ+CeSb+α-$CeSb_2$	τ	0.42373(7)	2.2833(4)	0.44483(7)
	CeSb	0.64241(5)	-	-
	α-$CeSb_2$	0.62621(1)	0.6175(2)	1.817(3)
τ+SbSn+L	τ	0.42301(6)	2.2867(2)	0.44768(3)
	SbSn	0.43218(5)	-	1.0690(4)
	(Sn)[1)]	0.58392(3)	-	0.31819(3)
CeSb+$CeSn_3$+L	CeSb	0.64235(8)	-	-
	$CeSn_3$	0.47225(4)	-	-
	(Sn)[1)]	0.58323(3)	-	0.31832(2)
τ+CeSb+L	τ	0.42238(5)	2.2852(3)	0.44826(4)
	CeSb	0.64225(3)	-	-
	(Sn)[1)]	0.58367(3)	-	0.31820(3)
200°C				
τ +SbSn+(Sb)	τ	0.0.42374(5)	2.2817(6)	0.44586(7)
	SbSn	0.4314(1)	-	1.0763(6)
	(Sb)	0.42586(5)	-	1.1458(4)
τ + α-$CeSb_2$ +(Sb)	τ	0.42390(7)	2.2837(6)	0.44501(8)
	α-$CeSb_2$	0.61278(8)	0.6162(8)	1.819(4)
	(Sb)	0.42666(8)	-	1.1448(4)
τ+CeSb+α-$CeSb_2$	τ	0.42543(2)	2.2824(7)	0.4458(1)
	CeSb	0.64236(5)	-	-
	α-$CeSb_2$	0.6275(3)	0.6165(5)	1.812(4)
τ+SbSn+(Sn)	τ	0.42253(5)	2.2848(8)	0.44787(7)
	SbSn	0.43375(2)	-	1.0701(4)
	L(Sn)[1)]	0.58385(5)	-	0.31807(3)
CeSb+$CeSn_3$+L	CeSb	0.64242(9)	-	-
	$CeSn_3$	0.4726(1)	-	-
	(Sn) [1)]	0.58333(4)	-	0.31824(3)
τ+CeSb+L	τ	0.42257(4)	2.2851(4)	0.44814(8)
	CeSb	0.64238(5)	-	-
	(Sn) [1)]	0.58396(5)	-	0.31817(5)

Table 6: Crystallographic data for $Ce_{12}Ge_{9-x}Sb_{23+x}$ ((3.3<x<4.2) and $CeSn_xSb_2$ (0.1<x<0.8) (X-ray powder diffraction room temperature data, image plate data, Cu $K_{\alpha 1}$ radiation); structure standardized with program *Structure Tidy* [27] (B_{iso} is given in 10^2 nm^2).

Parameter/compound	**$CeSn_xSb_2$ (x=0.8)**	**$Ce_{12}Ge_{9-x}Sb_{23+x}$ (3.3<x<4.2)**
Space group, Prototype	C*mcm*, $LaSn_{0.75}Sb_2$	C222, $Ce_{12}Ge_{9-x}Sb_{23+x}$ (x=3.8±0.1)
Composition, EMPA at.%	-	$Ce_{26.3}Sb_{61.3}Ge_{12.4}$
Composition from refinement	$Ce_{26}Sn_{21.9}Sb_{52}$	$Ce_{27.3}Sb_{60.9}Ge_{11.8}$
a ;b; c [nm], Ge standard	0.42370(1)); 2.2834(1); 0.44594(2)	0.86030(4); 2.1504(3); 2.6811(7)
Reflections measured	170	1636
Θ range	8≤2Θ≤100	8≤2Θ≤100
Number of variables	21	21
$R_F = \Sigma\|F_o-F_c\|/\Sigma F_o$	0.0511	0.0407
$R_I = \Sigma\|I_o-I_c\|/\Sigma I_o$	0.0809	0.0598
$R_{wP}=[\Sigma w_i\|y_{oi}-y_{ci}\|^2/\Sigma w_i\|y_{oi}\|^2]^{½}$	0.0534	0.0472
$R_P = \Sigma\|y_{oi}-y_{ci}\|/\Sigma\|y_{0i}\|$	0.0380	0.0359
$R_e = [(N-P+C)/\Sigma w_i y^2_{oi})]^{½}$	0.0182	0.0252
$\chi^2 = (R_{wP}/R_e)^2$	8.57	3.52
Atom parameters:	**Ce1:** 4*c* (0,0.13876(5),1/4); B_{iso} = 1.75 **M1:** 8*f* (0, 0.01531(2), 0.644(1)); occ. = 0.184(2) Sn; B_{iso} =1.16 **M2:** 4*c*(0,0.00833(4),1/4); occ. = 0.155(1) Sn; B_{iso} =1.06 **M3:** occ =0.315(1) Sn; 4*a*(0,0,0); B_{iso} =1.36 **4Sb1 in** 4*c*(0, 0.75123(6), 1/4); B_{iso} =1.97 **4Sb2 in** 4*c*(0, 0.40763(6), 1/4); B_{iso} =1.89	Fixed after single crystal refinement (Table 2b) Ce; B_{iso} = 0.224 Sb and M; B_{iso} = 0.763

8.4 Conclusions

Phase equilibria in the systems Ce-M-Sb (M = Si, Ge, Sn) were studied in the phase region $CeSb_2$-Sb-M. A maximum solubility of Ge in Sb was found to be 6.3 at. % at the eutectic temperature 591.6°C with a newly defined eutectic composition 22.5 at. % Ge.

No ternary compound was found in the Ce-Si-Sb system in the phase region CeSb-Si-Sb. In the Ce-Ge-Sb system a compound τ, $Ce_{12}Ge_{9-x}Sb_{23+x}$ exists in equilibrium with a homogeneity region extending from x=3.3 to x=4.2. From single crystal x-ray analysis $Ce_{12}Ge_{9-x}Sb_{23+x}$ was found to adopt a superstructure of the $La_6Ge_{2.8}Sb_{13.2}$ type with space group *C*222 and lattice parameters doubled in direction a (0.86075(2) nm) and b (2.15154(4) nm) while c (2.68227(5) nm) remains the same resulting in a unit cell with volume and Z four times bigger that of the $La_6Ge_{2.8}Sb_{13.2}$ type. Partial isothermal sections at 200 and 400°C are constructed for the Ce-Sn-Sb system. $CeSn_xSb_2$ (0.1<x<0.8) (*Cmcm*, $LaSn_{0.75}Sb_2$ type) exists in equilibrium at 200 and 400°C.

References

[1] A. Grytsiv, D. Kaczorowski, A. Leithe-Jasper, P. Rogl, M. Potel, H. Noël, A. P. Pikul and T. Velikanova,, J. Solid State Chem. 165 (2002) 178.

[2] A. Grytsiv, D. Kaczorowski, A. Leithe-Jasper, V. H. Tran, A. Pikul, P. Rogl, M. Potel, H. Noël, M. Bohn and T. Velikanova, J. Solid State Chem. 163 (2002) 178.

[3] A. Grytsiv, P. Rogl, S. Berger, C. Paul, H. Michor, E. Bauer, G. Hilscher, C, Godart, P. Knoll, M. Musso, W, Lottermoser, A, Saccone, R, Ferro, T. Roisnel, H. Noel, J. Phys: Condens. Matter 14 (2002) 7071.

[4] A. Grytsiv, E. Bauer, St. Berger, G. Hilscher, H. Michor, Ch. Paul, P. Rogl, A. Daoud-Aladine, L. Keller, T. Roisnel and H. Noel, J. Phys. Condens. Matter 15 (2003) 3053.

[5] M. J. Ferguson, R. W. Hushagen, and A. Mar, Inorg. Chem. 35 (1996) 4505.

[6] A. O. Stetskiv, V. V. Pavlyuk and O. I. Bodak, Pol. J. Chem. 72 (1998) 956.

[7] R. Lam, R. McDonald, and A. Mar, Inorg. Chem. 40 (2001) 952.

[8] L. Deakin, R. Lam, and A. Mar, Inorg. Chem. 40 (2001) 960.

[9] A. M. Mills, R. Lam, M. J. Ferguson, L. Deakin, A. Mar, Coord. Chem. Rev. 207- 222 (2002) 233.

[10] L. Nore´n, R. L. Withers, F. J. Brink, J. Solid State Chem. 178 (2005) 2133.

[11] Nonius Kappa CCD Program Package COLLECT, DENZO, SCALEPACK, SORTAV, Nonius Delft, The Netherlands, (1998).

[12] G. M. Sheldrick: SHELXL-97, Program for Crystal Structure Refinement. University of Göttingen, Germany; Windows version by McArdle, Natl. Univ. Ireland, Galway, (1997).

[13] T. B. Massalski, Binary Alloy PhaseDiagrams, 2nd ed., ASM International, Materials Park, OH, (1990).

[14] V. D. Abulkhaev, Russ. J. Inorg. Chem. 42 (1997) 283

[15] V. K. Ruttewit, G. Masing, Z. Metallkd. 32 (1940) 52.

[16] B. G. Zhurkin, V. S. Zemskov, D. A. Petrov, A. D. Suchkov, Izv. Akad. Nauk SSSR Otd. Tekh. Nauk Met. Topl. 5 (1959) 86.

[17] V. B. Predel, D. W. Stein, Z. Metallkd. 61 (1970) 909.

[18] S. Bordas, M. T. Clavaguera-Mora, B. Legendre, C. Hancheng, Thermochim. Acta. 107 (1986) 239.

[19] R. W. Olesinski, G. J. Abbaschian, Bull. Alloy Phase Diagrams 7 (1986) 219.

[20] W. P. Allen, J. H. Perepezko, Sci. Metall. Mater. 24 (1990) 2215.

[21] T. N. Kolobyanina, S. S. Kabalkina, L. F. Vereshchagin, M. F. Kachan, V. G. Losev, High Temp.-High Press. 4 (1972) 207.

[22] H. Bärnighausen, Commn. Math. 9 (1980) 139.

[23] H. Bärnighausen, U. Müller, Symmetriebeziehungen zwischen den Raumgruppen als Hilfsmittel zur straffen Darstellung von Strukturzusammenhängen in der Kristallchemie, University of Karlsruhe and University /GH Kassel, 1996.

[24] V. Vassiliev, M. Lelaurain, J. Hertz, J. Alloys Compd. 247 (1997) 223.

[25] V. Vassiliev,Y. Feutelais, M. Sghaier, B. Legendre, J. Alloys Compd. 314 (2001) 198.

[26] P. Villars, L. D. Calvert, Pearson's Handbook of Crystallographic Data for Intermetallic Phases, 2nd ed., ASM International, Materials Park, OH, 1991

[27] E. Parthé, L. Gelato, B. Chabot, M. Penzo, K. Cenzual, R. Gladyshevskii, TYPIX Standardized Data and Crystal Chemical Characterization of Inorganic Structure Types, Springer – Verlag, Berlin, Heidelberg, (1994).

9 The system Nd-Fe-Sb: Phase Equilibria, Crystal Structures and Physical Properties

9.1 Introduction

Ternary rare earth transition metal antimonides are a class of compounds with a large diversity in structure and physical properties [1-5]. Although systems RE-T-Sb (T is a transition element) have been in the focus of many investigations [6-14], phase diagrams at temperatures higher than 600°C are scarce, and information on ternary compounds and their crystal structures is incomplete. The high thermoelectric efficiency of ternary and multicomponent skutterudites RET_4Sb_{12} [15-17] has triggered intensive research on these Sb-rich compounds in general [18-21] and in layered structure antimonides with interesting magnetic properties e.g $RETSb_3$ [5, 22-27]. As a logical continuation of our previous studies on phase equilibria in systems formed by rare earth with p^2 elements (Si, Ge, Sn) and/or Sb [28], in this paper we focus on the system Nd-Fe-Sb, on the phase relations at 800°C (particularly in the region with more than 40 at.% Sb), on the formation and crystal structure of ternary compounds and their isotypes with the homologous light rare earth elements (La, Ce, Pr). A first investigation of the isothermal section at 800°C of the system Nd-Fe-Sb was performed by A. Leithe-Jasper in our institute as part of his PhD-thesis [6] revealing the phase relations at 800 °C characterized by five ternary compounds: τ_1- $Nd_6Fe_{13}Sb$ ($Nd_6Fe_{13}Si$-type [29], τ_2-$NdFe_3Sb_2$ (tetragonal, a = 0.42879(7), c = 2.5705(4) nm), and τ_2-$NdFe_{2-x}Sb_2$ (orthorhombic, a = 0.42965(1), b = 0.4276(2), c = 2.5789(5) nm) τ_3-$Nd_2Fe_{3-x}Sb_5$ (hexagonal, a = 1.31719(6), c = 0.41785(8) nm; structure unknown), τ_4-$NdFeSb_3$ (structure unknown) and τ_5-$NdFe_{1-x}Sb_2$ ($ZrCuSi_2$-type [30]). Whereas the crystal structures and physical properties of τ_1- $Nd_6Fe_{13}Sb$ ($Nd_6Fe_{13}Si$-type) [29], and of τ_5-$NdFe_{1-x}Sb_2$ ($ZrCuSi_2$-type) [30] have been elucidated in detail, the structure solutions for the crystal structure of τ_2-$NdFe_3Sb_2$ (tetragonal) and τ_2-$NdFe_{2-x}Sb_2$ (orthorhombic) were not considered to be satisfactory (R_F = 0.09 and 0.08 respectively) and remained unpublished. Compounds isotypic to the tetragonal structure were observed with La and Ce while compounds with Pr and Sm were found isostructural to the orthorhombic

structure. A more recent investigation of the Nd-Fe-Sb system by Zeng [10] at 500 °C showed the absence of τ_3 and a compound $NdFe_{2.5}Sb_2$ with unknown structure. Therefore the aim of the present work is threefold: (i) to investigate phase relations in the Sb-rich part of the Nd-Fe-Sb system (region Fe-NdSb-Sb) in a wider temperature range, (ii) to elucidate crystal structure and formation of ternary phases (τ_2, τ_3 and τ_4) including the light rare earth containing homologues, and (iii) to study their physical properties.

9.2 Experimental

All samples, each of a total amount of ca. 1-1.5 g, were prepared in an electric arc furnace on a water cooled copper heath under Ti-gettered argon and with a non-consumable tungsten electrode. The purity of RE (Nd, La, Pr) was 99.5 mass%, of antimony and Fe was better than 99.9%. The alloys were remelted three times in order to ensure complete fusion and homogeneity. Weight losses were found to be 2-4 mass% and were compensated beforehand for the most volatile element Sb. The reguli were cut into 2 to 4 pieces in order to perform heat treatments at various temperatures. The individual pieces were sealed in evacuated quartz tubes and annealed at temperatures (500, 600, 700, 800, 900, 1000 °C) for 10 to 14 days following quenching in water.

X-ray powder diffraction (XRPD) data from as-cast and annealed alloys were collected with a Guinier-Huber image plate system (Cu–$K_{\alpha 1}$ or Fe-$K_{\alpha 1}$; $8° < 2\theta < 100°$). Precise lattice parameters were calculated by least-squares fits to indexed 2θ-values employing Ge as internal standard ($a_{Ge} = 0.565791$ nm).

To determine the crystal structure of the ternary phases τ_2 (tetragonal and orthorhombic), and τ_3, single crystal fragments, suitable for X-ray structure determination were broken from alloys with nominal compositions (i) $La_{18}Fe_{36}Sb_{46}$ annealed at 1000 °C (30 days), (ii) $Nd_{19}Fe_{39}Sb_{42}$ annealed at 1000 °C (30 days) and (iii) $Nd_{22}Fe_{27}Sb_{51}$ annealed at 800 °C (20 days) prior to quenching in cold water. Inspection on an AXS-GADDS texture goniometer assured high crystal quality, unit cell dimensions and Laue symmetry of the specimens prior to X-ray intensity data collection on a four-circle Nonius Kappa diffractometer equipped with a CCD area detector and employing graphite monochromatic MoK_{α} radiation (λ = 0.071073 nm). Orientation matrix and unit cell parameters were derived using the program DENZO [31]. No

absorption correction was necessary because of the rather regular crystal shape and small dimensions of the investigated specimen. The structures were solved by direct/Patterson methods and refined with the SHELXL-97 and SHELXS-97 programs [32].

The as cast and annealed samples were polished using standard procedures and microstructures and compositions were examined by light optical microscopy (LOM) and scanning electron microscopy (SEM) via Electron Probe Micro-Analyses (EPMA) on a Carl Zeiss EVO 40 equipped with a Pentafet Link EDX system operated at 20 kV. Binary and ternary compounds $NdSb_2$ and $NdFeSb_3$ were used as EPMA standards. The differences between measured and nominal compositions were found to be <1 at. %.

Magnetic measurements were performed in the temperature range 1.72–400 K in applied magnetic fields up to 50 kOe using a Quantum Design MPMS-5 SQUID magnetometer. The electrical resistivity was measured over the temperature interval 4.2-300 K employing a dc four-probe technique and home-made setup. In the case of $NdFeSb_3$ the resistivity measurements were extended down to 0.4 K using a standard ac technique implemented in a Quantum Design PPMS platform. Specific heat studies were carried out in the 0.35-300 K temperature range by a relaxation method employing a Quantum Design PPMS platform.

9.3 Results and Discussion

9.3.1 Binary boundary systems

Binary boundary systems Nd-Sb, Fe-Sb and Fe-Nd were accepted after [33-35] respectively. The monoclinic binary phase Nd_5Sb_{12} (S.P. *Cc*) reported by [36] is not shown in any of the binary phase diagrams for the Nd-Sb system. It should be noted that this phase was not observed at any temperature in any sample investigated in the present work. Crystallographic data for the solid phases are summarized in Table 1.

9.3.2 Phase equilibria in the Nd-Fe-Sb system

In order to define a proper temperature for the isothermal section, alloys, annealed at various temperatures (500, 600, 700, 800, 900, 1000, and 1100°C), were subjected to XRPD and LOM analyses, which revealed that the annealing temperature of 500°C is

too low to achieve equilibrium condition: most of the alloys annealed at 500°C were unchanged with respect to the as cast state. As above 800 °C some of the alloys appeared completely melted, the optimal temperature for equilibration and for the formation of ternary compounds was defined as 800 °C. The isothermal section derived at 800 °C from EPMA and XRPD is presented in Figure 1. Phase equilibria in the composition range Fe-NdSb-Sb are accepted after [6]. All previously reported ternary phases, τ_1-$Nd_6Fe_{13}Sb$ ($Nd_6Fe_{13}Si$ type) [29], τ_2-$NdFe_{2-x}Sb_2$ [A. L-J] or ~$NdFe_{2.5}Sb_2$ (unknown type [10]), τ_3-$Nd_2Fe_{3-x}Sb_5$ [6], τ_4-$NdFeSb_3$ [6, 10], τ_5-$NdFe_{1-x}Sb_2$ ($ZrCuSi_2$-type) [30], τ_6-$NdFe_4Sb_{12}$ ($LaFe_4Sb_{12}$ type) [37] were observed in the present work. The crystal structures of τ_2 and τ_3 are determined by single crystal x-ray diffraction in the present work (see details in section 3.3 and 3.4) and the exact structure formula for τ_2 (tetragonal and orthorhombic) and τ_3 is now referred to as $Nd_2Fe_{5-x}Sb_{10-y}$ (tetragonal), $Nd_2Fe_{7-x}Sb_{6-y}$ (τ_2 orthorhombic) and $Nd_3Fe_3Sb_7$, respectively. τ_2-$Nd_2Fe_{5-x}Sb_{10-y}$, τ_2-$Nd_2Fe_{7-x}Sb_{6-y}$ corresponds to the phase ~$NdFe_{2.5}Sb_2$ reported by [10].

Microstructures of the selected as cast and annealed alloys documenting the phase equilibria are shown in Figures 2 and 3. The as cast alloy with nominal composition $Nd_{16}Fe_{12}Sb_{70}$ was multiphase with two different zones of crystallization. Figures 2a and 2b show primary crystallization of $NdSb_2$ with peritectic formation of τ_5, whilst Figure 2c presents τ_5 as primary grains with subsequent crystallization of $NdSb_2$ as secondary grains. The last liquid in both regions shows joint crystallization of τ_4, $NdSb_2$, $FeSb_2$ (Figure 2a, b, c). All phases were confirmed from XRPD. The alloy annealed at 800 °C shows a completely different microstructure consisting of only three phases as can be seen from Figure 2d which reveals big grains of τ_4 and $NdSb_2$ inside a matrix that represents liquid state at 800 °C. Morphology of the alloy annealed at 700 °C represents the equilibrium, τ_6 (skutterudite)-τ_4-$NdSb_2$ (Figure 2e) which is different from that observed at 800 °C (τ_4 - $NdSb_2$ - (L)). Solubility of Fe in $NdSb_2$ was found to be less than 0.5%. In an attempt to prepare a single-phased alloy $NdFeSb_3$ weak unindexed reflections were observed in the X-ray profile of the alloy annealed at 800 °C. The intensity of these reflections increased significantly in alloy $Nd_{22}Fe_{27}Sb_{51}$. A single crystal selected from the latter alloy yields the ternary compound τ_3 (for details refer to section 3.4). Microstructure of the alloy $Nd_{22}Fe_{27}Sb_{51}$ annealed at 800 °C (Figure 2f) represents the triangle τ_3–τ_2–τ_5. Ternary τ_3 and τ_2 are also in equilibrium $Fe_{2-x}Sb$ phase (see Figures 1, and 3a). Equilibrium of τ_3 with τ_4 and $Fe_{2-x}Sb$ is shown in the micrograph

of the alloy $Nd_{19}Fe_{25}Sb_{56}$ annealed at 800 °C (Figure 3b). Due to very small difference in compositions, the SEM contrast between the τ_3 and τ_4 phases is very low (Figure 3b), but compositions from EDX show a clear difference, which is also confirmed by x-ray analysis. Despite the presence of low melting Sb, kinetics in the system is quite slow and alloys with less than 50 at.% Sb were usually found to contain four to five phases after annealing at 800 °C for 7-10 days. In-order to clearly define phase equilibria, some alloys were repowderized and compacted into tablets sealed in evacuated quartz tubes and additionally annealed at 800 °C for 7-10 days. Microstructure of the as cast alloy $Nd_{19}Fe_{27}Sb_{54}$ shows a ternary eutectic structure (E) consisting of τ_4, τ_5 and $Fe_{2-x}Sb$ (Figure 3c) with composition $Nd_{17.2}Fe_{26.6}Sb_{56.2}$. Therefore most of the alloys in this composition range were found partially melted after annealing at 800 °C. Figure 3d shows the equilibrium microstructure of τ_3 and τ_5 in the alloy with nominal composition $Nd_{24}Fe_{20}Sb_{56}$. Microstructure of the alloy $Nd_{20}Fe_{35}Sb_{45}$ after cyclic heat treatment (slow heating and cooling between 1075-1025 °C) confirms very big grains of τ_2 with composition $Nd_{18.0}Fe_{37.6}Sb_{44.3}$ with well-defined grain boundaries (Figure 3d). The grains of τ_2 are separated by a very fine eutectic structure with composition $Nd_{8.2}Fe_{30.3}Sb_{72.4}$ (Figure 3f). However, no single crystal fragment suitable for X-ray single crystal investigations could be obtained from this sample.

The phase equilibria associated with structural polymorphism in τ_2 **(**tetragonal and orthorhombic structure) appear to be very complicated. The as cast alloy $Nd_{19}Fe_{37}Sb_{44}$ with primary crystallites of NdSb contains small amounts of orthorhombic τ_2 crystallizing from the last liquid. After anneal at 900 °C and 800 °C NdSb disappears and τ_2 appears as tetragonal modification whilst the sample annealed at 700 °C mainly consists of orthorhombic τ_2. As the sample annealed at 500 °C does not show any change in comparison with the as cast state, the sample first heat treated at 900 °C (containing the tetragonal modification) was subsequently annealed at 500 °C: the tetragonal modification transformed to the orthorhombic modification. However, some alloys from the triangle (Fe) – NdSb – τ_2 show the tetragonal modification at 1000 °C and at higher temperatures (1025 °C and 1050 °C) whilst some samples also show the orthorhombic modification at 1000, 1025 °C. Another point to note is that quenching rates are critical to obtain the tetragonal modification. We furthermore cannot exclude the possibility of compositional polymorphism in addition to temperature polymorphism. Therefore it is presently very difficult to interpret the complex behaviour of polymorphism of the τ_2

phase. At 800 °C both modifications are observed: the orthorhombic modification is in equilibrium with $Fe_{2-x}Sb$ and (α-Fe) whilst the tetragonal modification is observed in equillibrium with NdSb and (α-Fe).

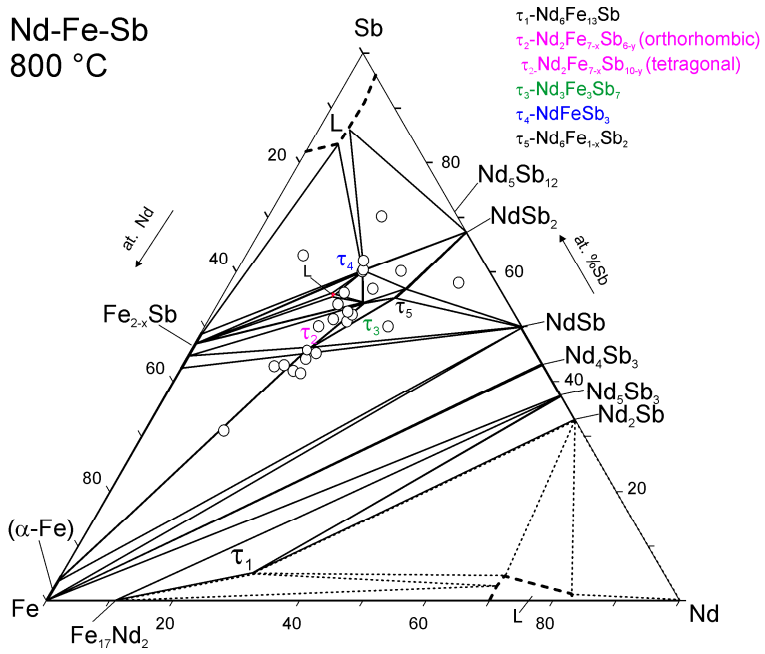

Figure 1. Isothermal section of Nd-Fe-Sb system at 800 °C.

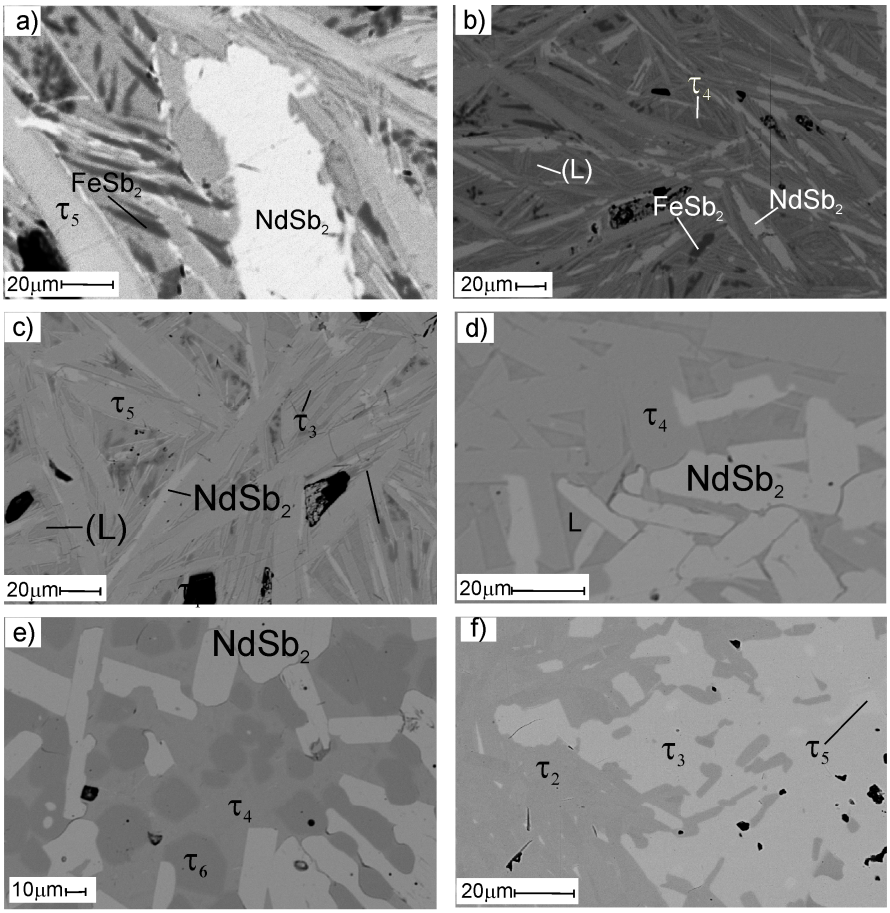

Figure 2. Microstructure of Nd-Fe-Sb alloys: a), b) and c) $Nd_{16}Fe_{12}Sb_{70}$ as cast; d) $Nd_{16}Fe_{12}Sb_{70}$ 800 °C; e) $Nd_{16}Fe_{12}Sb_{70}$ 700 °C; f) $Nd_{22}Fe_{27}Sb_{51}$ 800 °C.

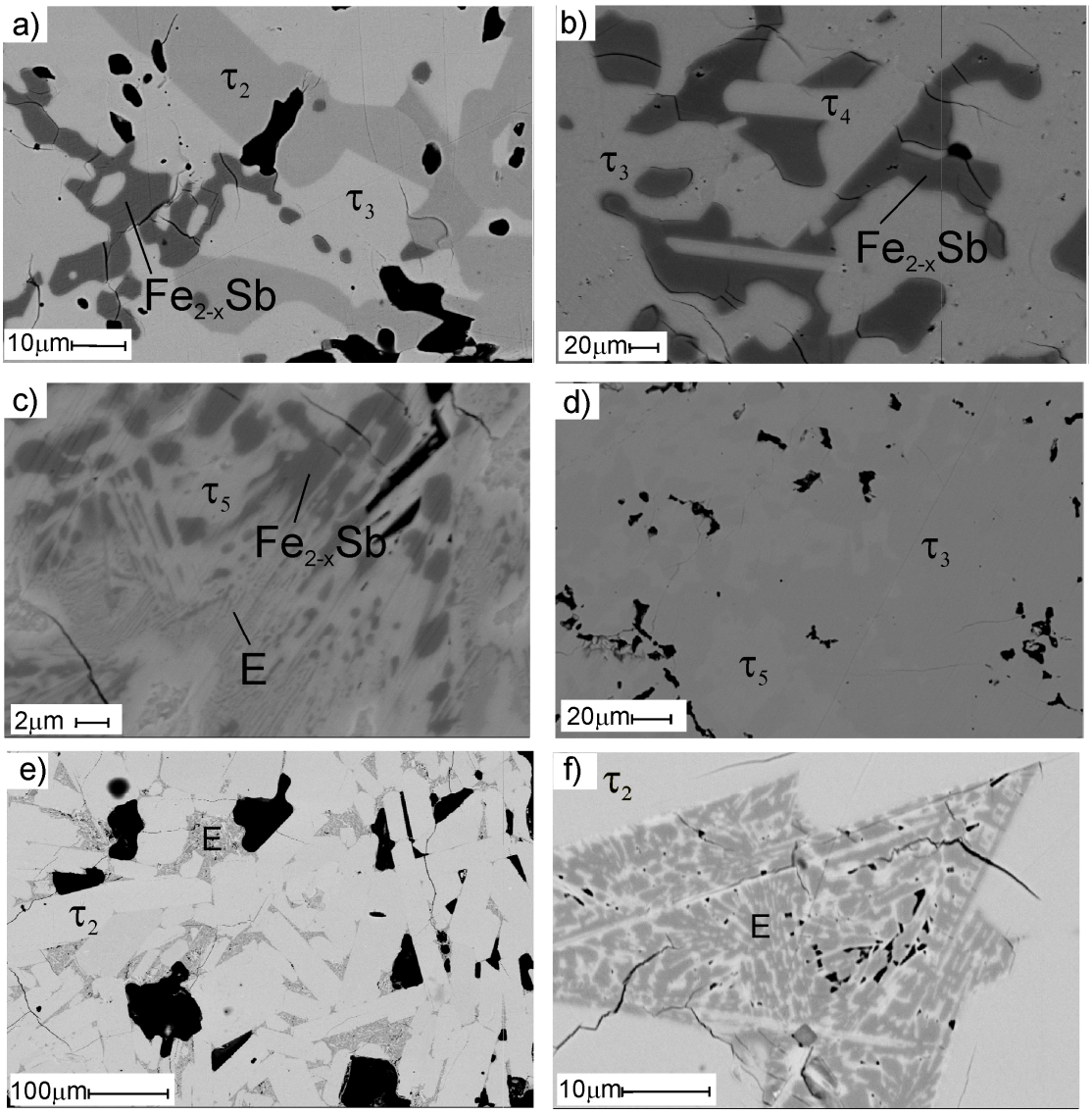

Figure 3. Microstructure of Nd-Fe-Sb alloys: a) $Nd_{21}Fe_{26}Sb_{53}$ (800 °C); b)$Nd_{19}Fe_{25}Sb_{56}$ (800 °C); c) $Nd_{19}Fe_{27}Sb_{54}$ (as cast); d) $Nd_{23}Fe_{20}Sb_{57}$ (800 °C); e) and f) $Nd_{20}Fe_{35}Sb_{45}$ (cycles (1025-1075 °C).

Table 1: Crystal structure data for relevant solid phases in the systems Nd-Fe-Sb.

Phase	**Pearson Symbol**	**Space group**	**Structure Type**	**Lattice Parameters (nm)**			**Reference**
				a	b	c	
(Sb)	hR2	$R\bar{3}m$	As	0.43084	-	1.1274	[34]
(α-Fe)	cI2	$Im\bar{3}m$	W	0.28665	-	-	[38l]
$Fe_{2-x}Sb$ (x=0.73)	hP6	$P6_3/mmc$	Ni_2In	0.4124	-	0.5173	[39]
NdSb	cF8	$Fm\bar{3}m$	NaCl	0.6321	-	-	[38]
$NdSb_2$	oC24	*Cmca*	$SmSb_2$	0.6207(4)	0.6098(4)	1.808(1)	[38]
Nd_4Sb_3	cI28	$I\bar{4}3d$	Th_3P_4	0.9370(8)	-	-	[38]
Nd_5Sb_3	hP16	$P6_3/mcm$	Mn_5Si_3	0.9199(8)	-	0.6454(5)	[38]
Nd_2Sb	tI12	$I4/mmm$	La_2Sb	0.451	-	1.761	[38]
$Nd_{9-x}Sb_{21-y}$	mC62	*Cc*	Nd_5Sb_{12}	2.8452(16)	0.4247(8) β = 95.42	1.3459(9);	[36] x=0.7: y=1.02

Phase	Pearson Symbol	Space group	Structure Type	Lattice Parameters (nm)			Reference
$Fe_{17}Nd_2$	hR57	$R\bar{3}mh$	Th_2Zn_{17}	0.85782	-	1.24611	[39]
$Nd_6Fe_{13}Sb$ (τ_1)	tI80	*I4/mcm*	$Nd_6Fe_{13}Si$	0.8090(1)	-	2.3192(6)	[29]
$La_2Fe_{5-x}Sb_{10-y}$	tI26	I4/mmm	$La_2Fe_{5-x}Sb_{10-y}$	0.43374(3)	-	2.6272(7)	This work x=1.125; y= 5.085
$Nd_2Fe_{7-x}Sb_{6-y}$ (τ_2)	oI26	Immm	$Nd_2Fe_{7-x}Sb_{6-y}$	0.42632(6)	0.43098(7)	2.5823(3)	This work x=3.04; y=1.03
$Nd_3Fe_3Sb_7$(τ_3)	hP26	$P6_3/m$	$Nd_3Fe_3Sb_7$	1.31808(3)		0.41819(3)	This work
$NdFeSb_3$(τ_4)	oP40	Pbcm	$LaPdSb_3$	1.2677(3)	0.61613(7)	1.2132(4)	This work
$NdFe_{1-x}Sb_2$ (τ_5)	tP8	P4/nmm	$ZrCuSi_2$	0.43514(6)	-	0.96518(13)	[30] x = 0.4
$NdFe_4Sb_{12}$ (τ_6)	cI34	$Im\bar{3}$	$LaFe_4P_{12}$	0.9130(1)	-	-	[37]

Table 2: Three-phase equilibria and lattice parameters for Nd–Fe–Sb (800°C).

Phase equilibria	Phase	Composition by EPMA at. %			Lattice Parameter (nm)		
		Nd	Fe	Sb	a	b	c
L-$Fe_{1.27-}$Sb-τ_4	(Sb)	-	-	-	0.43090(8)	-	1.1269(3)
	$Fe_{2-x}Sb$	-	-	-	0.40635(2)	-	0.51394(4)
	τ_4	-	-	-	1.2677(3)	0.61613(7)	1.2132(4)
L-$NdSb_2$-τ_4	(Sb)	1.8	1.2	97.1	0.43097(4)	-	1.1273(2)
	$NdSb_2$	32.9	0.3	66.8	0.6224(1)	0.6097(1)	1.8106(5)
	τ_4	19.8	18.4	61.9	1.2673(2)	0.61604(6)	1.2134(2)
$NdSb_2$-τ_4-τ_5	$NdSb_2$	32.8	-	67.2	0.6235(2)	0.6097(2)	1.8105(8)
	τ_4	-	-	-	1.2675(3)	0.61630(8)	1.2137(2)
	τ_5	28.0	14.6	57.4	0.43503(3)	-	0.9651(2)
τ_3-τ_4-τ_5	τ_3	23.1	23.6	53.3	1.3185(1)	-	0.41820(9)
	τ_4	-	-	-	1.2681(2)	0.61647(8)	1.2131(3)
	τ_5	27.9	16.0	56.1	0.43535(5)	-	0.9667(3)
$NdSb_2$-NdSb-τ_5	$NdSb_2$	-	-	-	0.6227(2)	0.6111(2)	1.814(1)
	NdSb	-	-	-	0.6355(3)	-	-
	τ_5	-	-	-	0.43509(4)	-	0.9649(2)
NdSb-τ_5-τ_2	NdSb	49.7	0.1	50.2	0.63378(4)	-	-
	τ_5	-	-	-	0.4346(5)	-	0.9710(6)
	τ_2	18.2	36.5	45.3	0.4302(1)	0.4286(1)	2.573(4)
(Fe)-NdSb-τ_2	(Fe)	0.1	96.0	3.9	-	-	-
	NdSb	48.5	0.5	51.0	0.6344(1)	-	-
	τ_2	18.0	35.9	46.1	0.42903(4)	-	2.5821(5)
(Fe)-Fe_{2-x}Sb-τ_2	(Fe)	-	-	-	-	-	-
	$Fe_{2-x}Sb$	0.4	55.9	43.7	0.41259(6)	-	0.5172(2)
	τ_2	18.0	35.6	46.4	0.42726(9)	0.4301(1)	2.5843(5)
Fe_{2-x}Sb-τ_2-τ_3	$Fe_{2-x}Sb$	-	53.1	47.0	0.411(1)	-	0.5149(3)
	τ_2	18.5	34.9	46.6	-	-	-
	τ_3	22.5	23.2	54.3	1.3185(2)	-	0.41846(4)
τ_2-τ_3-τ_5	τ_2	18.3	34.4	46.8	-	-	-
	τ_3	22.6	23.7	53.7	1.3185(2)	-	0.41846(4)
	τ_5	27.49	16.07	56.43	0.4368(2)	-	0.9648(9)
Fe_{2-x}Sb -τ_3-τ_4	$Fe_{2-x}Sb$	-	-	-	0.40742(2)	-	0.5145(2)
	τ_3	-	-	-	1.31899(8)	-	0.41814(4)
	τ_4	-	-	-	1.2680(4)	0.61658(9)	1.2131(3)

9.3.3 The crystal structure of τ_2

An unknown x-ray spectrum was observed for the alloy with nominal composition $Nd_{20}Fe_{35}Sb_{45}$ in as cast as well as in specimens annealed at 500, 800, 900 and 1000 °C. EMPA analysis reveals a ternary composition ~$Nd_{18.0}Fe_{36.5}Sb_{45.5}$. The ternary compound in this composition range was reported as τ_2-$NdFe_{2-x}Sb_2$ (orthorhombic) or $NdFe_3Sb_2$ (tetragonal) [6] and more recently as ~$NdFe_{2.5}Sb_2$ (unknown structure) by [10] in the isothermal section of Nd-Fe-Sb at 773 K. Whilst in the La-Fe-Sb and Pr-Fe-Sb systems at 773 K, the ternary compounds $LaFe_2Sb_2$ (a=0.45518, b=0.77737, 0.84207, β=128.3946) [11] and $PrFe_2Sb_2$ (a=0.60719, b=0.60867, 1.33051, β=103.1) [12] were tentatively indexed as monoclinic phases with Ga_2S_3 prototype (S. G. *Cc*), we were unable to index or refine the observed XRPD (mentioned above) with the Ga_2S_3 structure type, however, the observed pattern can be successfully indexed with the structure model given by [6] for τ_2-$NdFe_{2-x}Sb_2$ (orthorhombic) or $NdFe_3Sb_2$ (tetragonal). As discussed before these structure solutions were not satisfactory therefore attempts were made to select single crystal fragments from crushed alloys annealed at 1000 °C for about 10 days. These experiments were unsuccessful as the alloys yielded only very small crystallites. Cyclic heat treatment (slow heating and cooling ~10 °C/hr between 1075 and 1025 °C) gave very big grains of the phase in equilibrium with liquid (Figure 3e and f) but single crystal quality was poor. XRPD patterns show line splitting and a reduced intensity for some diffraction lines e.g. 2θ ~42.1° as compared to the powder pattern of the alloy $La_{18}Fe_{36}Sb_{45.5}$ which indicate a structural transformation. Single crystals were finally found from the alloys $La_{18}Fe_{36}Sb_{46}$ and $Nd_{19}Fe_{39}Sb_{42}$ annealed at 990 °C for 30 days. Inspection on a GADDS instrument reveals tetragonal symmetry for the crystal selected from $La_{18}Fe_{36}Sb_{46}$ (a ~ 0.434, c ~ 2.63 nm) and orthorhombic symmetry for the crystal selected from sample $Nd_{19}Fe_{39}Sb_{42}$ (a ~ 0.42, b ~ 0.43, c ~ 2.58 nm).

9.3.3.1 Crystal Structure of tetragonal τ_2 ($La_2Fe_{5-x}Sb_{10-y}$; x= 1.125; y=5.085)

Single crystal X-ray intensity data confirm a body centered tetragonal unit cell with a = 0.43410 nm, c = 2.63070 nm. The observed systematic extinctions suggest space groups *I*4/*mmm*, *I*-4*m*2, *I*-42*m*, *I*4*mm*, *I*422, *I*4/*m*, *I*-4, *I*4. Initial atomic positions for the highest symmetry *I*4/*mmm* were found from a three dimensional Patterson map. Although the

residual value approaches R_F = 0.045 a residual electron density of about 8 $e^-/Å^3$ was left close to the Wyckoff position 2*b* (0, 0, ½) occupied by Sb. Structure solution in space group *I*4 (lowest symmetry) also terminated with same electron density near the Wyckoff position 2b. Furthermore a test for higher symmetry prompted space group *I*4/*mmm*. The difference Fourier map around the site 2b (0, 0, ½,) (Figure 4a,b) revealed that the electron density on this site is not spherical but indicates an off-centre atom position (Figure 4b). Therefore the site 2b was split into 2 sites 4e and 8j for which partial occupancies were refined to 0.168(3) and 0.145(4) respectively and result in a final R_F value of 0.025 and residual electron densities 3.15 e^-/-2.81 $e^-/Å^3$. Interestingly the sum of the occupancies of site 4e and 8j corresponds to ~100 % of the occupancy in the 2b site. The effect of these two sites which appear as a cluster (Figure 5) is reflected in the anisotropy of neighbouring Fe2 at the 8g site. It seems that the split of these sites is originated by a partial occupancy of the Fe2-atoms. A difference Fourier map for the site 8g (Figure 6) reveals simple anisotropy. All crystallographic data and interatomic distances are given in Table 3. Although overall interatomic distances agree well with the sum of the atomic radii of the elements, the very short interatomic distances encountered, however, (Table 3b) correspond to the sites with partial occupancies. The resulting formula $La_2Fe_{5-x}Sb_{10-y}$ (x=1.125, y=5.085; $La_{18.5}Fe_{35.9}Sb_{45.5}$ in at. %) agrees well with the EMPA results of $La_{21.3}Fe_{37.7}Sb_{42.3}$. The structural model complies very well with observed XRPD pattern. Although the present structural model for $La_2Fe_{5-x}Sb_{10-y}$ confirm the main features of the structure model developed by [6] for "$NdFe_3Sb_2$" the main differences concern (i) the split of the 2b site (Fe-atoms in the model by [6]) into 4e and 8j (Sb-atoms) and (ii) the defect Fe-site 8g resulting in a different formula. The XRPD patterns of the almost single phase alloys $Nd_{18.5}Fe_{36}Sb_{45.5}$ and $Ce_{20}Fe_{35}Sb_{45}$ (both quenched from 1000 °C) refined successfully (Table 3) employing this structural model and thereby confirm isotypism of these compounds with the $La_2Fe_{5-x}S_{10-y}$.

Table 3a: X-Ray single crystal data for $La_2Fe_{5-x}Sb_{10-y}$ and Rietveld refinement for XRPD profiles of the isotypic compounds with Ce and Nd; standardized with program *Structure Tidy* [40]. Radiation: MoKα/CuKα). Anisotropic displacement parameters/Temperature factor [in $10^2 nm^2$].

Parameter/compound	**$La_2Fe_{5-x}Sb_{10-y}$ (XRSCD) (x = 1.125; y = 5.085)**	**$Nd_2Fe_{5-x}Sb_{10-y}$ (XRPD) (x = 1.48; y = 5.12)**	**$Ce_2Fe_{5-x}Sb_{10-y}$ (XRPD) (x = 1.16; y = 5.08)**
Prototype	$La_2Fe_{5-x}Sb_{5-y}$	$La_2Fe_{5-x}Sb_{5-y}$	$La_2Fe_{5-x}Sb_{5-y}$
Space group	*I4/mmm*	I4/mmm	I4/mmm
a ; c (nm), Ge standard	0.43374(3); 2.6272(7)	0.42897(2); 2.5693(4)	0.43098(3); 2.5994(6)
Z	2	2	2
Reflections measured	$353 \geq 4\sigma(F_o)$ of 379	122	123
Θ range	2≤2Θ≤70; 250 sec/frame	8≤2Θ≤100	8≤2Θ≤100
Total number of frames	515; 10 sets	-	-
Number of variables	22	24	24
$R_F^2 = \Sigma\lvert F_o^2 - F_c^2\rvert / \Sigma F_o^2$ / $R_F = \Sigma\lvert F_o - F_c\rvert / \Sigma F_o$	0.0250	0.0743	0.0594
$R_I = \Sigma\lvert I_o - I_c\rvert / \Sigma I_o$	R_{Int} = 0.0355	0.0846	0.0770
$R_{wP} = [\Sigma w_i\lvert y_{oi} - y_{ci}\rvert^2 / \Sigma w_i\lvert y_{oi}\rvert^2]^{1/2}$	wR2 = 0.071	0.0285	0.0360
$\chi^2 = (R_{wP}/R_e)^2$	GOF = 1.163	6.93	23.1
Mosaicity	<4.5	-	-
$R_e = [(N-P+C)/\Sigma w_i y^2_{oi})]^{1/2}$	-	0.0108	0.0075
Extinction	0.0013(2)	-	-
$R_P = \Sigma\lvert y_{oi} - y_{ci}\rvert / \Sigma\lvert y_{0i}\rvert$	-	0.0202	0.025
Residual density $e^-/Å^3$; max; min	3.15; -2.81	-	-
Atom parameters			
RE1 **in 4*e* (0, 0, *z*); *z*; Occ.**	0.34739(3); 1.01(2)	0.34745(4); 1.01(2)	0.34786(6); 1.01(2)
$U_{11}=U_{22};U_{33}$; $U_{eq.}$ or B_{iso}	0.0107(2); 0.0129(7); 0.0115(2)	1.09(4)	0.55(6)
Sb1 in 4*e* (0, 0, *z*); *z*; Occ.	0.10786(3); 1.01(2)	0.11071(4); 1.01(2)	0.10980(6); 1.01(2)
$U_{11}=U_{22};U_{33}$; $U_{eq.}$ or B_{iso}	0.0115(2); 0.0135(8); 0.0122(2)	1.01(3)	0.64(5)
Sb2 in **4*d* (0, ½ , ¼); Occ.**	1.01(2)	1.01(2)	1.01(2)
$U_{11}=U_{22};U_{33}$; $U_{eq.}$ or B_{iso}	0.0118(2); 0.0122(3); 0.0120(2)	1.01(3)	0.69(5)
Sb3 in **4*e* (0, 0, *z*); *z*; Occ.**	0.4851(5); 0.168(3)	0.4774(4); 0.12(5)	0.4763(7): 0.10(1)
sof; U_{11} or B_{iso}	0.0210(8); 0.029(2)	1.01(3)	0.56(5)
Sb4 **in 8*j* (*x*, ½ , 0); *x*; Occ.**	0.417(2); 0.145(4)	0.432(2); 0.16(8)	0.424(2); 0.18(9)
sof; U_{11} or B_{iso}	0.362(9); 0.029(2)	1.01(3)	0.35(5)
Fe1 in 2*a* (0, 0, 0); Occ.	1.01(2)	1.01(2)	1.02(2)
$U_{11}=U_{22};U_{33}$; $U_{eq.}$ or B_{iso}	0.0167(7); 0.0124(9); 0.0152(5)	1.42(7)	1.57(9)
Fe2 in 8*g* (0, ½, *z*); *z*; Occ.	0.04970(7); 0.719(7)	0.0540(2); 0.63(4)	0.0517(2); 0.71(4)
$U_{11};U_{22};U_{33}$ or B_{iso}	0.065(2); 0.0102(9); 0.0104(7)	1.94(7)	1.18(9)
$U_{eq.}$	0.284(7)	-	-
	Principal mean square atomic displacements U		
La1	0.0130; 0.0107; 0.0107	-	-
Sb1	0.0136; 0.0115; 0.0115	-	-
Sb2	0.0122; 0.0119; 0.0119	-	-
Fe1	0.0167; 0.0167; 0.0124	-	-
Fe2	0.0647; 0.0104; 0.0102	-	-

Table 3b: Interatomic distances [nm] for $La_2Fe_{5-x}Sb_{10-y}$ (x = 1.125; y = 5.085); Standard deviation ≤0.0004.

Sb2	-4Sb2	0.3070	Fe2	-2Sb4	0.2233		-4Fe2	0.2756
	-4La5	0.3359		-2Sb3	0.2356		-4Fe1	0.3094
Sb1	-4Fe2	0.2656		-2Fe1	0.2534		-1La5	0.3623
	-4La5	0.3288		-4Sb4	0.2559		-4Sb1	0.3925
	-4Sb3	0.3925		-1Fe2	0.2615	Sb4	-2Sb4	0.0509
Fe1	-8Fe2	0.2540		-2Sb1	0.2656		-2Sb3	0.0531
	-8Sb4	0.2827		-2Sb3	0.2756		-1Sb4	0.0719
	-2Sb1	0.2837		-2Sb4	0.2848		-6Fe2	0.2233
	-8Sb3	0.3094		-4Fe2	0.3070		-2Fe1	0.2827
	-8Sb4	0.3334		-2La5	0.3470		-2Fe2	0.2848
La1	-4Sb1	0.3288	Sb3	-4Sb4	0.0531		-2Fe1	0.3334
	-4Sb2	0.3358		-1Sb3	0.0782		-1Sb4	0.3621
	-4Fe2	0.3470		-4Fe2	0.2356		-4Sb4	0.3997
	-1Sb3	0.3623						

9.3.3.2 Crystal Structure of the orthorhombic τ_2 ($Nd_2Fe_{7-x}Sb_{6-y}$; x=3.04, y=1.03)

X-ray intensity data collected for a crystal selected from the sample with nominal composition $Nd_{19}Fe_{39}Sb_{42}$ confirm orthorhombic symmetry (a=0.42670, b=0.43100, c=2.58560) and a body centred Bravias lattice. Extinction conditions hint to the point group mmm, suggesting space groups *Immm*, *Imm*2, *I*2*mm*, *Im*2*m*, *Imm*2, *I*222, $I2_12_12_1$. The structure was successfully solved in the highest symmetry space group *Immm* using direct methods, whilst the structure solution by [6] was performed in space group Imm2. A huge anisotropy (U_{11}:U_{22}=1:8) was observed for Fe3 atoms at the 4j site. A difference Fourier map for the electron density (Figure 7) at this site suggested a split of the site whilst the difference Fourier map for Fe2 yields normal anisotropy. Therefore the 4j site was replaced by the 8l site (0, *y*, *z*), which on refinement reveals a partial occupancy of 0.404. The final least squares cycle gives R_F = 0.032 at a residual electron density of 2.58/-2.80 e-/Å^3. Refinement of the occupancies reveals partial occupation for the site 4i (occ=0.486) occupied by Sb3 and 4j occupied by Fe2 (occ=0.672) resulting in a formula $Nd_2Fe_{7-x}Sb_{6-y}$ (x=3.04, y = 1.025; $Nd_{18.3}Fe_{36.2}Sb_{45.5}$ in at %), which agrees very well with the microprobe analysis $Nd_{18.0}Fe_{35.9}Sb_{46}$. All crystallographic data and interatomic distances are given in Table 4a, b. Partial occupancy of the three sites is reflected from very short interatomic distances (Table 4b). The structural model fits very well with the XRPD pattern.

The transformation from tetragonal to orthorhombic symmetry can be seen in x-ray powder patterns where a reduction in intensity and the broadening or splitting of peaks in the XRPD patterns of the samples quenched from different temperatures is observed (Figure 8). Reflections (200) (105) and (107) in tetragonal space group split into (200) and (020), (015) and (105), (017) and (107) reflections respectively in orthorhombic symmetry. Broadening of peaks observed in most of the XRPD patterns can be associated with the presence of both modifications.

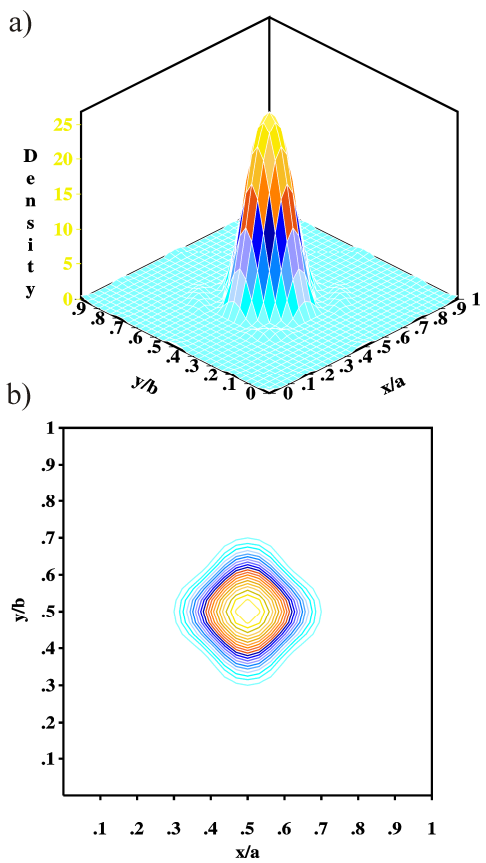

Figur 4. Fourier map for electron density at 2b (0, 0, ½) ; a) three dimensional view; b) Projection in x-y plane.

Table 4a: X-Ray single crystal data for $Nd_2Fe_{7-x}Sb_{6-y}$ (τ_2); standardized with program *Structure Tidy* [40]. Radiation: MoKα; 2Θ range (°) = 2≤2Θ≤70; ω-scans, scan width 2° = 140 sec/frame; Total number of frames & sets=564 & 11; Anisotropic displacement parameters [in $10^2 nm^2$].

Parameter/compound	**$Nd_2Fe_{7-y}Sb_{6-y}$ (x= 3.04, y=1.03)**
Prototype	$Nd_2Fe_{7-y}Sb_{6-y}$
Space group	Immm
a ; c [nm], Ge standard	0.42632(6); 0.43098(7); 2.5823(3)
Z	2
Reflections measured	592≥4σ(F_o) of 646
Number of variables	34
Mosaicity	<4.5
$R_F^2 = \Sigma\|F_o^2-F_c^2\|/\Sigma F_o^2$	0.0324
R_{Int}	0.0486
wR2	0.0898
GOF	1.131
Extinction	0.0009(3)
Residual density $e^-/Å^3$; max; min	2.58; -2.80
Atom parameters	
Nd1 **in 4*i* (0, 0, *z*); *z;* Occ.**	0.15348(2); 1.01(2)
U_{11};U_{22};U_{33}; $U_{eq.}$	0.0175(3); 0.0178(5); 0.0144(2); 0.0166(2)
Sb1 in 4*i* (0, 0, *z*); *z;* Occ.	0.38842(2); 1.01(2)
U_{11}; U_{22};U_{33}; $U_{eq.}$	0.0175(3); 0.0180(6); 0.0135(2); 0.0163(2)
Sb2 in **4*j* (½, 0, , *z*); Occ.**	0.25023(2); 1.02(2)
U_{11};U_{22};U_{33} ; $U_{eq.}$	0.0180(3); 0.0181(6); 0.0130(3); 0.0164(2)
Sb3 in **4*i* (0, 0, *z*); *z;* Occ.**	0.01678(7); 0.486(4)
U_{11};U_{22};U_{33}; $U_{eq.}$	0.042(1); 0.0324(9); 0.0199(6); 0.0316(5)
Fe1 **in 2*c* (½, ½ , 0); Occ.**	1.01(2)
U_{11};U_{22};U_{33} ; $U_{eq.}$	0.0207(9); 0.023(1); 0.0146(8); 0.0196(4)
Fe2 in 4*j* (½, 0, *z*); Occ.	0.0513(1); 0.672(9)
U_{11};U_{22};U_{33} ; $U_{eq.}$	0.062(2); 0.021(1); 0.0133(1); 0.0320(9)
Fe3 in 8*l* (0, *y, z;) y; z;* Occ.	0.4432(7); 0.05186(9); 0.404(5)
U_{11};U_{22};U_{33} ; $U_{eq.}$	0.015(1); 0.029(2); 0.0135(9); 0.0192(9)
Principal mean square atomic displacements U	
Nd1	0.0178; 0.0175; 0.0144
Sb1	0.0180; 0.0175; 0.0135
Sb2	0.0181; 0.0180; 0.0130
Sb3	0.0425; 0.0324; 0.0199
Fe1	0.0235; 0.0207; 0.0146
Fe2	0.0619; 0.0209; 0.0133
Fe3	0.0288; 0.0154; 0.0135

Table 4b: Interatomic distances [nm] for $Nd_2Fe_{7-x}Sb_{6-y}$ (x = 3.04: y= 1.03); Standard deviation ≤0.0004.

Nd1	-4Sb1	0.3220		-8Sb3	0.3063		-2Nd1	0.3396
	-2Fe3	0.3249	Sb3	-1Sb3	0.08678		-4Fe3	0.3913
	-2Sb2	0.3288		-2Fe3	0.2115	Fe3	-1Fe3	0.0489
	-2Sb2	0.3293		-2Fe2	0.2313		-1Sb3	0.2115
	-2Fe2	0.3396		-2Fe3	0.2565		-2Fe1	0.2532
	-1Sb3	0.3535		-2Fe3	0.2607		-1Sb3	0.2565
	-2Fe3	0.3558		-2Fe2	0.2766		-1Sb3	0.2607
Sb1	-4Fe3	0.2645		-2Fe3	0.2984		-2Sb1	0.2645
	-2Fe2	0.2660		-4Fe1	0.3063		-1Fe3	0.2682
	-1Fe1	0.2885		-1Nd1	0.3535		-1Fe3	0.2726
	-4Nd1	0.3220		-4Sb1	0.3899		-2Fe2	0.2864
	-4Sb3	0.3899	Fe2	-2Sb3	0.2313		-1Sb3	0.2984
Sb2	-4Sb2	0.3032		-2Fe1	0.2530		-2Fe2	0.3211
	-2Nd1	0.3288		-1Fe2	0.2653		-1Nd1	0.3249
	-2Nd1	0.3293		-2Sb1	0.2659		-1Nd1	0.3558
Fe1	-4Fe2	0.2530		-2Sb3	0.2766		-1Fe3	0.3821
	-8Fe3	0.2532		-4Fe3	0.2864		-2Fe2	0.3913
	-2Sb1	0.2885		-4Fe3	0.3211			

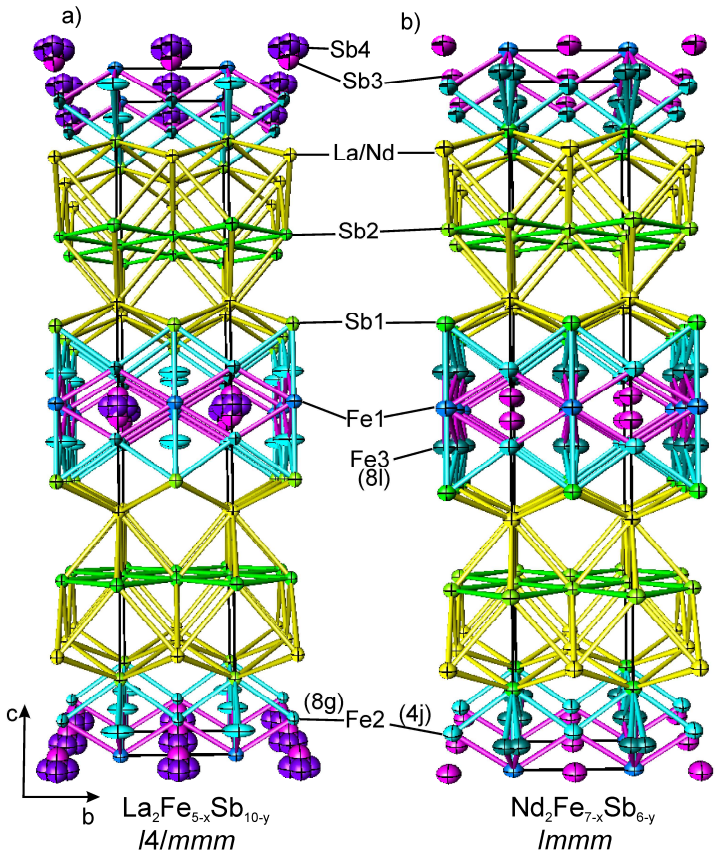

Figure 5. Extended view of crystal structure of $La_2Fe_{5-x}Sb_{10-y}$ (x = 1.125; y = 5.085) and $Nd_2Fe_{7-x}Sb_{6-y}$ (x= 3.04; y =1.03).

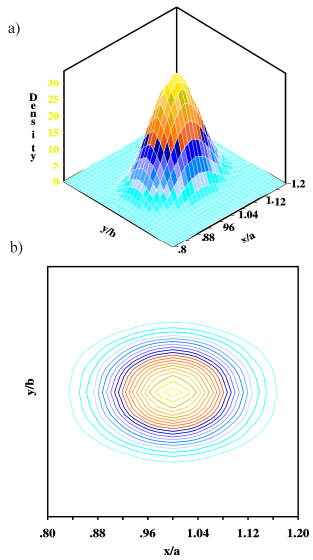

Figure 6. Fourier map for electron density at Fe2 in 8g site; a) three dimensional view; b) projection in x-y plane.

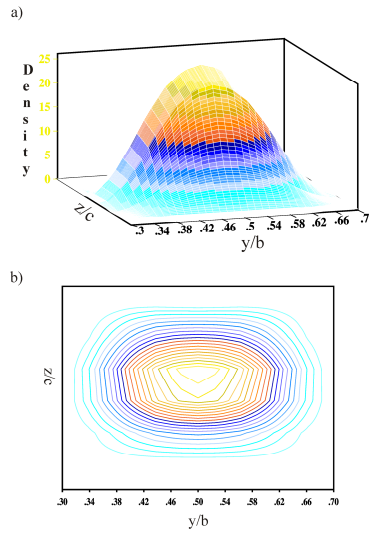

Figure 7. Fourier map for electron density at Fe3 in 8l site; a) three dimensional view; b) Projection in y-z plane.

9.3.3.3 Structural relations among the τ_2 modifications

The crystal structures of $La_2Fe_{5-x}Sb_{10-y}$ (tetragonal), and $Nd_2Fe_{7-x}Sb_{6-y}$ (orthorhombic) are shown in Figure 5. Both structures are closely related to each other forming almost similar coordination polyhedra (Fig.9). Rare earth atoms are at the centres of Archimedean antiprisms with 8 surrounding Sb atoms. Similar archimedean polyhedra are formed around Sb1, which has four rare earth and four Fe neighbours. Sb2 is in a tetrahedral environment of rare earth atoms while Fe1 has a coordination sphere of 10 atoms (see Figure 9). Tetragonal and orthorhombic structures can be related via group-subgroup relations in the Bärnighausen formalism [41, 42] as a 'translationengleiche' symmetry reduction of index 2 (Figure 10). Ideally, the 8g site in I4/mmm (occupied by Fe2) should split into two 4j sites but actually a distortion is observed for one 4j site which was replaced by a partially occupied 8l site as discussed above.

If we consider the ideal Wyckoff sequence 2c 34e 4d 8g, $La_2Fe_{5-x}Sb_{10-y}$ seems to be isotypic with the $Zr_3Cu_4Si_6$-type [43] with exactly the same arrangement of atoms in the unit cell as in $La_2Fe_{5-x}Sb_{10-y}$ (except for Sb4 in the 8j site). Structures of τ_2 whether tetragonal or orthorhombic like $Zr_3Cu_4Si_6$ can be considered as intergrowth of slabs of the $ZrCuSi_2$ type and cubic face-centred Fe (Figure 11). There are many structure types with space group *I*4/*mmm* e.g $U_2Cu_4As_5$, $Pd_3Ti_{0.667}Pb_{0.33}$, $Eu_2Pt_7AlP_3$, Ce_2NiGa_{10} which are closely related to these structures and are interpreted as composed of slabs of $BaAl_4$ and CaF_2 (see e.g. [40]). It seems that the presence of rare earths results in a distortion of the ideal position of electron density in both $La_2Fe_{5-x}Sb_{10-y}$ and $Nd_2Fe_{7-x}Sb_{6-y}$.

Isotypism with $La_2Fe_{5-x}Sb_{10-y}$ is observed also for $Ce_2Fe_{5-x}Sb_{10-y}$ compound with Pr exhibits both modifications orthorhombic and tetragonal. The plot of lattice parameters and volume vs. rare-earths shows the lanthanide contraction as was also shown by [6] (Figure 12). From the variation of lattice parameters one can expect a partial Ce^{+4} state for $Ce_2Fe_{5-x}Sb_{10-y}$.

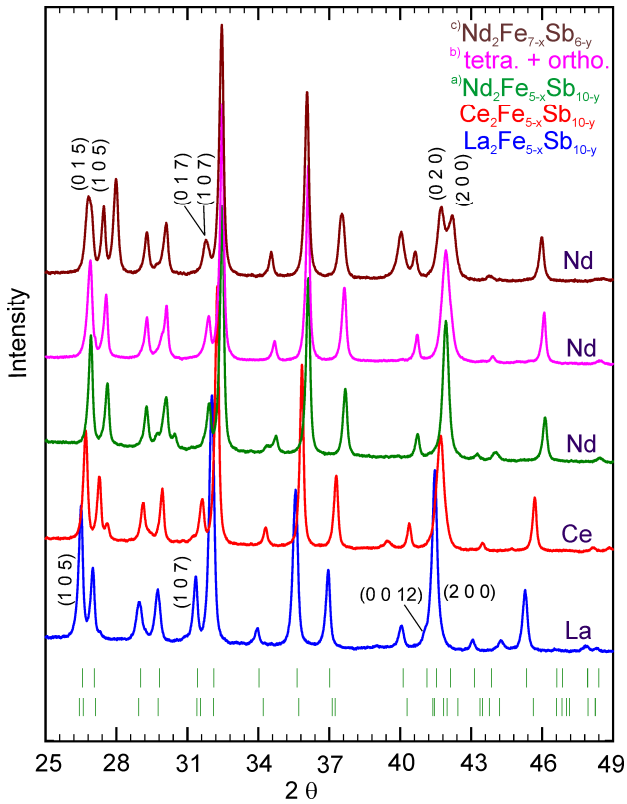

Figure 8. XRPD patterns of $RE_2Fe_{5-x}Sb_{10-y}$ (RE= La, Ce, Nd) and $Nd_2Fe_{7-x}Sb_{6-y}$: a) tetragonal; b) orthorhombic + tetragonal c) orthorhombic.

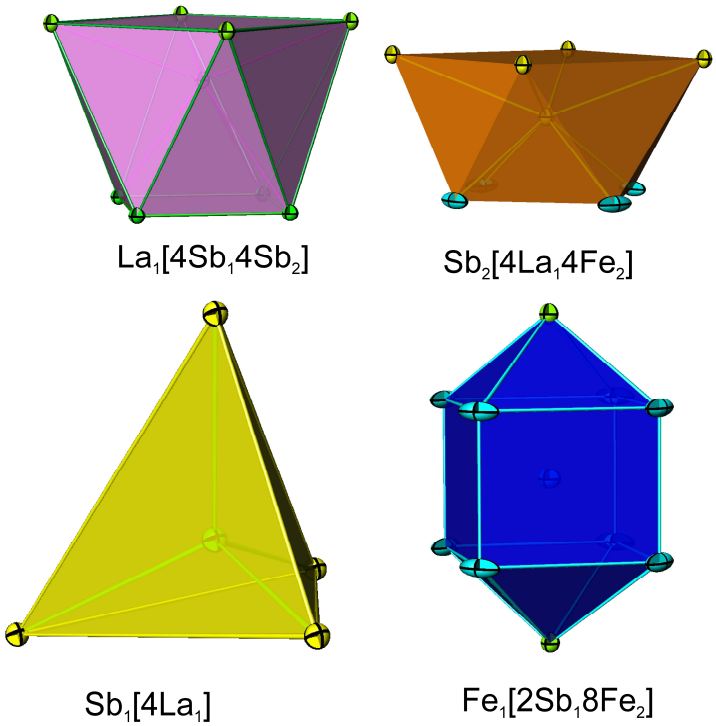

Figure 9. Atomic envirnment of La1, Sb1, Sb2 and Fe1 in crystal structure of $La_2Fe_{5-x}Sb_{10-y}$ (x = 1.125; y = 5.085).

$I4/m2/m2/m$	La1:4*e*	Sb1:4*e*	Sb2:4*d*	Sb3:4*e*	Fe1:2*a*	Fe2: 8g	Sb4: 8j
	4 *m m*	4 *m m*	$\bar{4}$ *m 2*	4 *m m*	4/*m m m*	2 *m m* .	*m* 2 *m* .
$La_2Fe_{5-x}Sb_{10-y}$	0	0	0	0	0	0	0.417
	0	0	½	0	0	½	½
	0.3474	0.1079	¼	0.4851	0	0.0497	0

t(2)
0, 0, 1/2

$I2/m2/m2/m$	Nd1:4*i*	Sb1:4*i*	Sb2:4*j*	Sb3:4*i*	Fe1:2*c*	Fe2:4*j*	Fe3:4*j*	Sb4:4e	Sb4:4g
	m m 2	*m m* 2	*m m* 2	*m m* 2	*m m m*	*m m* 2	*m m* 2	2 *m m*	*m* 2 *m*
$Nd_2Fe_{7-x}Sb_{6-y}$	0	0	½	0	½	½	½	*x*	0
	0	0	0	0	½	0	0	0	*y*
	0.1535	0.3884	0.2502	0.0168	0	0.0513	*z*	0	0

Figure 10. Group-subgroup relation for $La_2Fe_{5-x}Sb_{10-y}$ (x = 1.125; y = 5.085) and $Nd_2Fe_{7-x}Sb_{6-y}$ (x= 3.04; y =1.03) in Bärnighausen formalism [41, 42]. Fe3:4j in $Nd_2Fe_{7-x}Sb_{6-y}$ was replaced by Fe3:8l and Sb4: 4e and 4j in $Nd_2Fe_{7-x}Sb_{6-y}$ are vacant sites (see text).

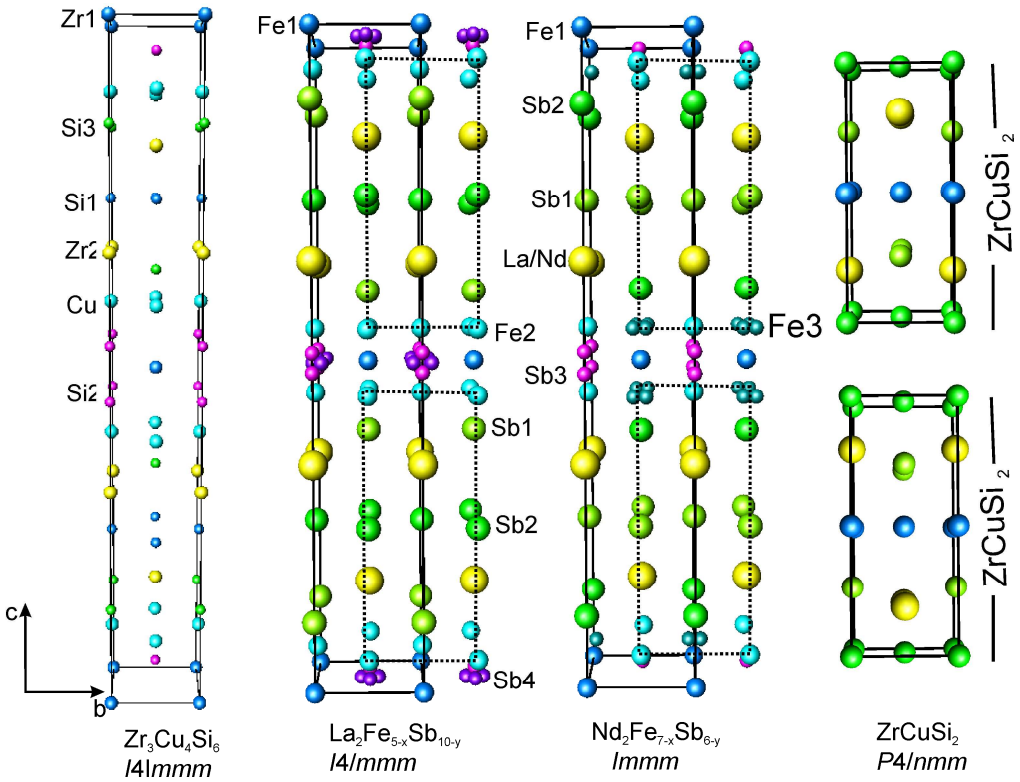

Figure 11. Structural relations of $La_2Fe_{5-x}Sb_{10-y}$ and $Nd_2Fe_{7-x}Sb_{6-y}$ (orthorhombic).

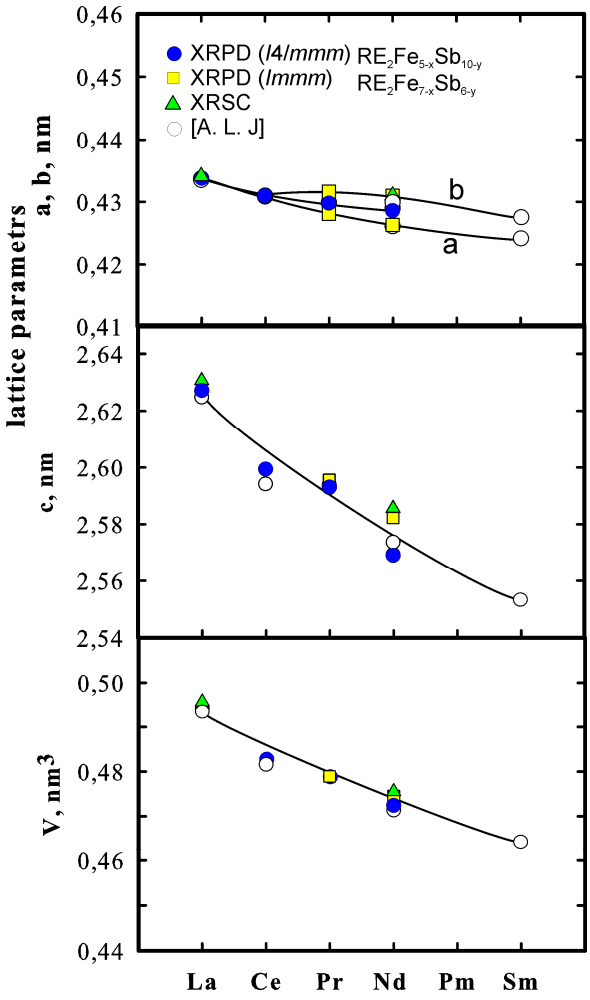

Figure 12. Lattice parameters vs. Rare earths for $RE_2Fe_{5-x}Sb_{10-y}$ (RE= La, Ce, Pr, Nd; tetragonal) and $RE_2Fe_{7-x}Sb_{6-y}$ (RE = Pr, Nd, Sm;orthorhombic).

9.3.4 Crystal Structure of τ_3 –$Nd_3Fe_3Sb_7$

XRPD analysis of the alloy with nominal composition $Nd_{22}Fe_{27}Sb_{51}$ annealed at 800 °C reveals a set of unindexed reflections which were not present in the XRPD patterns of the as cast alloys or in samples annealed at 500 °C and 900°. These reflections were automatically indexed by programme TREOR on the basis of a hexagonal cell (a ≈1.32 nm and c ≈ 0.42 nm), which was different from any of the known phases around, pointing to a new ternary compound. However, due to small grain size it was difficult to isolate a single crystal fragment from the alloy annealed at 800 °C for 7 days, therefore the sample was kept at annealing temperature for 30 days followed by quenching in cold water. XRSC measurements of a proper single crystal fragment confirm a new ternary compound with hexagonal symmetry and lattice parameters a ≈1.32nm and c ≈ 0.42nm.

The observed systematic extinctions indicated three possible space groups, $P6_322$, $P6_3/m$, $P6_3$. The crystal structure was successfully solved via direct methods in space group $P6_3/m$. The final least square cycle reveals residual electron densities as low as 3.195/-1.46 $e^-/Å^3$ corresponding to R_{F2}=0.0178. Structural details are given in Table 5a and b. The formula resulting from the refinement is $Nd_3Fe_3Sb_7$ ($Nd_{23.1}Fe_{23.1}Sb_{53.8}$ at. %) , which is in good agreement with EMPA ($Nd_{22.5}Fe_{24.3}Sb_{53.1}$). The structure of $Nd_3Fe_3Sb_7$ is shown in Figure 12. Wyckoff sequence of the atom positions is 6h 6h 6h 6h and 2c, which at first glance gives the impression of isotypism with the $Cu_{10}Sb_3$-type ($Au_{10}I_3$). However, τ_3 can be regarded as isopointal to $Cu_{10}Sb_3$ because even with similar Wyckoff positions changes in x, y parameters result in a different arrangement of Sb atoms forming walls as can be seen from Figure 12. In contrast to $Cu_{10}Sb_3$ there are two-dimensional channels of Sb with alternating short and long bonds (Figure 12b) typical for the structures of many of the antimonides [2, 28].

The structure of τ_3 can be considered as composed of three unique structural units: (i) centred triangular prisms of RE atoms, (ii) interconnected octahedra of Fe atoms running parallel to [001] (Figure 12c) forming a column of Fe atoms clusters, along the 6-fold rotation axis, and (iii) Sb ribbons which are running in between (i) and (ii) (Figure 12 a and b). Similar infinite parallel columns exist in the $Cu_{10}Sb_3$ and Ni_3Sn-type structure (S. G P63/mmm) and are formed by triangular prism (i) that are shifted against each other by c/2 (central atom at z = ¼ and ¾, Figure 13). Octahedral clusters (ii), which are linked to triangles in Ni_3Sn, are completely isolated in $Cu_{10}Sb_3$ and τ_3.

From EMPA a homogeneity range corresponding to a Fe/Sb substitution of ~ 1-1.5 at. % is observed for τ_3. However, lattice parameters and Rietveld refinement do not give any hint towards a solid solution. τ_3 was not observed in as-cast samples annealed directly at 500 °C or cooled at a rate ~ 2°/min from 900 °C to 500 °C. But if the sample which has been annealed at 800 °C containing this phase was kept at 500 °C for 30 days, the phase was still present. It seems from our observation that τ_3 formed by a solid state reaction with slow kinetics and once this phase formed it remains stable at 700 °C, 600 °C and 500 °C. The decomposition temperature of τ_3 lies somewhere between 820-900 °C, as the alloy annealed at 900 °C does not contain this phase whilst the alloy annealed at 850 °C contains this phase but only in small amounts. Annealing at 800 °C of the same alloy increases the amount of τ_3. Therefore due to improper choice of annealing temperature,

this phase was not caught by [10]. τ_3 is found to exist in equilibrium with three other ternary compounds τ_2, τ_4 and τ_5 (details in 3.2).

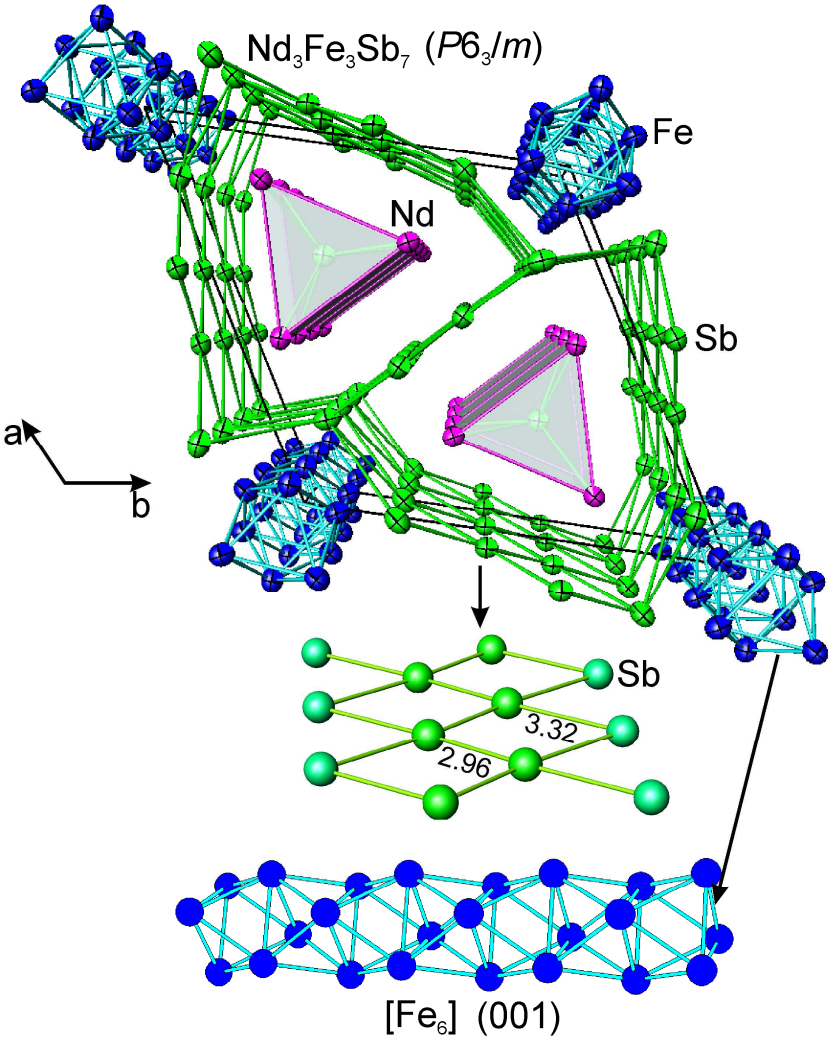

Figure 13. Crystal structure of $Nd_3Fe_3Sb_7$.

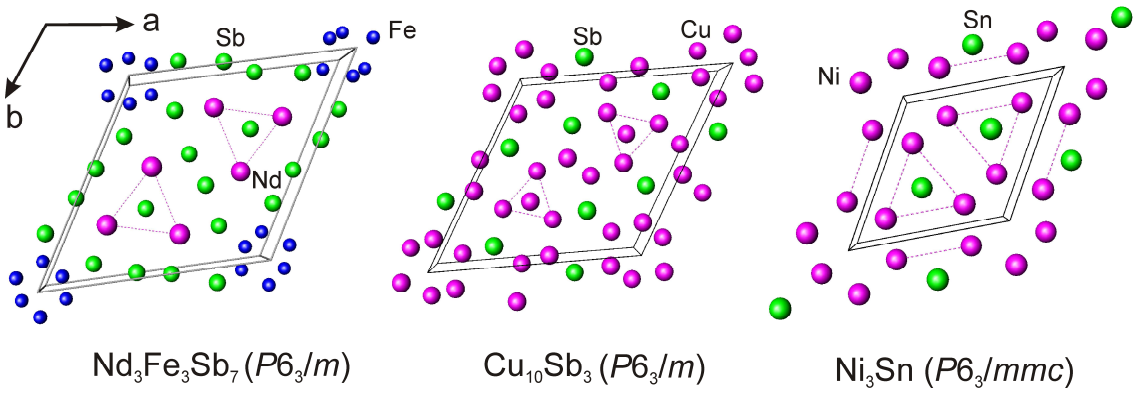

Figure 14. Comparison of structure of $Nd_3Fe_3Sb_7$ with $Cu_{10}Sb_3$ and Ni_3Sn.

Table 5a: X-Ray single crystal data for $Nd_3Fe_3Sb_7$ (τ_3); standardized with program *Structure Tidy* [40]. Radiation: MoKα; 2Θ range (°) = 2≤2Θ≤70; ω-scans, scan width 2° =280 sec/frame; Total number of frames =595 ; Anisotropic displacement parameters [in $10^2 nm^2$].

Parameter/compound	$Nd_3Fe_3Sb_7$
Prototype	$Nd_3Fe_3Sb_7$
Space group	$P6_3/m$
Composition, EMPA at.%	$Nd_{22.5}Fe_{24.3}Sb_{53.1}$
a ; c [nm], Ge standard	1.31808(3); 0.41819(3)
Z	2
Reflections measured	983≥4σ(F_o) of 1029
Number of variables	28
Mosaicity	<4.5
$R_F^2 = \Sigma\|F_o^2-F_c^2\|/\Sigma F_o^2$	0.018
R_{Int}	0.029
wR2	0.046
GOF	1.225
Extinction	0.0014
Residual density $e^-/Å^3$; max; min	3.195, -1.46
Atom parameters	
Nd1 in 6*h* (*x, y,* ¼); *x, y*	0.46133(2), 0.18310(2)
$U_{11};U_{22};U_{33}$	0.0113(1), 0.0098(1), 0.0103(1)
U_{12}; U_{eq}	0.00571(7); 0.01023(7)
Occ.	0.998(3)
Sb1 in 2*c* (1/3, 2/3, ¼); Occ.	1.012(6)
$U_{11}=U_{22};U_{33}$	0.0116(1), 0.0092(2),
U_{12}; U_{eq}	0.00581(6); 0.01081(9)
Sb2 in 6*h* (*x, y,* ¼); *x, y;* Occ.	0.08317(3), 0.27640(3); 0.994(4)
$U_{11};U_{22};U_{33}$	0.0133(1), 0.0115(1), 0.0118(1)
U_{12}; U_{eq}	0.00349(9); 0.01340(7)
Sb3 in 6*h* (*x, y,* ¼); *x, y;* Occ.	0.58845(2), 0.02317(2); 1.011(4)
$U_{11};U_{22};U_{33}$	0.0117(1), 0.0098(1), 0.0135(1)
U_{12}; U_{eq}	0.00477(9); 0.01196(7)
Fe1 in 6*h* (*x, y,* ¼); *x, y;* Occ.	0.13082(6), 0.07664(6); 1.00(1)
9.3.4.1.1.1 $U_{11};U_{22};U_{33}$	0.0148(3), 0.0123(2), 0.0104(3)
U_{12}; U_{eq}	0.0075(2); 0.0121(1)
Principal mean square atomic displacements U	
Nd1	0.0113, 0.0103, 0.0091
Sb1	0.0116, 0.0116, 0.0092
Sb2	0.0180, 0.0118, 0.0104
Sb3	0.0135, 0.0126, 0.0098
Fe1	0.0148, 0.0113, 0.0103

Table 5b: Interatomic distances [nm] for $Nd_3Fe_3Sb_7$ (τ_3); Standard deviation ≤0.0004.

Nd1-	-1Sb4	0.3205		-2Fe5	0.2737		-1Nd1	0.3288
	-2Sb2	0.3208		-1Fe5	0.3001		-2Sb3	0.3322
	-2Sb4	0.3231		-2Nd1	0.3269	Fe5-	-4Fe5	0.2578
	-2Sb3	0.3269		-2Sb4	0.3322		-2Fe5	0.2603
	-1Sb4	0.3288		-1Nd1	0.3526		-1Sb3	0.2620
	-1Sb3	0.3526		-4Sb3	0.3859		-2Sb3	0.2737
	-1Fe5	0.3856	Sb4-	-2Sb4	0.2964		-Sb3	0.30001
Sb2-	-2Nd1	0.3208		-1Nd1	0.3205		-2Fe5	0.3663
	-4Nd1	0.3208		-2Nd1	0.3231		-1Nd1	0.3856
Sb3-	-1Fe5	0.2620						

9.3.5 Crystal Structure of τ_4- $NdFeSb_3$

The crystal structure of $NdFeSb_3$ was recently determined from Rietveld refinement of the X-ray powder pattern [44] and was described as isotypic to $CeNiSb_3$ [22]. Quite recently the crystal structure of $REFeSb_3$ (RE = Pr, Nd, Sm, Gd and Tb) was reported as $LaPdSb_3$-type in an hitherto unpublished paper [45]. The model presented by [44] was not confirmed in the present work by Rietveld refinement of $NdFeSb_3$ annealed at 800°C (4 days) and 500°C (30 days). The observed XRPD pattern was successfully fitted as isotypic to the $LaPdSb_3$-type [5], which has double the c lattice parameter with respect to $RECrSb_3$ structure type [46]. $CeNiSb_3$ has a triple c-parameter as compared to $RECrSb_3$. Thomas et al. [25] discovered a new polymorph of $RENiSb_3$ with doubled c-parameter as compared to parent $RECrSb_3$ and regarded it as β modification of $RECrSb_3$ whilst $RENiSb_3$ with triple c-parameter was regarded as the α modification [22]. The β-modification was also reported recently for β-$RECoSb_3$ (RE=La-Nd, Sm) [27]. Therefore the structure of $NdFeSb_3$ (Table 6) with unit cell a=1.2677(3) nm, b=0.61613(7), c=1.2132(4) nm) with double c parameter as compared to parent $RECrSb_3$-type is regarded as β-$RECrSb_3$. The structures of the α and β-modifications are discussed in detail in Ref. [22, 27].

Table 6: X-Ray powder diffraction data for $NdFeSb_3$ (τ_4); standardized with program *Structure Tidy* [40]. Temperature factors in [in $10^2 nm^2$]).

Parameter/compound	**$NdFeSb_3$**
Prototype	$LaPdSb_3$
Space group	Pbcm
Composition, EMPA at. %	$Nd_{20.0}Fe_{19.9}Sb_{60.1}$
Composition, refinement at. %	$Nd_{20}Fe_{20}Sb_{60}$
a ;b; c [nm], Ge standard	1.2681(4); 0.61659(7); 1.2133(3)
Reflections measured	573
Θ range	8≤2Θ≤100
Number of variables	37
$R_F = \Sigma\|F_o-F_c\|/\Sigma F_o$	0.070
$R_I = \Sigma\|I_o-I_c\|/\Sigma I_o$	0.096
$R_{wP}=[\Sigma w_i\|y_{oi}-y_{ci}\|^2/\Sigma w_i\|y_{oi}\|^2]^{½}$	0.034
$R_P = \Sigma\|y_{oi}-y_{ci}\|/\Sigma\|y_{0i}\|$	0.024
$R_e = [(N-P+C)/\Sigma w_i y^2_{oi})]^{½}$	0.007
$\chi^2 = (R_{wP}/R_e)^2$	21.3
Atom parameters	
Nd1 in 4*c* **(*x*, ¼, 0); *x***	0.6999(3)
Occ. ; B_{iso}	1.01(2); 0.47
Nd2 in 4*d* **(*x, y*, ¾); *x, y***	0.31150(3), 0.2779(7)
Occ. ; B_{iso}	1.0(2); 1.7(1)
Fe in 8*e* **(*x, y, z*); *x, y, z***	0.1037(5), 0.025(1), 0.8596(5)
Occ. ; B_{iso}	1.01(2); 2.8(1)
Sb1 in 4*c* **(*x*, ¼, 0); *x***	0.9735(3)
Occ. ; B_{iso}	1.0(2); 2.24(8)
Sb2 in 4*d* **(*x, y*, ¾); *x, y***	0.7777(3), 0.2668(8)
Occ. ; B_{iso}	1.01(2); 0.98(1)
Sb3 in 8*e* **(*x, y, z*); *x, y, z***	0.5045(2), 0.5105(5), 0.8761(3)
Occ. ; B_{iso}	1.0(2); 0.59
Sb4 in 4*c* **(*x*, ¼, 0); *x***	0.2225(3)
Occ. ; B_{iso}	1.0(2); 1.2(1)
Sb5 in 4*d* **(*x, y*, ¾); *x, y***	0.9368(3), 0.9018(5)
Occ. ; B_{iso}	1.0(2); 1.8(1)

9.3.6 Magnetic and Transport Properties

The temperature dependence of the inverse molar magnetic susceptibility of $NdFeSb_3$ is shown in Figure 15a. Above about 50 K, the susceptibility follows a modified Curie-Weiss (MCW) law with the paramagnetic Curie temperature θ_p = -9.9(2) K, the effective magnetic moment μ_{eff} = 3.68(5) μ_B, and the temperature-independent term χ_0 = 5.56(2) x

10^{-4} emu/mol. The experimentally determined effective magnetic moment is very close to the free Nd^{+3} ion value of 3.62(4) μ_B, which shows that Fe atoms do not impart any magnetic influence to the magnetic properties of $NdFeSb_3$.

As is apparent from the upper inset to Figure 15a, $NdFeSb_3$ orders antiferromagnetically below T_N = 3.0(1). The isothermal magnetization at 1.7 K measured as a function of the magnetic field strength is typical for an antiferromagnetic ground state (see the lower inset to Figure 15a). Remarkably, a metamagnetic-like transition is observed near 15 kOe.

The resistivity data for $NdFeSb_3$ are presented in Figure 16a. The magnitude and shape of the resistivity curve is typical for rare earth intermetallics. The antiferromagnetic phase transition at 3.0 K manifests itself as a distinct kink in ρ (T) (see the inset to Figure 15a). Below 1 K the resistivity curve exhibits a downward curvature that may hint at another phase transition which could be associated with some spin reorientation. In the paramagnetic region, above about 70 K, the ρ(T) curve may be represented by the so-called Bloch-Grüneisen-Mott (BGM) expression [47]

$$\rho(T) = (\rho_0 + \rho_0^{\infty}) + 4RT\left(\frac{T}{\Theta_D}\right)^4 \int_0^{\Theta_D/T} \frac{x^5 dx}{(e^x - 1)(1 - e^{-x})} - KT^3$$

where $(\rho_0 + \rho_0^{\infty})$ stands for the sum of the residual resistivity due to static defects in the crystal lattice and the spin-disorder resistivity due to the presence of disordered magnetic moments, respectively. The second term describes the phonon contribution to the total resistivity (Θ_D is the Debye temperature), and the third term represents s-d interband scattering processes. Fitting the BGM model to the experimental data of $NdFeSb_3$ one obtains the values: $\rho_0 + \rho_0^{\infty}$ = 139.2(8) μΩcm, Θ_D = 193.6(9) K, R = 0.42(1) μΩcm/K and K = 1.23(3) x 10^{-6} μΩcm/K^3. Below ca. 70 K, the experimental ρ(T) curve markedly deviates from the BGM fit, likely due to crystal field contribution to the electrical resistivity that makes the ρ_0^{∞} term being temperature dependent.

The specific heat of $NdFeSb_3$ varies as a function of temperature in a usual sigmoid-shape manner (Figure 17). A small hump in C(T) centred around 7.0 K is probably due to crystal field effects (Figure 17b). At higher temperatures, the C/T vs. T^2 curve exhibits a straight-line behaviour, observed up to 24 K. From this region one may extrapolate an enhanced Sommerfeld coefficient of about 400 mJ/(mol K^2) (see the inset to Figure 17). The antiferromagnetic transition, as inferred from the magnetization and

resistivity data, is clearly corroborated by a pronounced lambda-shaped peak at T_N = 3.0 K.

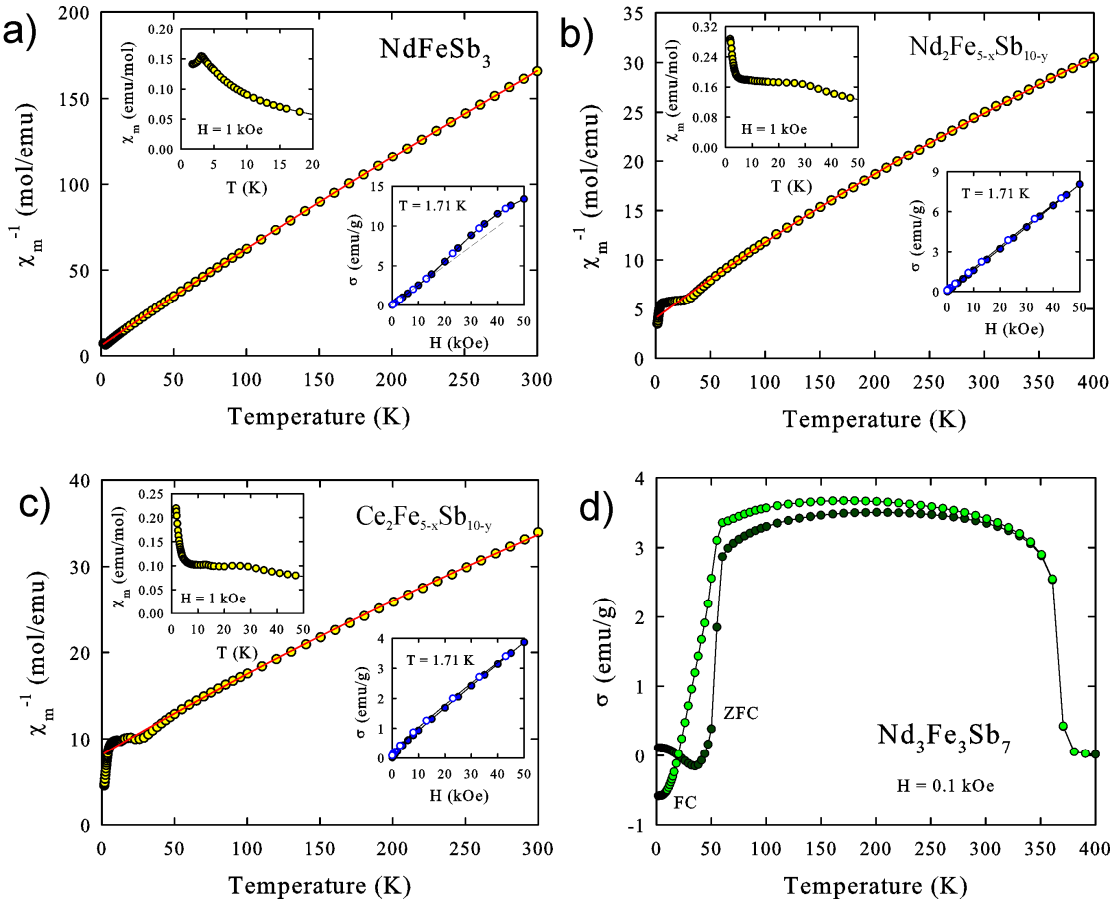

Figure 15. Temperature dependencies of the inverse magnetic susceptibility of a) $NdFeSb_3$ b) $Nd_2Fe_{5-x}Sb_{10-y}$ and c) $Ce_2Fe_{5-x}Sb_{10-y}$. The solid lines represent the modified Curie-Weiss fits discussed in the text. The upper insets show the low-temperature susceptibility measured in the field of 1 kOe, while the lower insets display the magnetization isotherms taken at 1.72 K with increasing (full symbols) and decreasing (open symbols) magnetic field. d) The magnetization vs. temperature measured for $Nd_3Fe_3Sb_7$ in a magnetic field of 0.1 kOe upon cooling the specimen in zero (ZFC) and applied field (FC).

The magnetic data obtained for $Nd_2Fe_{5-x}Sb_{10-y}$ (τ_2) and isotypic $Ce_2Fe_{5-x}Sb_{10-y}$ are presented in Figures 15b and 15c, respectively. For both compounds the magnetic susceptibility exhibits a plateau below 30 K and then shows an upturn below about 5 K (see the upper insets). The isothermal magnetization taken at 1.7 K is almost linear with the magnetic field strength (cf. the lower insets) and shows no hysteresis effect. For both compounds, above 50 K the magnetic susceptibility exhibits a modified Curie-Weiss behaviour. The least-squares fit of the MCW law to the experimental data yielded the following values: μ_{eff} = 9.6(1) μ_B, θ_p = -48.1(3) K and χ_0 = 7.0(5) x 10^{-3} emu/mol for the

Nd-based compound, and μ_{eff} = 8.6(1) μ_B, θ_p = -78.9(4) K and χ_0 = 5.2(5) x 10^{-3} emu/mol for the Ce-based phase. As the so-derived effective magnetic moments are much larger than the values for the respective free RE^{+3} ions, some magnetic contribution due to the Fe sublattice becomes obvious. Assuming that the magnetic moments on the Nd ions contribute to the total μ_{eff} the Russell-Saunders value of 3.63 μ_B, one obtains a value μ_{Fe} = 4.2 μ_B for the Fe-contribution in $Nd_2Fe_{7-x}Sb_{6-y}$. This magnetic moment is slightly smaller than the theoretical spin-only value of 4.97 μ_B for an Fe^{2+} ion.

If in $Ce_2Fe_{5-x}Sb_{10-y}$ the Fe sublattice contributes the same moment as in the Nd-based counterpart, then the effective magnetic moment associated with Ce ions is 1.7 μ_B, i.e. it is distinctly smaller than that expected for trivalent cerium (2.54 μ_B). The latter finding is in line with the indication from the lattice parameters towards a Ce^{4+} state. From these arguments one may expect that Ce ions in $Ce_2Fe_{5-x}Sb_{10-y}$ have an unstable 4f shell.

The latter conjecture finds further support in the behaviour of the electrical resistivity of the compound (Figure 16c) which is reminiscent of the properties of Ce intermetallics governed by Kondo effect. Apparently, the resistivity of $Ce_2Fe_{5-x}Sb_{10-y}$ exhibits a maximum near 30 K followed by a negative slope at higher temperatures. As displayed in Figure 16c, above about 70 K, ρ(T) may be approximated by the formula

$$\rho(T) = (\rho_0 + \rho_0^{\infty}) + c_{ph}T + c_K \ln T$$

where the second term stands for the phonon contribution to the total resistivity, while the third term represents the spin-flip Kondo scattering of conduction electrons on localised magnetic moments. The parameters derived from the least-squares fit are as follows: $\rho_0 + \rho_0^{\infty}$ = 241.0(2) μΩcm, c_{ph} = 0.037(4) μΩcm/K and c_K = -13.0(3) μΩcm. The enhanced value of the latter coefficient implies fairly large density of states at the Fermi level, and significant mass enhancement due to interactions of Ce 4f electronic states with conduction electron states. Further studies on the intriguing electrical transport phenomena in $Ce_2Fe_{5-x}Sb_{10-y}$ are presently underway and will be reported in a separate article.

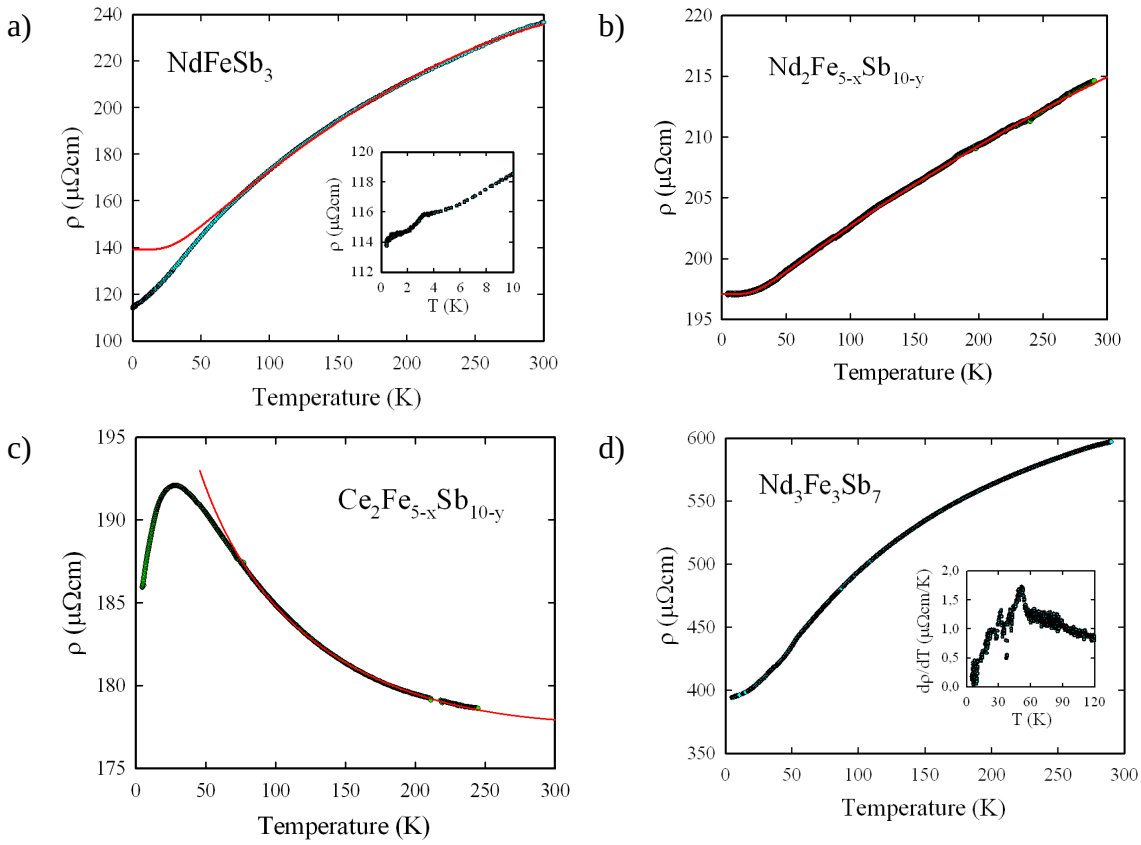

Figure 16. Temperature variations of the electrical resistivity of a) $NdFeSb_3$, b) $Nd_2Fe_{5-x}Sb_{10-y}$, c) $Ce_2Fe_{5-x}Sb_{10-y}$ and d) $Nd_3Fe_3Sb_7$. The inset to a) displays the low-temperature part of the electrical resistivity. The inset to b) shows the temperature derivative of the electrical resistivity in the low temperature range. The solid lines in a) and b) are the Bloch-Grüneisen-Mott fits discussed in the text. The solid line in c) is a Kondo fit (see the text).

In contrast to the Ce-based compound, the electrical resistivity of $Nd_2Fe_{5-x}Sb_{10-y}$ shows a regular metallic behaviour (Figure 16b). In the entire temperature range studied, the ρ(T) curve may be described within the BGM approach. Fitting the BGM model to the experimental data of $Nd_2Fe_{5-x}Sb_{10-y}$ one derives the values: $\rho_0 + \rho_0^{\infty} = 197.1(3)$ μΩcm, $\Theta_D = 167.9(6)$ K, R = 0.066(2) μΩcm/K and K = 6.0(1) x 10^{-8} μΩcm/K^3. As the BGM formalism neglects crystal field interactions that likely affect ρ(T) of $Nd_2Fe_{5-x}Sb_{10-y}$ at low temperatures, the above values should be considered as rough estimations only.

As documented in Figure 15d, the magnetic behaviour of $Nd_3Fe_3Sb_7$ is fairly complex. The compound orders magnetically at about 360 K, likely with a ferri- or ferromagnetic arrangement of both neodymium and iron magnetic moments. This magnetic state becomes unstable around 50 K, and at lower temperatures the magnetization curves measured in zero field cooling (ZFC) and field cooling (FC) regimes display very

unusual behaviour. In order to clarify these complex features, neutron diffraction studies are indispensable.

The electrical resistivity of $Nd_3Fe_3Sb_7$ has metallic character (Figure 16d). Because the compound is in the magnetically ordered state up to the upper temperature limit of the measurements performed, no attempts to analyse ρ(T) in terms of particular contributions were made. At the hypothetical phase transition at about 50 K the resistivity curve shows a clear kink, which brings about a pronounced anomaly in the temperature derivative of the resistivity (see the inset to Figure 16d).

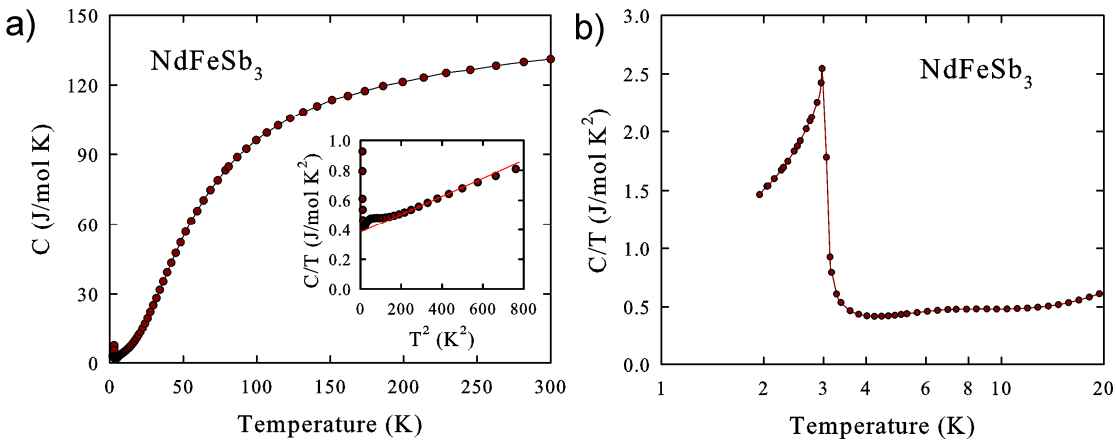

Figure17. a) Temperature dependence of the specific heat of $NdFeSb_3$. The inset presents C/T vs. T^2. The solid line represents the fit discussed in the text. b) Temperature variation of the C/T ratio at low temperatures on a logarithmic scale.

9.4 Conclusions

Systematic investigations using XRDP, XRSC, LOM and EPMA were made in the Nd-Fe-Sb system and an isothermal section at 800 °C was constructed. Five ternary compounds take part in the phase equilibria at 800 °C. The ternary compounds, $Nd_6Fe_{13}Sb$ (τ_1) and $NdFe_{1-x}Sb_2$ (τ_5), already known in literature, were confirmed in the present work, whilst the crystal structures for three ternary compounds $La_2Fe_{5-x}Sb_{10-y}$, $Nd_2Fe_{7-x}Sb_{6-y}$ (τ_2), $Nd_3Fe_3Sb_7$ (τ_3), and $NdFeSb_3$ (τ_4) were established in the present investigations. The crystal structure of τ_2, τ_3 were determined by single crystal x-ray diffraction. Two different modifications were found for τ_2: tetragonal is $La_2Fe_{5-x}Sb_{10-y}$ -type (S. G *I*4/*mmm*, a = 0.42897(2), c = 2.5693(4)) and orthorhombic is $Nd_2Fe_{7-x}Sb_{6-y}$-type (S.G. *Immm*, a = 0.42632(6), b = 0.43098(7), c = 2.5823(3)). $Ce_2Fe_{5-x}Sb_{10-y}$ was found isotypic to the tetragonal $La_2Fe_{5-x}Sb_{10-y}$–type, while compound with Pr and Nd were found in both modifications. $La_2Fe_{5-x}Sb_{10-y}$–type is found similar to $Zr_3Cu_4Si_6$-

type with one additional Wyckoff position. Structural relations between orthorhombic and tetragonal modification and with other structure types were described. τ_3 ($Nd_3Fe_3Sb_7$) was found to crystallize with a unique structure type (S. G $P6_3/m$, a=, c=) and is isopointal to the $Cu_{10}Sb_3$-type. Similarities among the structures of τ_3($Nd_3Fe_3Sb_7$), $Cu_{10}Sb_3$ and Ni_3Sn were discussed in detail. The structure of (τ_4) was solved by Rietveld refinement of the X-ray powder pattern and was found isotypic to $LaPdSb_3$, which is the β-modification of the $RECrSb_3$ type with a doubled c-parameter.
$NdFeSb_3$ orders antiferromagnetically below ~3.0 K, as manifested in all the bulk characteristics of the compound: temperature variations of the magnetic susceptibility, the specific heat and the electrical resistivity. The latter data hint at another order-order phase transition at about 1 K. In this compound the magnetic features are associated exclusively with Nd ions. In contrast, in all the other ternaries studied likely also the Fe sublattices significantly contribute to the overall magnetic behaviour. As a result, $Nd_2Fe_{5-x}Sb_{10-y}$, $Ce_2Fe_{10-x}Sb_{6-y}$ and, $Nd_3Fe_3Sb_7$ exhibit very complex physical properties that call for further studies with the use of other experimental techniques, especially neutron diffraction.

References

[1] O. L. Sol, P. S. Salamakha, in: K. A. Gschneidner Jr., J. C. G. Bünzli, V. K. Pecharsky (Eds.), Handbook on the Physics and Chemistry of Rare Earth, Elsevier, Amsterdam 33 (2003).

[2] A. M. Mills, R. Lam, M.J. Ferguson, L. Deakin, A. Mar, Coord. Chem. Rev. 207–222 (2002) 233.

[3] C. Rizzoli, O. L. Sologub, L. P. Salamakha, A. P. Goncalves, J. Alloys Compd. 431 (2007) 85.

[4] O. L. Sologub, L. P. Salamakha, H. Noel, T. Roisnel, A. P. Concalves, J. Alloys Compd. 45 (2008) 215.

[5] E. L. Thomas, D. P. Gautreaux, J. Y. Chan, Acta Cryst. E62 (2006), i96.

[6] A. Leithe-Jasper, PhD thesis, University of Vienna (1994).

[7] P. Salamakha, J. Alloys Compd. 267 (1998) L16.

[8] O. Sologub, P. Salamakha, J. Alloys Compd. 285 (1999) L16.

[9] S. I. Chykhrij, V. B. Smetana, Inorg. Mater. 42 (2006) 503.

[10] Z. Lingmin; Q. Pingli, N. Liangqin; Z. Jiliang; L. Jiangping, J. Alloys Compd. 437 (2007) 84.

[11] L. Jingqi; W. Lina, C. Xuehong, L. Wenjun, Zong Bo; L. Junqin, J. Alloys Compd. 456 (2008) 135.

[12] L. Jingqi, L. Wenjun, Zong Bo, W. Lina, C. Xuehong, L. Junqin, J. Alloys Compd. 456 (2008), (1-2) 101.

[13] R. M. Luo, F. S. Liu, J. Q. Li, X. W. Feng, J. Alloys Compd. 471 (2009) 60.

[14] Jingqi Liu, Bo Zong, Xiaomao Yang, Xuehong Cui, Kunpeng Su, Xina Wang, Junqin Li, J. Alloys Compd. 468 (2009) 103-106.

[15] C. Uher, Semiconduct. Semimet. 69 (2001) 139.

[16] G. S. Nolas, J. Sharp, H. J. Goldsmid, Thermoelectrics: Basic Principles and New Materials Developments, Springer-Verlag, Heidelberg (2001).

[17] J. P. Fleurial, A. Borshchevsky, T. Caillat, D. T. Morelli, G. P. Meisner, Proc. 15th Int. Conf. on Thermoelectrics (ICT 1996) IEEE, New York, pp. 91.

[18] X. Shi, H. Kong, C.P. Li, C. Uher, J. Yang, J.R. Salvador, H. Wang, L. Chen, W. Zhang, Appl. Phys. Lett. 92 (2008) 182101.

[19] L. Zhang, A. Grytsiv, P. Rogl, E. Bauer, M. J. Zehetbauer, J. Phys. D: Appl. Pys. 42 (2009) 225405.

[20] G. Rogl, A. Grytsiv, E. Bauer, P. Rogl, M. Zehetbauer, Intermetallics 18 (2010) 394.

[21] G. Rogl, A. Grytsiv, E. Bauer, P. Rogl, M. Zehetbauer, Intermetallics. 18 (2010) 57.

[22] R. T. Macaluso, D. M. Wells, R. E. Sykora, T. E. Albrecht-Schmitt, A. Mar, S. Nakatsuji, H. Lee, Z. Fisk, and J. Y. Chan, J. Solid State Chem. 177 (2004) 293-298.

[23] E. L. Thomas, R. T. Macaluso, Han-Oh Lee, Z. Fisk, J. Y. Chan, J. Solid Stat Chem. 177 (2004) 4228.

[24] E. L. Thomas, J. N. Millican, E. K. Okudzeto, J. Y. Yan, Comm. Inorg. Chem. 27 (2006) 1.

[25] E. L. Thomas, D. P. Gautreaux, H. O. Lee, Z. Fisk and Julia Y. Chan, Inorg. Chem. 46 (2007) 3010.

[26] D. P. Gautreaux, C. Capan, J. F. DiTusa, D. P. Young, J. Y. Chan, J. Solid State Chem. 181 (2008) 1977.

[27] Wei-Zhao Cai, Li-Ming Wu, Long-Hua Li, and Ling Chen, Eur. J. Inorg. Chem. (2009) 230.

[28] N. Nasir , A. Grytsiv , P. Rogl , A. Saccone , G. Giester, J. Solid Stat Chem. 182 (2009) 645.

[29] J. M. D. Coey, Qi. Qinian, K. G. Knoch, A. Leithe-Jasper, P. Rogl, J. Magnetism and Magnetic Mater. (1994), 129(1), 87-97.

[30] A. Leithe-Jasper, P. Rogl, J. Alloys Compd. 203 (1994) 133-136.

[31] Nonius Kappa CCD Program Package COLLECT 1998 DENZO, SCALEPACK, SORTAV, Nonius Delft, The Netherlands.

[32] G. M. Sheldrick, SHELXL-97, Program for Crystal Structure Refinement. University of Göttingen, Germany; Windows version by McArdle, Natl. Univ. Ireland, Galway (1997).

[33] G. Cacciamani, R. ferro, H. L. Lukas, Zeitschrift für Metallkunde 83 (1992) 669.

[34] T. B. Masasalski, Binary Alloy Phase Diagrams, 2nd ed., ASM International, Materials Park, OH, (1990).

[35] K. Hennemann, H. L. Lukas, H. J. Schaller, Zeitschrift für Metallkunde, 84 (1993) 668.

[36] T. Schmidt, R. O. Altmeyer, W. Jeitschko, J. Solid State Chem. 173 (2003) 259.

[37] C. B. H. Evers, W. Jeitschko, L. Boonk, D. J. Braun, T. Ebel, U. D. Scholz, J. Alloys Compd. 224 (1995) 184.

[38] P. Villars, L. D. Calvert, Pearson's Handbook of Crystallographic Data for Intermetallic Phases, 2nd ed., ASM International, Materials Park, OH, 1991

[39] Pauling File Binaries Edition, Version 1.0, Realize 2002/1, ASM Intl, Materials Park, OH, USA.

[40] E . Parthé Gelato L, B. Chabot, M. Penzo, K. Cenzual, and R. Gladyshevskii, TYPIX - Standardized Data and Crystal Chemical Characterization of Inorganic Structure Types (Berlin Heidelberg: Springer – Verlag) (1994)

[41] H. Bärnighausen, Commun. Math. 9 (1980) 139.

[42] H.Bärnighausen, U.Müller, Symmetriebeziehungen ZwischendenRaum- gruppen als Hilfsmittelzur Straffen Darstellung von Strukturzusammenha¨n-gen in der Kristallchemie, University of Karlsruhe and University of GH Kassel (1996).

[43] F. Thirion, G. Venturini, B. Malaman, J. Steinmetz, B. Roques, J. Less Common Metals 95 (1983) 47-54.

[44] Q. Pingli, N. Liangqin, Z. Jiliang, Q. Haiqing, L. Jiangping, Z. Lingmin, Key Engineering Mater. .353-358 (2007) 3043.

[45] W. A. Phelan, M. Parent, T. A. Dobbins, D. P. Young , J. Y. Chan , Abstracts of Papers, 238th ACS National Meeting, Washington, DC, United States, August 16-20 (2009).

[46] M. I. Fergusen, R. W. Hushagen, A. Mar, J. Alloys Compd. 249 (1997) 191.

[47] N. F. Mott and H. Jones, The Theory of the Prop. Metals and Alloys, Oxford University Press (1958)

10 Antimony rich corner of Ce-TM-Sb Systems (TM= Ti, Zr, Hf, V, Nb, Ta, Cr, Mo, W, Mn, Re, Cu, Ag, Zn, Cd) at 600 °C.

10.1 Introduction

Ternary transition metal antimonides with rare earths represent a large group of compounds with diverse structural and physical properties. One of the antimony rich examples is the filled skutterudites with $LaFe_4Sb_{12}$ structure, which are an emerging class of compounds with promising thermoelectric properties [1, 2, 3, 4, 5]. As a logical continuation of our research for new thermoelectric materials, we attempt to prepare a series of antimony rich alloys with cerium and transition metal elements (TM= Ti, Zr, Hf, V, Nb, Ta, Cr, Mo, W, Mn, Re, Cu, Ag, Zn, Cd) in order to find new promising phases and their phase relations. The list of the selected transition metals cover a broad field of transition metals in the periodic chart (Figure 1). The TM from group VIII are from complex antimonides including the skutterudite type. We studied phase relations, crystal structures of ternary compounds and physical properties in the Nd-Fe-Sb system (See Chapter 9). Some of the known ternary compounds in the antimony rich corner are RE_6TMSb_{15} (RE= La, Ce; TM=Mn, Cu, Zn) [6], $REZn_{1-x}Sb_2$ (RE=La, Ce, Pr, Nd, Sm, Gd, Tb) [7] $RETM_{1-x}Sb_2$ RE, $CeAgSb_2$ [8], $CeCuSb_2$ [9] and $RE_2Ti_7Sb_{12}$ (RE=La, Ce, Pr, Nd) [10].

10.2 Experimental

Alloys (1-2g) with nominal composition $CeTMSb_6$ were prepared by powder metallurgy in the following way. Master alloy $CeSb_2$ was prepared by reaction of elemental ingots of Ce (99.9%) and Sb (99.99%) in evacuated quartz tubes at 600 °C. The reaction product was then powderized to get a homogenous master alloy. Stoichiometeric amounts of $CeSb_2$ master alloy and fine filings of the corresponding transition metal element (each with purity 99.99%) or fine powders in case of Re, Mn, W were mixed and compacted into tablets of 1 cm diameter prior to cold pressing in steel die. Each

sample was sealed in an evacuated quartz tube and reactions were carried out at 600 °C except for Zn, Cd containg alloys which were reacted at 300-400 °C first and then temperature was slowly increase to 600 °C. After one week the alloys samples were quenched in cold water and tablets were repowderized and cold compacted again and placed again at 600 °C for one week in order to ensure complete reaction. After one week the samples were quenched in cold water.

X-ray powder diffraction data from each alloy were collected employing a Guinier-Huber image plate system with Cu–$K_{\alpha 1}$ or Fe-$K_{\alpha 1}$ (8° < 2θ < 100°). Precise lattice parameters were calculated by least-squares fits to indexed 4θ-values employing Ge as internal standard (a_{Ge} = 0.5657906 nm).

10.3 Results and Discussion

Information on the binary boundary systems Ce-Sb, TM-Sb, Ce-TM were accepted after [11, 12]. Crystallographic data for all unary, binary and ternary phases are compiled in Table 1. X-ray powder analysis of the alloys annealed at 600 °C reveals three-phase equilibria in the antimony rich corner of the Ce-TM-Sb systems (TM =Ti, Zr, Hf, V, Nb, Ta, Cr, Mo, W, Mn, Re, Cu, Ag, Zn, Cd). Partial isothermal sections at 600 °C for the antimony rich corner for all these systems are presented in Figure. 1. No ternary compound was found with Ti, Zr, Hf, V, Nb, Cr, Re. Ternary compounds, $CeCuSb_2$ and $CeAgSb_2$ (S.G *P*4/*nmm* with $ZrCuSi_2$ structure [8, 9], Ce_6ZnSb_{15}, Ce_6CuSb_{15}, and Ce_6MnSb_{15} (S. G. *Imm*2, with La_6MnSb_{15} structure [6] were confirmed. The compound Ce_6CuSb_{15} reported in the ref. 6] was not mentioned by Morozkin et al. [13] in the Ce-Cu-Sb system at 670/870 K. However a small intensity corresponding to Ce_6CuSb_{15} was observed in the present work. The unknown peaks in the x-ray profiles of the alloys with Mo, W and Cd were indexed as new compounds Ce_6MoSb_{15}, and Ce_6WSb_{15}, and Ce_6CdSb_{15} with La_6MnSb_{15} structure type. A series of compounds $RE_6Zn_{1+x}Sb_{14+y}$ (RE=Pr, Sm, Gd-Ho) related to the La_6ZnSb_{15} type is reported by Liu et al. [14] also with orthorhombic symmetry but in space group *Immm*. X-ray powder pattern of τ_1 observed in present work resemble more closely to the La_6ZnSb_{15} type. However complete structural determinations are needed. Data for phase equilibria are summarized in Table 2. The derived phase equilibria for all transition metals studied can be classified into three types depending on the existence of binary or ternary compounds as shown in

Figure 1. Type I with no ternary compound and (Sb) is in equilibrium with (i) $CeSb_2$ and $TMSb_2$ (TM= Ti, Zr, Hf, V, Nb, Ta, Cr) and (ii) $CeSb_2$ and TM (TM=Re). Type II is with one ternary compound τ_1 where τ_1 and (Sb) are in equilibrium with τ_1 and binary compounds Mo_3Sb_7 or MnSb or with transition metal (W). In type III two ternary compounds and τ_1 (Ce_6TMSb_{15}) and τ_2 ($CeTMSb_2$) (where TM=Ag, Cu, Zn, Cd) are in equilibrium with (Sb). This classification can be seen in the Periodic chart shown in Figure 2. TM is from group IVB, VB, Cr (VIB) and Re (VIIB) belong to type I phase equilibria and TM is from Group IB and IIB belong to type III equilibria, Whilst TM is from group VIB belong to Type II with the exception of Cr which comes with Type I. Mn from VIIB shows type II equilibria while Re belongs to type I.

IVB	VB	VIB	VIIB	VIII	VIII	VIII	IB	IIB
Ti I	V I	Cr I	Mn II	Fe	Co	Ni	Cu III	Zn III
Zr I	Nb I	Mo II	Tc	Ru	Rh	Pd	Ag III	Cd III
Hf I	Ta I	W II	Re I	Os	Ir	Pt	Au	Hg

Figure 2. Periodic chart highlighting the TM used in present work and corresponding class of phase equilibria I, II, III indicate types of phase equilibria.

Table 1. Crystallographic data for relevant solid phases in the Ce-TM-Sb systems (TM= TM =Ti, Zr, Hf, V, Nb, Ta, Cr, Mo, W, Mn, Re, Cu, Ag, Zn, Cd).

Phase	Space Group	Structure type		Lattice parameter		Reference
(Sb)	$R\bar{3}m$	As	0.43084	-	1.12470	[11]
(W)	$Im\bar{3}m$	W	0.31652	-	-	[11]
(Re)	$P6_3/mmc$	Mg	0.27609	-	0.4458	[11]
$CeSb_2$	*Cmca*	$SmSb_2$	0.6280	0.6130	1.8240	[11]
$ZrSb_2$	Pnma	$PbCl_2$	0.7393(1)	0.39870(7)	0.9581(1)	[15]
$TiSb_2$	*I*4/*mcm*	$CuAl_2$	0.66531(5)	-	0.58092(7)	[16]
α-$HfSb_2$	Pnnm	$TiAs_2$	0.9869(5)	1.4981(12)	0.3848(3)	[17]
VSb_2	*I*4/*mcm*	$CuAl_2$	0.65541	-	0.56385	[16]
$TaSb_2$	*C*12/*m*1	$OsGe_2$	1.022	0.3644; β=120.4	0.828	[18]
$NbSb_2$	*C*12/*m*1	$OsGe_2$	1.0239	0.36319 β=120.07	0.8333	[19]
$CrSb_2$	Pnnm	FeS_2	0.60183(4)	0.68736(2)	0.32704(2)	[20]
Mn1.1Sb	$P6_3/mmc$	Ni_2In	0.4230	-	0.5700	[21]
Mo_3Sb_7	$Im\bar{3}m$	Ru_3Sn_7	0.95713(8)	-	-	[22]
Ce_6MoSb_{15} (τ_1)	*Imm*2	La_6MnSb_{15}	1.5237(2)	1.9291(3)	0.4313(8)	This work
Ce_6WSb_{15} (τ_1)	*Imm*2	La_6MnSb_{15}	0.4326(1)	1.5242(9)	1.926(3)	Thist work
Ce_6CdSb_{15}(τ_1)	*Imm*2	La_6MnSb_{15}	1.5228(3)	1.9321(8)	0.43240(6)	Thist work
Ce_6MnSb_{15}(τ_1)		La_6MnSb_{15}	1.5150(4)	1.9387(7)	0.42931(8)	Thist work
			1.51538(2)	1.93646(3)	0.427422(7)	[6]
Ce_6ZnSb_{15} (τ_1)	*Imm*2	La_6MnSb_{15}	1.5221(7)	1.9276(8)	0.43203(6)	This work
			1.5215(2)	1.9264(6)	o.43215(5)	[6]
$CeCuSb_2$ (τ_2)	*P4/nmm*	$ZrCuSi_2$	0.43346(4)	-	1.0257(3)	This work
			0.43378(6)	-	1.0233(5)	[9]
$CeAgSb_2$ (τ_2)	*P4/nmm*	$ZrCuSi_2$	0.43718(3)	-	1.0741(7)	This work
			0.43641(9)	-	1.0722(4)	[9]

Table 2. Three phase equilibria and lattice parameters for the antimony rich corner of the Ce-TM-Sb systems(TM= Ti, Zr, Hf, V, Nb, Ta, Cr, Mo, W, Mn, Re, Cu, Ag, Zn, Cd).

Nominal Composition	**Phase equilibria**	**Phases**	**Lattice parameters, nm**		
			a	***b***	***c***
$CeTiSb_6$	(Sb)– $TiSb_2$– $CeSb_2$	$TiSb_2$	0.66525(2)	-	0.58081(6)
		(Sb)	0.43074(6)	-	1.1279(2)
		$CeSb_2$	0.6271(4)	0.6150(2)	1.822(1)
$CeZrSb_6$	(Sb)– $ZrSb_2$– $CeSb_2$	$ZrSb_2$	1.4967(9)	0.9966(3)	3.8814(3)
		Sb	0.43057(8)	-	1.126(1)
		$CeSb_2$	0.6275(2)	0.6152	1.8231(3)
$CeHfSb_6$	(Sb)– $HfSb_2$– $CeSb_2$	Sb	0.43072(5)	-	1.1282(2)
		$CeSb_2$	0.62954(7)	0.61497(8)	1.82493)
		$HfSb_2$	1.4996(7)	0.9878(2)	0.38511(3)
$CeVSb_6$	(Sb)– VSb_2– $CeSb_2$	VSb_2	0.65528(8)	-	0.5640(1)
		Sb	0.43094(6)	-	1.1276(4)
		$CeSb_2$	0.6275(1)	0.6153(1)	1.823(2)
$CeNbSb_6$	(Sb)– $NbSb_2$– $CeSb_2$	Sb	0.43068(5)	-	1.1276(3)
		$CeSb_2$	0.62769(8)	0.6154(9)	1.823(4)
		$NbSb_2$	1.0233(8)	0.36301(3)	0.8328(7)
$CeTaSb_6$	(Sb)– $TaSb_2$– $CeSb_2$	Sb	0.43066(5)	-	1.1278(4)
		$CeSb_2$	0.6275(2)	0.6149(3)	1.820(2)
		$TaSb_2$	1.0221(6)	0.36460(2)	0.82917(5)
$CeCrSb_6$	(Sb)– $CrSb_2$– $CeSb_2$	Sb	0.43082(3)	-	1.1283(4)

Nominal Composition	Phase equilibria	Phases	Lattice parameters, nm		
			a	***b***	***c***
		$CeSb_2$	0.62778(4)	0.61560(2)	1.824(1)
		$CrSb_2$	0.60274(9)	0.6873(2)	0.32714(2)
$CeMoSb_6$	(Sb)– Mo_3Sb_7– τ_1	Sb	0.43073(6)	-	1.1274(7)
		Mo_3Sb_7	0.95711(4)	-	-
		Ce_6MoSb_{15} (τ_1)	1.5237(2)	1.9291(3)	0.4313(8)
$CeWSb_6$	(Sb)– (W)– τ_1	Sb	0.43092(8)	-	1.1274(7)
		W	0.31653(1)	-	-
		Ce_6WSb_{15} (τ_1)	1.5242(9)	1.926(3)	0.4326(1)
$CeMnSb_6$	(Sb)– MnSb– τ_1	Sb	0.43092(8)	-	1.1274(7)
		MnSb	0.41299(4)	-	0.5792(1)
		Ce_6MnSb_{15} (τ_1)	1.5150(4)	1.9387(7)	0.42931(8)
$CeReSb_6$	(Sb)– (Re)–$CeSb_2$	Sb	0.43056(3)	-	1.1280(3)
		$CeSb_2$	0.6278(2)	0.6153(2)	1.819(3)
		Re	0.27611(1)	-	0.44582(3)
$CeCuSb_6$	(Sb)– τ_1– τ_2	Sb	0.43075(7)	-	1.1285(4)
		$CeCuSb_2$ (τ_2)	0.43346(4)	-	1.0257(3)
		Ce_6CuSb_{15} (τ_1)	1.6311	2.0765	0.4162
$CeAgSb_6$	(Sb)– τ_1– τ_2	Sb	0.43055(3)	-	1.1274(5)
		τ_1	-	-	-
		$CeAgSb_2$ (τ_2)	0.43718(3)	-	1.0741(7)
$CeZnSb_6$	(Sb)– τ_1– τ_2	Sb	0.43070(8)	-	1.1269(4)
		Ce_6ZnSb_{15} (τ_1)	1.5221(7)	1.9276(8)	0.43203(6)
		$CeZn_{1-x}Sb_2$ (τ_2)	-	-	-
$CeCdSb_6$	(Sb)– τ_1– τ_2	Sb	0.43075(6)	-	1.1282(3)
		Ce_6CdSb_{15} (τ_1)	1.5228(3)	1.9321(8)	0.43240(6)
		$CeCd_{1-x}Sb_2$ (τ_2)	-	-	-

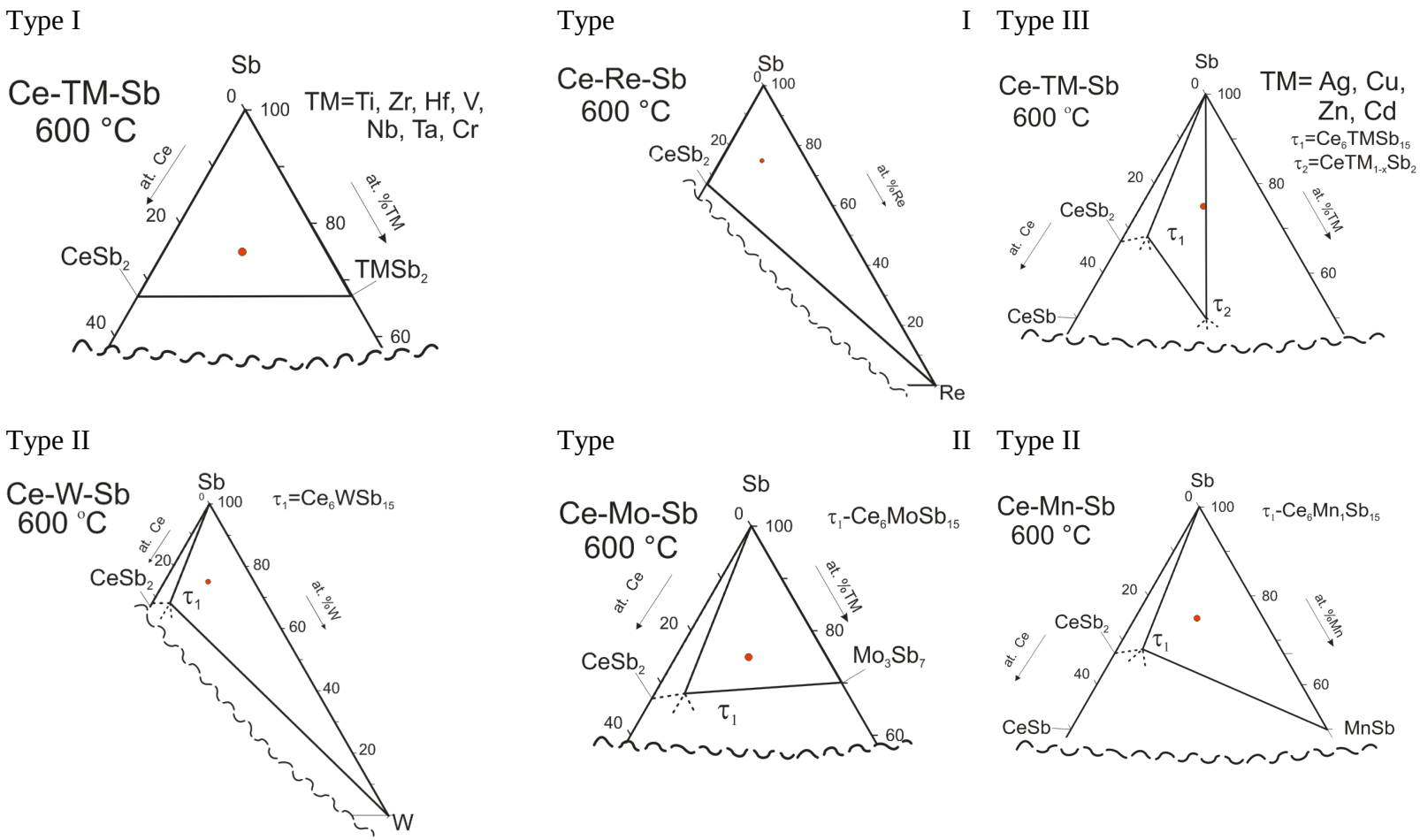

Figure 1. Partial isothermal sections for Ce-TM-Sb systems at 600 °

References

[1] G. S. Nolas, D. T. Morelli, T. M. Tritt, Annu. Rev. Mater. Sci. 29 (1999) 89.

[2] C. Uher, Semiconduct. Semimet. 69 (2001) 139–253.

[3] W. Schnelle, A. Leithe-Jasper, H. Rosner, R. Cardoso-Gi, R. Gumeniuk, D. Trots, J.A. Mydosh, Y. Grin, Phys. Rev. B 77 (2008) 094421.

[4] M. M. Koza, M. R. Johnson, R. Viennois, H. Mutka, L. Girard, D. Ravot, Nature Mater. 7 (2008) 80$\tilde{5}$710.

[5] G.J. Snyder, E.S. Toberer, Nature Mater. 7 (2008) 105−114.

[6] O. Sologub, M. Vybornov, P. Rogl, K. Hiebl, G. Cordier, P. Woll, J. Solid State Chem. 122 (1996) 266.

[7] O. Ya. Zelinska, A. Mar, J. Solid State Chem. 179 (2006) 3776.

[8] O. Sologub, H. Noel, A. Leithe-Jasper, P. Rogl, , O. I. Bodak, J. Solid State Chem. 115 (1995) 441.

[9] O. Sologub, K. Hiebl, P. Rogl, H. Noel, O. Bodak, J. Alloys Comp. 210 (1994) 153.

[10] Haiying Bie, S. H. D. Moore, D. G. Piercey, A. V. Tkachuk, O. Y. Zelinska, A. Mar, J. Solid State Chem. 180 (2007) 2216.

[11] T. B. Masasalski, Binary Alloy Phase Diagrams, 2nd ed., ASM International, Materials Park, OH, (1990).

[12] Pauling File Binaries Edition, Version 1.0, Realize 2002/1, ASM Intl, Materials Park, OH, USA.

[13] A. V. Morozkin, V. N. Nikiforov, N. Imaoka, I. Morimoto, J. Alloys Comp. 422 (2006) L5.

[14] Yi Liu, L. Chen, Long-Hua Li, Li-Ming Wu, Inorg. Chem. 47 (2008) 11930.

[15] E. Garcia, J. D. Corbett, J. Solid State Chem. 73 (1988) 440.

[16] J. D. Donaldson, A. Kjekshus, D. G. Nicholson, T. Rakke, J. Less- Common Metals 41 (1975) 255.

[17] F. Hulliger, Nature (LONDON) 204 (1964) 991.

[18] F. Hulliger, Nature (LONDON) 204 (1964) 775.

[19] S. Furuseth, A. Kjekshus, Nature (London) 203 (1964) 512.

[20] H. Holseth, A. Kjekshus, A. F. Andresen, Acta Chem. Scand. 24 (1970) 3309.

[21] V. G. Vanyarkho, N. A. Moshchalkova, V. M. Gunchenko, N. V. Fadeeva, Inorg. Mater. 24 (1988) 762.

[22] P. Jensen, A. Kjekshus, Acta Chem. Scand. 20 (1966) 417.

Summary

Throughout this thesis the synthesis, crystal structure of the new/unknown ternary compounds and phase equilibria in the systems potential for thermoelectric applications were studied using classical arc melting and powder metallergical techniques, X-ray Powder Diffraction (XRPD), X-ray Single Crystal Diffraction (XRSCD), Light Optical Microscopy (LOM), and Electron Probe Micro Analysis (EPMA).

Novel compounds $Ba_8\{Zn,Cd\}_{\sim 7}Si_{\sim 39}$ with clathrate type I structure and with no appreciable homogeneity range were discovered and their crystal structure was elucidated with x-ray single crystal data for the Zn compound and Rietveld refinement of the x-ray powder pattern for the Cd compound. Einstein temperature of about 80 K for Ba (2) was derived from the temperature dependent Debye-Waller factor for the Zn clathrate.

Vacancy-free quaternary clathrate solid solutions $Ba_8Zn_xGe_{46-x-y}Si_y$, $Ba_8(Zn,Cu)_xGe_{46-x}$ and $Ba_8(Zn,Pd)_xGe_{46-x}$ were synthesised and complete structural evaluations were made on the basis of x-ray powder diffraction and x-ray single crystal analyses. The isothermal section at 800 °C was constructed for the quaternary system Ba-Pd-Zn-Ge and partial isothermal sections ″Ba_8Ge_{46}″-″Ba_8Pd_{46}″-″Ba_8Zn_{46}″, ″Ba_8Ge_{46}″-″Ba_8Cu_{46}″-″Ba_8Zn_{46}″ and ″Ba_8Ge_{46}″-″Ba_8Si_{46}″-″Ba_8Zn_{46}″ at 800 °C were presented.

Phase equilibria in the systems Ce-M-Sb (M = Si, Ge, Sn) were studied in the phase region $CeSb_2$-Sb-M. No ternary compound was found in the Ce-Si-Sb system in the phase region CeSb-Si-Sb. The ternary compound $Ce_{12}Ge_{9-x}Sb_{23+x}$ was found to adopt a superstructure of the $La_6Ge_{2.8}Sb_{13.2}$ type with space group *C*222 and lattice parameters doubled in direction a (0.86075(2) nm) and b (2.15154(4) nm) while c (2.68227(5) nm) remains the same resulting in a unit cell with volume and Z four times bigger that of the $La_6Ge_{2.8}Sb_{13.2}$ type. The group subgroup relations for symmetry reduction was work out. Partial isothermal sections at 200 and 400°C were constructed for the Ce-Sn-Sb system.

Phase relations were derived in the Sr-poor regions of the systems Sr–Ni–Si (at 900 °C) and Sr–Cu–Si (at 800 °C). Two new ternary compounds τ_2-$SrNiSi_3$ ($BaNiS_{n3}$-type), τ_3-$SrNi_{9-x}Si_{4+x}$ (own type) were found and the structure of τ_3 $SrNi_{9-x}Si_{4+x}$ (own

type) was solved by x-ray single crystal analysis and was found to be a primitive tetragonal variant of the $NaZn_{13}$-type with S. G. *P*4/*nbm*. Compositional polymorphism was observed for $SrCu_{13-x}Si_x$ ($1.8 \leq x \leq 4$) ($NaZn_{13}$-type) and $SrCu_{9-x}Si_{4+x}$ ($0 \leq x \leq 1.0$) ($CeNi_{8.5}Si_{4.5}$-type).

The crystal structure of a novel compound $BaCo_{5-x}Ge_9$ (x=0.29) was determined from X-ray single crystal counter data as a unique structure type. Isotypic compounds were found for $SrCo_{5-x}Ge_9$ and $EuCo_{5-x}Ge_9$ (x~0.3). Structural details were provided for numerous new compounds in the related systems Ba-M-X (M=Pd, Pt, Cu, Zn, Cd, Rh, Ir; X=Si, Ge).

An isothermal section at 800 °C was constructed for the Nd-Fe-Sb system. Crystal structures for four ternary compounds $Nd_2Fe_{7-x}Sb_{6-y}$ (τ_2), $La_2Fe_{5-x}Sb_{10-y}$, $Nd_3Fe_3Sb_7$ (τ_3), and $NdFeSb_3$ (τ_4) were established. Two different modifications were found for τ_2: tetragonal is $La_2Fe_{5-x}Sb_{10-y}$–type (S. G *I*4/*mmm*, a=0.42897(2), c=2.5693(4)) the structure of which is also established in present work and orthorhombic is $Nd_2Fe_{7-x}Sb_{6-y}$-type (S.G. *Immm*, a=0.42632(6), b=0.43098(7), c=2.5823(3)). Isotypic compounds were found with Ce and Pr. Compound with Ce is adopt tetragonal structure and compounds with Pr exhibit both modifications. τ_3 ($Nd_3Fe_3Sb_7$) crystallizes with a unique structure type (S. G $P6_3/m$, *a =1.31808(3)nm, c = 0.41819(3)*) exhibiting interesting structural features and is isopointal to the $Cu_{10}Sb_3$-type. τ_4 adopts the $LaPdSb_3$-type, which is the β-modification of the $RECrSb_3$ type with doubled c-parameter. Physical properties including magnetism, electrical conductivity and specific heat were measured for selected compounds in Nd-Fe-Sb system and isotypic compounds with La and Ce. $NdFeSb_3$ orders antiferromagnetically below ~3.0 K, as manifested in all the bulk characteristics of the compound: temperature variations of the magnetic susceptibility, the specific heat and the electrical resistivity. In this compound the magnetic features are associated exclusively with Nd ions. In contrast Fe sublattices significantly contribute to the overall magnetic behaviour of $RE_2Fe_{5-x}Sb_{10-y}$ (RE= Nd, Ce). $Nd_3Fe_3Sb_7$ exhibits very complex physical properties that call for further studies with the use of other experimental techniques, especially neutron diffraction.

List of Publications

1. *Phase equilibria in systems Ce–M–Sb (M = Si, Ge,Sn) and superstructure* $Ce_{12}Ge_{9-x}Sb_{23+x}$ *(x = 3.870±1)*
   N. Nasir, A. Grytsiv, P. Rogl, A. Saccone, G. Giester, J. Solid State Chem. 182 (2009) 645-656.

2. *Crystal structure and physical properties of* $EPCo_{4.7}Ge_9$ *(EP = Sr, Ba, Eu)*
   N. Nasir, N. Melnychenko-Koblyuk, A. Grytsiv, P. Rogl, E. Bauer, E. Royanian, H. Michor, G. Hilscher, G. Giester Intermetallics, 17 (2009) 471-476.

3. *Clathrates* $Ba_8\{Zn, Cd\}_xSi4_{6-x}$, *x ~ 7: synthesis, crystal structure and thermoelectric properties*
   N. Nasir, A. Grytsiv, N. Melnychenko-Koblyuk, P. Rogl, E. Bauer, R. Lackner, E. Royanian, G. Giester and A. Saccone, , J. Phys.: Condens. Matter 21 (2009) 385404/1-12.

4. *Ternary systems Sr–{Ni,Cu}–Si: Phase equilibria and crystal structure of ternary phases*
   N. Nasir , N. Melnychenko-Koblyuk , A. Grytsiv , P. Rogl, G. Giester , J. Wosik , G. E. Nauer , J. Solid State Chem., 183 (2010) 565-574.

5. *Crystal Structure and Physical Properties of Quaternary Clathrates* $Ba_8Zn_xGe_{46-x-y}Si_y$, $Ba_8(Zn,Cu)_xGe_{46-x}$ *and* $Ba_8(Zn,Pd)_xGe_{46-x}$.
   N. Nasir, A. Grytsiv, N. Melnychenko-Koblyuk, P. Rogl, I. Bednar, E. Bauer, submitted.

6. *The system Nd-Fe-Sb: Phase equilibria, crystal structures and physical properties.*
   N. Nasir, A. Grytsiv, P. Rogl, H. Effenberger, D. Kaczorowski, submitted.

7. *Formation of clathrates Ba-M-Ge (M = Mn, Fe, Co),*
   A. Grytsiv, N. Melnychenko-Koblyuk , N. Navida, P. Rogl , A. Saccone, H. Scmid, Int. J. Mater. Res. 100 (2009) 189-202.

8. *Lattice dynamics of clathrates (I) type* $Ba_8Zn_xGe_{46-x-y}\square_y$.
   M. M. Koza, M. Johnson, M. Rotter, N. Nasir, A. Grytsiv, P. Rogl, to be submitted.

9. *Giant thermopower at low temperatures in novel clathrates* $Ba_8\{Cu,Zn\}_xGe_{46-x}$
   I. Bednar, G. Csaszar, M. Menhart, S. Bühler-Paschen, E. Bauer, N. Nasir, A. Grytsiv, N. Melnychenko-Koblyuk, P. Rogl, International Conference on Thermoelectrics (ICT), Freiburg, Germany (2009).

CURRICULUM VITAE

Name:	Navida Nasir
Father's Name:	Talab Din
Husband" Name:	Nasir Mehboob
Nationality:	Pakistani
Religion:	Islam
Date of Birth:	21-04-75

2001.03-2002-03: Exective I (Reasearch, Development and Quality Control), Tripack films, Hattar Industrial State, Pakistan.

2001: Master of Philosophy (M. Phil), Physical Chemistry, Quaid-i-Azam University, Islamabad, Pakistan.

1999: Master of Science (M. Sc), Chemistry, Quaid-i-Azam University, Islamabad, Pakistan.

1996: Bachelor of Science, Punjab University, Pakistan.

1994: Higher Secondary School Certificate, Govt. Post. Grad. College for Women St.Town Rawalpindi, Pakistan.

1991: Secondary School Certificate, Govt High School Pindigheb, Pakistan.

Distinctions & Awards

- Award for Ph. D studies Abroad (Austria), Higher Education Commission of Pakistan.
- Distinction in M. Phil and M. Sc (Gold Medals & Certificate of Merit), Quaid-i-Azam University Islamabad, Pakistan.
- Distinction in Secondary School Certificate Examination (1991).
- President Scholarship of UGC for Master Studies (1997-99)
- Merit Scholarship for M. Phil Studies, Quaid-i-Azam University Islamabad (1999-2000).
- Merit Scholarship for Higher Secondary School Studies (1991-93)

Publications

- M. Mohammad, A. Y. Khan, M. S Subhani, N. Bibi, S. Ahmad, S. Saleemi, *Kinetics & Electrochemical studies on superoxide*, Res. Chem. Intermed. 27, (2001) 259-267.
- N. Bibi, M. I. Sarwar, M. Ishaq, Z. Ahmad. *Mechanical and thermal properties of nanocomposites of poly (vinyl chloride) and co-poly (vinyl chloride-vinyl alcohol-vinyl acetate) with montmorillonite.* Polymers & Polymer Composites 15 (2007) 313-319.